

**GUILHERME FEITOSA ROSETTI**

IMPROVEMENTS IN THE NUMERICAL MODELING OF  
TURBULENCE AND FLUID-STRUCTURE INTERACTION FOR  
THE VORTEX-INDUCED VIBRATIONS OF A RIGID CYLINDER

SÃO PAULO

2015



**GUILHERME FEITOSA ROSETTI**

**IMPROVEMENTS IN THE NUMERICAL MODELING OF  
TURBULENCE AND FLUID-STRUCTURE INTERACTION FOR  
THE VORTEX-INDUCED VIBRATIONS OF A RIGID CYLINDER**

Thesis submitted to the Escola Politécnica da  
Universidade de São Paulo for the partial fulfil-  
ment of the requirements for the degree of  
Doctor of Science

SÃO PAULO  
2015



**GUILHERME FEITOSA ROSETTI**

IMPROVEMENTS IN THE NUMERICAL MODELING OF  
TURBULENCE AND FLUID-STRUCTURE INTERACTION FOR  
THE VORTEX-INDUCED VIBRATIONS OF A RIGID CYLINDER

Thesis submitted to the Escola Politécnica da  
Universidade de São Paulo for the partial fulfil-  
ment of the requirements for the degree of  
Doctor of Science

Research Area:  
Naval Architecture and Ocean Engineering

Supervisor: Prof. Dr. André Luis C. Fajarra

SÃO PAULO  
2015

Este exemplar foi revisado e corrigido em relação à versão original, sob responsabilidade única do autor e com a anuência de seu orientador.

São Paulo, \_\_\_\_\_ de \_\_\_\_\_ de \_\_\_\_\_

Assinatura do autor: \_\_\_\_\_

Assinatura do orientador: \_\_\_\_\_

### Catálogo-na-publicação

Rosetti, Guilherme Feitosa

Improvements in the Numerical Modeling of Turbulence and Fluid Structure Interaction for the Vortex-Induced Vibrations of a Rigid Cylinder / G. F. Rosetti -- versão corr. -- São Paulo, 2015.  
247 p.

Tese (Doutorado) - Escola Politécnica da Universidade de São Paulo.  
Departamento de Engenharia Naval e Oceânica.

1.CFD 2.Modelos de turbulência 3.Modelos de transição 4.Interação fluido estrutura 5.Cilindro rígido I.Universidade de São Paulo. Escola Politécnica. Departamento de Engenharia Naval e Oceânica II.t.

This thesis is dedicated to my mother Miriam,  
to my father Edson, for all the dedication and  
love to me.

To Priscila, for the patience and love, which  
were so necessary along the way.



# ACKNOWLEDGMENTS

I would like to express my gratitude to my supervisor and friend Prof. André Luis Condino Fajarra, who has supervised my scientific work for many years and with whom I have shared numerous enriching discussions.

I deeply thank my good friend and supervisor at MARIN, Guilherme Vaz, for so many years of friendship, guidance, discussions and trust. I hope we can continue learning from each other.

I gratefully acknowledge Prof. Kazuo Nishimoto for providing me many academic opportunities and for the perseverance in maintaining an industry-oriented research environment, which is something of great need in our country. I am also very thankful to Prof. Eduardo Aoun Tannuri, Prof. Claudio Mueller Prado Sampaio and Prof. Alexandre Nicolaos Simos of the laboratory TPN-USP for the research opportunities.

I acknowledge the Department of Naval Architecture and Ocean Engineering of USP and MARIN and all their staff for the opportunities and assistance.

I also thank Prof. Celso Pupo Pesce, Prof. Fábio Saltara and Prof. Guilherme Franzini for the relevant technical advice and help with my thesis.

I would like to thank Chris Klaij from MARIN and James Hawkes from the University of Southampton for the discussions and their technical help in executing some of the tasks in this thesis. I also thank Prof. Luís Eça from Instituto Superior Técnico in Lisbon for the chance to learn from him and his help during this work.

I acknowledge FAPESP (Fundação de Amparo à Pesquisa do Estado de São Paulo) for the financial support through grants 2010/10939-4 and 2011/20137-5. I also thank the

technical advisors and administrative staff for their work and help with the affairs related with this doctoral work. Special thanks to my friends and colleagues at MARIN, Bastien Abeil, Douwe Rijpkema, Adam Peddle, Jaap de Wilde, Bas Buchner and Arjen Koop. Also from TPN-USP: Rodolfo Gonçalves and Edgard Malta, for fruitful discussions.

My gratefulness to my friends Rafael Watai, Felipe Ruggeri and Rodrigo Lavieri with whom I have shared great and tough moments, always with perseverance and good spirit.

To my good friends Emílio Gallucci, Fábio Gallucci, Haroldo Júnior, special thanks for sharing good times for so many years.

I thank my fiancée Priscila, for sharing dreams and strength to continue building a great future. Your patience, perseverance, joy and love have pushed me forwards in all times. I also thank her family, for making me feel they are my own.

Finally and foremost, I cannot be grateful enough to my parents, Miriam and Edson, to my sister and brother, Mariana and Gustavo and to my aunt and uncle, Mary and Derli, for so much support and love throughout my life. I hope I can be as important to you as you are to me.

# RESUMO

Esta tese apresenta o desenvolvimento e aplicação de modelos de turbulência, transição laminar-turbulenta e de interações fluido-estrutura ao escoamento externo em cilindro rígido estacionário e em vibrações induzidas por vórtices. Tais desenvolvimentos foram realizados no código ReFRESCO, baseado em técnicas de dinâmica de fluidos computacional (CFD). Realizou-se um estudo quanto ao desempenho do modelo  $k-\omega$  SST em extensa faixa de números de Reynolds, segundo o qual se identificaram as deficiências de modelagem para este escoamento. A modelagem adaptativa às escalas (SAS) e o modelo de transição por correlações locais (LCTM), ambos combinados ao SST, melhoraram a aderência aos resultados experimentais para este escoamento, em uma contribuição original deste trabalho. A aplicação de técnicas de verificação e validação possibilitou a estimativa de incertezas e erros para os modelos e números de Reynolds e também é identificada como outra contribuição deste trabalho. A combinação da modelagem em SST, SAS e LCTM com movimentos impostos é realizada para números de Reynolds moderados, diferentes frequências e amplitudes de vibração, algo que poucas publicações abordam em detalhes. Com relação aos movimentos livres, este trabalho traz contribuições com a aplicação dos modelos SST e SAS ao estudo de vibrações induzidas por vórtices em dois graus de liberdade, baixa razão de massa e números de Reynolds moderados, mais altos do que normalmente observados na literatura. Por fim, a investigação da importância relativa de efeitos da turbulência aos casos de movimentos livres e impostos, com relação ao caso de cilindro estacionário, comprovou a conjectura formulada na parte inicial deste trabalho, no que tange à escolha do modelo de turbulência em determinadas aplicações. Tal escolha mostrou-se menos decisiva no caso do cilindro em movimento imposto e ainda menos nos movimentos livres, em comparação ao caso estacionário, uma vez que a resposta em movimentos do corpo filtra grande parte dos efeitos turbulentos de ordem superior. Esta observação mostra-se relevante, uma vez que pode permitir simplificações na modelagem e aplicação de ferramentas de CFD em uma classe importante de projetos de engenharia.

**Palavras-chave:** CFD, modelos de turbulência, modelos de transição, interação fluido-estrutura, cilindro rígido



# ABSTRACT

This thesis presents the development, implementation and application of turbulence and laminar-turbulent transition models and fluid-structure capabilities to address the vortex-shedding and vortex-induced vibrations of a rigid cylinder. These numerical developments have been carried out in the computational fluid dynamics (CFD) code ReFRESKO. In the current work, an investigation of the performance of the turbulence modeling with  $k-\omega$  SST in a broad range of Reynolds numbers is carried out identifying its modeling deficiencies for this flow. The implementation and systematic application of the scale adaptive simulations (SAS) and the local correlation transition model (LCTM), both combined with the SST, have improved the agreement with experimental results for the cylinder flow, in a novel contribution of this work. The application of verification and validation technique has allowed the estimation of numerical errors and uncertainties for the different models. That is also identified as a contribution of this thesis. The combination of SST modeling with imposed motions is carried out as well as with the SAS and LCTM for moderate Reynolds numbers, different vibration frequencies and amplitudes, which is considered novel, as few publications address this issue in extent. Regarding the free-moving cylinder capabilities, the present work brings contributions with the application of SST and SAS-SST with free-moving cylinder for the study of VIV of two degrees-of-freedom, low mass ratio and moderate Reynolds numbers, higher than commonly seen in the literature. Finally, the investigation of the relative importance of turbulence effects on the free-moving cylinder and the imposed-motions case, with respect to the fixed case is carried out. A natural conjecture that has been raised early on this work and proved correct is that, for engineering applications, the choice of turbulence modeling strategy is less decisive when the cylinder is moving with prescribed motion and even less stringent, for free motions as the body response filters most of the higher order turbulence effects. That is a relevant observation as it might allow modeling simplifications and the application of CFD tools to a range of engineering problems.

**Keywords:** CFD, turbulence models, transition models, fluid-structure interaction, rigid cylinder



# List of Figures

Figure 2.1: Writing the fluid equations of motion in inertial and non-inertial coordinate frames. . . . .	50
Figure 2.2: Eccentricity vector. . . . .	57
Figure 3.1: Sketch representing the stages of transition (SCHLICHTING H., 2000). . . . .	73
Figure 4.1: Fluid-structure coupling with explicit weak Rung-Kutta coupling scheme. . . . .	87
Figure 4.2: Fluid-structure coupling with implicit weak Adams-Bashforth-Mouton coupling scheme. . . . .	88
Figure 4.3: Fluid-structure coupling with implicit strong Adams-Bashforth-Moulton coupling scheme. . . . .	89
Figure 6.1: The steady wake behind the cylinder for $Re < 49$ (WILLIAMSON, 1996). . . . .	102
Figure 6.2: The laminar and two-dimensional vortex shedding at $Re = 150$ (WILLIAMSON, 1996). . . . .	103
Figure 6.3: Flow pictures showing mode A on the left frame and mode B on the right one. Mode B is marked by finer structures and smaller wave length than in mode A. Pictures taken from Williamson (1996). . .	104
Figure 6.4: Particle Image Velocimetry measurements of the shear layer vortices showing the flow at $Re = 10,000$ . Picture taken from Williamson (1996). . . . .	105
Figure 6.5: Pre-critical Reynolds numbers flow (BASU, 1985). Laminar separation takes place upstream of the transition. . . . .	106
Figure 6.6: Transitional Reynolds numbers flow (BASU, 1985). Separation-reattachment bubble causes turbulent separation downstream compared to lower Reynolds numbers. . . . .	106

Figure 6.7:	Post critical Reynolds numbers flow (BASU, 1985). The transition takes place upstream of separation causing the formation of a narrow wake and low drag coefficients. . . . .	107
Figure 6.8:	Grid and domain used in the calculations. . . . .	110
Figure 6.9:	Detail of the mesh close to the cylinder. The shapes seen are typical of a nested-refinement technique. . . . .	111
Figure 6.10:	Infinity and RMS norms for evaluating the residuals of the flow quantities in the case $Re = 40$ . . . . .	113
Figure 6.11:	Infinity and RMS norms for evaluating the residuals of the flow quantities in the case $Re = 1 \times 10^5$ . (a) Velocities and pressure. (b) Turbulent kinetic energy and turbulent frequency. Illustration of the worst iterative convergence obtained for all calculations of the present work. . . . .	113
Figure 6.12:	Surface fit for $St$ and $Re = 100$ . The size of the blocks indicate the uncertainty of each data point. The convergence orders are $p = 1.0$ for space and $p = 1.6$ for time. . . . .	115
Figure 6.13:	Surface fit for $C_{Davg}$ and $Re = 200$ . The size of the blocks indicate the uncertainty of each data point. The convergence orders are $p = 2.0$ for space and $p = 1.4$ for time. . . . .	116
Figure 6.14:	Drag coefficient calculations for $Re = 1 \times 10^3$ . The size of the blocks indicate the uncertainty of each data point. In this case, the order of convergence of time and space are, respectively, $p = 1.5$ and $p = 1.7$ . . . . .	117
Figure 6.15:	Time step refinement for the calculation of Strouhal numbers for $Re = 5 \times 10^5$ . Oscillatory behavior is identified in this case. . . . .	117
Figure 6.16:	Sensitivity of the drag coefficient to different space and time discretizations for turbulent range. (a) Different grids with the finest time steps. (b) Different time step discretization with the finest grid. . . . .	118
Figure 6.17:	Drag coefficient results from laminar calculations. Experimental data from Schlichting H. (2000), ESDU (1985). The label “Experiments” denotes the average experimental values and the uncertainty bars are calculated both for the experiments and for the calculations. . . . .	119
Figure 6.18:	Field plots of normalized velocity. (a) $Re = 5$ . (b) $Re = 10$ . (c) $Re = 20$ . (d) $Re = 30$ . (e) $Re = 40$ . (f) $Re = 50$ . . . . .	120
Figure 6.19:	Drag coefficient results from laminar calculations. Experiments from Schlichting H. (2000), ESDU (1985). The label “Experiments” denote the average experimental values and the error bars are calculated both for the experiments and for the calculations. . . . .	121
Figure 6.20:	Strouhal number results from laminar calculations. Experimental formulas from Norberg (2003). . . . .	122

Figure 6.21: Drag and lift time traces and power spectrum densities from calculation with finest grid and time step for $Re = 100$ . Only steady-state portion is used for the statistics. . . . .	123
Figure 6.22: Time traces of separation angles and power spectrum densities from calculations with finest grid and time step for $Re = 200$ . Both upper and lower separation angles are shown. Only steady-state portion is used for the statistics. . . . .	123
Figure 6.23: Field plots of normalized velocity at the point of largest lift coefficient. (a) $Re = 100$ . (b) $Re = 200$ . . . . .	124
Figure 6.24: Drag coefficient results from turbulent calculations. Experiments from Schlichting H. (2000), ESDU (1985), Franzini et al. (2012), Achenbach & Heinecke (1981) and from MARIN. The label “Experiments” denotes the average experimental values and the error bars are calculated both for the experiments and for the calculations. . .	125
Figure 6.25: Strouhal number results from turbulent calculations. Experimental formulas from Norberg (2003). . . . .	126
Figure 6.26: Time traces of separation angles for $Re = 1,000$ with finest grid and time step. Only steady-state portion is used for the statistics. .	126
Figure 6.27: Time traces of separation angles for $Re = 10,000$ with finest grid and time step. Only steady-state portion is used for the statistics. .	127
Figure 6.28: Strouhal number results from turbulent calculations. Experimental formulas from Norberg (2003). . . . .	127
Figure 6.29: Field plots of normalized vorticity, $\omega D/U_{ref}$ at the point of largest lift coefficient. (a) $Re = 1,000$ . (b) $Re = 10,000$ . (c) $Re = 100,000$ . (d) $Re = 500,000$ . . . . .	128
Figure 6.30: Field plots showing streamlines at the point of largest lift coefficient. (a) $Re = 1,000$ . (b) $Re = 10,000$ . (c) $Re = 100,000$ . (d) $Re = 500,000$ . . . . .	129
Figure 6.31: Field plots of normalized eddy viscosity, $\nu_t/\nu$ at the point of largest lift coefficient. (a) $Re = 1,000$ . (b) $Re = 10,000$ . (c) $Re = 100,000$ . (d) $Re = 500,000$ . . . . .	130
Figure 6.32: Drag coefficient results from the complete range of calculations. Experiments from Schlichting H. (2000), ESDU (1985), Franzini et al. (2012), Achenbach & Heinecke (1981) and from MARIN. . . . .	134
Figure 6.33: Drag coefficient results from the complete range of calculations. Experiments from Norberg (2003). . . . .	134
Figure 6.34: Drag coefficient results from the complete range of calculations. Experiments from Norberg (2003). . . . .	135

Figure 7.1: Grid and domain used in the calculations. . . . .	139
Figure 7.2: Infinity and RMS norms for evaluating the residuals of the flow quantities in the case $Re = 6.31 \times 10^4$ . (a) Velocities and pressure. (b) Turbulent kinetic energy and turbulent frequency. Illustration of typical iterative convergence obtained for three-dimensional calculations. . . . .	141
Figure 7.3: Convergence studies for the SAS calculations at $Re = 3,900$ and $Re = 100,000$ . The different lines represent calculations done with the same grids and the finest time steps are denoted by $t_i/t_{min} = 1$ . . . . .	142
Figure 7.4: Drag and lift time traces and power spectrum densities from calculation with finest grid and time step for $Re = 20,000$ with three-dimensional SST-SAS. The steady-state portion is used for the statistics. . . . .	144
Figure 7.5: Drag and lift time traces and power spectrum densities from calculation with finest grid and time step for $Re = 100,000$ with three-dimensional SST-SAS. The steady-state portion is used for the statistics. . . . .	144
Figure 7.6: Drag coefficients from calculations with three-dimensional SST-SAS compared to two-dimensional SST results and experiments from Schlichting H. (2000), ESDU (1985), Franzini et al. (2012), Achenbach & Heinecke (1981) and from MARIN. . . . .	145
Figure 7.7: Strouhal number results from three-dimensional SST-SAS and two-dimensional SST models. Experimental values from Norberg (2003). . . . .	145
Figure 7.8: Strouhal numbers from calculations with three-dimensional SST-SAS compared to two-dimensional SST results and experiments from Norberg (2003). . . . .	146
Figure 7.9: Q criterion isosurfaces ( $Q = \frac{1}{2}(W^2 - S^2)/\ [S]\ ^2 = 0.2, 0.5, 1.0$ ) colored with nondimensional longitudinal velocity for calculations at $Re = 3,900$ with ReFRESKO. (a) Two-dimensional calculations with SST model extracted from Pereira, Vaz & Eça (2015). (b) Three-dimensional calculations with SST model extracted from Pereira, Vaz & Eça (2015). (c) Present SST-SAS calculations. . . . .	147
Figure 7.10: Q-criterion iso-surfaces ( $Q = \frac{1}{2}(W^2 - S^2)/\ [S]\ ^2 = 0.2, 0.5, 1.0$ ) for $Re = 3,900$ : (a) colored by turbulence intensity and (b) colored by nondimensional eddy viscosity. . . . .	148
Figure 7.11: Q-criterion iso-surfaces ( $Q = \frac{1}{2}(W^2 - S^2)/\ [S]\ ^2 = 0.2, 0.5, 1.0$ ) for $Re = 20,000$ : (a) colored by turbulence intensity and (b) colored by nondimensional eddy viscosity. . . . .	149

Figure 7.12: Activation of the SST-SAS term in equation 3.20, $Q_{SAS}$ . Iso-surfaces with $(Q_{SAS}D^2/U_{ref}^2 = 0.2, 0.5, 1.0)$ colored by nondimensional eddy viscosity for: (a) $Re = 20,000$ and (b) $Re = 100,000$ . . . . .	149
Figure 7.13: Infinity and RMS norms for evaluating the residuals of the flow quantities in the case $Re = 757,000$ with the finest grid. (a) Velocities and pressure. (b) Turbulent kinetic energy (k), turbulent frequency ( $\omega$ ), intermittency factor $\gamma$ and the correlation $Re_{\theta t}$ . Typical iterative convergence obtained for the calculations of the present work.	152
Figure 7.14: Example of grid and time step convergence of drag coefficients for $Re = 128,000$ calculated with LCTM. The space convergence order is $p_x = 1.0$ , whereas convergence order in time is $p_t = 2.0$ . . . . .	153
Figure 7.15: Drag and lift time traces and power spectrum densities from calculation with finest grid and time step for $Re = 757,000$ with two-dimensional LCTM. The steady-state portion is used for the statistics. . . . .	155
Figure 7.16: Drag coefficients for the present calculations with the LCTM in comparison with experiments from Schlichting H. (2000), ESDU (1985), Achenbach & Heinecke (1981), kindly contributed by MARIN and with previous numerical results shown in this thesis. . . . .	155
Figure 7.17: RMS of lift coefficients for the present calculations with the LCTM compared with experiments from Norberg (2003) and with previous numerical results shown in this thesis. . . . .	156
Figure 7.18: Strouhal numbers for the present calculations with the LCTM compared with experiments from Norberg (2003) and with previous numerical results shown in this thesis. . . . .	156
Figure 7.19: Field plots of normalized eddy viscosity and intermittency for $Re = 128,000$ . . . . .	157
Figure 7.20: Field plots of normalized eddy viscosity and intermittency for $Re = 757,000$ . . . . .	158
Figure 7.21: Drag coefficient results from the complete range of calculations. Experiments from Schlichting H. (2000), ESDU (1985), Franzini et al. (2012), Achenbach & Heinecke (1981) and from MARIN. . . . .	161
Figure 7.22: RMS of lift coefficient results from the complete range of calculations. Experiments from Norberg (2003). . . . .	162
Figure 7.23: Strouhal number results from the complete range of calculations. Experiments from Norberg (2003). . . . .	162
Figure 8.1: Setup and grid layout used in the calculations with imposed motion.	167

Figure 8.2: Grid and time step convergence analysis for the imposed motion calculations. . . . .	168
Figure 8.3: Typical velocity and pressure residuals for the calculations with imposed motions using two-dimensional $k-\omega$ SST. Results for $U_R = 4.0$ in the first set of experiments (GOPALKRISHNAN, 1993). . . .	169
Figure 8.4: Typical turbulent quantities residuals for the calculations with imposed motions using two-dimensional $k-\omega$ SST. Results for $U_R = 4.0$ in the first set of experiments (GOPALKRISHNAN, 1993). . . . .	169
Figure 8.5: Imposed motion and lift coefficient traces with $U_R = 3.0$ and two-dimensional SST for the first set of experiments (GOPALKRISHNAN, 1993). . . . .	171
Figure 8.6: Drag and lift time traces on the cylinder with $U_R = 3.0$ and two-dimensional SST for the first set of experiments (GOPALKRISHNAN, 1993). . . . .	171
Figure 8.7: Nondimensional instantaneous velocity in the near wake of oscillating cylinder at $U_R = 3.0$ and two-dimensional SST for the first set of experiments (GOPALKRISHNAN, 1993). Taken from the point of minimum lift coefficient. . . . .	172
Figure 8.8: Imposed motion and lift coefficient traces with $U_R = 10.0$ and two-dimensional SST for the first set of experiments (GOPALKRISHNAN, 1993). . . . .	172
Figure 8.9: Drag and lift time traces on the cylinder with $U_R = 10.0$ and two-dimensional SST for the first set of experiments (GOPALKRISHNAN, 1993). . . . .	173
Figure 8.10: Nondimensional instantaneous velocity in the near wake of oscillating cylinder at $U_R = 10.0$ and two-dimensional SST for the first set of experiments (GOPALKRISHNAN, 1993). Taken from the point of minimum lift coefficient. . . . .	173
Figure 8.11: Imposed motion and lift coefficient traces with $U_R = 5.0$ and two-dimensional SST for the first set of experiments (GOPALKRISHNAN, 1993). . . . .	174
Figure 8.12: Drag and lift time traces on the cylinder with $U_R = 5.0$ and two-dimensional SST for the first set of experiments (GOPALKRISHNAN, 1993). . . . .	175
Figure 8.13: Nondimensional instantaneous velocity in the near wake of oscillating cylinder at $U_R = 5.0$ and two-dimensional SST for the first set of experiments (GOPALKRISHNAN, 1993). Taken from the point of minimum lift coefficient. . . . .	175
Figure 8.14: Drag coefficients for the calculations compared to Gopalkrishnan (1993). . . . .	177

Figure 8.15: Lift coefficients in phase with velocity for the calculations compared to Gopalkrishnan (1993). . . . .	177
Figure 8.16: Lift coefficients in phase with acceleration for the calculations compared to Gopalkrishnan (1993). . . . .	178
Figure 8.17: Lift time traces from calculations with two-dimensional SST and three-dimensional SST-SAS for $U_R = 4.50$ and the conditions of Sarpkaya (2004). . . . .	179
Figure 8.18: Lift time traces from calculations with two-dimensional SST and three-dimensional SST-SAS for $U_R = 10.0$ and the conditions of Sarpkaya (2004). . . . .	180
Figure 8.19: Lift time traces from calculations with two-dimensional SST and three-dimensional SST-SAS for $U_R = 5.50$ and the conditions of Sarpkaya (2004). . . . .	180
Figure 8.20: Drag coefficients for the calculations compared to the results from MARIN. . . . .	181
Figure 8.21: Lift coefficients in phase with velocity for the calculations compared to MARIN data. . . . .	182
Figure 8.22: Lift coefficients in phase with velocity for the calculations compared to Sarpkaya (2004) data. . . . .	182
Figure 8.23: Lift coefficients in phase with acceleration for the calculations compared to MARIN data. . . . .	183
Figure 8.24: Lift coefficients in phase with acceleration for the calculations compared to Sarpkaya (2004) data. . . . .	183
Figure 8.25: MARIN experimental time traces of imposed motions (in red) and measured lift coefficient(in blue) filtered retaining $f < 8Hz$ for $U_R = 5.43$ . The imposed motion frequency in this case is $f = 0.20$ Hz and the force trace is filtered to remove the carriage vibration and other high frequency noise. . . . .	184
Figure 8.26: MARIN experimental time traces of imposed motions (in red) and measured lift coefficient(in blue) filtered retaining $f < 8Hz$ for $U_R = 7.80$ . The imposed motion frequency in this case is $f = 0.14$ Hz and the force trace is filtered to remove the carriage vibration and other high frequency noise. . . . .	185
Figure 8.27: Non-dimensional vorticity and streamlines in the z-direction at the point of maximum lift coefficient with $U_R = 3.50$ for the Sarpkaya (2004) set of calculations. (a) Calculations with two-dimensional SST. (b) Calculations with three-dimensional SST-SAS (slice taken from mid-span). . . . .	185

Figure 8.28: Non-dimensional vorticity and streamlines in the $z$ -direction at the point of maximum lift coefficient with $U_R = 5.50$ for the Sarpkaya (2004) set of calculations. (a) Calculations with two-dimensional SST. (b) Calculations with three-dimensional SST-SAS (slice taken from mid-span). . . . .	186
Figure 8.29: Line contours of vorticity in the $z$ -direction at the point of maximum lift coefficient with $U_R = 3.50$ for the Sarpkaya (2004) set of calculations. Two superimposed slices (mid-span, in black, and at a distance of 5% of the cylinder length from the top boundary, in red) are showed from calculation done with three-dimensional SST-SAS. . . . .	186
Figure 9.1: Nondimensional transverse ( $A_Y^*$ ) and in-line ( $A_X^*$ ) responses and transverse response frequency ( $f_Y^*$ ) over reduced velocity ( $U^*$ ) for $m^* = 7.0$ , $Re = 2000 - 11000$ and $(m^* + C_a)\zeta = 0.0117$ . The black symbols correspond to Y-only case and the white, to XY motions (JAUVITS; WILLIAMSON, 2004). . . . .	190
Figure 9.2: Nondimensional transverse ( $A_Y^*$ ) and in-line ( $A_X^*$ ) responses and transverse response frequency ( $f_Y^*$ ) over reduced velocity ( $U^*$ ) for $m^* = 2.60$ , $Re = 1000 - 15000$ and $(m^* + C_a)\zeta = 0.013$ (JAUVITS; WILLIAMSON, 2004). . . . .	191
Figure 9.3: Setup and grid layout used in the calculations with two degree-of-freedom motions. . . . .	194
Figure 9.4: Typical iterative convergence for the velocity and pressure. . . . .	195
Figure 9.5: Typical iterative convergence for the turbulent quantities. . . . .	196
Figure 9.6: Time traces of the transverse motions in the decay calculations. (a) two-dimensional calculations with $k-\omega$ SST. (b) three-dimensional calculations with $k-\omega$ SST-SAS. . . . .	197
Figure 9.7: Non-dimensional amplitudes over reduced velocity of two degrees-of-freedom free oscillating cylinder compared to Franzini (2013) and Jauvits & Williamson (2004). . . . .	199
Figure 9.8: Ratio between transverse vibration frequency and transverse natural frequency over reduced velocity for two degrees-of-freedom free oscillating cylinder compared to Franzini (2013) and Jauvits & Williamson (2004). . . . .	200
Figure 9.9: Average drag coefficients over reduced velocity for the two degrees-of-freedom free oscillating cylinder compared to the experimental results in Franzini (2013) and Jauvits & Williamson (2004). . . . .	201
Figure 9.10: RMS of drag coefficients over reduced velocity for the two degrees-of-freedom free oscillating cylinder compared to the experimental results in Franzini (2013). . . . .	201

Figure 9.11: RMS of lift coefficients for the two degrees-of-freedom free oscillating cylinder over reduced velocity compared to the experimental results in Franzini (2013) and Jauvits & Williamson (2004). . . . .	202
Figure 9.12: Added mass coefficients over reduced velocity for the two degrees-of-freedom free oscillating cylinder compared to the experimental results in Franzini (2013). . . . .	204
Figure 9.13: Time traces of transverse vibrations and forces comparing two-dimensional SST and three-dimensional SST-SAS for the peak-response reduced velocities (respectively $U_R = 7.1$ and $U_R = 7.5$ ). . . . .	204
Figure 9.14: Time signatures of non-dimensional in-line and transverse motions and power spectra for $U_R = 4.0$ with the two-dimensional $k-\omega$ SST. The frequencies are made non-dimensional by multiplication with $D/V$ . . . . .	205
Figure 9.15: Time signatures of drag and lift coefficients and power spectra for $U_R = 4.0$ with the two-dimensional $k-\omega$ SST. The frequencies are made non-dimensional by multiplication with $D/V$ . . . . .	206
Figure 9.16: Non-dimensional $z$ -vorticity at the instant of minimum transverse displacement for $U_R = 4.0$ calculated with the two-dimensional $k-\omega$ SST. . . . .	206
Figure 9.17: Time signatures of non-dimensional in-line and transverse motions and power spectra for $U_R = 7.5$ with the two-dimensional $k-\omega$ SST. The frequencies are made non-dimensional by multiplication with $D/V$ . . . . .	207
Figure 9.18: Time signatures of drag and lift coefficients and power spectra for $U_R = 7.5$ with the two-dimensional $k-\omega$ SST. The frequencies are made non-dimensional by multiplication with $D/V$ . . . . .	208
Figure 9.19: Non-dimensional $z$ -vorticity at the instant of minimum transverse displacement for $U_R = 7.5$ calculated with the two-dimensional $k-\omega$ SST. . . . .	208
Figure 9.20: Time signatures of non-dimensional in-line and transverse motions and power spectra for $U_R = 13.0$ with the two-dimensional $k-\omega$ SST. The frequencies are made non-dimensional by multiplication with $D/V$ . . . . .	209
Figure 9.21: Time signatures of drag and lift coefficients and power spectra for $U_R = 13.0$ with the two-dimensional $k-\omega$ SST. The frequencies are made non-dimensional by multiplication with $D/V$ . . . . .	210
Figure 9.22: Non-dimensional $z$ -vorticity at the instant of minimum transverse displacement for $U_R = 13.0$ calculated with the two-dimensional $k-\omega$ SST. . . . .	210

Figure A.1: Annotated view of the flat plate domain, showing an example grid.	230
Figure A.2: Example of iterative convergence at $Re = 10^{7.5}$ with G1. Residuals of velocities and pressure are presented.	232
Figure A.3: Example of iterative convergence at $Re = 10^{7.5}$ with G1. Residuals of turbulence variables are presented.	233
Figure A.4: Uncertainty quantification for all turbulence models in the entire range of Reynolds numbers. Overall, low uncertainties are observed.	234
Figure A.5: Orders of grid convergence for all turbulence models. Consistent behavior is observed as orders are between $p = 1.0$ and $p = 2.0$ .	234
Figure A.6: Grid convergence of the drag coefficients for $Re = 10^{3.5}$ with LCTM.	235
Figure A.7: Grid convergence of the drag coefficients for $Re = 10^{6.0}$ with LCTM.	235
Figure A.8: Grid convergence of the drag coefficients for $Re = 10^{9.0}$ with LCTM.	235
Figure A.9: Grid sensitivity of $C_f$ line for $Re = 10^{7.0}$ .	236
Figure A.10: Grid sensitivity of $C_f$ line for $Re = 10^{7.5}$ .	237
Figure A.11: Friction lines for $Re = 10^{3.5}$ . For this Reynolds number, behavior is expected to be fully laminar and all turbulence models here exhibit consistent solutions.	239
Figure A.12: Friction lines for $Re = 10^{6.0}$ . This Reynolds number fall into the range of transitional numbers and only LCTM does not predict turbulent behavior.	239
Figure A.13: Friction lines for $Re = 10^{9.5}$ , a fully turbulent Reynolds number.	240
Figure A.14: Near wall behavior for $Re = 10^{6.5}$ at $x/L = 0.50$ ( $Re_x = 1.58 \times 10^6$ ) with SST and LCTM. $u^+ - y^+$ relations differ in the two models.	241
Figure A.15: Near wall behavior for $Re = 10^{9.5}$ at $x/L = 0.50$ ( $Re_x = 1.58 \times 10^9$ ) with SST and LCTM. Both boundary layers are turbulent and $u^+ - y^+$ relations show nearly no difference.	241
Figure A.16: $k^+ - y^+$ relation for $Re = 9.50$ at $x/L = 0.50$ with SST and LCTM. Differences in $k^+$ are very small, but one notices a milder transition of boundary layer with LCTM.	242
Figure A.17: $\nu_t/\nu - y^+$ relation for $Re = 9.50$ at $x/L = 0.50$ with SST and LCTM. Almost no differences are observed.	242
Figure A.18: Sensitivity of the friction coefficients to variations in the inflow turbulence for $Re = 10^{6.5}$ .	244
Figure A.19: Sensitivity of the friction coefficients to variations in the inflow turbulence for $Re = 10^{9.5}$ .	244

Figure A.20: Order of convergence ( $p$ ) of the ERCOFTAC calculations on the left and uncertainty results ( $U, \%$ ) on the right. . . . .	246
Figure A.21: Turbulence intensity measured at an horizontal line placed 0.1m above the plate for the case T3A. . . . .	247
Figure A.22: fig: Turbulence intensity measured at an horizontal line placed 0.1m above the plate for the case T3A-. . . . .	247
Figure A.23: Turbulence intensity measured at an horizontal line placed 0.1m above the plate for the case T3B. . . . .	248
Figure A.24: Friction lines obtained with SST and LCTM models in comparison with experimental results (SCHUBAUER; KLEBANOFF, 1955) for case S&K with EV and EV+TU. EV+TU shows better comparison with the experiments because of a better turbulence decay prediction. . . . .	248
Figure A.25: Friction lines obtained with SST and LCTM models in comparison with experimental results (ERCOFTAC, 1990) for case T3A- with EV and EV+TU. EV+TU shows better comparison with the experiments because of a better turbulence decay prediction. . . . .	249
Figure A.26: Friction lines obtained with SST and LCTM models in comparison with experimental results (ERCOFTAC, 1990) for case T3A with EV and EV+TU. EV+TU shows better comparison with the experiments because of a better turbulence decay prediction. . . . .	249
Figure A.27: Friction lines obtained with SST and LCTM models in comparison with experimental results (ERCOFTAC, 1990) for case T3B with EV and EV+TU. EV+TU shows better comparison with the experiments because of a better turbulence decay prediction. . . . .	250
Figure A.28: Non-dimensional eddy viscosity field for case T3A- on the left plane and T3B on the right. Both are done with EV+TU option. . . . .	250
Figure A.29: Turbulence intensity field for case T3A- on the left plane and T3B on the right. Both are done with EV+TU option. . . . .	251
Figure A.30: Intermittency factor field for case T3A- on the left plane and T3B on the right. Both are done with EV+TU option. . . . .	251



# List of Tables

Table 6.1:	Details of the finest grids used in the steady laminar calculations. . . . .	108
Table 6.2:	Details of the finest grids used for the unsteady laminar calculations.	109
Table 6.3:	Details of the finest grids used for the turbulent calculations. . . . .	109
Table 6.4:	Time discretization for the unsteady laminar and turbulent calculations. The largest and smallest number of point per cycle used for the calculations are indicated . . . . .	109
Table 6.5:	Uncertainty estimation for the laminar calculations. . . . .	116
Table 6.6:	Uncertainty estimation for the turbulent calculations. . . . .	118
Table 6.7:	Uncertainty estimation of the experimental drag coefficients by means of the standard deviations and variation coefficients, with a 90% level of confidence. . . . .	131
Table 6.8:	Validation results for drag coefficients. . . . .	132
Table 6.9:	Summary of numerical results for the cases presented herein. . . . .	133
Table 7.1:	Details of the finest grids used for the turbulent calculations. . . . .	141
Table 7.2:	Finest time discretization for the SAS calculations. . . . .	142
Table 7.3:	Details of the finest grids and the number of time steps in each shedding cycle used for the calculations. . . . .	151
Table 7.4:	Uncertainty estimation and order of convergence for the calculations.	153
Table 7.5:	Uncertainty estimation for the experiments . . . . .	158
Table 7.6:	Validation exercise done for the calculations . . . . .	159
Table 7.7:	Summary of numerical results obtained with the finest grids and three-dimensional SST-SAS. . . . .	160
Table 7.8:	Summary of numerical results obtained with the finest grids and two-dimensional LCTM. . . . .	161

Table 8.1:	Details of the finest grids used for the two-dimensional imposed motions calculations ( $y^+$ values showed are for SST). . . . .	168
Table 8.2:	Details of the finest grids used for the three-dimensional imposed motions calculations with SST-SAS. . . . .	168
Table 9.1:	Details of the dynamic setup in the experiments reported in Jauvits & Williamson (2004), Franzini (2013) and the dynamic properties of the system considered herein. . . . .	192
Table 9.2:	Details of the grid and sensitivity analysis for the two-dimensional $k-\omega$ SST calculations. . . . .	194
Table 9.3:	Details of the grid and sensitivity analysis for the three-dimensional $k-\omega$ SST-SAS calculations. . . . .	195
Table 9.4:	Natural periods and damping values for the two-dimensional and three-dimensional calculations. . . . .	197
Table A.1:	Grid Sizes . . . . .	231
Table A.2:	Test cases and inlet conditions for the transition test cases. . . . .	245

# Acronyms and Abbreviations

**ABM** - Adams-Bashfourth-Moulton Method

**AFM** - Absolute Formulation Method

**ALE** - Arbitrary Lagrangian-Eulerian Method

**CFD** - Computational Fluid Dynamics

**DDES** - Delayed Detached Eddy Simulations

**DES** - Detached Eddy Simulations

**DNS** - Direct Numerical Simulations

**DOF** - Degree of Freedom

**DVM** - Discrete Vortex Method

**FDM** - Finite Difference Method

**FEM** - Finite Element Method

**FSI** - Fluid Structure Interaction

**FVM** - Finite Volume Method

**HPC** - High-Performance Computing

**IVP** - Initial-Value Problem

**LBM** - Lattice Boltzmann Method

**LCTM** - Local Correlation Transition Model

**LES** - Large Eddy Simulations

**MARIN** - Maritime Research Institute Netherlands

**MVG** - Moving Grid Method

**PANS** - Partially-Averaged Navier Stokes

**QUICK** - Quadratic Upstream Interpolation for Convective Kinematics

**ReFresco** - Reliable & Fast Rans Equations solver for Ships and Constructions

Offshore

**RFM** - Relative Formulation Method

**RK** - Runge Kutta Method

**RMS** - Root Mean Square

**SAS** - Scale Adaptive Simulations

**SE** - Spectral Elements Method

**SIMPLE** - Semi-Implicit Pressure-Linked Equations

**SST** - Shear Stress Transport

**TLP** - Tension Leg Platform

**TPN** - Tanque de Provas Numérico

**URANS** - Unsteady Reynolds Averaged Navier Stokes Equations

**VIV** - Vortex-Induced Vibrations

# Contents

<b>1</b>	<b>Introduction</b>	<b>37</b>
1.1	Preliminary Aspects . . . . .	37
1.1.1	Fixed Cylinder Flow . . . . .	37
1.1.2	Moving Cylinder Flow . . . . .	40
1.2	Summarizing the Present Doctoral Work . . . . .	42
1.3	Objectives . . . . .	43
1.4	ReFRESCO and the Research Environment Around the Code . . . . .	43
1.5	Engineering Relevance . . . . .	44
1.6	Thesis Outline . . . . .	45
<b>2</b>	<b>Finite Volume Code ReFRESCO</b>	<b>47</b>
2.1	Unsteady Reynolds Averaged Navier-Stokes Equations in Inertial Reference Frame . . . . .	47
2.2	URANS Equations in Non-Inertial Reference Frames . . . . .	49
2.3	Geometry Handling . . . . .	53
2.4	Numerical Discretization . . . . .	54
2.4.1	Unsteady Term . . . . .	55
2.4.2	Gradients . . . . .	55
2.4.3	Convective Term . . . . .	57
2.4.3.1	Upwind Differencing Scheme . . . . .	58
2.4.3.2	QUICK Scheme . . . . .	58
2.4.4	Diffusive Term . . . . .	60

2.4.5	Source and Pressure Terms . . . . .	61
2.5	Solution Process . . . . .	61
2.5.1	Under Relaxation Procedure . . . . .	63
2.5.2	Pressure-Correction Scheme . . . . .	63
<b>3</b>	<b>Turbulence Modeling</b>	<b>65</b>
3.1	$k - \omega$ SST Model . . . . .	65
3.2	SST-SAS Model . . . . .	68
3.2.1	A Discussion on the Scales . . . . .	70
3.2.2	Comparison with Other URANS Models . . . . .	71
3.3	Transition Modeling . . . . .	73
<b>4</b>	<b>Fluid Structure Interaction</b>	<b>83</b>
4.1	Dynamics of the Rigid Body . . . . .	83
4.2	Coupling of Fluid and Structure Equations . . . . .	85
4.3	Weakly Coupled Scheme . . . . .	86
4.4	Strongly Coupled Scheme . . . . .	88
4.4.1	Implicit Adams-Bashforth-Moulton Scheme . . . . .	90
4.4.1.1	Predictor Step . . . . .	90
4.4.1.2	Corrector Step . . . . .	90
4.4.1.3	On the Error Estimation and the Evaluation Criteria . . . . .	91
<b>5</b>	<b>Verification and Validation</b>	<b>93</b>
5.1	Steady Analysis . . . . .	95
5.2	Unsteady Analysis . . . . .	97
5.3	Experimental Uncertainty . . . . .	98
5.4	Validation . . . . .	99
<b>6</b>	<b>The Rigid Fixed Cylinder Flow - Traditional Modeling</b>	<b>101</b>
6.1	Phenomenological Background of Flow Around Fixed Cylinder . . . . .	101
6.1.1	Steady Laminar Regime - $Re < 49$ . . . . .	101

6.1.2	Laminar Vortex Shedding - $49 < Re \lesssim 194$ . . . . .	103
6.1.3	Wake-Transition Regime - $190 \lesssim Re < 260$ . . . . .	104
6.1.4	Increasing Disorder in the Fine-Scale Three Dimensionalities - $260 < Re \lesssim 1,000$ . . . . .	105
6.1.5	Shear-Layer Transition Regime - $1,000 < Re < 200,000$ . . . . .	105
6.1.6	Critical Transition Regime - $200,000 < Re \lesssim 500,000$ . . . . .	106
6.1.7	Post-Critical Transition Regime - $Re > 500,000$ . . . . .	107
6.2	Outline of the Calculations . . . . .	107
6.3	Numerical Details and Grids . . . . .	109
6.4	Solution Verification . . . . .	112
6.4.1	Iterative Convergence . . . . .	112
6.4.2	Discretization and Uncertainty Studies . . . . .	114
6.5	Forces and Flow Analysis . . . . .	118
6.5.1	Steady Laminar Calculations . . . . .	118
6.5.2	Unsteady Laminar Calculations . . . . .	121
6.5.3	Turbulent Regime . . . . .	124
6.6	Experimental Uncertainty . . . . .	131
6.7	Validation . . . . .	131
6.8	Final Remarks of the Chapter . . . . .	132
<b>7</b>	<b>The Rigid Fixed Cylinder Flow - Modern Modeling</b>	<b>137</b>
7.1	Outline of the Calculations . . . . .	137
7.2	Discretization Details . . . . .	138
7.3	Scale Adaptive Simulations . . . . .	139
7.3.1	Solution Verification . . . . .	140
7.3.1.1	Iterative Convergence . . . . .	140
7.3.1.2	Convergence Analysis . . . . .	140
7.3.2	Improved Flow Prediction in Range II . . . . .	142
7.4	Local Correlation Transition Model . . . . .	150

7.4.1	Background Work for the LCTM . . . . .	150
7.4.2	Outline of the Calculations . . . . .	150
7.4.3	Verification . . . . .	151
7.4.3.1	Iterative Convergence . . . . .	151
7.4.3.2	Numerical Uncertainty . . . . .	151
7.4.4	Improved Flow Prediction in Range III . . . . .	153
7.4.5	Flow Analysis . . . . .	157
7.4.6	Experimental Uncertainty . . . . .	158
7.4.7	Validation . . . . .	158
7.5	Final Remarks of the Chapter . . . . .	159
<b>8</b>	<b>Rigid Cylinder in 1 Degree-of-Freedom Imposed Motions</b>	<b>163</b>
8.1	Background . . . . .	163
8.2	Description of the Cases . . . . .	166
8.3	Setup and Grids . . . . .	166
8.4	Iterative Convergence . . . . .	169
8.5	Results with $Re = 10,000$ and $A/D = 0.3$ . . . . .	170
8.6	Results with $Re = 40,000 - 45,000$ and $A/D = 0.5$ . . . . .	178
8.7	Final Remarks of the Chapter . . . . .	187
<b>9</b>	<b>Rigid Cylinder in 2 Degrees-of-Freedom Free Motions</b>	<b>189</b>
9.1	Background . . . . .	189
9.2	Description of the Cases . . . . .	192
9.3	Setup and Discretization . . . . .	193
9.4	Iterative Convergence . . . . .	195
9.5	Decay Analysis . . . . .	196
9.6	Vortex-Induced Vibrations . . . . .	198
9.7	Initial Branch . . . . .	205
9.8	Super Upper Branch . . . . .	207
9.9	Lower Branch . . . . .	209

9.10 Final Remarks of this Chapter . . . . .	211
<b>10 Conclusions</b>	<b>213</b>
10.1 Main Conclusions . . . . .	213
10.2 Perspectives . . . . .	217
<b>References</b>	<b>219</b>
<b>Appendix A Investigation of the Properties of the LCTM in the Flat Plate Flow</b>	<b>229</b>
A.1 Calculation Setup . . . . .	229
A.1.1 Description of Test-Cases . . . . .	229
A.1.2 Domain and Boundary Conditions . . . . .	230
A.1.3 Grids . . . . .	230
A.1.4 Numerical Details . . . . .	231
A.2 Numerical Friction Line Study . . . . .	232
A.2.1 Iterative Convergence . . . . .	232
A.2.2 Order of Convergence and Uncertainty . . . . .	232
A.2.3 Grid Sensitivity . . . . .	236
A.2.4 Nominal Results . . . . .	236
A.2.5 Influence of Inflow Turbulence . . . . .	240
A.3 ERCOFTAC calculations . . . . .	243
A.3.1 Setup and Settings . . . . .	243
A.3.2 Nominal Results . . . . .	245
A.3.3 Analysis of the Flow Field . . . . .	246



# Chapter 1

## Introduction

### 1.1 Preliminary Aspects

#### 1.1.1 Fixed Cylinder Flow

The flow around circular cylinder is considered as one of the canonical problems in fluid mechanics, condensing a wide range of interesting aspects also observed in flows around many other blunt bodies (WILLIAMSON, 1996; SARPKAYA, 2004).

The fixed cylinder flow was approached from the numerical perspective as of the late 60's, primarily by making use of Finite Difference Methods (FDM) to study low Reynolds numbers, see Takami & Keller (1969), Dennis & Chang (1970), Dennis (1973). As of the 80's, not only FD methods were used (FORNBERG, 1980; FORNBERG, 1985) but also Finite Element methods (FEM), such as Tuann & Olson (1978) and Spectral Elements methods (SE) (NIEUWSTADT; KELLER, 1973), Finite Volume methods (FVM), such as Braza, Chassaing & Minh (1986), all for relatively low Reynolds numbers. The 90's have brought some different techniques into use for this problem, such as Discrete Vortex methods (DVM), see Meneghini & Bearman (1993) and Lattice-Boltzmann methods (LBM), see He & Doolen (1997). Also in that decade, the development of computer power made it possible to reach higher Reynolds numbers, such as in Mittal, Kumar & Raghuvanshi (1997), using FEM, and Henderson (1995), using SE methods.

Within the conventional CFD methods, all of which solving the Navier-Stokes equations, a more important issue than the numerical approaches to discretize these equations (FD, FE, FV methods) are the simplifications with respect to physical modeling and, foremost, turbulence modeling. In Direct Numerical Simulation (DNS), all spatial and temporal scales of turbulence are resolved. In theory, it is the only numerical method capable

of solving the cylinder problem in all of its scales. However, DNS calculations are extremely expensive, even for low and moderate Reynolds numbers and simple geometries. Blackburn, Govardhan & Williamson (2000) have reported on the difficulties of doing high Reynolds numbers computations with DNS. Conversely, Braza, Chassaing & Minh (1990) have done two-dimensional calculations for the cylinder flow with Reynolds numbers ranging from 2,000 to 10,000. They have shown that the transition waves develop in the separated shear layers leading to mixing layer eddies and concluding that the instability leading to mixing layer eddies has a two-dimensional origin. Dong & Karniadakis (2005) have done three-dimensional calculations for the cylinder flow at an impressively high Reynolds number of 10,000.

The next step in turbulence modeling fidelity is a Large Eddy Simulation (LES) approach. A growing amount of calculations has been reported using LES also for higher Reynolds numbers and complex geometries, such as in With, Holdo & Huld (2003). The turbulence scales simulated in free-shear layer zones are accurately captured, once appropriated time, space discretization and numerical schemes which do not introduce filtering of these scales are used. However, in LES, the treatment of turbulence close to the objects is usually modeled (simplified, using sub-grid scale models or even wall functions) and not simulated such as in DNS, with serious consequences for wall-bounded flows. That has been seen in Singh & Mittal (2005), who have done two-dimensional LES calculations for a wide range of Reynolds numbers, up to  $Re = 10^7$ . It is clear that the simplifications introduced by subgrid models, two-dimensional computations and insufficient grid and time step discretization cause drag coefficients to be up to 50% larger than experimental results. From their results one infers that LES computations are accurate with the currently feasible discretization at Reynolds numbers up to  $Re = 10,000$ . It is therefore observed that, in order to correctly capture the turbulent scales inside the boundary layers, the computational costs for LES increase sharply, reaching similar needs as the ones for DNS (VON KÁRMÁN INSTITUTE, 2008).

The Unsteady Reynolds Average Navier Stokes (URANS) methods, in which turbulence spatial and time scales are averaged, modeled by turbulence models, and therefore not simulated, is nowadays the engineering tool to address this problem.

The decomposition of the flow into mean and turbulent isolates the effects of the fluctuations on the mean flow. However, the Reynolds stress tensor present in the averaged equation has yielded the so-called closure problem. The Reynolds stress tensor is symmetric and thus there are six new unknowns to the conservation equations. The elements of the matrix diagonal are normal stresses (pressures) and they often contribute little to the transport of mean momentum. On the other hand, the off-diagonal elements, the shear stresses, are more important in the turbulent transport of momentum. It is important

to notice at this point that the Reynolds stress tensor results from a manipulation of the conservation equations that involves averaging. It rises as a more palatable way to see the effects of turbulence on the flow. Nevertheless, it shall be stressed that turbulence is the general solution of the Navier-Stokes equations as it is intrinsic of the velocity and pressure responses.

With its simple geometry, the cylinder flow encompasses the issues cited above and even more related to the evolution of the turbulent wake and shear layers, instabilities, transition, all changing appreciably with Reynolds numbers. The modeling simplification thus brings important consequences to flow prediction with URANS. Traditional URANS calculations for the cylinder flow have been performed in Vaz et al. (2007), Liu, Zheng & Sung (1998), Ong et al. (2007), to cite a few. It has been observed that the current “traditional” URANS turbulence models are not sufficient to capture both qualitatively and quantitatively all subtle characteristics of such an intricate type of flow. It is clear that the main direction of research points to turbulence and transition modeling, as they are the main shortcoming of most approaches for this type of flow.

Pengan (2010) have identified the monochromatic behavior of the traditional two-dimensional modeling as one of the important issues that make comparison with experimental results more troublesome in moderate Reynolds numbers. The cylinder flow displays important three-dimensional features throughout the pre-critical range influencing the loads and other quantities. That was also explored by Vaz et al. (2007), Pengan (2010), Klaij (2008) with SST, showing the limitations of the three-dimensional modeling with traditional modeling and identifying the need of better assessment of the three-dimensional turbulent behavior within URANS. In the last years, different models have been developed with that objective, such as the Partially-Average Navier Stokes (PANS) equations (GIRIMAJI, 2006), Detached Eddy Simulations (DES) (TRAVIN et al., 1999), Delayed Detached Eddy Simulations (DDES) (SPALART et al., 2006) among others. Pereira, Vaz & Eça (2014) present a comparison of RANS, SAS, DES and PANS models for the backward facing step case, shedding light on some of their differences and capabilities.

The understanding and prediction of transition is a state-of-the-art research topic and, to date, the most comprehensive prediction approach is based on the DNS, as only then the fine scale disturbances that trigger the transition process are accurately captured. As shall be discussed later on, a more engineering-oriented approach was developed based on empirical approach, as proposed by Langtry & Menter (2009), Menter, Langtry & Volker (2006). In this Local Correlation Transition Model (LCTM), a framework for empirical correlations obtained from experiments is set and coupled with a turbulence model in order to predict transition onset and length. In fact, Langtry & Menter (2009) have shown results for different applications, including few results for the cylinder flow

in the drag crisis region, but without assessment of numerical errors or much exploration of modeling issues. Quite a reasonable improvement is observed compared to traditional modeling.

### 1.1.2 Moving Cylinder Flow

As mentioned before, turbulence is a key player in the fixed cylinder-flow mechanics, as well as in the case of moving cylinder. Several contributions are identified in the literature in this issue, thus being quite a challenge to set a chronological line of contributions, such as in the work done by Williamson & Govardhan (2004) and Gabbai & Benaroya (2004). Gopalkrishnan (1993) and Sarpkaya (2004) have also thoroughly studied the vortex-induced vibrations of a cylinder, however by means of imposed sinusoidal motions bracketing the resonance range. They have reported on different Reynolds numbers, wide ranges of vibration amplitudes and frequencies setting an important benchmark for the study of vortex-induced vibrations and for the CFD calculations. It has been recognized that the imposed motions studied did elucidate several issues related to VIV, however the behavior of freely-moving two degrees-of-freedom VIV cannot be inferred from the imposed motions case in every instance, as commented by Sarpkaya (2004). This issue here is treated from a modeling perspective: the imposed motions results are seen as the transition from fixed and freely-moving cylinder, with the complexity regarding numerical models increasing, despite a constant and high level of physical complexity. CFD calculations of forced vibrations have been done by Placzek, Sigrist & Hamdouni (2009) using a two-dimensional approach with finite volume method discretization at a low Reynolds number, exploring and characterizing the different flow and dynamic responses in the locked and unlocked configurations of resonance. Blackburn & Henderson (1999) have also studied wake structures and flow dynamics associated with two-dimensional flows past cylinder in forced vibration at  $Re = 500$ . Dong & Karniadakis (2005) have used direct numerical simulations employing a spectral method for  $Re = 10,000$  for a few vibration frequencies, finding very good agreement with the experimental results from Gopalkrishnan (1993).

As commented by Gabbai & Benaroya (2004), the issues to be considered in a numerical method that aims at solving the VIV are the modeling of the flow field, modeling of the structural vibration, modeling of the fluid-structure interaction (FSI) and data analysis. Within the first issue, the approaches commented above can handle the calculations in order to obtain the velocity and pressure fields, forces and moments upon the cylinder. On the other hand, six degree-of-freedom rigid-body motions are calculated by means of equations of motion based on conservation of linear and angular momentum, see e.g.

Wilson, Carrica & Stern (2006), Bettle (2012), Leroyer (2004).

With regards to the reference frames, absolute (inertial) or relative (non-inertial) formulations can be used. The Arbitrary Lagrangian-Eulerian method (ALE) or moving-grid approach deals with the motions of the grid cells; see Hirt, Amsden & Cook (1997). The nodes can move with the fluid (Lagrangian) or can be kept still (Eulerian). In fact, with this approach, the grid nodes may be moved with an arbitrary velocity, commonly with the cylinder velocity, as done by Mendes & Branco (1999), Marzouk (2011) and Nobari & Naderan (2006). The coupling between these equations and the fluid equations can be done weakly, at every time-step, or strongly, inside the non-linear fluid flow solution loop, which is seen to be more stable but more expensive.

Regarding the numerical prediction of vortex-induced vibrations using CFD tools, a large number of important works are found for elastically mounted cylinders of high mass ratios (structural mass over displacement) with one degree-of-freedom and in smaller extent, for low mass ratios and two degrees-of-freedom systems. Usually very low Reynolds numbers are explored due to the difficulties inherent of full scale. Within the examples of low Reynolds numbers one can cite the work of Carmo (2009), who has developed a numerical method based on an Arbitrary Lagrangian-Eulerian approach that coupled the solution of the structure equations with that of the flow to calculate one degree-of-freedom VIV. In this case, a weakly coupled scheme was appropriate and reasonable results were obtained. The final goal of the project was to study wake interference of two cylinders. Shiels, Leonard & Roshko (2001) also explore one degree-of-freedom cylinder oscillations studying sensitivity to different dynamic parameters, in particular the mass ratio, but in this case the vibration amplitudes for low mass ratios did not reach high amplitudes as seen in Jauvits & Williamson (2004). In a different line of work, Saltara (1999) has showed that the discrete vortex method is not appropriate to simulate VIV at  $Re \approx 10,000$  and used instead a Fractional Step method with a finite volume approach, comparing the results for one degree-of-freedom VIV with those of Khalak & Williamson (1996). Conversely, Mittal & Kumar (2001) have used a finite-element formulation to study two degrees-of-freedom VIV of light structures at similar Reynolds numbers as will be done in the present study but at higher mass ratio in their case. They have not observed the super-upper response branch in the results. Al-Jamal & Dalton (2004) have used two-dimensional and three-dimensional large eddy simulations with a finite difference scheme to simulate free vibrations of a cylinder at 8,000 and low mass ratios concluding that the two-dimensional representation of the flow was appropriate to simulate vortex-induced vibrations in their case. Results with Reynolds numbers higher than  $Re = 10,000$ , low mass ratio, two degrees-of-freedom and URANS such as the ones proposed herein have not been observed in the open literature.

## 1.2 Summarizing the Present Doctoral Work

The applications of CFD tools in practical offshore engineering problems is restricted by the required computational power, especially for complex flows and geometries. Solving the flow equations without simplifications and in full scale is presently unfeasible. The Reynolds Averaged Navier Stokes approach considerably reduces the computational power due to the less stringent grid and time step requirements, but that comes at a price: turbulence is modeled and not solved. That may be of higher order in many problems, but it is of central importance for the cylinder flow problem.

Within the modeling issues related to the flow around cylinders in restrained condition, under imposed motions and free to move, this doctoral work is mainly focused on the modeling of turbulence, transition and fluid-structure interaction capabilities within the Reynolds Averaged Navier Stokes approach.

The present work firstly brings an investigation of the performance of the traditional turbulence modeling with  $k-\omega$  SST (previously implemented in ReFRESKO) in a broad range of Reynolds numbers encompassing most of the engineering applications. Deficiencies related to the traditional modeling are identified and more advanced turbulent and transition models are implemented and used with the objective of improving the flow modeling and force quantification in the range of turbulent Reynolds numbers. As commented above, similar investigations have been carried out for the fixed cylinder flow with both Scale Adaptive Simulations and the Local Correlation Transition Model. However, the present work has reported the application of these modeling strategies to a larger number of Reynolds numbers and in a more systematic manner, in order to better understand their capabilities, limitations and range of validity. The application of a very important tool has permeated this investigation permitting more sound conclusions regarding both traditional and more advanced modeling, namely the Verification and Validation technique. This has allowed the estimation of numerical errors and uncertainties for the different models and Reynolds numbers, in a novel contribution of this thesis.

Aiming at the development and application of a tool for engineering design and analysis, the motions of a rigid body immersed in the flow field stands out as one of the important issues approached herein. The combination of the traditional SST modeling under imposed motions is carried out as well as with the SAS and LCTM at several moderate Reynolds numbers, different vibration frequencies and amplitudes, results which have not been published to date. Regarding the implementation and calculation of free-moving cylinder capability, the present work brings novel contributions with the combination of SST and SAS with free-moving cylinder for the study of VIV of two degrees-of-freedom, low mass ratio and moderate Reynolds numbers, higher than commonly seen in the literature.

A more practical issue related to this thesis that has been on its background is the investigation of the relative importance of turbulence effects on the free-moving cylinder and the imposed-motions case, with respect to the fixed case. A natural conjecture that has been raised early in this work is that, for practical applications, the choice of turbulence modeling strategy becomes less decisive when the cylinder is moving with prescribed motion and even less, for free motions. Evidently, this applies from an engineering perspective, i.e. mainly observing forces and response amplitudes and frequencies.

The above mentioned issues compose the background and motivation for the present thesis, in which the cylinder flow was used as the prototype-problem due to its relevance, complexity and extensibility to several other types of flows in which turbulence and transition are major issues.

### 1.3 Objectives

The main objectives of this work are as follows: improve current turbulence and transition modeling by the development and application the state-of-the-art turbulence models within the ReFRESKO framework for the fixed cylinder flow; apply modern Verification and Validation techniques and establish the capabilities of URANS together with different turbulence models; investigate modeling and numerical issues of fluid-structure coupling of rigid cylinders and the performance of the investigated models in those cases; develop mathematical and numerical models to handle rigid cylinder vibrations coupled with the CFD code ReFRESKO for the study of vortex induced vibrations; study the coupling of the state-of-the-art turbulence and transition models with structural solver for rigid body motions; evaluate in practice which classes of turbulence models can be used in each type of situation and how these models can be applied.

### 1.4 ReFRESKO and the Research Environment Around the Code

ReFRESKO (REFRESKO, 2015) is a viscous-flow CFD code that solves multiphase (unsteady) incompressible flows using the Navier-Stokes equations, complemented with turbulence models, cavitation models and volume-fraction transport equations for different phases. The equations are discretised using a finite-volume approach with cell-centered collocated variables, in conservation form and a pressure-correction equation based on the SIMPLE algorithm is used to ensure mass conservation.

ReFRESKO stands for “Reliable and Fast Rans Equations Code for Ships and Constructions Offshore”, and it is a spinoff from the FreSCo project started in 2005, together with the Technical University of Hamburg-Harburg and HSVA. In 2009, the cooperation ended and ReFRESKO was born then. Nowadays, several users and developers are concentrated at MARIN, Instituto Superior Técnico, University of São Paulo, University of Southampton, Delft University of Technology, University of Twente, Chalmers University, University of Groningen and Damen Shipyards.

This code has been chosen in this work for a few reasons, as follows: it is a CFD code under constant development and at the core of the cooperation between the University of São Paulo and MARIN, which provided a very positive environment for discussions and learning, due to the interaction with the large group of developers; the code is also applied for engineering purposes, but with a scientific rigour, thus creating an environment in which academia meets practice providing an engineering perspective to the use of CFD; the source code has been made totally available and could thus be installed in the HPC (high-performance computing) cluster of the Numerical Offshore Tank (TPN) at the University of São Paulo, allowing the work developed herein to be more directed to the specific purposes than if a commercial code or a completely new code had been used or implemented. That has also enabled the learning of issues related to high-performance computing, parallel applications and programming in a large group of developers. It has also been rewarding to observe that the applications developed in the current thesis are present in ReFRESKO source code and several users have been working with them.

It should also be acknowledged that such a large number of numerically complex simulations has only been possible due to the extensive use of the HPC clusters of TPN-USP and of the Maritime Institute Research Netherlands (MARIN). The total amount of cluster-hours used in the present work is estimated at over 3,600,000 hours, which makes the previous points very clear.

## 1.5 Engineering Relevance

The flow about circular cylinder is one of the most important flows in fluid mechanics. It is not only considered as a toy problem, but also of high practical importance in itself as many structures present similar geometric details. On the other hand the cylinder flow condenses a wide range of interesting aspects also observed in flows around many other blunt bodies. The interaction of boundary layer, separating free shear layers and wake shear give rise to the vortex shedding phenomenon, three dimensional instabilities, laminar-turbulent transition, vortex-induced vibrations and more. A great deal of modeling aspects must

be quite well developed in a CFD code if one is to correctly capture the most important features of this flow in different Reynolds numbers.

Observations and conclusions herein achieved are directly available to the study and modeling of engineering problems including vortex-induced vibrations of risers and piles, vortex-induced motions of floating platforms such as spars, monocolumns, semi-submersibles and TLPs and the use of energy-harvesting devices.

## 1.6 Thesis Outline

This thesis is organized as described to reflect how the work was carried out but also to explore the turbulence modeling and fluid structure interaction in different situations and in a sequential manner: from the fixed body to the two degrees-of-freedom system flows. Throughout the text, a very large amount of results are presented mostly to study and demonstrate the capabilities, limitations and performance of the numerical tools implemented and used for the cylinder flow in different conditions. It has been attempted to maintain the main objectives clear at all parts of the text, which is the reason why some of the results are explored in more depth than others. Moreover, due to the large amount of results, flow visualizations and individual comments are made only when needed and not uniformly, with a preference to explore integral quantities such as forces and response amplitudes and frequencies. Moreover, conclusions are often drawn based on similar responses observed in groups of calculations for the sake of generality.

The present Chapter discussed an overview of contributions from different researchers to the issues touched by the present work. A more bibliographic approach is chosen for conciseness. A more detailed review of chosen works is presented in each of the following chapters, when the theoretical subsidies and literature results are needed, for discussions or for comparison with the ones presented herein. However, prior to the chapters showing results, the main theoretical aspects that permeate the entire thesis are presented.

Chapter 2 presents the mathematical and numerical formulation of the fluid equations that constitutes the basis of the Finite Volume Code ReFRESCO, upon which the implementation of the new turbulence equations and fluid-structure capabilities for free motions has been done. This description basically shows the status of the code prior to the developments of the present work. Chapter 3 presents the formulation of the turbulence and transition models implemented for this work, together with a discussion on the capabilities of each of these models in the scope of this thesis. Following the same lines, Chapter 4 shows the mathematical formulation and details of the numerical implementation of the interaction between the solid and fluid domains which was done in this work. Finally, in

Chapter 5 the basic theoretical aspects of the Verification and Validation activities that were pursued in this work.

Following the Chapters presenting the theoretical aspects, Chapter 6 shows the application of some of the previous issues to the flow around a fixed circular cylinder in a wide range of Reynolds numbers with the traditional modeling adopted in the many engineering applications. The capabilities and limitations of this modeling are investigated giving the direction of the following steps. According to these observations, Chapter 7 presents the application of the newly implemented state-of-the-art turbulence models for the cylinder flow in the ranges in which a poor performance of the traditional models was observed enhancing the flow prediction in these situations.

After a thorough investigation of the flow around the fixed cylinder focusing on the issue of turbulence, Chapter 8 presents the results and comparison with original experiments of one degree-of-freedom imposed motions to the rigid cylinder. The issue of turbulence is now observed in comparison to its effects in a fixed cylinder, mainly with respect to forces. In turn, Chapter 9 shows the results and studies concerning the implementation of fluid-structure interaction capabilities in ReFRESKO for this thesis: the two-degrees-of-freedom vibrations of the cylinder are studied and the turbulence modeling issue is again observed in this case comparing it to the previous cases. Chapter 10 shows the conclusions and perspectives of this work.

# Chapter 2

## Finite Volume Code ReFRESKO

*This chapter presents the mathematical formulation of the fluid equations that constitute the basis of the Code ReFRESKO. This code is used in this thesis as a framework for the implementation of turbulence, transition models and moving body capabilities.*

### 2.1 Unsteady Reynolds Averaged Navier-Stokes Equations in Inertial Reference Frame

Consider the Navier-Stokes equations in inertial, fixed reference frame  $(x_1, x_2, x_3) \equiv (x, y, z)$ , for Newtonian fluid in incompressible flow<sup>1</sup> written in differential form:

$$\frac{\partial \rho u_i}{\partial x_i} = 0, \quad (2.1)$$

$$\frac{\partial \rho u_i}{\partial t} + \frac{\partial \rho u_i u_j}{\partial x_j} = -\frac{\partial p}{\partial x_i} + \frac{\partial}{\partial x_j} \left[ \mu \left( \frac{\partial u_i}{\partial x_j} + \frac{\partial u_j}{\partial x_i} \right) \right]. \quad (2.2)$$

In these equations, fluid pressure, density and kinematic viscosity are, respectively,  $p, \rho, \nu$  and body forces and free surface effects are not considered.

The differential form showed above is somewhat more practical and concise than the integral form, as far as notation goes. However, the numerical formulation of the fluid equations is done here by employing the Finite Volume Method (FVM). Some preference

---

<sup>1</sup>Even though the problem at hand is incompressible and thus  $\rho$  is uniform and constant, option has been made to keep  $\rho$  in the flow equations for completeness.

is given to the differential form of the equations, but the integral form shall be presented when appropriate. Hence, for the sake of completeness, consider a control volume  $\mathbf{V}$ , enclosed by the surface  $\mathbf{S}$ , with outwards-pointing normal vector  $\mathbf{n}$  and integrate these equations in the referred control volume. By applying Gauss' divergence theorem, one obtains the integral form of these equations, here conveniently written in conservative form:

$$\int_S \rho u_i n_i dS = 0, \quad (2.3)$$

$$\frac{\partial}{\partial t} \int_V \rho u_i dV + \int_S \rho u_i u_j n_j dS = \int_S \left[ \mu \left( \frac{\partial u_i}{\partial x_j} + \frac{\partial u_j}{\partial x_i} \right) \mathbf{e}_j - p \mathbf{e}_i \right] \cdot \mathbf{n} dS, \quad (2.4)$$

in which  $\mathbf{e}_i$  is the Cartesian unit vector in the direction of coordinate  $x_i$ .

As discussed in Chapter 1, amongst the various approaches to solve equations 2.1 and 2.2, URANS is an appropriate engineering approach as the computer power requirements are less severe compared to DNS and LES. This approach is the basis of the mathematical and numerical formulation of ReFRESKO, also being used herein.

The Reynolds average and fluctuation<sup>2</sup> of a certain quantity  $\phi(\mathbf{x}, t)$  are written as

$$\phi(\mathbf{x}, t) = \Phi(\mathbf{x}, t) + \phi'(\mathbf{x}, t). \quad (2.5)$$

By applying this concept to the flow variables one obtains:

$$\begin{aligned} u_i(\mathbf{x}, t) &= U_i(\mathbf{x}, t) + u'_i(\mathbf{x}, t), \\ p(\mathbf{x}, t) &= P(\mathbf{x}, t) + p'(\mathbf{x}, t). \end{aligned} \quad (2.6)$$

Equations 2.6 are then substituted into equation 2.1 and into eq. 2.2 to yield the Reynolds-averaged equations of motion:

$$\frac{\partial \rho U_i}{\partial x_i} = 0, \quad (2.7)$$

---

<sup>2</sup>By averaging, one can make use of three processes which, for this application, yield analogous results. They can be spatial, time or ensemble average. The former two operate by choosing appropriate length and time scales, respectively, so that the average flow does vary with respect to the chosen variable. In those cases, the flow must be steady and/or homogeneous and isotropic. The latter averaging, however, is a two-variable dependent quantity averaged by means of several samples of the desired quantity in that flow. If the turbulent quantity is both stationary and homogeneous, the three averages are equal and the process is ergodic.

$$\frac{\partial \rho U_i}{\partial t} + \frac{\partial}{\partial x_j} (\rho U_i U_j + \overline{\rho u'_i u'_j}) = -\frac{\partial P}{\partial x_i} + \frac{\partial}{\partial x_j} \left[ \mu \left( \frac{\partial U_i}{\partial x_j} + \frac{\partial U_j}{\partial x_i} \right) \right]. \quad (2.8)$$

In the integral form, the same equations read:

$$\int_S \rho U_i n_i dS = 0, \quad (2.9)$$

$$\frac{\partial}{\partial t} \int_V \rho U_i dV + \int_S \rho (U_i U_j + \overline{u'_i u'_j}) n_j dS = \int_S \left[ \mu \left( \frac{\partial U_i}{\partial x_j} + \frac{\partial U_j}{\partial x_i} \right) \mathbf{e}_j - P \mathbf{e}_i \right] \cdot \mathbf{n} dS. \quad (2.10)$$

By comparing the original and averaged equations, one notices firstly that the conservation of mass has the mean velocity replacing the instantaneous velocity. That is because the divergence of the fluctuating velocity is also zero. Furthermore, the new term in equations 2.8 and 2.10, namely  $\overline{u'_i u'_j}$ , is the specific Reynolds stress tensor and it gives the distribution of the fluctuating stresses due to the fluid motion. In its most common form, the Reynolds stress tensor is given by

$$\tau_{ij} = -\overline{\rho u'_i u'_j}. \quad (2.11)$$

The closure within URANS is generally achieved by means of the eddy viscosity concept introduced in the Boussinesq hypothesis:

$$\tau_{ij} = \mu_t \left( \frac{\partial U_i}{\partial x_j} + \frac{\partial U_j}{\partial x_i} \right) - \frac{2}{3} \rho \delta_{ij} k - \frac{1}{3} \delta_{ij} \frac{\partial U_k}{\partial x_k}, \quad (2.12)$$

in which  $k$  is the turbulent kinetic energy. For incompressible flow, the last term in equation 2.12 yields zero.

One of the main contributions of this thesis is the implementation, evaluation and improvement of state-of-the-art turbulence modeling in order to more accurately predict complex three-dimensional and transitional flows.

## 2.2 URANS Equations in Non-Inertial Reference Frames

Derivation of the URANS equations in non-inertial reference frames will be shown below with the purpose of doing moving body calculations in this thesis. Consider the inertial

and non-inertial reference frames in figure 2.1. The non-inertial one is attached to the rigid body, which displays arbitrary translational and rotational motion. Furthermore,  $\mathbf{X}_O$  is the origin of the moving (translating and rotating) body-fixed reference frame. Consider the motion of the particle at  $\mathbf{P}$  and let its velocity be written as  $\mathbf{V}$ . Hence, the position of a fluid particle at  $\mathbf{P}$  with body-referenced position  $\mathbf{x}$  in the earth-fixed reference system is defined as:

$$\mathbf{X} = \mathbf{X}_O + \mathbf{x}. \quad (2.13)$$

The velocity and acceleration of the fluid particle seen by an observer at the inertial reference system are:

$$\begin{aligned} \mathbf{U} &= \mathbf{U}_O + \boldsymbol{\Omega} \wedge \mathbf{x} + \mathbf{V} \\ \frac{D\mathbf{U}}{Dt} &= \mathbf{a} + 2\boldsymbol{\Omega} \wedge \mathbf{V} + \mathbf{A}_O + \dot{\boldsymbol{\Omega}} \wedge \mathbf{x} + \boldsymbol{\Omega} \wedge [\boldsymbol{\Omega} \wedge \mathbf{x}], \end{aligned} \quad (2.14)$$

in which one identifies  $\mathbf{U}_g = \mathbf{U}_O + \boldsymbol{\Omega} \wedge \mathbf{x}$  as the velocity of the body-fixed reference system. In order to model a general rigid-body motion (translation and/or rotation) of one object

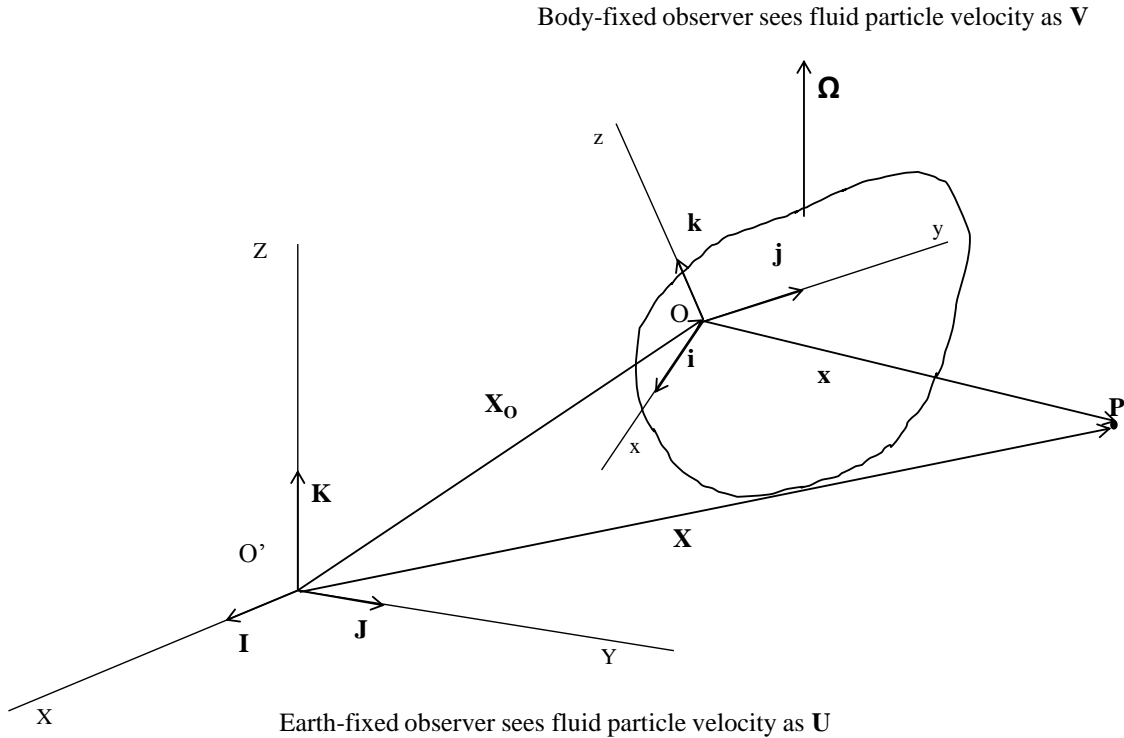


Figure 2.1: Writing the fluid equations of motion in inertial and non-inertial coordinate frames.

within URANS, three different main approaches are possible:

- Relative-formulation, *RFM*, or body-forces-approach: the fluid transport equations are written and solved in the moving or relative reference frame. Extra volumic terms, or body-forces, have to be considered coming from equation 2.14;
- Absolute-formulation, *AFM*: the fluid transport equations are solved in the moving reference frame but written in terms of absolute or inertial reference frame quantities;
- Moving-grid-formulation, *MVG*: the fluid transport equations are written and solved in the earth-fixed reference frame. Due to the motion of the objects, the equations are inherently unsteady, even for steady motions.

In the **RFM formulation** the conservation equations are rewritten as:

$$\frac{\partial \rho V_i}{\partial x_i} = 0, \quad (2.15)$$

$$\begin{aligned} \frac{\partial \rho V_i}{\partial t} + \frac{\partial}{\partial x_j} (\rho V_i V_j) = & \frac{\partial}{\partial x_j} \left[ (\mu + \mu_t) \left( \frac{\partial V_i}{\partial x_j} + \frac{\partial V_j}{\partial x_i} \right) \right] \\ & - \frac{\partial}{\partial x_i} \left( P + \frac{2}{3} \rho k \right) \\ & - \rho [\ddot{X}_{Oi} + \epsilon_{ijk} \dot{\Omega}_j x_k + 2\epsilon_{ijk} \Omega_j V_k + \epsilon_{ijk} \Omega_j (\epsilon_{ijk} \Omega_i x_j)]. \end{aligned} \quad (2.16)$$

In integral form, the same equations are written:

$$\int_S \rho V_i n_i dS = 0, \quad (2.17)$$

$$\begin{aligned} \frac{\partial}{\partial t} \int_V \rho V_i dV + \int_S \rho V_i V_j n_j dS = & \int_S (\mu + \mu_t) \left( \frac{\partial V_i}{\partial x_j} + \frac{\partial V_j}{\partial x_i} \right) e_j n_j dS \\ & - \int_V \frac{\partial}{\partial x_j} \left( P + \frac{2}{3} \rho k \right) e_i n_i dV \\ & - \int_V \rho [\ddot{X}_{Oi} + \epsilon_{ijk} \dot{\Omega}_j x_k + 2\epsilon_{ijk} \Omega_j V_k + \epsilon_{ijk} \Omega_j (\epsilon_{ijk} \Omega_i x_j)] dV. \end{aligned} \quad (2.18)$$

In this case, boundary conditions are usually defined in the body-fixed reference system.

In the **AFM formulation** the URANS equations are rewritten in differential form as:

$$\frac{\partial \rho (U_i - U_{gi})}{\partial x_i} = 0, \quad (2.19)$$

$$\begin{aligned}
\frac{\partial \rho U_i}{\partial t} + \frac{\partial}{\partial x_j} (\rho U_i (U_j - U_{gj})) &= \frac{\partial}{\partial x_j} \left[ (\mu + \mu_t) \left( \frac{\partial U_i}{\partial x_j} + \frac{\partial U_j}{\partial x_i} \right) \right] \\
&\quad - \frac{\partial}{\partial x_i} \left( P + \frac{2}{3} \rho k \right) \\
&\quad - \rho \epsilon_{ijk} \Omega_j U_k.
\end{aligned} \tag{2.20}$$

In integral form, these equations are written:

$$\int_S \rho (U_i - U_{gi}) n_i dS = 0 \tag{2.21}$$

$$\begin{aligned}
\frac{\partial}{\partial t} \int_V \rho U_i dV + \int_S \rho U_i (U_j - U_{gj}) n_j dS &= \int_S (\mu + \mu_t) \left( \frac{\partial U_i}{\partial x_j} + \frac{\partial U_j}{\partial x_i} \right) e_j n_j dS \\
&\quad - \int_V \frac{\partial}{\partial x_j} \left( P + \frac{2}{3} \rho k \right) e_i n_i dV \\
&\quad - \int_V \rho (\epsilon_{ijk} \Omega_j U_k) dV.
\end{aligned} \tag{2.22}$$

Notice that  $\int_S V_g dS$  or  $\frac{\partial V_{gi}}{\partial x_i} = 0$ , since rigid-body motions are dealt with herein. Also, boundary-conditions may be defined both in body and earth-fixed reference system.

In the **MVG formulation** the URANS equations are rewritten as:

$$\frac{\partial \rho (U_i - U_{gi})}{\partial x_i} = 0, \tag{2.23}$$

$$\begin{aligned}
\frac{\partial \rho U_i}{\partial t} + \frac{\partial}{\partial x_j} (\rho U_i (U_j - U_{gj})) &= \frac{\partial}{\partial x_j} \left[ (\mu + \mu_t) \left( \frac{\partial U_i}{\partial x_j} + \frac{\partial U_j}{\partial x_i} \right) \right] \\
&\quad - \frac{\partial}{\partial x_i} \left( P + \frac{2}{3} \rho k \right).
\end{aligned}$$

In integral form, these equations are written:

$$\int_S (U_i - U_{gi}) n_i dS = 0, \tag{2.24}$$

$$\begin{aligned}
\frac{\partial}{\partial t} \int_V \rho U_i dV + \int_S \rho U_i (U_j - U_{gj}) n_j dS &= \int_S (\mu + \mu_t) \left( \frac{\partial U_i}{\partial x_j} + \frac{\partial U_j}{\partial x_i} \right) e_j n_j dS \\
&\quad - \int_V \frac{\partial}{\partial x_j} \left( P + \frac{2}{3} \rho k \right) e_i n_i dV,
\end{aligned}$$

in which case, boundary conditions are always defined in the earth-fixed reference system.

The three approaches are equivalent in terms of their formulation and, if solved with the same accuracy, should produce the same results. However, considering the nature of these equations, their discretized forms are somewhat different.

Consider the momentum conservation equation in the relative formulation, equation 2.18. The right hand side of that equation may result very large (in absolute sense) if the body motions are large, thus impairing convergence, both in inner and outer loop procedures. For that reason, this formulation is not used herein. An important issue to be considered at this point is that one must also solve transport equations for the turbulent and transition quantities and, in fact, any other transported quantity considering the AFM and MVG approaches. This is done conveniently by simply changing the convection of the generic variable  $\phi$  from its original form written as:

$$\int_S \rho \phi U_j n_j dS, \quad (2.25)$$

to the following one, which is valid for both AFM and MVG:

$$\int_S \rho \phi (U_j - U_{gj}) n_j dS. \quad (2.26)$$

It is worth noting that an arbitrary choice in favor of MVG approach has been made in the applications of this thesis, since there is no fundamental difference in the MVG and AFM when translational motion is considered.

## 2.3 Geometry Handling

The volume and the location of the center of each cell have to be determined for the description of the domain. Moreover, for each of the faces, the area, the normal vector and the center also have to be computed as showed below.

Each cell face has three or more vertices  $\mathbf{x}_l$ , ( $l = k, \dots, N_v$ ), ( $N_v \geq 3$ ), and the face area vector is found, after subdividing the face into  $N_v - 2$  triangles, from the following sum:

$$\mathbf{S}_f = \frac{1}{2} \sum_{l=3}^{N_v} (\mathbf{x}_{l-1} - \mathbf{x}_1) \times (\mathbf{x}_l - \mathbf{x}_1). \quad (2.27)$$

If the vertices are visited in clockwise sense when viewing the face from the cell center,

$\mathbf{S}_f$  points out of the cell. The face area is the magnitude of this vector,  $S_f = |\mathbf{S}_f|$ , while the face unit normal vector is the unit vector in the direction of  $\mathbf{S}_f$ :

$$\mathbf{n}_f = \frac{\mathbf{S}_f}{|\mathbf{S}_f|}, \quad \mathbf{S}_f = \mathbf{n}_f |\mathbf{S}_f|. \quad (2.28)$$

The face center is taken as the average of the centers of each triangle, weighted by the area of the triangle:

$$\mathbf{x}_f = \left( \frac{1}{N_v - 2} \right) \frac{\sum_{l=3}^{N_v} [(\mathbf{x}_{l-1} - \mathbf{x}_1) \times (\mathbf{x}_l - \mathbf{x}_1)] \frac{1}{3} [\mathbf{x}_l + \mathbf{x}_{l-1} + \mathbf{x}_1]}{\sum_{l=3}^{N_v} [(\mathbf{x}_{l-1} - \mathbf{x}_1) \times (\mathbf{x}_l - \mathbf{x}_1)]} \quad (2.29)$$

The cell volume is obtained by using Gauss' theorem:

$$\Delta V = \frac{1}{3} \sum_{i=1}^{N_f} \mathbf{x}_{f_i} \cdot \mathbf{S}_{f_i}, \quad (2.30)$$

where  $N_f$  is the number of cell faces. The location of the cell center is chosen as the average of the face centers:

$$\mathbf{x}_c = \frac{1}{N_f} \sum_{i=1}^{N_f} \mathbf{x}_{f_i}. \quad (2.31)$$

## 2.4 Numerical Discretization

Taking advantage of the similarity of transport equations for different variables, ReFRESKO uses the same framework to discretize the equations and solve for the different flow variables (velocities, turbulent quantities, energy etc). The general transport equation is written in integral form as (PATANKAR, 1980):

$$\frac{\partial}{\partial t} \int_V (\rho \phi) dV + \int_S \phi U_j n_j dS = \int_S \left( \Gamma \frac{\partial u_i}{\partial x_j} \mathbf{e}_j \right) \cdot \mathbf{n} dS + \int_V q_\phi dV, \quad (2.32)$$

in which  $\mathbf{n}$  is the normal vector,  $\Gamma$  is a diffusive coefficient and  $q_\phi$  is a source or sink term. In this general equation, the first and second terms on the left-hand side are the unsteady and convective terms, respectively. The first and second terms on the right-hand side are respectively the diffusive and source/sink terms.

ReFRESKO uses a collocated approach, thus all flow variables are defined in cell centers and interpolation practices are used when face values are needed as showed below.

The volume integrals of quantities  $\phi$  are calculated as:

$$\int_V \phi dV \approx \phi_c \Delta V, \quad (2.33)$$

in which  $\phi_c$  is the value of  $\phi$  at the cell center. The surface integrals are approximated as:

$$\int_S \phi dS \approx \sum_{i=1}^{N_f} \phi_{f_i} S_{f_i}, \quad (2.34)$$

in which  $\phi_{f_i}$  is the variable value in the cell face center and  $S_{f_i}$  is the cell face area.

The following sections will address the numerical tools to deal with each of the transport equation terms.

### 2.4.1 Unsteady Term

The time derivative of a conserved variable  $\phi$  in an invariant control volume  $V$  is as follows:

$$\frac{\partial}{\partial t} \int_V (\rho\phi) dV. \quad (2.35)$$

Discretization of this term in the applications showed in this thesis is done by means of an second-order, implicit, three-time-level backwards approximation:

$$\frac{\partial}{\partial t} \int_V (\rho\phi) dV \approx [1.5(\rho_c\phi_c\Delta V)^n - 2.0(\rho_c\phi_c\Delta V)^{n-1} + 0.5(\rho_c\phi_c\Delta V)^{n-2}]/\Delta t, \quad (2.36)$$

in which  $n$  is the time level,  $\Delta t$  is the time step,  $\Delta V$  is the control volume, and  $\phi_c$  is the variable value in the volume center.

### 2.4.2 Gradients

Gradients of variables are also needed in the conservation equations. Gauss' Theorem is applied to derive the expression for the gradient of  $\phi$  at the cell center<sup>3</sup>:

$$(\nabla\phi)_c \approx \frac{1}{\Delta V} \sum_{i=1}^{N_f} \phi_{f_i} S_{f_i}. \quad (2.37)$$

---

<sup>3</sup>The vector notation for  $\frac{\partial\phi}{\partial x_j}$ ,  $\nabla\phi$ , is here used as it is somewhat more practical.

As seen above, gradients at face centers are needed in the discretization of some terms. A few comments in that regard will be made in what follows, but first some preliminary definitions are needed: each cell face has two neighboring cell centers, denoted here by the indices  $c_1$  and  $c_2$  (unless it is a face on the domain boundary; the center of the virtual cell is then assumed to be the face center).

The distance vector between the cell centers is:

$$\mathbf{d} = \mathbf{x}_{c_2} - \mathbf{x}_{c_1}, \quad (2.38)$$

with magnitude

$$d = |\mathbf{x}_{c_2} - \mathbf{x}_{c_1}|, \quad (2.39)$$

while the distances between cell and face centers are denoted as:

$$d_1 = |\mathbf{x}_f - \mathbf{x}_{c_1}| \quad , \quad d_2 = |\mathbf{x}_f - \mathbf{x}_{c_2}|. \quad (2.40)$$

Based on these distances, one defines an interpolation coefficient as

$$\alpha = \frac{d_2}{d_1 + d_2}. \quad (2.41)$$

Notice that due to the choice of the center of virtual cells to be the face center, these distances have a special interpretation for boundary faces:  $d_1 = d; d_2 = 0$ .

Furthermore one defines an eccentricity vector, being the vector from the point obtained by orthogonal projection of  $\mathbf{x}_f$  on the line connecting the two cell centers to the face center  $\mathbf{x}_f$  itself (see figure 2.2), as:

$$\mathbf{e} = \mathbf{x}_f - [\alpha \mathbf{x}_{c_1} + (1 - \alpha) \mathbf{x}_{c_2}]. \quad (2.42)$$

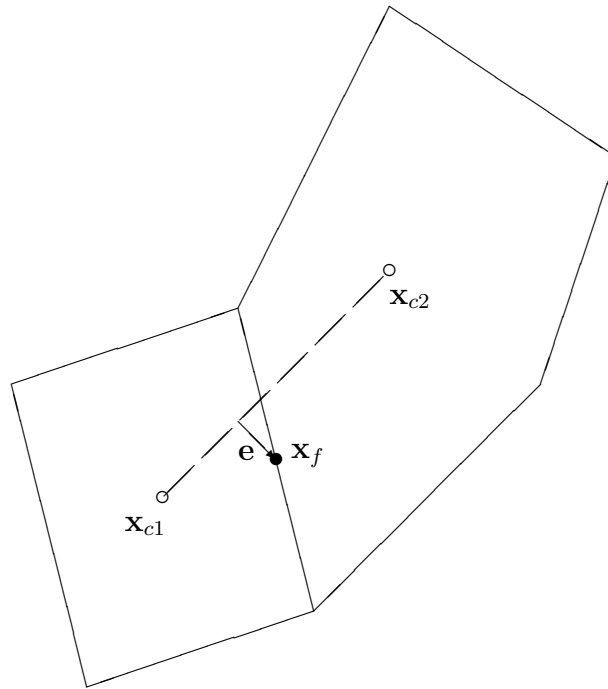


Figure 2.2: Eccentricity vector.

The gradient of  $\phi$  in the face center is computed from:

$$(\nabla\phi)_f = \alpha\nabla\phi_{c_1} + (1 - \alpha)\nabla\phi_{c_2}. \quad (2.43)$$

Along similar lines, the face value of  $\phi$  can be derived from:

$$\phi_f = \alpha\phi_{c_1} + (1 - \alpha)\phi_{c_2}, \quad (2.44)$$

and when needed the eccentricity correction is added:

$$\phi_f = \alpha\phi_{c_1} + (1 - \alpha)\phi_{c_2} + \nabla\phi_f \cdot \mathbf{e}. \quad (2.45)$$

### 2.4.3 Convective Term

The convective term in the general transport equation reads:

$$\int_S \phi U_j n_j dS = \int_S \phi (\mathbf{U} \cdot \mathbf{n}) dS, \quad (2.46)$$

which can be discretized following a face cell approach as:

$$\sum_{i=1}^{N_f} (\mathbf{U}_{f_i} \cdot \mathbf{S}_{f_i}) \phi_{f_i} = \sum_{i=1}^{N_f} q_{f_i}^{\phi}, \quad (2.47)$$

in which  $q_{f_i}^{\phi}$  is the flux of the quantity  $\phi$  in the face  $i$ . As commented above, a collocated approach is used and thus the face values ought to be related to the cell center values and that is achieved by means of interpolation practices. In the calculations showed in this thesis, two types of interpolation practices are applied, namely the upwind differencing scheme and the Quadratic Upstream Interpolation for Convective Kinematics (QUICK), see Ferziger & Peric (2002), Leonard (1979).

#### 2.4.3.1 Upwind Differencing Scheme

For each cell face  $i$  (the index is here abandoned) the convection flux  $q_f^{\phi}$  is then:

$$(\mathbf{U}_f \cdot \mathbf{S}_f) \phi_{cu}, \quad (2.48)$$

where  $\phi_{cu}$  is the value of  $\phi$  at the cell center on the upstream side of the face. It is thus a first order scheme.

First-order discretization for turbulence and transition equations is preferred in this thesis (except for the SST-SAS model as discussed further ahead) as the increased diffusion (eddy viscosity) generally represents dominant contribution to the momentum equations only inside boundary layers; incidentally, it is precisely near walls that second-order discretization of the convection terms of turbulence and transition equations cause convergence problems, specially for the turbulent dissipation variable ( $\omega$ ), as shall be discussed later. Therefore, by using first-order discretization, convergence problems are avoided, but not at a cost of lowering the general accuracy of the solution. This argument has proven reasonable as calculated grid convergence is normally close to the theoretical one, as shall be presented in some results of this thesis.

#### 2.4.3.2 QUICK Scheme

The QUICK scheme is applied in this thesis for the momentum equations and also for the turbulence equations, when the SST-SAS is used. When applying QUICK, besides using the variable values on both sides of a face, the gradient of that variable on the upstream

side of the face is also used. Therefore, at this point, the upstream and downstream cells to each face have to be determined.

Identifying the cell center on the upstream side of the face with the index  $cu$  and the cell center on the downstream side with  $cd$  and let the parameter  $s$  be defined along the straight line between the cell centers  $\mathbf{x}_{cu}$  and  $\mathbf{x}_{cd}$ :

$$s = \frac{|\mathbf{x} - \mathbf{x}_{cu}|}{|\mathbf{x}_{cd} - \mathbf{x}_{cu}|}. \quad (2.49)$$

Then, the quadratic function  $\phi(s)$  along that line is:

$$\phi(s) = a s^2 + b s + c, \quad (2.50)$$

while the first derivative is:

$$\frac{d\phi}{ds}(s) = \nabla\phi(s) \cdot (\mathbf{x}_{cd} - \mathbf{x}_{cu}) = 2a s + b.$$

With the three conditions:

$$\phi(0) = \phi_{cu}, \quad (2.51)$$

$$\phi(1) = \phi_{cd}, \quad (2.52)$$

$$\frac{d\phi}{ds}(0) = (\nabla\phi)_{cu} \cdot (\mathbf{x}_{cd} - \mathbf{x}_{cu}). \quad (2.53)$$

the coefficients  $a, b$  and  $c$  are solved, yielding:

$$a = \phi_{cd} - \phi_{cu} - (\nabla\phi)_{cu} \cdot (\mathbf{x}_{cd} - \mathbf{x}_{cu}), \quad (2.54)$$

$$b = (\nabla\phi)_{cu} \cdot (\mathbf{x}_{cd} - \mathbf{x}_{cu}), \quad (2.55)$$

$$c = \phi_{cu}, \quad (2.56)$$

so that:

$$\phi(s) = \phi_{cu} + s^2(\phi_{cd} - \phi_{cu}) + s(1 - s) [\nabla\phi_{cu} \cdot (\mathbf{x}_{cd} - \mathbf{x}_{cu})]. \quad (2.57)$$

Let  $s_f$  denote the value of  $s$  where the line between the cell centers intersects the cell face, then the value of  $\phi$  at the intersection point is given by the expression above with  $s$  replaced by  $s_f$ :

$$\phi_f = \phi_{cu} + s_f^2(\phi_{cd} - \phi_{cu}) + s_f(1 - s_f) [\nabla\phi_{cu} \cdot (\mathbf{x}_{cd} - \mathbf{x}_{cu})]. \quad (2.58)$$

Quadratic interpolation may result in overshoots, particularly when jumps in the variable  $\phi$  are encountered. Therefore a flux limiter was necessary to make sure that wiggles in the solution are avoided. The reader is referred to the work of Leonard (1979) for the background of such flux-limiting schemes.

The idea behind the limiting criteria is simple, in that it only prevents the variable value in the face to undershoot/overshoot the range defined by the upstream and downstream cell centers. If that happens, then the limiter can change the approximation from QUICK to Upwind, taking the value of the upstream center.

The convection term of the momentum equations is non-linear due to the velocity:  $\mathbf{U}(\mathbf{U} \cdot \mathbf{n})$ . This issue is dealt with by means of the Picard linearization, which is taking an explicit contribution from the previous iteration, i.e. the mass flux  $(\mathbf{U} \cdot \mathbf{n})$  on the face is taken from the previous iteration.

#### 2.4.4 Diffusive Term

The diffusion flux in the generic equation reads:

$$\int_S \Gamma \left( \frac{\partial \phi}{\partial x_j} \right) \mathbf{e}_j \cdot \mathbf{n} dS = \int_S \Gamma \nabla \phi \cdot \mathbf{n} dS, \quad (2.59)$$

which is approximated as:

$$\sum_{i=1}^{N_f} \Gamma_{f_i} (\nabla \phi)_{f_i} \cdot \mathbf{S}_{f_i}. \quad (2.60)$$

The tensor  $\nabla \phi$  can be interpolated to cell faces as in the convection scheme. However, the face value  $\nabla \phi_f$  depends on  $\nabla \phi$  at neighbor cell centers, which in turn depends on  $\phi$  values at cell faces etc, making a large stencil. In order to avoid that, the approach proposed by Ferziger & Peric (2002) is adopted, which consists in splitting the the flux into an implicit part and a deferred correction (i.e. from the previous iteration), showed inside the box in the equation below:

$$\nabla \phi_f \cdot \mathbf{S}_f = \frac{\phi_{c2} - \phi_{c1}}{d} |\mathbf{S}_f| + \boxed{\nabla \phi_f \cdot \left( \mathbf{S}_f - \frac{\mathbf{d}}{d} |\mathbf{S}_f| \right)}. \quad (2.61)$$

## 2.4.5 Source and Pressure Terms

The source terms for the momentum equations or for any transport equation can be written in an integral form for an arbitrary scalar  $\phi$  as:

$$Q^\phi = \int_V \mathbf{q}_\phi dV, \quad (2.62)$$

which can be discretized simply at the center of the cell  $c$  as:

$$Q_c^\phi \approx \mathbf{q}_{\phi_c} \Delta V. \quad (2.63)$$

For the pressure term in the momentum equations, a conservative approach is considered and the pressure term is considered as a surface force:

$$Q^p = - \int_S p n_i e_i dS = - \int_S p \mathbf{I} \cdot \mathbf{n} dS. \quad (2.64)$$

The discretization form is then:

$$Q_c^p \approx - \sum_{i=1}^{N_f} p_f \mathbf{I} \cdot S_f, \quad (2.65)$$

in which  $p_f$  is interpolated from the cell values.

## 2.5 Solution Process

In ReFRESKO, the conservation equations are solved in a segregated manner, i.e., in spite of being coupled equations, they are solved individually for each variable assuming the others as known and then an iteration procedure restores the coupling of the equations, by satisfying all the equations within certain tolerances, which are quantified by means of residuals.

In particular, the pressure-velocity coupling is dealt with by an iterative method based on the Semi-Implicit Method for Pressure Linked Equations (SIMPLE) (FERZIGER; PERIC, 2002; PATANKAR, 1980). The SIMPLE and some of its variants were firstly developed for application with staggered configuration, but in ReFRESKO, the discretization scheme is collocated. Spurious pressure oscillations are avoided by means of introducing a correction to the velocity fluxes at the cell faces, the so-called pressure weighted interpolation, see Ferziger & Peric (2002).

When the convective and source terms are non-linear, they are linearized by means of the Picard method, see Ferziger & Peric (2002). In that manner, linear systems are derived from each transport equation nested within the outer loops. Moreover, for unsteady computations, the iteration process is to be performed within each time step. The schematic process is showed below.

```

initialization
do (time loop)
  increment t
  do (outer loop)
    solve the momentum equations with guesses or values from
    previous iteration
    do (inner loop)
      solve linear system of equations
    enddo (inner loop)
    solve the poisson pressure equation
    do (inner loop)
      solve linear system of equations
    enddo (inner loop)
    correct velocity field
    solve turbulence model equations
    do (inner loop)
      solve linear system of equations
    enddo (inner loop)
    solve transition model equations (when needed)
    do (inner loop)
      solve linear system of equations
    enddo (inner loop)
  enddo (outer loop)
enddo (time loop)

```

As seen above, there are three levels of loops: a time loop, an outer loop and the inner loops. The time loop occurs in the unsteady calculations and when finished, time is incremented. Within the outer loop, all of the equations will be solved and once all conservation equations are satisfied within some tolerance, the outer loops are finished and the next time loop starts. Finally, the inner loops take place when solving each of the matrix system which result from the discretization of the equations for each component.

There are several choices of solvers available in the code, but in this thesis, the linear systems are first pre-conditioned and solved iteratively by a method based on the conjugate gradient method, see Ferziger & Peric (2002). The pre-conditioning of the linear systems is done with the objective of replacing the original system with one that presents the same solution, but a smaller condition number,  $\kappa = \lambda_{max}/\lambda_{min}$ , in which  $\lambda_{max}$  and  $\lambda_{min}$  are,

respectively, the largest and smallest matrix eigenvalues.

The momentum equations are pre-conditioned by block-Jacobi's method and solved by the Generalized Minimum Residual method; the pressure equation is pre-conditioned by block-Jacobi's method and solved by the conjugate gradient method; the turbulence and transition equations are pre-conditioned by block-Jacobi's method and solved by the Generalized Minimum Residual method. These methods are showed in Balay et al. (2013) and Ferziger & Peric (2002).

In the following sections some details are presented on the discretization of the different terms in the transport equations, alternating between tensor and vector notation, whenever one or the other is more convenient.

### 2.5.1 Under Relaxation Procedure

Within the outer loops an under relaxation of the newly calculated variables is usually applied in order to smooth the variation from the previously to the newly calculated variable. For some flow property  $\phi$ , the following expression is used:

$$\phi = \phi^{old} + \beta(\phi^{new} - \phi^{old}), \quad (2.66)$$

in which  $\beta$  is the under-relaxation parameter varying between 0 and 1.

### 2.5.2 Pressure-Correction Scheme

The pressure-correction scheme is obtained by the steps to follow. First the momentum equations are solved in a segregated manner, assuming the pressure to be known, yielding a predictor for the velocity field, which is not divergence free, however. With this preliminary velocity field the Poisson equation for the pressure is solved, and with the new pressure a correction on the velocity is made so that it satisfies the continuity equation. This process is repeated until convergence criteria on the residuals of the equations is satisfied.

Let the velocity field resulting from the first step be denoted as  $\mathbf{U}^*$ . The second step

involves the solution of the Poisson equation for the pressure<sup>4</sup>:

$$\nabla \cdot (\nabla p) = -\nabla \cdot \left\{ \nabla \cdot (\rho \mathbf{U}\mathbf{U}) - \nabla \Gamma \cdot \nabla \phi \right\}. \quad (2.67)$$

By writing  $p = p^{n-1} + p'$ , the contribution related to  $p^{n-1}$  can be subtracted from the original Poisson equation and the resulting equation for  $p'$  be simplified to yield:

$$\nabla \cdot \nabla p' = -\nabla \cdot \mathbf{U}^*. \quad (2.68)$$

Integration for a cell volume using Gauss' theorem gives the relation:

$$\int_S \nabla p' \cdot \mathbf{n} \, dS = - \int_S \mathbf{U}^* \cdot \mathbf{n} \, dS, \quad (2.69)$$

which is discretized as

$$\sum_{i=1}^{N_f} \nabla p'_f \cdot \mathbf{S}_f = - \sum_{i=1}^{N_f} \mathbf{U}_f^* \cdot \mathbf{S}_f, \quad (2.70)$$

Finally the velocity field is updated with:

$$\mathbf{U} = \mathbf{U}^* - \frac{\Delta V}{A_c^u} (\nabla p' - \overline{\nabla p'}), \quad (2.71)$$

where  $A_c^u$  is a coefficient obtained from the discretization of the momentum equation and  $\overline{\nabla p'}$  is a pressure weighted interpolation correction.

The elements showed above are combined with the turbulence modeling aspects of the following Chapter to support large part of the work presented herein.

---

<sup>4</sup>This Poisson equation can be obtained by taking the divergence of the momentum equations and combining it with the continuity equation (FERZIGER; PERIC, 2002).

# Chapter 3

## Turbulence Modeling

*This chapter presents the formulation and details of the turbulence models implemented for the applications developed in this doctoral work. The details of the implementation as done within the framework of ReFRESKO and discussion concerning the capabilities of the models are carried out aiming at their application to the cylinder flow problem.*

### 3.1 $k - \omega$ SST Model

In its original version, Menter (1994) developed this turbulence model based on two transport equations, one for the turbulent kinetic energy,  $k$ , and one transport equation for the dissipation per unit kinetic energy,  $\omega$ . The Shear Stress Transport (SST) model is similar to Menter's Baseline model (BSL). The BSL model was based on Wilcox's  $k - \omega$  formulation in the near wall region and on the standard  $k - \epsilon$  model (LAUNDER; SHARMA, 1974) in the outer wake region and in free shear layers. The SST additionally includes modifications to the eddy viscosity. Furthermore, Menter, Kuntz & Langtry (2003) further improved it by again changing the definition of the eddy viscosity, limiters and model constants, modifications implemented in ReFRESKO during this work.

The equation for transport of turbulent kinetic energy,  $k$ , is given by:

$$\frac{\partial \rho k}{\partial t} + \frac{\partial}{\partial x_j} (\rho U_j k) = P_k - \beta^* \rho \omega k + \frac{\partial}{\partial x_j} \left[ (\mu + \sigma_k \mu_t) \frac{\partial k}{\partial x_j} \right]. \quad (3.1)$$

In this equation, the production term is  $P_k = \mu_t S^2 - \mu_t \frac{2}{3} \left( \frac{\partial U_k}{\partial x_k} \right)^2 - \rho k \frac{2}{3} \left( \frac{\partial U_k}{\partial x_k} \right)^2$ , in which  $S^2 = S_{ij} S_{ij}$  and  $S_{ij} = \frac{1}{2} \left( \frac{\partial U_i}{\partial x_j} + \frac{\partial U_j}{\partial x_i} \right)$ . For incompressible flow, the two latter terms of the

production vanish. It is worth noting that a realizability condition limiting the growth of turbulence in stagnation regions is advisable:  $\tilde{P}_k = \min(P_k, 20\beta^*k\omega)$  for  $k-\omega$  SST 1994 and  $\tilde{P}_k = \min(P_k, 10\beta^*k\omega)$  for  $k-\omega$  SST 2003.

The equation for transport of turbulent frequency,  $\omega$ , is:

$$\frac{\partial \rho \omega}{\partial t} + \frac{\partial}{\partial x_j} \left[ \rho U_j \omega - (\mu + \sigma_\omega \mu_t) \frac{\partial \omega}{\partial x_j} \right] = \gamma \rho \Omega^2 - \beta \rho \omega^2 + 2(1 - F_1) \frac{\rho \sigma_{w2}}{\omega} \frac{\partial k}{\partial x_j} \frac{\partial \omega}{\partial x_j}, \quad (3.2)$$

where  $\Omega^2 = 2\Omega_{ij}\Omega_{ij}$  and  $\Omega_{ij} = \frac{1}{2} \left( \frac{\partial U_i}{\partial x_j} - \frac{\partial U_j}{\partial x_i} \right)$ . The auxiliary function  $F_1$  seen in equation 3.2 makes the transition between the  $k-\omega$  original model and the  $k-\epsilon$ , connecting the shear areas and the free-stream areas:

$$F_1 = \tanh \left[ \min \left[ \max \left( 2 \frac{\sqrt{k}}{0.09d\omega}, \frac{500\nu}{d^2\omega} \right), \frac{4\rho\sigma_{w2}\kappa}{CD_{k\omega}d^2} \right] \right]^4, \quad (3.3)$$

$$\beta^* = 0.09, \quad \kappa = 0.41,$$

in which  $d$  is the distance from the nearest grid point to the wall and the term  $CD_{k\omega}$  is defined in  $k-\omega$  SST 1994 as:

$$CD_{k\omega} = \max \left( \frac{2\rho\sigma_{w2}}{\omega} \frac{\partial k}{\partial x_j} \frac{\partial \omega}{\partial x_j}, 1 \times 10^{-20} \right), \quad (3.4)$$

whereas, in  $k-\omega$  SST 2003, it is defined differently:

$$CD_{k\omega} = \max \left( \frac{2\rho\sigma_{w2}}{\omega} \frac{\partial k}{\partial x_j} \frac{\partial \omega}{\partial x_j}, 1 \times 10^{-10} \right). \quad (3.5)$$

The coefficients  $\beta$ ,  $\gamma$ ,  $\sigma_k$  and  $\sigma_w$  provide the transition between the original Wilcox's  $k-\omega$  model (WILCOX, 1988), denoted by 1, and the  $k-\epsilon$  model (LAUNDER; SHARMA, 1974), denoted by 2:

$$\phi = F_1\phi_1 + (1 - F_1)\phi_2, \quad \phi = \{\beta, \gamma, \sigma_k, \sigma_w\}, \quad (3.6)$$

with the coefficients being:

$$\begin{aligned} \sigma_{k1} &= 0.85, & \sigma_{\omega1} &= 0.50, & \beta_1 &= 0.075, \\ \sigma_{k2} &= 1.00, & \sigma_{\omega2} &= 0.856, & \beta_2 &= 0.0828. \end{aligned} \quad (3.7)$$

The constant  $\gamma$  is defined in  $k-\omega$  SST 1994 as:

$$\begin{aligned} \gamma_1 &= \beta_1/\beta_* - \sigma_{\omega1}K^2/\sqrt{\beta_*} = 0.553, \\ \gamma_2 &= \beta_2/\beta_* - \sigma_{\omega2}K^2/\sqrt{\beta_*} = 0.4404, \end{aligned} \quad (3.8)$$

whereas, for the  $k - \omega$  SST 2003:

$$\begin{aligned}\gamma_1 &= \beta_1/\beta_* - \sigma_{\omega 1}K^2/\sqrt{\beta_*} = 0.556, \\ \gamma_2 &= \beta_2/\beta_* - \sigma_{\omega 2}K^2/\sqrt{\beta_*} = 0.4400.\end{aligned}\quad (3.9)$$

The eddy viscosity in  $k - \omega$  SST 1994 is determined by:

$$\mu_t = \frac{\rho a_1 k}{\max(a_1 \omega, \Omega F_2)}, \quad a_1 = 0.31. \quad (3.10)$$

The auxiliary function  $F_2$  is defined using the wall distance  $d$ :

$$F_2 = \tanh \left[ \max \left( 2 \frac{\sqrt{k}}{0.09 d \omega}, \frac{500 \nu}{d^2 \omega} \right) \right]^2. \quad (3.11)$$

In the latter version  $k - \omega$  SST 2003, the eddy viscosity is defined differently:

$$\mu_t = \frac{\rho a_1 k}{\max(a_1 \omega, S F_2)}, \quad a_1 = 0.31, \quad (3.12)$$

in which  $S = \sqrt{2S_{ij}S_{ij}}$  replaces  $\Omega$  in the previous definition.

In order to initialize and set the inflow values for the turbulent quantities in ReFRESCO, the values are set for eddy viscosity by means of a relation with laminar viscosity:

$$f = \mu_t/\mu, \quad (3.13)$$

because it is easier to relate to that than to kinetic energy itself. The quantities are then imposed by setting  $f$  or  $\mu_t/\mu$  and computing  $k$  and  $\omega$  using dimensional considerations:

$$k = f \nu \times 10 \frac{U_{ref}}{L_{ref}}, \quad (3.14)$$

and:

$$\omega = 10 U_{ref}/L_{ref}. \quad (3.15)$$

Furthermore, the following conditions hold on the wall:

$$k = 0, \quad \omega = 10 \frac{6\nu}{\beta} d^2. \quad (3.16)$$

In these equations,  $U_{ref}$  and  $L_{ref}$  are reference values. The  $\omega$  boundary condition usually causes convergence problems in the convective term, where the face values are needed. Flux limiters are important for that issue and, furthermore, it has been observed that  $y^+$  has to be small (of the order 1 – 0.1 for the asymptotic trend of  $\omega$  to be captured (see

also Eça & Hoekstra (2008)).

This model has been widely applied due to the good performance in adverse pressure gradients and is known not to be largely sensitive to far-field turbulence values. The improvements brought by the  $k$ - $\omega$  SST compared to the previous ones within RANS have predicated its use together with the modern hybrid models such as PANS, DES, DDES, SAS and the LCTM showed below.

### 3.2 SST-SAS Model

The concept of Scale-Adaptive Simulations (SAS) arises from the need to improve the modeling with regards to the turbulent scales. In this class of models, the first transport equation still treats turbulent kinetic energy, but the second transported variable is now directly related to the integral length scale, calculated from the two-point correlation tensor,  $R_{ij} = \overline{u'_i u'_j}$ , measured in two different places which span the field at time  $t$ :

$$L(\mathbf{x}, t) = \frac{3}{16} \int_0^\infty \frac{R_{ii}(\mathbf{x}, t; r)}{k(\mathbf{x}, t)} dr. \quad (3.17)$$

Rotta (see Wilcox (1993)) was the first to formulate a transport equation for the variable  $kL$ . However, despite the somewhat superior theoretical content of this model, it did not really succeed in its original form, since it could not comply with the logarithmic law on the wall without further adjustments. It was not until about 30 years later that this model was revisited by Menter & Egorov (2004), Menter, Langtry & Volker (2006), Menter & Egorov (2010), in which the authors argument that in Rotta's model, a second derivative term from the Taylor expansion of  $kL$  did not vanish for inhomogeneous turbulence. Therefore, Menter and co-workers kept that term in the derivation of the equations and the boundary layer solution then followed the logarithmic law without any adjustments.

In fact, Menter enthusiastically argues in favor of the SAS-based models, pointing out some features that make them more suitable than the commonly used RANS models. Firstly, he points out that the only input from the flow to the turbulence equations is the flow strain,  $S = \sqrt{2S_{ij}S_{ij}}$ , which has dimension  $1/T$  and thus could not carry enough information to yield two output scales. Therefore, in the new model, another input is used, namely the length scale is included in the source term of the second transport equation.

In fact, Menter & Egorov (2010) analyze the traditional two-equations models and conclude that the integral length scale produced is  $L \sim \sqrt{k}/\omega$ . This means that the maximum length of eddies formed in a turbulent flow calculated with standard two-equations models

is proportional to the thickness of the shear layer itself. Menter argues that this is appropriate for steady shear flows, but not unsteady ones, as it damps the larger resolved scales.

One of the most interesting features brought by the SAS model is its ability to adjust the local flow scales. That is only achieved due to the additional source term in the transport equation for the second scale which relies on higher derivatives of the velocity, besides strain rate or vorticity. Egorov & Menter (2008) showed the adaptation of the concept inherent of the SAS to the  $k - \omega$  SST turbulence model. Firstly, the transformation of  $\omega$  to  $\sqrt{k}L$  is done as follows:

$$\omega = \frac{k}{c_\mu^{1/4} \sqrt{k}L}. \quad (3.18)$$

Therefore, applying the chain rule:

$$\frac{D\omega}{Dt} = \frac{1}{c_\mu^{1/4}} \left( \frac{1}{kL} \frac{Dk}{Dt} - \frac{k}{(kL)^2} \frac{D(kL)}{Dt} \right). \quad (3.19)$$

This was introduced by Egorov & Menter (2008), Menter & Egorov (2010) into the  $k - \omega$  SST 2003 model. The equations for  $k$  and  $\omega$  are derived as:

$$\begin{aligned} \frac{\partial \rho k}{\partial t} + \frac{\partial}{\partial x_j} (\rho U_j k - (\mu + \sigma_k \mu_t) \frac{\partial k}{\partial x_j}) &= P_k - \beta^* \rho \omega k, \\ \frac{\partial \rho \omega}{\partial t} + \frac{\partial}{\partial x_j} (\rho U_j \omega) &= P_\omega - \beta \rho \omega^2 + \frac{\partial}{\partial x_j} \left[ (\mu + \sigma_\omega \mu_t) \frac{\partial \omega}{\partial x_j} \right] + 2\rho (1 - F_1) \frac{\sigma_{\omega 2}}{\omega} \frac{\partial k}{\partial x_j} \frac{\partial \omega}{\partial x_j} \\ &+ \rho \max \left[ \zeta_2 S^2 \left( \frac{L}{L_{vK}} \right)^2 - 2 \frac{2k}{\sigma_\Phi} \max \left( \frac{1}{\omega^2} \frac{\partial \omega}{\partial x_j} \frac{\partial \omega}{\partial x_j}, \frac{1}{k^2} \frac{\partial k}{\partial x_j} \frac{\partial k}{\partial x_j} \right), 0 \right], \end{aligned} \quad (3.20)$$

in which one notices that: i) the first equation is unchanged from the SST 2003 model and ii) in order to recover the performance of SST model in boundary layers, the SAS model was reformulated as an additional term to the  $\omega$  equation,  $Q_{SAS}$ , not disturbing the boundary layer performance of the SST, but allowing the SAS performance in unsteady situation. Moreover, the term  $L_{vk}$  introduced above is a generalization of the von Kármán length of boundary layer formulation to three-dimensional flows. It represents a natural

length scale for the flow. It is defined as:

$$L_{vK} = \kappa \left| \frac{\sqrt{2S_{ij}S_{ij}}}{\sqrt{\frac{\partial^2 U_i}{\partial x_k^2} \frac{\partial^2 U_i}{\partial x_j^2}}} \right|. \quad (3.21)$$

### 3.2.1 A Discussion on the Scales

From the model formulation, the Scale Adaptive Simulations allows one to determine the turbulent scales directly from Eq. 3.18 and the term  $Q_{SAS}$  takes not only the shear strain, but also the natural length scale, thus diffusion does not play a role in determining the local scales. Hence, it arrives (MENTER; EGOROV, 2010):

$$L = \sqrt{\frac{\zeta_1 - \zeta_3/c_\mu^{3/4}}{\zeta_2}} L_{vK}. \quad (3.22)$$

This means that the maximum order of magnitude of the turbulent scales will adjust to the von Kármán length scale ( $L \sim L_{vK}$ ). Restating the conclusions so far:

- The two equation models normally solve one transport equation for the turbulent kinetic energy and another for the second scale, providing closure;
- The second scale is normally chosen as the dissipation or some variation of that, producing an inconsistency as, at this point, turbulence is less important than viscous dissipation. More physically consistent, closure should be obtained by using the integral (turbulent) length scale;
- For the usual two-equation models, the maximum integral length scale that is predicted in a shear flow is of the order of magnitude of the shear layer thickness:  $L \sim \delta$ . This happens because there is only one physical input in the source terms of the turbulent equations, thus diffusion plays a role in determining the output scales;
- On the other hand, models based on the SAS concept predict turbulent length scales of down to the order of magnitude of the natural length scale, represented by the von Kármán length scale,  $L \sim L_{vK}$ . This is because the turbulent equations now present two input scales (the strain and another based on higher derivatives - von Kármán scale), thus the source terms determine both scales.

### 3.2.2 Comparison with Other URANS Models

Some question that might be raised are the following: What is the fundamental difference between the usual two-equation models and the SAS-based models and why do they respond organically in different manners?

In order to try to answer those questions, it is useful to first take a step back and discuss a more fundamental question regarding the very nature of the URANS equations. As stated by Menter & Egorov (2010), there are mainly two schools of thought regarding the URANS approach: for the first, there is a separation of scales and URANS averages out all turbulent fluctuations and resolves only frequencies far lower than those of the turbulent fluctuations, which typically result from the variations in geometry or boundary conditions. For the other, URANS means application of turbulence models, derived based on the forming arguments of RANS, to the unsteady simulations, independent of the resolution content. The difference is subtle, but it will be more clear with the discussion to follow.

Revisiting the fundamental difference between equation 3.2 and the second of equations 3.20, the source terms of the former only contains an input from the flow field in the shear strain,  $S$ . For the latter, the  $Q_{SAS}$  term actually contain not only the strain, but also an information regarding the local scale,  $L_{vK}$ , which contains a higher derivative of velocities. Therefore, there is more information available in the source term of the latter than in the former. Now, as a result, in order to get closure from the turbulence equations (two turbulent scales should be determined), the diffusion term in equations 3.2 has to play a role, since convection is less important inside the logarithmic layer. Because of that, the scales that were resolved by the averaged momentum equations are actually damped and the effective length scale predicted by the model is limited by the thickness of the turbulent layer, due to the diffusion term. On the other hand, as equations 3.20 do present enough input to determine the two output scales, adjusting to the scales that the momentum equations actually resolved. Yet another question that might be raised concerns the reason why the von Kármán length scale is the appropriate additional term in the length scale equation. In constant shear, the turbulent frequency is constant in the shear layer and proportional to the shear strain, thus different eddies can merge and, in the limit, the eddies can grow to infinity. For nonhomogeneous shear, the shear strain is no longer constant, varying in the shear layer as  $S = S(y)$  ( $y$  is the distance from the wall) and so does the turbulent frequency:  $\omega = \omega(y)$ . Therefore, eddies with different frequencies can no longer merge and thus the eddies are limited in size. Their size depends, in first order, on the shear strain and its variation, which is in turn given by the von Kármán length scale,  $L_{vK}$ .

Therefore, SAS models are able to adjust the inherent scales of the flow because diffusive term does not play a role in determining the length scale produced in the second equation; contrary to that, the additional  $Q_{SAS}$  is able to produce that in the shear layer. Furthermore, and most importantly, the RANS equations are able to reproduce the scales of the flow, of course, up to a certain frequency, but the usual models normally damp those scales, returning the shear layer scale instead. That is why one can only observe the very low frequencies, which are mostly associated with variation of geometry and boundary conditions. Moreover, expanding this concept to the unsteady calculations, some important part of the turbulent spectrum should also be possible to calculate, since the SAS model allows adjustment to local scales and the break-up of eddies into smaller ones is merely a result of the interaction between non-linear convection term and the viscous one.

Finally, perhaps a more philosophical issue can be raised concerning the different schools of thought. Following the author's line of thought, the URANS equations combined with the usual turbulence models may have followed a path which did not favor it so much, precisely because of its fundamental flaws: the inconsistency in the turbulent scales and its inability to adjust to the local flow. This means that the biggest problems attributed to URANS would actually reside in the poor turbulence modeling. Of course, there is also a very important issue slightly overlooked here and there is the fact that, as Bradshaw stated, turbulence is a solution of the Navier-Stokes equations, which are strongly non-linear, especially when the perturbing parameter, Reynolds numbers, are high. Hence, one cannot really decouple turbulence from the mean equations. That is indeed a drawback. Nevertheless, even the averaged equations are still non-linear, so one should still expect an important amount of non-linear behavior up to some frequencies. That is why it is possible to observe instabilities in all directions of the flow with SAS models.

In summary, regarding the SAS models:

- They are based on the modeling of a second mechanical scale in the source terms in addition to the strain rate tensor or vorticity tensor;
- Provide RANS solutions in stable flow regions;
- Allow break-up of turbulent structures for unstable flow;
- Provide better damping of high-frequency resolved content;
- Contrary to other models such as DES and LES, the previous features are achieved without explicit dependency on the grid or time-step other than the physical one.

### 3.3 Transition Modeling

The transition from laminar to turbulent flow is a process in which a series of events drives an initially laminar flow to the fully turbulent state. These events are essentially triggered by small perturbations with characteristic lengths and amplitudes which, as in a nonlinear mechanical system, can be amplified or damped.

In boundary layer flows, the primary instability is known as Tollmien-Schlichting waves. These waves are essentially two-dimensional and are superimposed onto the laminar flow as of the so-called indifference Reynolds number, which features the beginning of the transition process. This phenomenon can be shown by linearizing the equations of motion (leading to the Orr-Sommerfeld equations) and analyzing their stability.

The secondary instability is, on the other hand, three-dimensional because three dimensional waves are superimposed onto the flow downstream. This instability leads to the formation of  $\Lambda$ -structures, after which turbulent spots appear giving rise to fully turbulent flow.

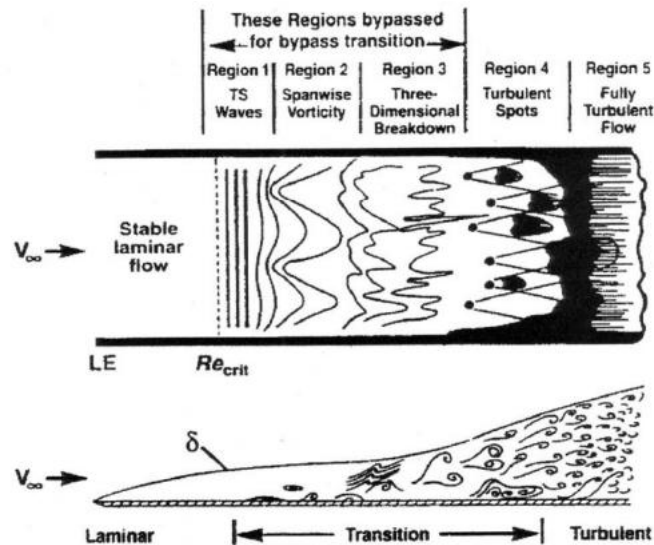


Figure 3.1: Sketch representing the stages of transition (SCHLICHTING H., 2000).

The transition phenomenon described above is characteristic of boundary layers flow developing about a solid wall with small curvature and low inflow turbulence levels. Therefore this transition is more gradual and soft and thus called natural. In natural transition, one sees the developing of the events above described, namely the two-dimensional instabilities, followed by three-dimensional ones, the appearance of turbulent spots and finally full turbulence.

The flow can also be more largely disturbed triggering a more abrupt transition process.

When this abrupt transition occurs, the first events are bypassed, thus the name bypass transition. Bypass transition can be triggered by large free-stream turbulence, yielding transition from namely laminar flow to a flow with some turbulent spots and fully turbulent downstream. Figure 3.1 depicts this process.

Transition is also influenced by separated flows, such as flows with recirculation regions. Laminar boundary-layer separates under the influence of pressure gradient, which causes transition to develop in the separated shear layer.

The prediction of transitional flows is a topic, as transition itself, in the edge of knowledge. There is a lot of research being carried out about it. The following approaches are some of the ones used nowadays:

- Only full Direct-Numerical-Simulations (DNS) can predict correctly all types of transitions. The computational demands are still nowadays impossible for industry purposes;
- Large Eddy Simulations with subgrid-scale modelling are an interesting option to DNS, but some transitional flows are not well computed and computations are still expensive;
- Parabolized stability equations and the  $e^n$  method are used, with good results, for natural transition parallel flows, such as wing flows. They rely on calibration with experimental data from wind tunnels, mostly;
- Empirical correlations rely on the experimental data regarding the Reynolds numbers for each transitional flow. If used with RANS models, only after this local Reynolds number, the turbulence modelling is activated;
- The Local Correlation Transition Modeling (LCTM) is based on transport equations forming a framework in which empirical correlations can be used in order to control the boundary layer quantities, such as turbulent kinetic energy.

In the present work, the LCTM presented by Langtry & Menter (2009) is used in the framework of ReFRESCO. As Menter, Langtry & Volker (2006) mention, the cornerstone of this approach is that the concept of strain rate Reynolds number can provide the connection between the transition onset Reynolds number and empirical correlations to obtain the local boundary-layer quantities. Thus, the integration of the boundary-layer velocity profile is avoided when determining the onset of transition. This complies with the general idea of forming a local-based model, thus dispensing non-local operations.

The strain rate Reynolds number is defined as:

$$Re_v = \frac{\rho d^2}{\mu} S. \quad (3.23)$$

In order to broaden the applicability of the model to different types of flows, Langtry & Menter (2009) have scaled  $Re_v$  in a Blasius boundary layer such that, at its maximum, it reaches unity. The scaling is performed by means of the Reynolds momentum thickness,  $Re_\theta$ , that is, the Reynolds number calculated with the momentum thickness  $\theta$ . The relation between the Reynolds numbers is then written as:

$$Re_\theta = \frac{\max(Re_v)}{2.193}. \quad (3.24)$$

It is shown by Langtry & Menter (2009) that, for moderate pressure gradients, the difference between the actual Reynolds momentum thickness and the strain rate Reynolds is less than 10% and thus the scaling is valid, furthermore because most of the experimental available data on transition falls in this range. For strongly adverse pressure gradients, the difference can be quite large, but this can even work in favor of the model, since it can better capture separation-induced transition.

The idea behind this procedure is to make it possible to use the experimental data on a common basis, but also because there is a physical relation between strain rate Reynolds and the growth of the disturbances in the boundary layer, leading to turbulent flow. The use of the strain rate Reynolds number combined with experimental transition correlations and transport equations comprises the main idea of the model. The transported quantities are the intermittency factor,  $\gamma$ , which models the local laminar/turbulent state of the flow and the transition onset momentum thickness Reynolds number,  $\tilde{Re}_{\theta t}$ , which is a non-local quantity that, by means of the transport equation can be calculated locally.

Furthermore, it ties the empirical correlation (which is given in terms of Reynolds momentum thickness) to the onset criteria in the intermittency equation, allowing for general geometries.

In Langtry & Menter (2009), the intermittency is coupled to the  $k-\omega$  SST-1994 turbulence model (MENTER, 1994), however coupling with  $k-\omega$  SST-2003 is done herein. The intermittency function works together with the  $k$ -equation production term, increasing downstream of the transition point, which is determined based on the relation between strain rate and transition momentum thickness Reynolds number. In what follows, the equations and correlations as derived by Langtry & Menter (2009) are presented and

therefore, only the most important parts are described.

The intermittency transport equation reads:

$$\frac{\partial(\rho\gamma)}{\partial t} + \frac{\partial}{\partial x_j}(\rho U_j \gamma) = P_\gamma - E_\gamma + \frac{\partial}{\partial x_j} \left[ \left( \frac{\mu_t}{\sigma_f} + \mu \right) \frac{\partial \gamma}{\partial x_j} \right]. \quad (3.25)$$

The production term,  $P_\gamma$  is the production of  $\gamma$  that works with two empirical correlations: the first correlation determines the transition onset (regulating where  $\gamma$  increases) and the second determines the transition length regulating the intensity of the production. The term  $E_\gamma$  determines the destruction of  $\gamma$  (or relaminarization). It is relevant to note that such correlations are determined from flat plate experiments, hence other applications with geometries very dissimilar to that ought to be analyzed carefully, as done here for the fixed and moving cylinder.

The production term is calculated as:

$$P_\gamma = F_{length} c_{a1} \rho S [\gamma F_{onset}]^{0.5} (1 - c_{e1} \gamma), \quad (3.26)$$

in which  $F_{length}$  is the empirical correlation that controls the transition length and  $F_{onset}$ , the transition onset location.

The destruction/relaminarization is defined as:

$$E_\gamma = c_{a2} \rho \Omega \gamma F_{turb} (c_{e2} \gamma - 1), \quad (3.27)$$

in which  $\Omega$  is the absolute vorticity,  $\Omega = \sqrt{2\Omega_{ij}\Omega_{ij}}$  and  $F_{turb}$  is employed to disable the destruction term outside a laminar boundary layer or in the viscous sublayer. It is defined as:

$$F_{turb} = e^{-\left(\frac{R_T}{4}\right)^4}, \quad (3.28)$$

where:

$$R_T = \frac{\rho k}{\mu \omega}. \quad (3.29)$$

The following functions control the transition onset:

$$\begin{aligned}
F_{onset1} &= \frac{Re_v}{2.193\tilde{Re}_{\theta c}}, \\
F_{onset2} &= \min(\max(F_{onset1}, F_{onset1}^4), 2.0), \\
F_{onset3} &= \max(1 - (\frac{R_T}{2.5})^3, 0), \\
F_{onset} &= \max(F_{onset2} - F_{onset3}, 0).
\end{aligned} \tag{3.30}$$

The variable  $Re_{\theta c}$  is the critical Reynolds number where intermittency first rises, which happens upstream of the transition Reynolds number  $\tilde{Re}_{\theta t}$ . The difference between them is obtained from an empirical correlation.

Based on experimental results for flat plate, the following correlations for  $F_{length}$  are sought:

$$F_{length} = \begin{cases} [398.189 \cdot 10^{-1} + (-119.270 \cdot 10^{-4})\tilde{Re}_{\theta t} + (-132.567 \cdot 10^{-6})\tilde{Re}_{\theta t}^2], \\ (\tilde{Re}_{\theta t} < 400) \\ [263.404 + (-123.939 \cdot 10^{-2})\tilde{Re}_{\theta t} + (194.548 \cdot 10^{-5})\tilde{Re}_{\theta t}^2 + (-101.695 \cdot 10^{-8})\tilde{Re}_{\theta t}^3], \\ (400 \leq \tilde{Re}_{\theta t} < 596) \\ [0.5 - (\tilde{Re}_{\theta t} - 596.0) \cdot 3.0 \cdot 10^{-4}], \\ (596 \leq \tilde{Re}_{\theta t} < 1200) \\ [0.3188], \\ (1200 \leq \tilde{Re}_{\theta t}) \end{cases} \tag{3.31}$$

Langtry & Menter (2009) argue that, in certain cases,  $\tilde{Re}_{\theta t}$  will decrease to very small values shortly after transition, causing a local increase in the source term of the intermittency equation, causing in turn a sharp and unphysical increase in skin friction. In order to avoid that,  $F_{length}$  is forced to return to its maximum value in the viscous sublayer:

$$F_{sublayer} = e^{-\left(\frac{R_\omega}{0.4}\right)^2}, \tag{3.32}$$

$$R_\omega = \frac{\rho d^2 \omega}{500\mu}, \tag{3.33}$$

$$F_{length} = F_{length}(1 - F_{sublayer}) + 40.0 \cdot F_{sublayer}. \tag{3.34}$$

Finally, the correlations for  $Re_{\theta c}$  as function of  $\tilde{Re}_{\theta t}$  are:

$$Re_{\theta c} = \begin{cases} [\tilde{Re}_{\theta t} - (396.035 \cdot 10^{-2} + (-120.656 \cdot 10^{-4})\tilde{Re}_{\theta t} + (868.230 \cdot 10^{-6})\tilde{Re}_{\theta t}^2 + (-696.506 \cdot 10^{-9})\tilde{Re}_{\theta t}^3 + (174.105 \cdot 10^{-12})\tilde{Re}_{\theta t}^4)], & \tilde{Re}_{\theta t} \leq 1870 \\ [\tilde{Re}_{\theta t} - (593.11 + (\tilde{Re}_{\theta t} - 1870.0) \cdot 0.482)], & \tilde{Re}_{\theta t} > 1870 \end{cases} \quad (3.35)$$

The constants for the intermittency equation are:

$$c_{e1} = 1.0, \quad c_{a1} = 2.0, \quad c_{e2} = 50, \quad c_{a2} = 0.06, \quad \sigma_f = 1.0. \quad (3.36)$$

Separation-induced transition is achieved by means of the following modification to the intermittency:

$$\gamma_{sep} = \min(s_1 \max[0, (\frac{Re_v}{3.235 Re_{\theta c}}) - 1] F_{reattach}, 2) F_{\theta t}, \quad (3.37)$$

$$F_{reattach} = e^{-\left(\frac{R_T}{20}\right)^4}, \quad (3.38)$$

$$\gamma_{eff} = \max(\gamma, \gamma_{sep}), \quad (3.39)$$

$$s_1 = 2. \quad (3.40)$$

The boundary condition of  $\gamma$  is zero normal flux at the walls and  $\gamma = 1$  elsewhere.

The experimental data for transition correlate the Reynolds number at the transition onset,  $Re_{\theta t}$  to some variables of the flow in the free-stream, which configures a non-local operation. Thus the idea behind the second transport equation is to transform the non-local correlations  $Re_{\theta}$  (which are functions of free-stream quantities) into local variables,  $\tilde{Re}_{\theta t}$ . These are then used to calculate transition length and the critical Reynolds number,  $Re_{\theta c}$  at every location of the flow so that the intermittency equation can be solved. Thus, the following transport equation for the transition momentum thickness Reynolds number,  $\tilde{Re}_{\theta t}$  is proposed:

$$\frac{\partial(\rho \tilde{Re}_{\theta t})}{\partial t} + \frac{\partial}{\partial x_j}(\rho U_j \tilde{Re}_{\theta t}) = P_{\theta t} + \frac{\partial}{\partial x_j}[(\mu + \mu_t) \frac{\partial \tilde{Re}_{\theta t}}{\partial x_j}], \quad (3.41)$$

in which  $P_{\theta t}$  is the production term.

The production term,  $P_{\theta t}$ , is calculated as:

$$P_{\theta t} = c_{\theta t} \frac{\rho}{t} (Re_{\theta t} - \tilde{R}e_{\theta t})(1.0 - F_{\theta t}), \quad (3.42)$$

and  $t$  is a time scale:

$$t = \frac{500\mu}{\rho U^2}. \quad (3.43)$$

Outside of the boundary layer, the production term forces  $\tilde{R}e_{\theta t}$  to match the local value of  $Re_{\theta t}$  calculated from the empirical correlations of the latter with some other variables of the flow. These will be presented ahead. Furthermore, the blending function  $F_{\theta t}$  is applied to turn off the production term inside the boundary layer and allow  $\tilde{R}e_{\theta t}$  to diffuse in from the free-stream. This blending function is zero in the free-stream and one in the boundary layer. It is defined as:

$$F_{\theta t} = \min(\max(F_{wake} \cdot e^{-\left(\frac{d}{\delta}\right)^4}, 1.0 - \left(\frac{\gamma - 1/c_{e2}}{1.0 - 1/c_{e2}}\right)^2), 1.0) \quad (3.44)$$

The following variables are also calculated:

$$\theta_{BL} = \frac{\tilde{R}e_{\theta t}\mu}{\rho U_{\infty}}, \quad \delta_{BL} = \frac{15}{2}\theta_{BL}, \quad \delta = \frac{50\Omega d}{U}, \quad (3.45)$$

$$Re_{\omega} = \frac{\rho\omega d^2}{\mu}, \quad (3.46)$$

$$F_{wake} = e^{-\left(\frac{Re_{\omega}}{10^5}\right)^2}. \quad (3.47)$$

Equation 3.47 ensures that the blending function is inactive in wake zones. Finally, the constants to these equations are:

$$C_{\theta t} = 0.03, \quad \sigma_{\theta t} = 2.0. \quad (3.48)$$

The boundary condition for  $\tilde{R}e_{\theta t}$  at the walls is zero flux and in the inlet, should be calculated from the empirical correlations for transition onset showed below. The following parameters are needed:

$$\lambda_{\theta} = \frac{\rho\theta^2}{\mu} \frac{dU}{ds}, \quad (3.49)$$

where  $U = \sqrt{\sum_{i=1}^3 u_i^2}$  and  $\frac{dU}{ds}$  is the streamwise direction derivative of  $U$ , which will be calculated applying the chain rule. The turbulence intensity is:

$$Tu = 100 \frac{\sqrt{2k/3}}{U}. \quad (3.50)$$

The empirical correlations for transition onset are defined as follows:

$$\begin{cases} Re_{\theta t} = [1173.51 - 589.428Tu + \frac{0.2196}{Tu^2}]F(\lambda_{\theta}), & Tu \leq 1.3 \\ Re_{\theta t} = 331.50[Tu - 0.5658]^{-0.671}F(\lambda_{\theta}), & Tu > 1.3 \end{cases} \quad (3.51)$$

and

$$\begin{cases} F(\lambda_{\theta}) = 1 - [-12.986\lambda_{\theta} - 123.66\lambda_{\theta}^2 - 405.689\lambda_{\theta}^3]e^{-[\frac{Tu}{1.5}]^{1.5}}, & \lambda_{\theta} \leq 0 \\ F(\lambda_{\theta}) = 1 + 0.275[1 - e^{-35.0\lambda_{\theta}}]e^{-[\frac{Tu}{0.5}]}, & \lambda_{\theta} > 0 \end{cases} \quad (3.52)$$

Moreover, the following limiters are applied:

$$-0.1 \leq \lambda_{\theta} \leq 0.1, \quad Tu \geq 0.027, \quad Re_{\theta t} \geq 20. \quad (3.53)$$

Equations 3.51-3.52 have to be solved iteratively as  $\lambda_{\theta}$  depends on  $\theta_t$ .

The transition model interacts with the k- $\omega$  SST 2003 model as follows:

$$\frac{\partial(\rho k)}{\partial t} + \frac{\partial}{\partial x_j}(\rho U_j k) = \tilde{P}_k - \tilde{D}_k + \frac{\partial}{\partial x_j}[(\mu + \sigma_k \mu_t) \frac{\partial k}{\partial x_j}], \quad (3.54)$$

in which

$$\tilde{P}_k = \gamma_{eff} P_k, \quad \tilde{D}_k = \min(\max(\gamma_{eff}, 0.1), 1.0) D_k, \quad (3.55)$$

$$R_y = \frac{\rho d \sqrt{k}}{\mu}, \quad F_3 = e^{-\left(\frac{R_y}{120}\right)^8}, \quad F_1 = \max(F_{1orig}, F_3). \quad (3.56)$$

The parameters  $P_k$  and  $D_k$  in equation 3.54 and  $F_{1orig}$ , in equation 3.56 are the original ones proposed by Menter (1994). One notices, therefore, that when the LCTM is considered, there are two additional transport equations which are added to the momentum and turbulence equations in a grand total of seven transport equations being solved simultaneously. This will evidently lead to more difficult iterative and overall convergence.

The theoretical elements showed in this Chapter are the basis of the turbulence models used in this work and their application for the stationary cylinder and the coupling with

the moving cylinder are an important part of the contributions presented herein.



# Chapter 4

## Fluid Structure Interaction

*This chapter shows the mathematical formulation and details of the numerical implementation of the interaction between the solid and fluid domains. The detailed approach for handling body motions in the URANS/ReFRESKO framework is presented, which is one of the contributions of the present work*

### 4.1 Dynamics of the Rigid Body

The dynamic equations for the rigid body enables one to describe the attitude of the body subjected to external loads. The following external forces are considered: hydrodynamic forces, herein calculated with ReFRESKO,  $\mathbf{F}_H$ ; the linear mechanical restoring forces,  $\mathbf{F}_K$ ; and the linear viscous (Coulomb-type) mechanical damping forces,  $\mathbf{F}_C$ .

In general, the dynamic equations can either be formulated in inertial, earth-fixed or non-inertial, body-fixed reference systems, with advantages and disadvantages pertaining to each alternative. Writing the equations in inertial frame system dispenses the additional non-inertial contributions to the equations of motion as well as dispensing transformation between coordinate systems. On the other hand, a major disadvantage of writing the equations in global system is that moments and products of inertia are then function of time as the body changes the attitude and thus have to be recalculated. In any case, the equations are formulated by using energy considerations, e.g. Lagrange or Hamilton formulations, or by means of Newton's second law, arriving at equations for up to six degrees-of-freedom:

$$\mathbf{M}\ddot{\mathbf{r}} = \mathbf{F}_T, \tag{4.1}$$

in which  $\mathbf{M}$  is a mass matrix which is here constant,  $\ddot{\mathbf{r}}$  is a state vector and  $\mathbf{F}_T$  is the total generalized forces vector.

In the non-inertial system formulation, an inertial generalized forces vector,  $\mathbf{F}_I$  must be included in the right-hand side of equation 4.1 to yield:

$$\mathbf{M}\ddot{\mathbf{r}} = \mathbf{F}_{\text{ext}} - \mathbf{F}_I. \quad (4.2)$$

In the present case, the interest falls upon two degrees-of-freedom (DOF) motions, that is, motions transverse and aligned with the flow direction. In this situation, it follows that the inertial and non-inertial formulations coalesce because  $\mathbf{F}_I \equiv \mathbf{0}$ . For that reason, implementation and use of the inertial-frame formulation has been carried out as showed below. Nevertheless, Bettle (2012), Leroyer (2004) and others have shown that, for general six degrees-of-freedom motions, the non-inertial reference frame formulation is more convenient and normally constitutes the preferred choice.

In the inertial reference frame associated with two DOF systems, the equation 4.1 can be written for the center of gravity of the body,  $G$ , resulting in the following mass matrix:

$$\mathbf{M} = \begin{bmatrix} m & 0 \\ 0 & m \end{bmatrix}, \quad (4.3)$$

and the state vector:

$$\mathbf{r} = \{ X_G, Y_G \}^T. \quad (4.4)$$

The total force then corresponds to  $\mathbf{F}_H$ ,  $\mathbf{F}_K$  and  $\mathbf{F}_C$ :

$$\mathbf{F}_T = \mathbf{F}_H + \mathbf{F}_C + \mathbf{F}_K. \quad (4.5)$$

The restoring and damping forces are respectively written as:

$$\mathbf{F}_C = -\mathbf{C}\dot{\mathbf{r}}, \quad (4.6)$$

$$\mathbf{F}_K = -\mathbf{K}\mathbf{r}. \quad (4.7)$$

The dynamic equations are then rewritten as:

$$\mathbf{M}\ddot{\mathbf{r}} = \mathbf{F}_H - \mathbf{C}\dot{\mathbf{r}} - \mathbf{K}\mathbf{r}, \quad (4.8)$$

in which the terms of the damping and stiffness matrices are positive. These equations form a second-order non-linear initial value problem (IVP). It is non-linear because the

hydrodynamic forces,  $F_H$ , keep a non-linear relation with  $\dot{\mathbf{r}}$ , which evidently cannot be explicitly derived as they are obtained through the solution of the Navier-Stokes equations. That non-linear, two-way coupled relation is the core of the fluid-structure interactions herein studied and their solution strategies constitute one of the great issues of this research.

In order to solve the IVP by means of traditional methods, let us reduce the order of the differential equations to one by writing:

$$\dot{\kappa} = \mathbf{M}^{-1}(\mathbf{F}_H - \mathbf{C}\dot{\mathbf{r}} - \mathbf{K}\mathbf{r}) \quad (4.9)$$

$$\dot{\mathbf{r}} = \kappa, \quad (4.10)$$

in which  $\mathbf{M}$  is assumed non singular.

These equations are conveniently combined as:

$$\mathbf{y} = \{ \kappa \quad \mathbf{r} \}^T, \quad (4.11)$$

and

$$\mathbf{h} = \{ \mathbf{M}^{-1}(\mathbf{F}_H - \mathbf{C}\dot{\mathbf{r}} - \mathbf{K}\mathbf{r}) \quad \kappa \}^T. \quad (4.12)$$

## 4.2 Coupling of Fluid and Structure Equations

The information exchanged between the fluid and the solid domains basically consist on the loads exerted on the cylinder by the fluids and on the body velocity, fed back into the fluid domain equations iteratively upon solution of the problem.

The hydrodynamic loads are calculated as follows:

$$F_i = \int_{SB} \left( -Pn_i + \mu \left( \frac{\partial U_i}{\partial x_j} + \frac{\partial U_j}{\partial x_i} \right) \right) dS, \quad (4.13)$$

$$M_i = \int_{SB} (\epsilon_{ijk} d_j F_k) dS, \quad (4.14)$$

in which  $\mathbf{d}$  is the distance vector from the surface point where force is applied to the pole about which the moment is calculated and  $SB$  is the body surface.

The grid velocity is calculated as showed in Chapter 2:

$$\mathbf{U}_g = \mathbf{U}_O + \boldsymbol{\Omega} \wedge \mathbf{x}, \quad (4.15)$$

in which the translation velocity is identified as  $\mathbf{U}_O$  and the rotation velocity, as  $\boldsymbol{\Omega} \wedge \mathbf{x}$ .

Different coupling schemes have been developed for CFD calculations of VIV of rigid cylinders. Weakly or loosely coupled schemes have shown robust for this application and have been largely applied, such as in Carmo (2009). In this type of scheme, body motion is coupled with the flow solver in the time-step level, thus generally requiring fine time steps for convergence of the equations. Furthermore, in this case, both explicit and implicit time integration methods can be used to solve the dynamics of the rigid body, with similar performance for small time steps. Conversely, strong or tight schemes were also developed and constitute a necessary choice when mass ratios are low and in cases when the added mass causes instabilities, see Leroyer (2004), Bettle (2012). In this case, implicit schemes are normally used due to the nesting of iterative rigid body motions with the iterative flow solution. During the course of this research, both weakly and strongly coupled schemes have been developed, with very similar results. In spite of somewhat more costly calculations for the strongly coupled one, it has been chosen due to greater robustness. Nevertheless, both methods shall be presented herein.

### 4.3 Weakly Coupled Scheme

In the weakly coupled scheme, the communication between fluid and structure is done at the time step level. In the work carried out for this thesis, this was carried out either with the explicit second-order Runge-Kutta (RK) scheme, or with the implicit second-order Adams-Bashforth-Moulton (ABM) scheme. In either case, the schematic solution process becomes:

```

initialization
do (time loop)
  increment t
  solve equations of motion of the solid domain
  calculate grid velocity
  update grid position
  update velocity field and boundary conditions
do (outer loop)
  solve the momentum equations
do (inner loop)
  solve linear system of equations
enddo (inner loop)

```

```

solve the pressure Poisson equation
do (inner loop)
    solve linear system of equations
enddo (inner loop)
correct velocity field
solve turbulence model equations
do (inner loop)
    solve linear system of equations
enddo (inner loop)
solve transition model equations (when required)
do (inner loop)
    solve linear system of equations
enddo (inner loop)
enddo (outer loop)
enddo (time loop)

```

In the explicit Runge-Kutta Scheme, figure 4.1, the structural solver gets as input the hydrodynamic force and moment and the structural response at time level  $n$  in order to calculate the structural response at the time level  $n + 1$ . The calculated structural velocity (which is, in fact the grid velocity) is then updated in the field solution before the outer loop begins. This explicit scheme normally requires smaller time steps than an implicit one, however, it is found that the necessary time steps required for stability of the structural solver are normally not lower than the required by the flow solver for a reasonable accuracy and time-discretization independent solutions.

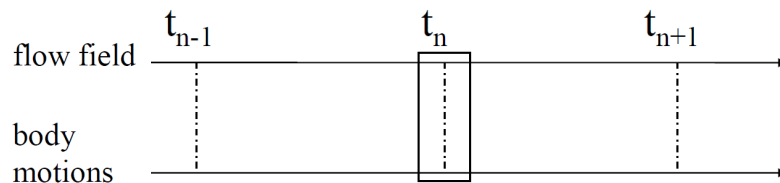


Figure 4.1: Fluid-structure coupling with explicit weak Runge-Kutta coupling scheme.

In the implicit predictor-corrector scheme, figure 4.2, the communication between fluid and structure solvers is also done at the time step level, i.e. the time loop. For this reason, it is still regarded as a weak coupling. However, as it is implicit and iterative within the structural solver, it is more stable than Runge-Kutta, for the same order of accuracy. At the time level  $n$  the predictor scheme produces an estimate of the solution at the time level  $n + 1$  based on fluid and structure solutions at two time levels  $(n, n - 1)$ . Then the corrector step iterates to derive the solution at time level  $n + 1$  with the structural solutions at time levels  $n + 1, n$ . Notice that the fluid solution at the time level  $n + 1$  is not included, since it has not been yet calculated. Hence, this scheme is implicit in terms

of the structural solver, but not with respect to the fluid solver, which is the reason why it is still regarded as weakly coupled.

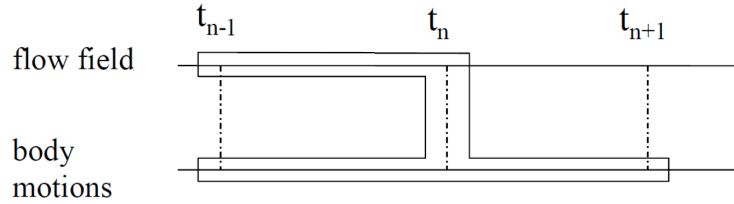


Figure 4.2: Fluid-structure coupling with implicit weak Adams-Bashforth-Mouton coupling scheme.

## 4.4 Strongly Coupled Scheme

Leroyer (2004) and Bettle (2012) have discussed the stability of the coupling methods with regards to the structural mass and added mass. It has been shown that when the ratio between added mass and structural mass is larger than one, instability problems might occur due to the build-up of numerical error in the iterative procedure. The strongly coupled approach adopted herein showed to be a remedy for this situation and stability was unconditionally achieved by applying this approach. The strongly coupled scheme used here is based on the second-order Adams-Bashforth-Mouton scheme<sup>1</sup>, but differently from the weak coupling, the communication is done at the time loop level with the predictor and at the outer loop level with the corrector, as the schematic procedure below shows.

```

initialization
do (time loop)
  increment t
  solve equations for the solid domain with predictor Adams-Bashforth
  scheme
  calculate grid velocity
  update grid position
  update velocity field and boundary conditions
  do (outer loop)
    solve the momentum equations
    do (inner loop)
      solve linear system of equations
    enddo (inner loop)
    solve the pressure Poisson equation
    do (inner loop)

```

<sup>1</sup>It is worth noting that the order of the method used for solving the dynamics of the rigid body need not be of higher order than two since the global order of convergence is limited by the flow domain discretization.

```

    solve linear system of equations
  enddo (inner loop)
  correct velocity field
  solve turbulence model equations
  do (inner loop)
    solve linear system of equations
  enddo (inner loop)
  solve transition model equations (when required)
  do (inner loop)
    solve linear system of equations
  enddo (inner loop)
  solve equations for the solid domain with corrector Adams-Moulton
  scheme
  calculate grid velocity
update grid position
update velocity field and boundary conditions
  enddo (outer loop)
enddo (time loop)

```

Figure 4.3 shows the schematic procedure of the strongly coupled solution. This scheme includes the flow field solution at time level  $n+1$ , which is the reason why it is also implicit for the fluid solver and therefore, strongly coupled. Note that this procedure is not the same done by Bettle (2012), in which a more expensive strongly coupled procedure is done, namely with the outer loops nested within the predictor-corrector scheme. In that case, each correction loop of the structural equation requires a new set of outer iterations. On the other hand, in the present approach it might happen that too large a correction for each outer loop is imposed. However, an efficient remedy is an implicit-explicit under-relaxation procedure in which the velocity corrections are more mildly updated.

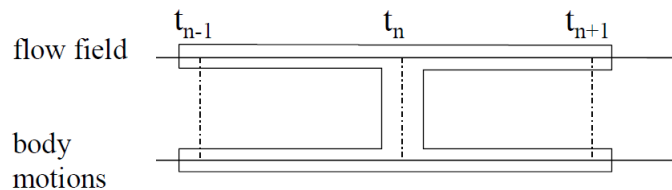


Figure 4.3: Fluid-structure coupling with implicit strong Adams-Bashforth-Moulton coupling scheme.

### 4.4.1 Implicit Adams-Bashforth-Moulton Scheme

Restating the matrix equation 4.10 to be solved in the form expressed by Butcher (2000):

$$\dot{\mathbf{y}} = \mathbf{h}(t, \mathbf{y}) \quad (4.16)$$

The multi-step method herein applied is based on the Adams-Bashforth-Moulton scheme. The Adams-Bashforth part is the explicit predictor (P) step, in which an initial value is provided for the function  $\mathbf{h}$  at  $n + 1$ , followed by evaluation (E) and correction (C) steps based on Adams-Moulton scheme. This type of method is referred to as  $P(EC)^k$ , in which  $k$  is the number of iterations required for certain convergence level.

#### 4.4.1.1 Predictor Step

The predictor step in this scheme provides an initial guess for the step  $n + 1$  to be used at the corrector step. It is an explicit second-order Adams-Bashforth which takes the following form:

$$\mathbf{y}_{n+1}^0 = \mathbf{y}_n + \frac{h}{2}(3\mathbf{F}_n - 1\mathbf{F}_{n-1}), \quad (4.17)$$

in which the  $\mathbf{F}$  values are evaluations of  $\dot{\mathbf{y}}$  in previous steps and with the local error  $E = \frac{5}{12}h^3\mathbf{F}''$  (BUTCHER, 2000). This procedure is stable, but the stability of the corrector is more relevant than that of the predictor. As commented by Bettel (2012), the largest influence of the predictor step is on the number of steps it takes for the corrector to converge to the solution and thus the accuracy is determined by the corrector step.

#### 4.4.1.2 Corrector Step

The corrector step is based on an Adams-Moulton procedure as follows:

$$\mathbf{y}_{n+1}^k = \mathbf{y}_n + \frac{h}{2}(1\mathbf{F}_{n+1} + 1\mathbf{F}_n), \quad (4.18)$$

with the local error  $E = -\frac{1}{12}h^3\mathbf{F}''$  (BUTCHER, 2000), which is smaller than the local error of the predictor step, showing that the accuracy of the Adams-Moulton is higher than the Adams-Bashforth. The Adams-Moulton method is also stable, as a consequence of Dahlquist's barrier theorem, according to which linear multi-step methods can only be A-stable with order up to second. Since this method depends on previous calculations, it is not self-starting, therefore, it was combined with the first-order explicit Adams-Bashforth

scheme for the initial time step.

#### 4.4.1.3 On the Error Estimation and the Evaluation Criteria

One of the interesting characteristics of linear multi-step methods is that they allow for the error estimation in each time step. This can be accomplished using the local truncation errors of both predictor and corrector calculations to arrive at the following type of expression:

$$\mathbf{y}(t_{n+1}) - \mathbf{y}_{n+1}^k \approx C(\mathbf{y}_{n+1}^k - \mathbf{y}_{n+1}^{k-1}), \quad (4.19)$$

in which  $C$  is a constant. With this error estimation, the evaluation step is based on the following criteria:

$$\frac{\mathbf{y}_{n+1}^{k+1} - \mathbf{y}_{n+1}^k}{\mathbf{y}_{n+1}^{k+1}} < 10^{-6}. \quad (4.20)$$

The predictor-corrector algorithm outlined above is equivalent to performing a fixed point iteration for the solution of the nonlinear equations on  $\mathbf{y}_{n+1}$ . This iteration is rather slow, since the rate of convergence is only linear in the neighborhood of the solution (BETTLE, 2012). Furthermore, the convergence of this iterative procedure imposes a condition on the time step used in the calculations, therefore requiring that it is small enough not only for stability of the integration scheme itself but also for the convergence of this procedure. Nevertheless, for the calculations presented in this thesis, the requirement of very refined time steps due to the flow solver has been observed. Due to that requirement, any conditions on low time steps for the solution of rigid body equations have been automatically satisfied.

This Chapter presented the theoretical aspects of the fluid-structure capabilities developed in this thesis and applied to the moving body calculations showed further ahead. The systematic application of these models together with different turbulence models within URANS is a contribution of this work.



# Chapter 5

## Verification and Validation

*This chapter presents the basic theoretical aspects of the Verification and Validation activities that were applied in this thesis. Herein, the procedures used to estimate the uncertainties for steady and unsteady calculations as well as the procedure used for the estimation of the experimental uncertainty are described. A validation procedure is also proposed. This activity is very rarely done in such extent in publications available in the literature and this constitutes other contribution of this thesis.*

In the early years of the development of CFD, it was an achievement already to demonstrate the ability to address the problems using numerical solutions. However, in many current applications of CFD it is no longer enough to produce a “solution”. The credibility of the simulations must be established with Verification and Validation (V&V), which are distinct activities. Verification is a purely mathematical exercise consisting of two parts: 1) Code Verification, intending to demonstrate by error evaluation the correctness of the code that contains the algorithm to solve a given mathematical model; 2) Solution Verification, attempting to estimate the error/uncertainty of a given numerical solution, for which, in general, the exact solution is unknown. Validation is a science/engineering activity meant to show that the selected model is a good representation of the “reality”. This means that Verification deals with numerical (and coding) errors, whereas Validation is related to modeling errors. Also Validation can only be done after Verification.

Solution verification is the major issue in the current work, and it is done in order to assess the real numerical errors of the turbulence models for the cylinder problem. This means that one must keep all errors: round-off, iterative and discretization errors under tight control, and if possible, quantified. In order to use V&V modern techniques (AAIA-GUIDE, 1998; EÇA; VAZ; HOEKSTRA, 2010) and following the ASME standard

(ASME-GUIDE, 2008) numerical solutions in a grid and time-step asymptotic range have also to be reached.

This is almost never done by the CFD community, and one can see a great deal of papers in the literature where coarse grids and coarse time-steps are used together with all kinds of turbulence models in order to assess the accuracy of the calculations. This approach sometimes called “engineering approach” is dangerous since the conclusions cannot be easily translated even for very similar problems, it is very much code dependent and not model dependent and the results are obtained due to error cancelation. Here this approach will not be followed, but rather a “scientific approach”, where first verification studies are performed, asymptotic range reached in space and in time, numerical uncertainties estimated based on the method presented by Eça (2009), Eça, Vaz & Hoekstra (2010) and only afterwards the best numerical results will be compared with the experiments and validation can be carried out.

For Validation, one also needs the experimental uncertainty to be quantified, an activity rarely done for the cylinder case. For this purpose, data has been collected in the literature and from experiments obtained from collaboration with other researchers so that uncertainties relying on the standard deviation of all experimental results for the same condition are calculated.

Considering the three types of numerical errors, the round-off error is essentially dictated by machine precision and for most calculations, double-precision suffices to minimize them (EÇA, 2009). The iterative error arises from the non-linearity of the system of equations solved for the flow quantities. An attractive way of evaluating this error is the infinity norm of the residuals:

$$L_{\infty}(\phi) = \max(|res(\phi)/A_i\phi_i|), 1 \leq i \leq N_T, \quad (5.1)$$

in which  $N_T$  is the total number of nodes in the grid,  $\phi$  is one of the unknowns of the Navier Stokes equations and  $A_i$  is the diagonal coefficient in the system matrix that multiplies  $\phi_i$ .

Although this type of norm might result in a poor estimate of iterative error for some flows, in this work it is assumed that the iterative error evaluated by its infinity norm is a few orders of magnitude smaller than the discretization error and thus the infinity norm shall be used herein.

The discretization error is considered the largest error amongst the three above mentioned. Equations 5.2 and 5.3, which are based on Richardson extrapolation, are used to perform

the error estimation for the steady and unsteady problems:

$$\delta_{RE} = \phi_i - \phi_0 = \alpha_x h_i^{p_x}, \quad (5.2)$$

$$\delta_{RE} = \phi_i - \phi_0 = \alpha_x h_i^{p_x} + \alpha_t \tau_i^{p_t}. \quad (5.3)$$

In these equations,  $h_i$  and  $\tau_i$  are the typical cell size and time step in the calculations,  $p_x$  and  $p_t$  are, respectively, the observed orders of accuracy of the space and time discretization, and  $\alpha_x$  and  $\alpha_t$  are constants of the expansion and  $\phi_0$  is the estimated exact solution. Hence, in the former case, three unknowns must be determined and, in the latter, five unknowns should be calculated requiring, at least, three and five data points, respectively. Notice that the unsteady problems require calculations with different time steps and grids.

As CFD results may be quite noisy, a robust way to evaluate the error is to perform more than three (or five) calculations and solve equation 5.2 or 5.3 in the least-squares sense, which lead to sets of non-linear equations that might be solved by a shooting method, such as Newton's method. This procedure is applied assuming that: (1) iterative and round-off errors are negligible compared to the discretization error and (2) the data show asymptotic monotonic convergence. The latter condition is mandatory if one is to consistently use Richardson Extrapolation to estimate the error, as stressed by Eça (2009). In both steady and unsteady computations, the goal in this uncertainty analysis is to estimate with 95% of confidence:

$$\phi_i - U(\phi_i) \leq \phi_{exact} \leq \phi_i + U(\phi_i), \quad (5.4)$$

in which  $U(\phi_i)$  is the uncertainty obtained from the estimated discretization error.

The steady and unsteady cases will be presented separately below, in order to show the procedure more clearly.

## 5.1 Steady Analysis

As commented above, in order to perform the uncertainty analysis in the data resulting from steady computations, one should determine the apparent convergence order of the results. This is achieved by determining  $p_x$  in equation 5.2 from the least-squares fit.

If  $p_x > 0$ , there is apparent monotonic convergence, otherwise, apparent monotonic di-

vergence. If there is no  $p_x$  that fits the data,  $p'_x$  should be determined from the fit to  $\phi'_i = |\phi_{i+1} - \phi_i|$  to determine oscillatory convergence,  $p'_x > 0$ , or divergence,  $p'_x < 0$ . If it is not possible to determine  $p_x$  or  $p'_x$ , oscillatory convergence is assumed.

As the only possibility of using Richardson extrapolation is with monotonic convergence, one must determine other error estimator for the other possibilities. The suggestion made by Eça (2009) is adopted and the maximum difference between the available solutions is used:

$$\Delta_M = (\phi_i)_{max} - (\phi_i)_{min}, \quad 1 \leq i \leq N_T. \quad (5.5)$$

When the theoretical order of the space discretization is two, then following Eça (2009), if the apparent convergence order is monotonic,  $0.95 < p_x < 2.05$ , the Grid Convergence Index is used (AAIA-GUIDE, 1998), applying the safety factor of 1.25:

$$U(\phi_i) = 1.25\delta_{RE} + \sigma, \quad (5.6)$$

in which  $\sigma$  is the standard deviation of the least-squares fit. If  $p_x \leq 0.95$ , the Richardson-based estimation tends to be over-conservative, thus the error estimator is taken as:

$$U(\phi_i) = \min(1.25\delta_{RE} + \sigma, 1.25\Delta_M). \quad (5.7)$$

If super-convergence is observed,  $p_x > 2.05$ , the Richardson-based estimated is unreliable. However, Eça (2009) arguments that, in most cases, this is not real but a consequence of numerical shortcomings. Thus, the theoretical order of convergence replaces the calculated apparent order of convergence and the least-squares fit is performed once more, yielding  $\delta_{RE}^*$ . Then the uncertainty is determined as:

$$U(\phi_i) = \max(1.25\delta_{RE}^* + \sigma^*, 1.25\Delta_M), \quad (5.8)$$

in which  $\sigma^*$  is the newly determined standard deviation of the fit.

Finally, if monotonic convergence is not observed, the estimation is penalized by a factor of 3:

$$U(\phi_i) = 3\Delta_M. \quad (5.9)$$

## 5.2 Unsteady Analysis

In the unsteady case, the analysis performed is somewhat different as one must estimate the error by dealing with equation 5.3. As done before for the steady calculations, one must determine the apparent orders of convergence of space and time discretization and the standard deviation,  $\sigma$ , of the fit. Let  $p$  be the order of convergence of time or space discretization ( $p$  replaces  $p_x$  or  $p_t$ ), then if  $p > 0$ , there is apparent monotonic convergence; otherwise, if  $p < 0$ , apparent monotonic divergence. If there is no value  $p$  that fits the data, there might be oscillatory convergence/divergence.

The standard deviation of the fit should be compared to the mean change of data:

$$\Delta_\phi = \frac{\max|\phi_i - \phi_j|}{n_d - 1}. \quad (5.10)$$

where  $n_d$  is the number of data points.

As commented above, the estimated error depends on whether the results show apparent monotonic convergence or not. If the data does not show apparent monotonic convergence or not all of the data is in the asymptotic range, one might use different apparent orders of convergence in time and space or also define a modified error estimator that does not assume monotonic convergence:

$$\delta' = \phi_i - \phi_0 = \alpha_{x1}h_i + \alpha_{x2}h_i^2 + \alpha_{t1}\tau_i + \alpha_{t2}\tau_i^2. \quad (5.11)$$

Once again, the discussion is restricted to the present case, in which the theoretical discretization is at most second-order, both in time and in space<sup>1</sup>. Then, if the observed order of convergence is monotonic, with  $p$  between 0.5 and 2.1, a safety factor  $F_s = 1.25$  is assumed, otherwise  $F_s = 3.0$ .

Furthermore, one must compare the calculated value of the standard deviation of the fit,  $\sigma$  and the mean change of data,  $\Delta_\phi$  in order to determine if the noise level in the data is too high, thus making the estimated uncertainty unreliable. In this case, the estimated uncertainty should be penalized by a safety factor  $F_s = 3.0$ . Therefore, if  $\sigma < \Delta_\phi$ :

$$U(\phi_i) = 1.25\delta + \sigma + |\phi_i - \phi_{fit}|, \quad (5.12)$$

---

<sup>1</sup>Overall order of convergence might be lowered when QUICK with limiters or first order interpolation locally decrease the order of the approximation.

otherwise, if  $\sigma \geq \Delta_\phi$ :

$$U(\phi_i) = 3 \frac{\sigma}{\Delta_\phi} (\delta + \sigma + |\phi_i - \phi_{fit}|). \quad (5.13)$$

In equations 5.12 and 5.13,  $\phi_{fit}$  is the value of the dependent variable obtained from the least-squares fit at  $(h_i, \tau_i)$  and  $\delta$  is the chosen error estimator given by  $|\phi_i - \phi_{fit}|$ .

### 5.3 Experimental Uncertainty

In order to make a consistent validation procedure, one must also determine the uncertainties in the experimental data. However, it is quite rare to see experimental uncertainties in publications, thus one should attempt to obtain some estimation of these uncertainties from the experimental data at hand. For that, one should firstly obtain the mean values of the samples,  $\bar{\zeta}$ , and the standard deviation of the same sample,  $s$ . These will be the estimators of the mean value,  $\mu$ , and standard deviation,  $\sigma$ , of a hypothetical infinite set of experiments, for which case, gaussian distribution is assumed. Thus, we should obtain same range around  $\bar{\zeta}$  in which the real mean value should be located, with some confidence level,  $1 - \alpha$ .

The experimental data that we will be able to present in this and in the following sections is somewhat scarce. Therefore, in order to keep the amplitudes of the confidence interval (CI) at a reasonably small level, the confidence level has been set at 90%. Therefore, the standard deviation and variation coefficients of the experimental sample are calculated by using the relations:

$$s = \frac{\sqrt{\sum_{i=1}^n (\zeta_i - \bar{\zeta})^2}}{n - 1}, \quad c = s/\bar{\zeta}, \quad (5.14)$$

in which  $n$  is the number of results,  $\zeta_i$  is the  $i$ -th result and  $\bar{\zeta}$  is the mean value. The amplitude of the CI,  $U_D$ , is calculated using:

$$P(\bar{\zeta} - U_D \leq \mu \leq \bar{\zeta} + U_D) = 90\%. \quad (5.15)$$

The amplitude  $U_D$  is calculated by the relation:

$$U_D = t_{n-1, \alpha/2} s / \sqrt{n}, \quad (5.16)$$

in which  $n$  is the number of data points in the sample, and  $t_{n-1, \alpha/2}$  is the Student-t

distribution value at  $n - 1$  and  $\alpha/2$ , which is given in several references, such as in Neto (2005).

## 5.4 Validation

According to Eça, Vaz & Hoekstra (2010), the aim of Validation is to estimate the modeling error of a mathematical model compared to a set of experimental data, which represents the physical model.

Once validation is carried out, one can say that the model/code is valid for that particular problem and conditions<sup>2</sup>. The procedure proposed by ASME-Guide (2008) is based on the comparison of the quantities,

$$U_{val} = \sqrt{U_{num}^2 + U_{input}^2 + U_D^2}, \quad (5.17)$$

and

$$E = S - D. \quad (5.18)$$

In equations 5.17 and 5.18,  $U_{num}$  is the numerical uncertainty estimated for a certain quantity, equation 5.4;  $U_{input}$  is the uncertainty of the parameter inputs (which are considered negligible for the present exercise);  $U_D$  is the experimental uncertainty, equation 5.16;  $S$  is the numerical prediction of the parameter value; and  $D$  is the experimental value. The comparison between  $U_{val}$  and  $E$  may lead to two possibilities:

- $|E| \gg U_{val}$  means that the comparison is poor most likely because the modeling errors are of most importance;
- $|E| < U_{val}$  means that the solution is within the noise imposed by the different sources of uncertainty. In this case, if  $|E|$  is small enough, then the solution is validated with the experiment at  $U_{val}$  precision. Otherwise, the quality of the numerical solution and/or the experiment should be improved for a better comparison.

The theoretical elements and procedures presented in this Chapter were used in this thesis to estimate numerical uncertainties and orders of convergence, mainly for the stationary cylinder application presented further ahead.

---

<sup>2</sup>It is worth noting that a CFD code cannot be validated: solution validation is the correct concept.



# Chapter 6

## The Rigid Fixed Cylinder Flow - Traditional Modeling

*In this chapter, the flow around a fixed circular cylinder will be approached from steady laminar to unsteady turbulent regimes. Computations for Reynolds numbers ranging from 1 to  $5 \times 10^5$  will be presented. Two-dimensional setup combined with  $k - \omega$  SST is applied, in an approach called herein as “traditional”. The numerical details will be discussed together with the discretization, verification and validation analyses.*

*The objectives of this chapter are i) to delineate the capabilities of traditional turbulence modeling; ii) assess the numerical and modeling errors of the approach; iii) consolidate the knowledge of traditional RANS-modeling for the cylinder flow in a wide range of Reynolds numbers, but more importantly in the drag-crisis region, which is important for several practical applications.*

### 6.1 Phenomenological Background of Flow Around Fixed Cylinder

#### 6.1.1 Steady Laminar Regime - $Re < 49$

Experiments and computations presented in the literature show that the flow around a fixed circular cylinder is approximately steady and two-dimensional for Reynolds numbers up to  $Re \approx 49$  (WILLIAMSON, 1996; HENDERSON, 1995).

For very low Reynolds number, up to about  $Re \approx 5$ , the boundary layer is attached and

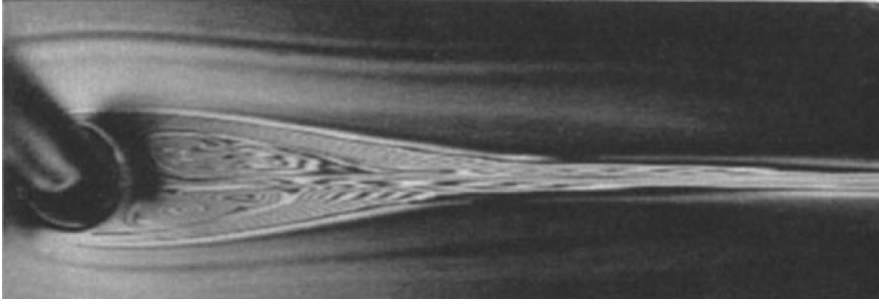


Figure 6.1: The steady wake behind the cylinder for  $Re < 49$  (WILLIAMSON, 1996).

the streamlines resemble those of an ideal fluid flow. However, the pressure and velocity distributions are very different from that case. In fact, in this flow, also known as creeping flow, the viscous effects are very important. When  $Re > 5$ , the boundary layer separates from the surface of the cylinder and the wake is known to present a steady recirculation region of two symmetrical vortices, as depicted in figure 6.1.

The drag force is aligned with the flow direction and is defined in general as (HENDERSON, 1995):

$$\mathbf{F}_D = \mathbf{e}_1 \oint [-P\mathbf{n} + \mu(\nabla\mathbf{v} + \nabla\mathbf{v}^T)\mathbf{n}]ds, \quad (6.1)$$

where  $\mathbf{n}$  is the outward-pointing vector normal to the cylinder surface;  $\mathbf{e}_1$  is a unit-vector aligned with the fluid velocity upstream of the cylinder.

The lift force is in general defined as (HENDERSON, 1995):

$$\mathbf{F}_L = \mathbf{e}_2 \oint [-P\mathbf{n} + \mu(\nabla\mathbf{v} + \nabla\mathbf{v}^T)\mathbf{n}]ds. \quad (6.2)$$

The drag coefficient is defined as:

$$C_D = \frac{\|\mathbf{F}_D\|}{\frac{1}{2}\rho DLV_\infty^2}, \quad (6.3)$$

whereas the lift coefficient is defined as:

$$C_L = \frac{\|\mathbf{F}_L\|}{\frac{1}{2}\rho DLV_\infty^2}. \quad (6.4)$$

Throughout the text, references will also be made to RMS (root mean square) of the lift

coefficient, which is calculated as the standard deviation of the lift coefficient time trace (since its average is zero and the trace, ergodic).

In the steady laminar range, as the boundary-layer separation point transits downstream on the cylinder surface, the drag force decreases, as well as the suction coefficient and at  $Re \approx 49$  the flow radically changes, as seen below.

### 6.1.2 Laminar Vortex Shedding - $49 < Re \lesssim 194$

For  $Re > 49$ , instabilities in the recirculation bubble downstream of the cylinder drive the flow to reach a stable limit cycle oscillation with the Strouhal frequency,  $f_s = StU/D$ , in which vortices are shed in the wake. This was found to be a manifestation of a Hopf-type bifurcation, in an analogy between the flow field and a dynamic system.

The Laminar Vortex Shedding persists in the range of approximately  $50 < Re < 194$ . In this range, the flow is still basically laminar and two-dimensional, in spite of three-dimensional instabilities that eventually trigger the transition to turbulence. Also in this range, variation of the base suction with Reynolds numbers sharply deviates in its trend from the steady wake regime, showing the tendency to increase (HENDERSON, 1995). Furthermore, the drag forces tend to decrease and, consistently, the separation point moves downstream.

Almost purely periodical wake oscillations are to be expected as seen in figure 6.2.



Figure 6.2: The laminar and two-dimensional vortex shedding at  $Re = 150$  (WILLIAMSON, 1996).

### 6.1.3 Wake-Transition Regime - $190 \lesssim Re < 260$

In this range, the wake is the first of the shear layers that goes through transition to turbulent state. This is clearly seen by two discontinuities in the wake formation as  $Re$  is increased. This is noticeable both in the variation of Strouhal number and base suction with  $Re$ , being named mode A discontinuity,  $Re \approx 180 - 194$ , and mode B discontinuity,  $Re \approx 230 - 250$ , see figure 6.3. In both cases, stream-wise vortical structures are present, making the flow pattern three-dimensional.

The two-dimensional computations showed here disregard this three-dimensional character, however it seems acceptable when analyzing the forces and shedding frequencies, as shall be seen later on.

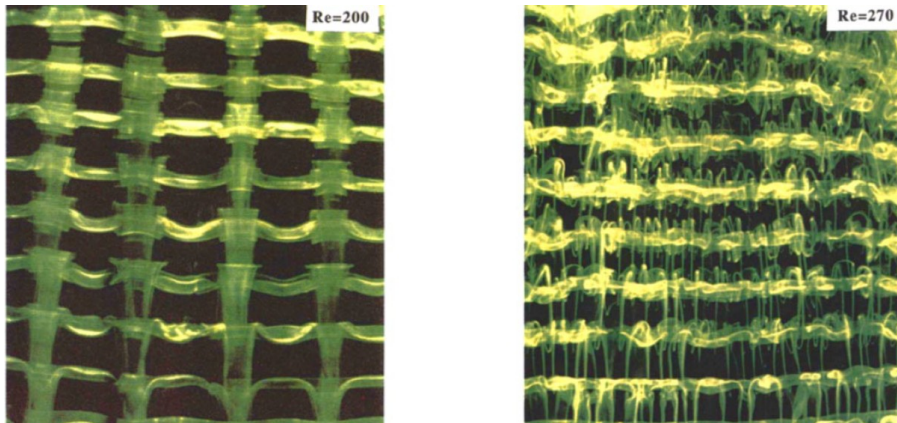


Figure 6.3: Flow pictures showing mode A on the left frame and mode B on the right one. Mode B is marked by finer structures and smaller wave length than in mode A. Pictures taken from Williamson (1996).

In this range, base suction and Strouhal frequency tend to increase, but with a lower level than could be extrapolated from the laminar shedding regime. Braza, Chassaing & Minh (1986) have found a weak instability of the shear layers next to the separation point and Williamson (1996) has reported small vortices in the separating shear layer in another instability of the wake.

### 6.1.4 Increasing Disorder in the Fine-Scale Three Dimensionalities - $260 < Re \lesssim 1,000$

In this range, one notices that the streamwise vortical structures that increase the three-dimensionality of the flow becomes finer in scale and gradually more disordered, causing reduction in the base suction, two-dimensional Reynolds stresses, drag forces and formation region (WILLIAMSON, 1996). At this point, in spite of instabilities that might be attributed to transitional features, the flow is still essentially laminar in the shear layers and near wake.

### 6.1.5 Shear-Layer Transition Regime - $1,000 < Re < 200,000$

Williamson (1996), Singh & Mittal (2005) have identified the range  $1,000 < Re < 200,000$  as the Shear-Layer Transition Regime. In this regime, the base suction increases and the formation length of the mean recirculation region decreases. An increase in drag is observed while the point of laminar-turbulent transition in the separating shear layers moves upstream. These trends take place with the developing instability of the separating shear layers. As commented by Williamson (1996), the shear layer vortices amalgamate in the near wake, as seen in figure 6.4.

Figure 6.5 shows a schematic representation of the boundary layer in the pre-critical region, at  $Re = 20,000$ . The boundary layer goes through laminar boundary layer separation, triggering laminar-turbulent transition downstream.

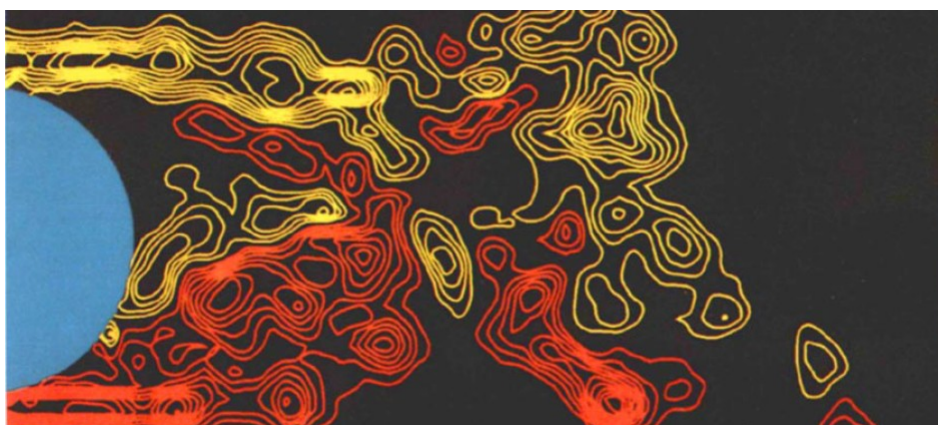


Figure 6.4: Particle Image Velocimetry measurements of the shear layer vortices showing the flow at  $Re = 10,000$ . Picture taken from Williamson (1996).

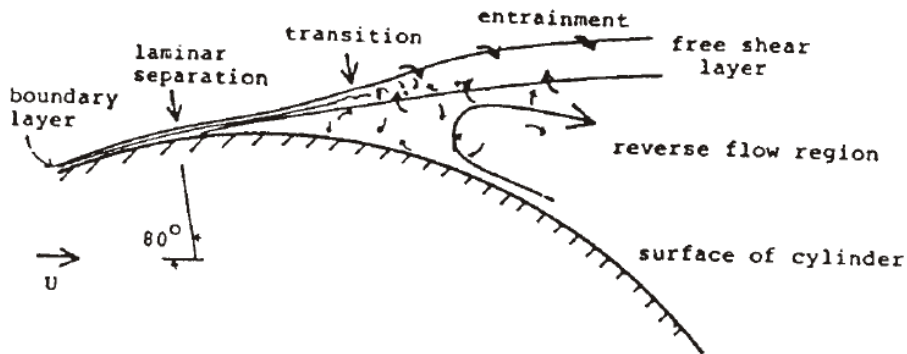


Figure 6.5: Pre-critical Reynolds numbers flow (BASU, 1985). Laminar separation takes place upstream of the transition.

### 6.1.6 Critical Transition Regime - $200,000 < Re \lesssim 500,000$

In the Critical Transition Regime, approximately  $200,000 < Re < 500,000$ , base suction and drag decrease sharply, mainly associated with the separation-reattachment bubble, which energizes the boundary layer making it separate further downstream and causing a narrower wake than there was so far, see figure 6.6. This region is commonly known as the drag crisis region.

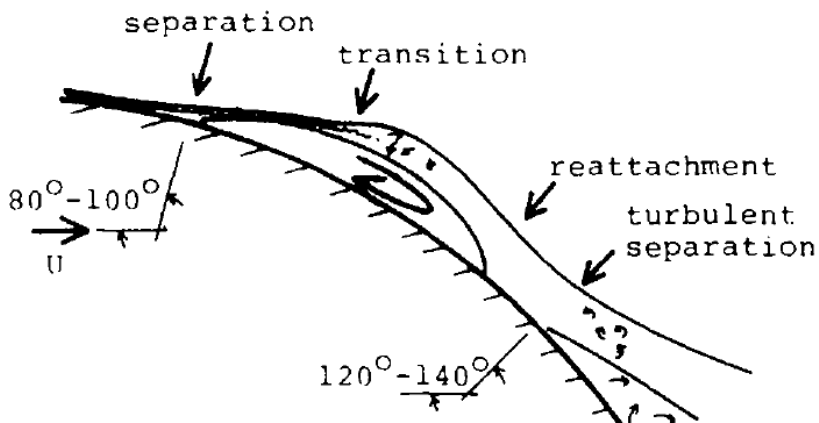


Figure 6.6: Transitional Reynolds numbers flow (BASU, 1985). Separation-reattachment bubble causes turbulent separation downstream compared to lower Reynolds numbers.

### 6.1.7 Post-Critical Transition Regime - $Re > 500,000$

As Reynolds number is increased above 500,000, the post-critical regime is reached, in which the boundary layer itself becomes turbulent, and the wake remains narrow. The drag coefficients increase slightly above the values in the drag crisis as well as the Strouhal number. Figure 6.7 depicts the transition taking place upstream of separation.

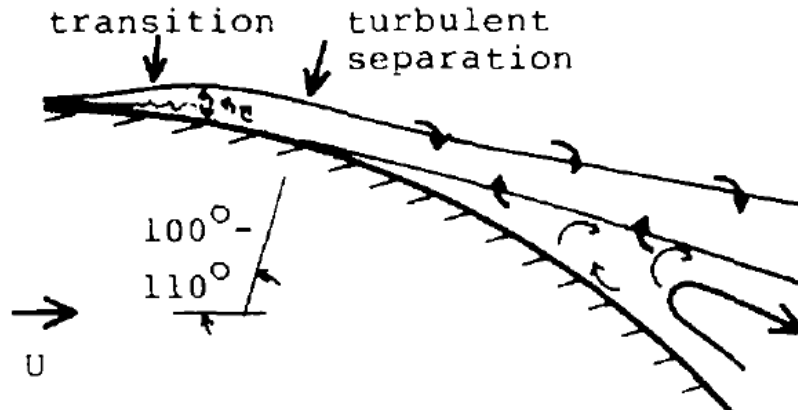


Figure 6.7: Post critical Reynolds numbers flow (BASU, 1985). The transition takes place upstream of separation causing the formation of a narrow wake and low drag coefficients.

The phenomenological background showed above is relevant for the following sections and remainder of the thesis, as it subsidizes the analysis of great part of the calculations that were carried out.

## 6.2 Outline of the Calculations

The calculations with smooth fixed cylinder presented in this Chapter were carried out at Reynolds numbers from  $Re = 5$  to  $Re = 500,000$ , thus ranging from steady laminar to the end of the critical regime. This Chapter presents the results with the approach herein named “traditional modeling”.

Two-dimensional laminar steady and unsteady calculations are done for  $Re = 5; 10; 20; 30; 40; 50; 100; 200$ . The  $k-\omega$  SST turbulence model (MENTER, 1994) is used for the turbulent Reynolds numbers, 1,000; 10,000; 100,000; 500,000. These results are considered as the numerical benchmark since this model is the industry standard. Conversely, the following Chapter will present improved results obtained with more modern turbulence and transition models.

It has been discussed (PEREIRA; VAZ; EÇA, 2015) that two dimensional calculations can

indeed disregard relevant effects of three dimensional span-wise communication. While this is sound, the following points are raised as counterpoint. As one of the main objectives that has permeated this work is to map the capabilities of different turbulence models and modeling techniques, it is worth exploring the two-dimensional calculations since they represent a more common approach in engineering applications due to the lesser required computational time and power compared to three-dimensional calculations. In that regard, a relevant practical fact is also mentioned: the grid resolution necessary in the span-wise direction to capture the relevant three dimensional dynamics that influence loads and vortex dynamics is quite large, thus increasing computational load and time to levels unfeasible for the number of calculations showed herein. Finally, it is pointed out that in the drag crisis region, which concentrates large portion of the engineering applications, the two-dimensional calculations showed quite appropriate, as loads are strongly influenced by the transition location in the boundary layer, that in turn revealed quite well predicted by the two-dimensional approach.

Tables 6.1 and 6.2 show, respectively, the details of the finest grids used for steady and unsteady calculations. For both sets of steady and unsteady laminar calculations, the same grids were used, as they were fine enough for the largest Reynolds number,  $Re = 200$ . The five grids used had from 6,992 to 27,360 cells. Table 6.3 shows the details of the finest grids for the turbulent calculations done with  $k-\omega$  SST. In these turbulent cases, from three to five grids were used in total for uncertainty estimation and the grids ranged from 213,750 to 586,264 cells. Table 6.4 shows the number of time steps at each shedding cycle period for the coarsest and finest laminar and turbulent calculations.

Table 6.1: Details of the finest grids used in the steady laminar calculations.

$Re$	Number of Cells	Circumferential Cells	$y_{max}^+$
5	27,360	608	0.02
10	27,360	608	0.0002
20	27,360	608	0.0003
30	27,360	608	0.0003
40	27,360	608	0.11
50	27,360	608	0.1

Table 6.2: Details of the finest grids used for the unsteady laminar calculations.

$Re$	Number of Cells	Circumferential Cells	$y_{max}^+$
100	27,360	608	0.47
200	27,360	608	0.81

Table 6.3: Details of the finest grids used for the turbulent calculations.

$Re$	Number of Cells	Circumferential Cells	$y_{max}^+$
1,000	213,750	1,900	0.97
10,000	542,944	2,432	0.36
100,000	542,944	2,432	0.85
500,000	586,264	2,888	0.74

Table 6.4: Time discretization for the unsteady laminar and turbulent calculations. The largest and smallest number of point per cycle used for the calculations are indicated

$Re$	Time Steps per Shedding Cycle
100	10-50
200	10-50
1,000	8-200
10,000	10-240
100,000	20-240
500,000	40-240

### 6.3 Numerical Details and Grids

A rectangular domain is used, as shown in figure 6.8, which also presents the boundary conditions and the grid layout used in the calculations.

Regarding the size of the domain, the sensitivity analysis done by Penga (2010) is used, which confirmed that it is appropriate to set the inlet and lateral boundaries  $10D$  away

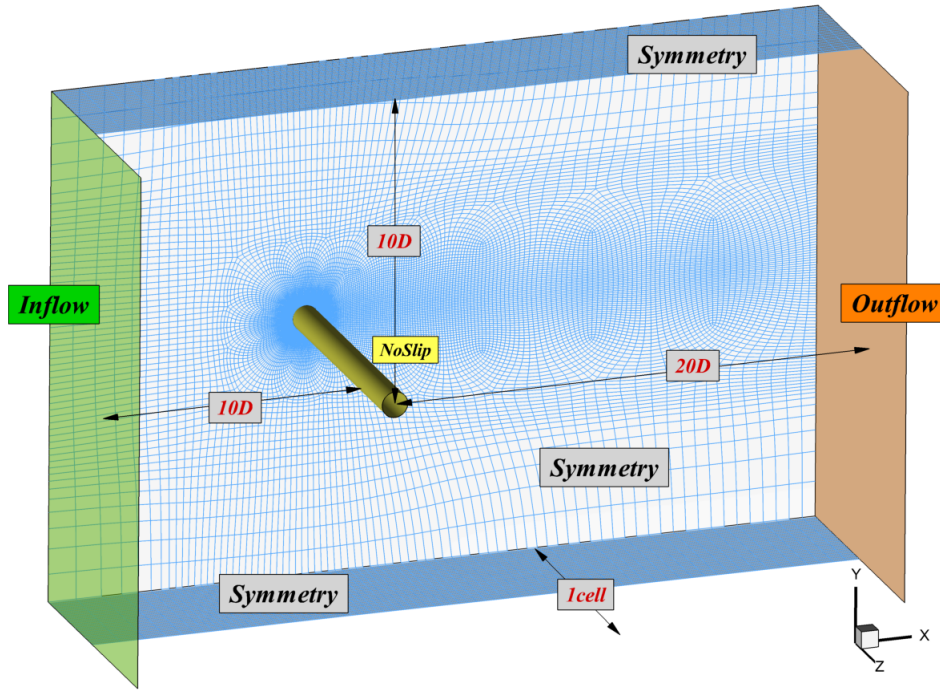


Figure 6.8: Grid and domain used in the calculations.

from the cylinder axis whereas the outlet boundary can be located  $20D$  away from the cylinder.<sup>1</sup> For the two-dimensional calculations showed in this chapter, there is one cell in the  $z$ -direction. The grids are structured, with the vicinity of the cylinder made with an O-grid, in order to refine the boundary layer and wake zones.

The shapes seen in fig. 6.9 are typical of the refinement method which consists in avoiding the emergence of hanging nodes, thus improving the quality of the mesh, so-called nested refinement. The intermediate grids between the finest and the coarsest one are build by interpolation. In all the results with the finest grids showed in this thesis,  $y^+ \leq 1$  in the nodes adjacent to the cylinder, assuring that the first nodes were well inside the viscous sub-layer and thus dispensing wall functions, an essential condition for the calculation of the cylinder flow (EÇA et al., 2015). The aspect ratio of the near-wall cells is up to ca. 5 in all grids, ensuring that  $x^+$  is also very low.

<sup>1</sup>The influence of the domain size is expected to decrease with increasing Reynolds numbers, due to stronger convection.

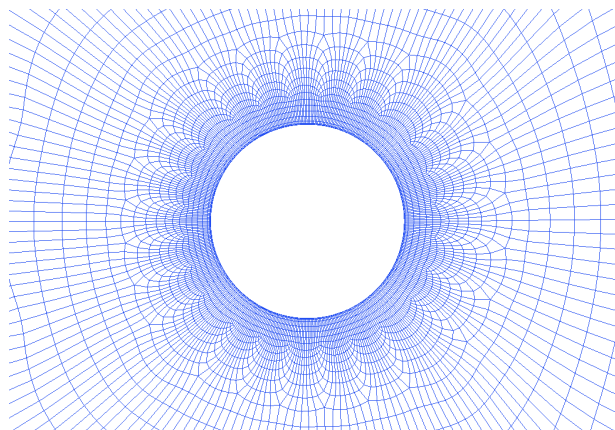


Figure 6.9: Detail of the mesh close to the cylinder. The shapes seen are typical of a nested-refinement technique.

In the two-dimensional calculations showed in the present chapter, four to six grids were used in each Reynolds numbers, with the number of cells ranging from approximately 7,000 to 586,264 cells.

The finest grid and time step for each Reynolds number were evidently the ones of interest for analysis, but the results obtained with the coarser grids and time steps were useful to carry out the convergence analysis and derive the numerical uncertainties for the two-dimensional calculations.

It is worth pointing out that the two dimensional calculations showed in this chapter took from a few days (with the coarse discretization and lowest Reynolds numbers) up to several weeks in the TPN HPC cluster when the finest calculations were done due to the adopted strict convergence criteria presented further ahead. Normally, the unsteady laminar calculations were carried with up to 16 cores, whereas the turbulent calculations were usually carried out with up to 64 cores (2.8GHz clock speed and 3GB of RAM per core).

The boundary conditions of the equations solved are defined on physical rather than mathematical grounds, as presented in figure 6.8. The following boundary conditions are applied in the calculations presented herein:

- Wall: Non-slip condition applies on the wall boundary. The velocities are taken as equal to the wall velocity, i.e. zero for the stationary cylinder (Dirichlet condition);
- Symmetry: When a symmetry boundary condition applies, the convective fluxes of all quantities are zero on that boundary, as well as the normal gradients of the velocity components parallel to the symmetry plane and of the scalar quantities (mixed Dirichlet/Neumann conditions);

- Inlet boundary: Here the velocity and turbulent quantities distribution are specified with Dirichlet boundary condition; pressure is extrapolated from the interior solution (zeroth-order extrapolation - Neumann condition); This combination is referred to as inflow condition;
- Outlet boundary: The outlet boundary condition should be positioned far enough from the cylinder in such a way that the pressure modes decay and that the flow solution near the cylinder is not influenced by the position of the outlet. That being the case, one out of two conditions may be applied in the outlet: the so-called outflow boundary condition, in which velocities, turbulent quantities and pressure are extrapolated (zeroth-order is used for developed flow - Neumann-type condition); or a pressure boundary condition can be enforced, in which the pressure is fixed and the other variables are extrapolated. It is worth mentioning that the absolute value of pressure is unimportant, since the incompressible Navier-Stokes equations deal with the variations of pressure, thus both conditions should have the same effect if the boundary is positioned far enough downstream of the body. The former is enforced in all the fixed cylinder calculations, whereas the latter, for the moving cylinder calculations presented further ahead;
- Initial conditions: The initial velocity field is assumed uniform with magnitude equal to the current velocity. Likewise, the turbulent quantities are uniform, deduced from a laminar initial field ( $\mu_t/\mu = 0.01$ ).

## 6.4 Solution Verification

As mentioned above, results for several Reynolds numbers will be showed. In each case four to six grids and three to six time steps, with total of seven to twenty five calculations at each Reynolds number. In spite of such a large number of calculations, only one value for each Reynolds number (corresponding to the finest grid and time step) is presented and the other results are used for the convergence analysis and uncertainty estimation of  $C_{Davg}$  (average drag coefficient). Moreover, the parameters showed for analyses and comparisons are mainly  $C_{Davg}$ ,  $St$  (Strouhal number) and  $C_{Lrms}$  (RMS of the lift coefficient).

### 6.4.1 Iterative Convergence

The iterative convergence criteria has been set low enough in all cases so that the iterative error was always at least two orders of magnitude lower than the discretization errors. In the steady calculations, the iterative convergence criteria was defined as  $L_\infty \leq 10^{-12}$  for all

equations, as the example in figure 6.10 shows. The criteria for the unsteady calculations, both laminar and turbulent, was  $L_\infty < 10^{-6}$  for all residuals in each time step, as the example in figure 6.11 shows.

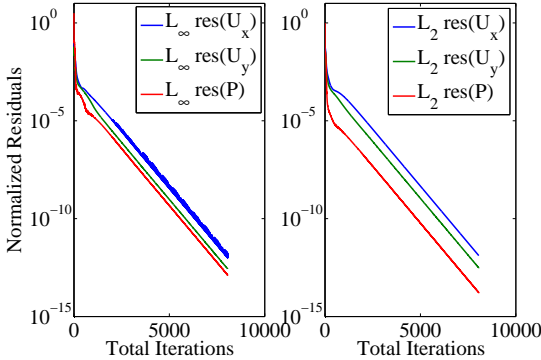


Figure 6.10: Infinity and RMS norms for evaluating the residuals of the flow quantities in the case  $Re = 40$ .

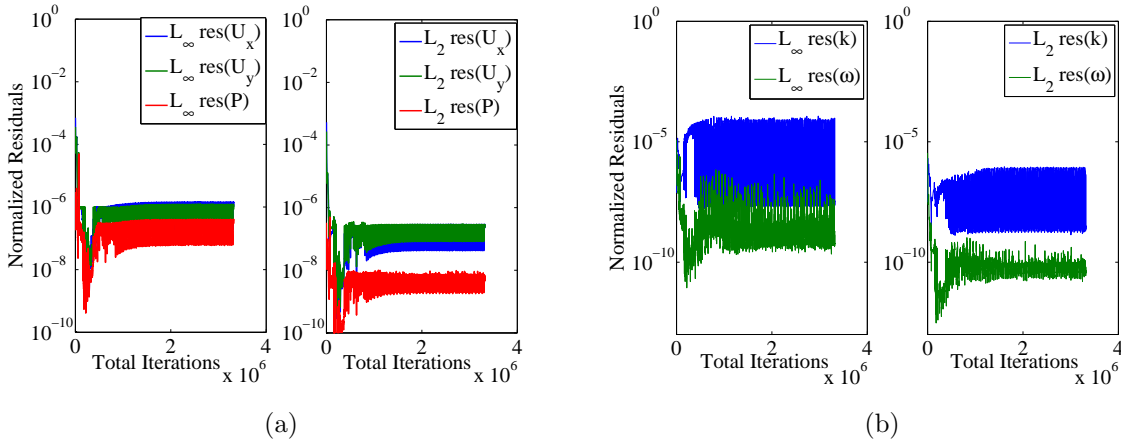


Figure 6.11: Infinity and RMS norms for evaluating the residuals of the flow quantities in the case  $Re = 1 \times 10^5$ . (a) Velocities and pressure. (b) Turbulent kinetic energy and turbulent frequency. Illustration of the worst iterative convergence obtained for all calculations of the present work.

The results of the fixed cylinder calculations showed herein were found to be very sensitive to the residuals. At times, preliminary calculations with less strict criteria did result in drag coefficients closer to the experiments than the ones with more strict residuals control.

In fact, Eça et al. (2014) have shown that the calculated loads and pressure distribution are highly sensitive to the iterative errors attained at the end of each time loop and the average drag coefficient can vary up to 10% with different iterative criteria. It was also

concluded that the usual “three orders of magnitude” of residual drop might be insufficient to achieve results free from iterative errors.

### 6.4.2 Discretization and Uncertainty Studies

Regarding the time discretization, the time steps were chosen in such a way that limit, or steady-state, cyclic solutions were reached and at least ten cycles could be analyzed in order to obtain reliable statistics. Furthermore, the Strouhal number is calculated from the peak of the power spectrum density of the lift coefficient time trace.

In the following plots, the time steps have been identified by:

$$t_i/t_{min} = \Delta t_i/(\Delta t)_{min}, \quad (6.5)$$

in which  $(\Delta t)_{min}$  is the finest time step used in the calculations and  $\Delta t_i$  is the time step used in the analyzed calculation. This way, the finest time step to be looked at has the value  $t_i/t_{min} = 1$  and the others, larger than one.

On the other hand, the grid parameter is  $h = 1/\sqrt{N_{cells}}$  as the calculations are two-dimensional. Therefore, the grid is identified by:

$$h_i/h_{min} = \sqrt{\frac{(N_{cells})_{max}}{(N_{cells})_i}}, \quad (6.6)$$

in which  $(N_{cells})_{max}$  is the finest grid and  $(N_{cells})_i$  is the case under analysis. Once again, the finest grid is identified by  $h_i/h_{min} = 1$ , and the others, larger than one.

In general, integral quantities, such as the drag coefficient, tend to present smaller uncertainties than local quantities, such as angle of boundary layer separation. The reason is that exact geometrical similarity is not always achieved and interpolation between grids may lead to some noise in the data. Despite indication of good discretization (for instance, large number of cells in the boundary layers and low  $y^+$ ), it is usually necessary in cases with large uncertainty to use very refined grids or time steps for a correct uncertainty estimation.

Some examples of the calculated surface fits for the investigated flow parameters and different Reynolds numbers are presented below. In these graphs, the flow parameters are plotted for each calculation as function of grid and time parameters. The size of the blocks give a visual indication of the level of uncertainty.

The example in figure 6.12 shows the surface fit for the Strouhal number for  $Re = 100$ , which presents convergence orders of  $p = 1.0$  for space and  $p = 1.6$  for time.

The plot in figure 6.13 shows that the uncertainty of drag coefficient for  $Re = 200$  is very low with the finest discretization because the fit presents good quality and the data points are all inside the asymptotic convergence range.

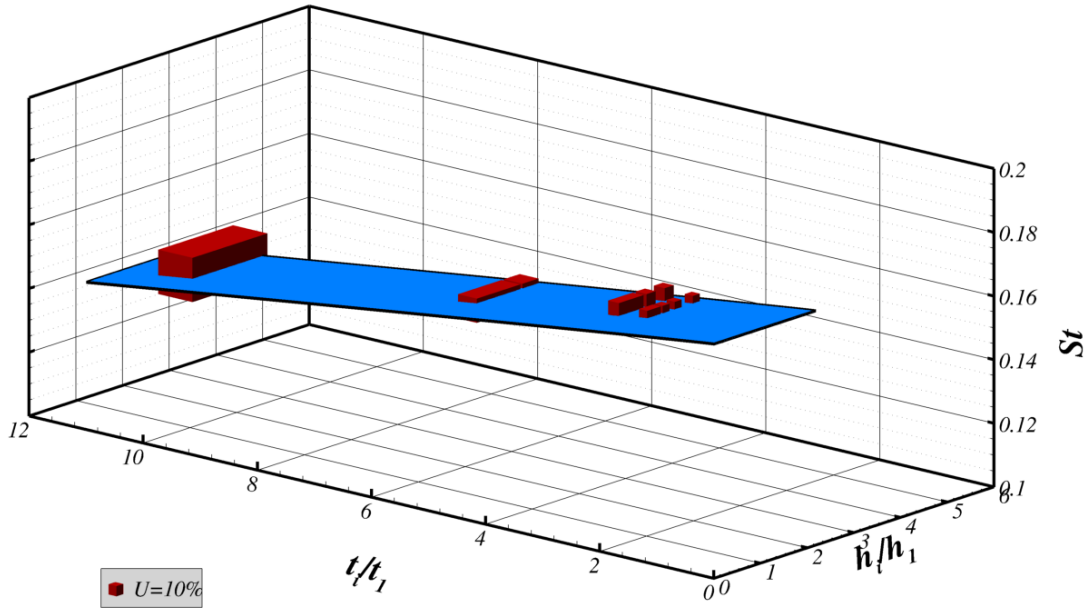


Figure 6.12: Surface fit for  $St$  and  $Re = 100$ . The size of the blocks indicate the uncertainty of each data point. The convergence orders are  $p = 1.0$  for space and  $p = 1.6$  for time.

Table 6.5 summarizes the uncertainties for the laminar calculations. There is very low uncertainty overall for the steady calculations whereas, somewhat higher for the unsteady laminar case.

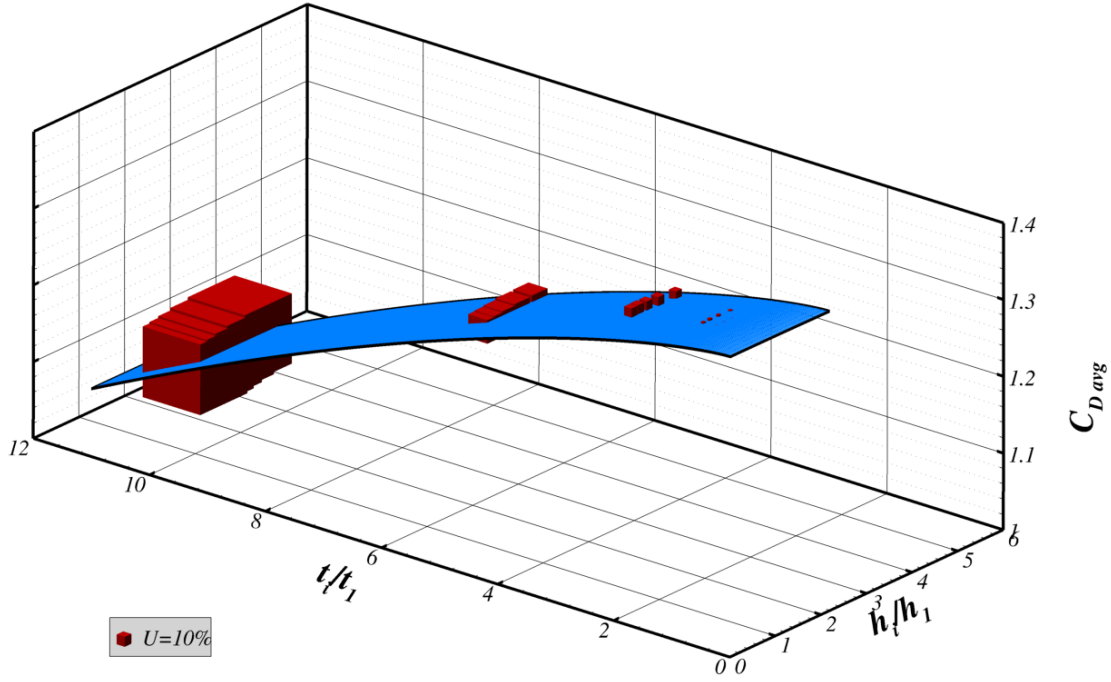


Figure 6.13: Surface fit for  $C_{D,avg}$  and  $Re = 200$ . The size of the blocks indicate the uncertainty of each data point. The convergence orders are  $p = 2.0$  for space and  $p = 1.4$  for time.

Table 6.5: Uncertainty estimation for the laminar calculations.

$Re$	5	10	20	30	40	50	100	200
$U(C_{D,avg})(\%)$	0.01	0.02	0.02	0.02	0.04	0.02	3.38	2.72

Considering the uncertainty quantification for the turbulent simulations, figure 6.14 shows the calculated surface that fits the  $Re = 1 \times 10^3$  data for the average drag coefficient. All of the data is in the monotonic convergence range, which results in a very good surface fit (low standard deviation over mean data change) and with decreasing uncertainty as grid or time step are refined. On the other hand, an interesting behavior occurs for  $Re = 5 \times 10^5$ : close inspection of the results showed that oscillatory convergence of  $St$  is verified, particularly for the time discretization, as figure 6.15 shows.

Table 6.6 shows the uncertainties calculated from the turbulent data. The uncertainties are somewhat higher than in the laminar calculations, reflecting the increasing complexity of the phenomenon with the onset of turbulence.

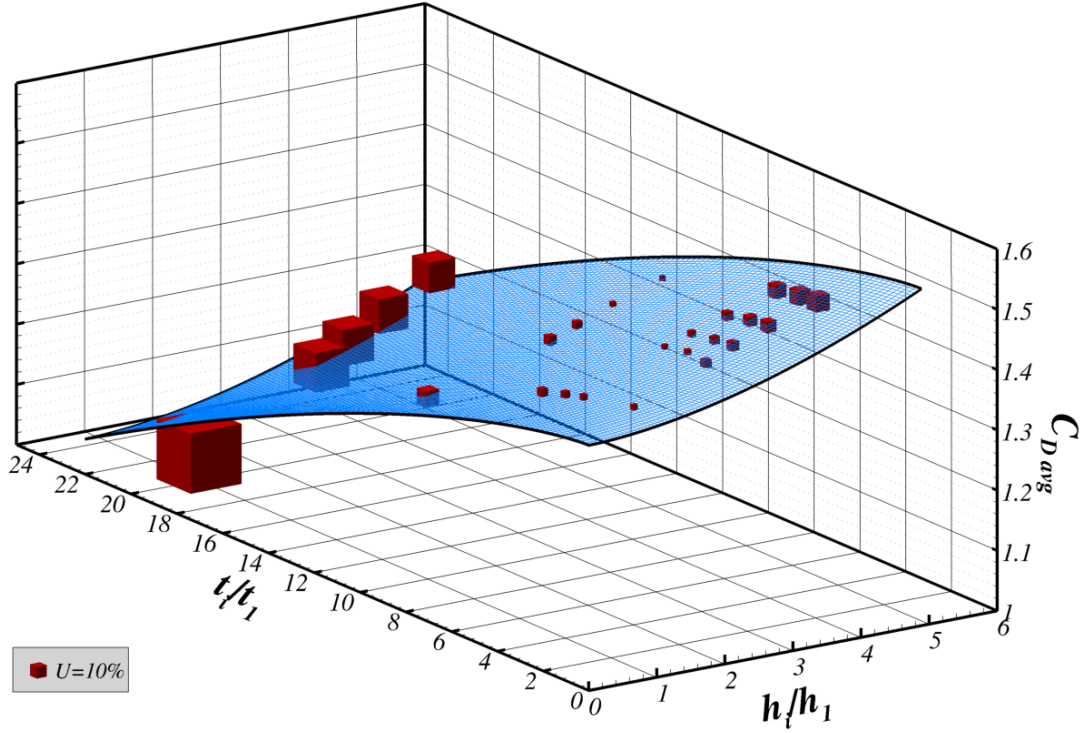


Figure 6.14: Drag coefficient calculations for  $Re = 1 \times 10^3$ . The size of the blocks indicate the uncertainty of each data point. In this case, the order of convergence of time and space are, respectively,  $p = 1.5$  and  $p = 1.7$ .

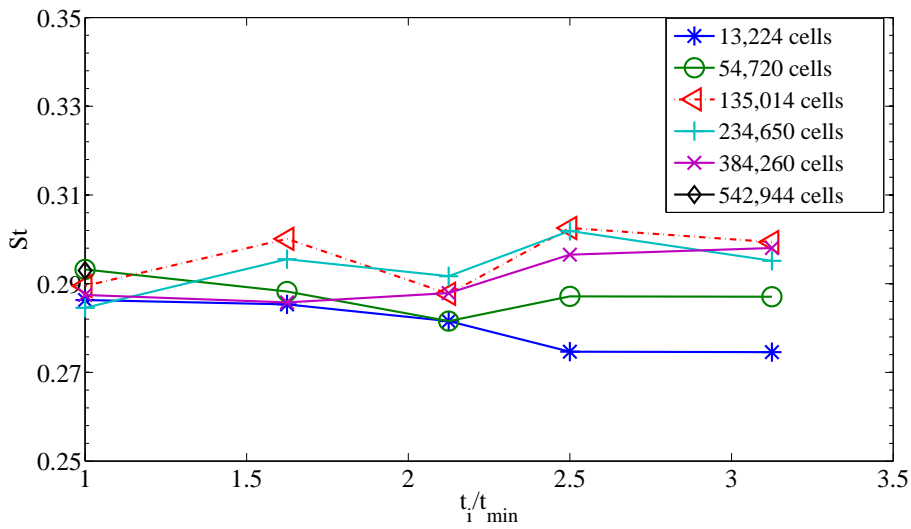


Figure 6.15: Time step refinement for the calculation of Strouhal numbers for  $Re = 5 \times 10^5$ . Oscillatory behavior is identified in this case.

Table 6.6: Uncertainty estimation for the turbulent calculations.

$Re$	1,000	10,000	100,000	500,000
$U(C_{Davg})(\%)$	4.62	3.19	3.08	13.03

In order to complement this discussion, it is worth noting that, as Rosetti, Vaz & Fujarra (2012) have showed, the uncertainty of the Strouhal number is the most troublesome quantity to determine, which shows that the refinement has to be very fine to capture the “exact” value that the code can provide.

Figure 6.16 presents the sensitivity of the drag coefficient results to the variation of the number of cells and time steps for four Reynolds numbers.

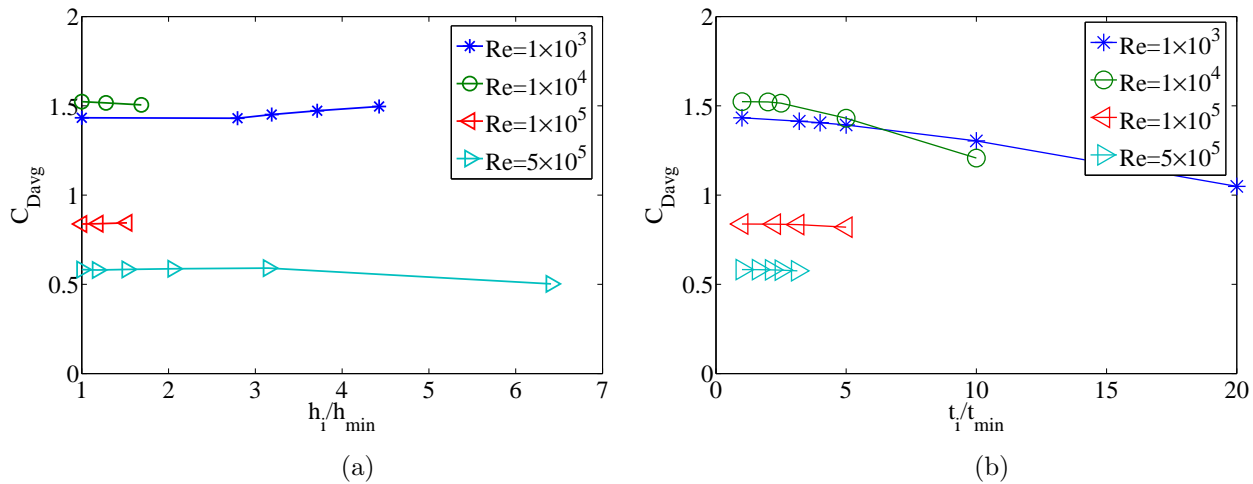


Figure 6.16: Sensitivity of the drag coefficient to different space and time discretizations for turbulent range. (a) Different grids with the finest time steps. (b) Different time step discretization with the finest grid.

## 6.5 Forces and Flow Analysis

### 6.5.1 Steady Laminar Calculations

Figure 6.17 presents the calculated drag coefficients compared with the experimental results for the steady laminar computations. In these results, the differences between numerical and experimental results are small and the graphical comparison of the results with their uncertainties shows that the present results can be considered quite accurate.

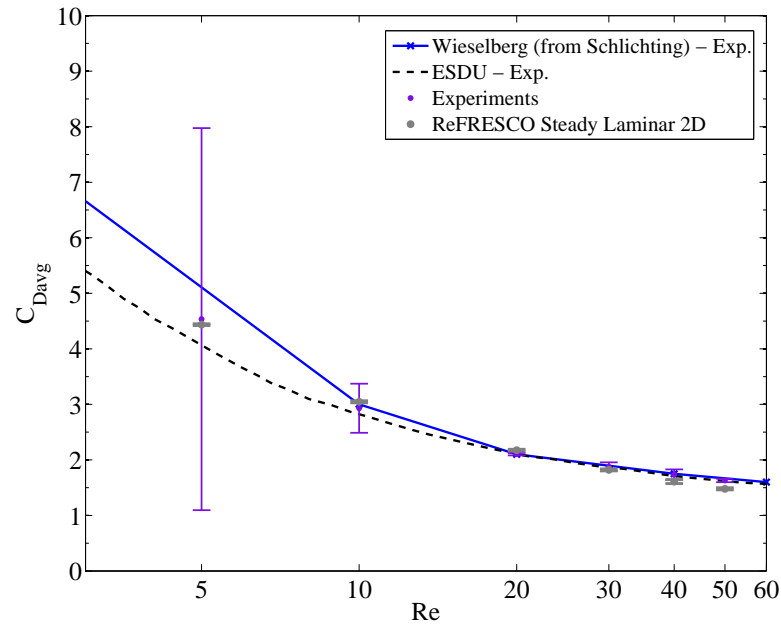


Figure 6.17: Drag coefficient results from laminar calculations. Experimental data from Schlichting H. (2000), ESDU (1985). The label “Experiments” denotes the average experimental values and the uncertainty bars are calculated both for the experiments and for the calculations.

The field plots with normalized velocities are presented in figure 6.18, with the purpose of showing the narrowing of the wake and increase of the recirculation bubble when the Reynolds number is increased in the steady laminar regime.

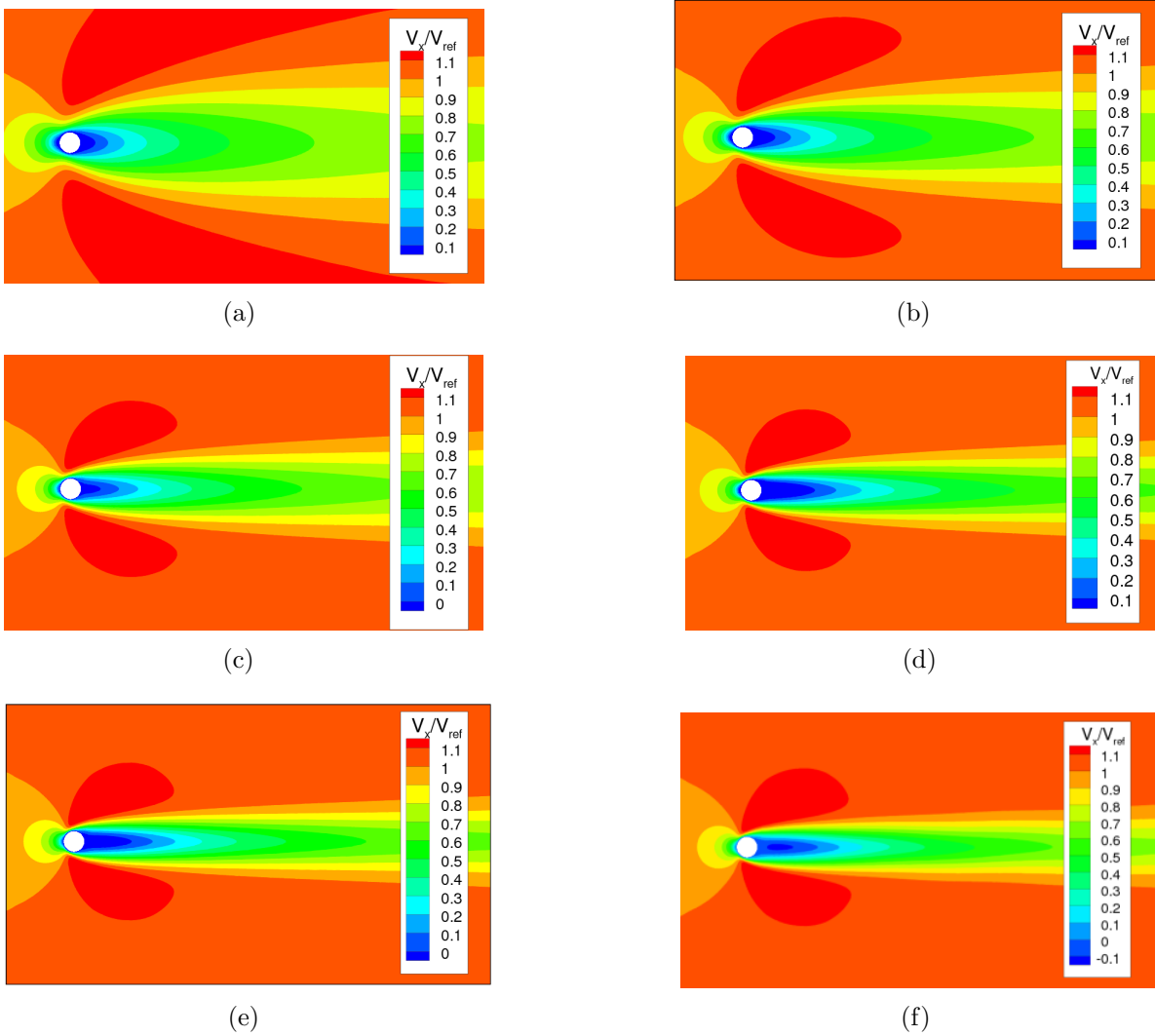


Figure 6.18: Field plots of normalized velocity. (a)  $Re = 5$ . (b)  $Re = 10$ . (c)  $Re = 20$ . (d)  $Re = 30$ . (e)  $Re = 40$ . (f)  $Re = 50$ .

### 6.5.2 Unsteady Laminar Calculations

Figure 6.19 presents the calculated drag coefficients compared with the experimental results for  $Re = 100$  and  $Re = 200$ : the uncertainties in the drag coefficients are rather small and the agreement with the experimental trend is remarkable.

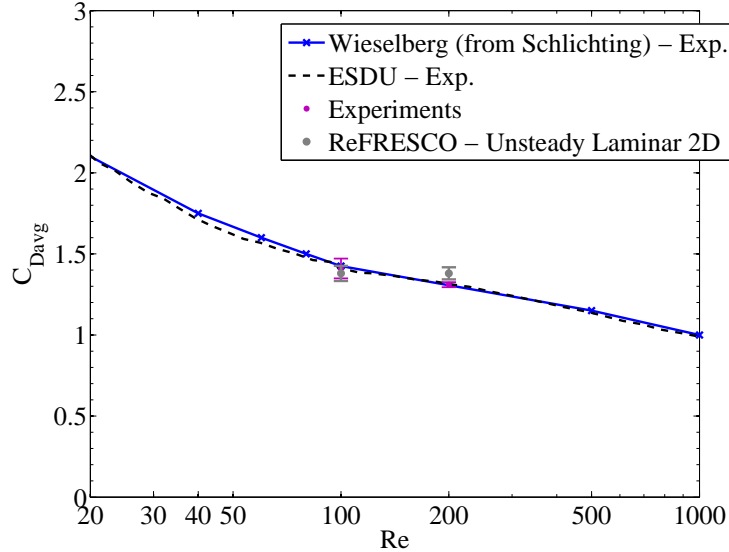


Figure 6.19: Drag coefficient results from laminar calculations. Experiments from Schlichting H. (2000), ESDU (1985). The label “Experiments” denote the average experimental values and the error bars are calculated both for the experiments and for the calculations.

Figure 6.20 presents the Strouhal frequencies (in nondimensional form, Strouhal number), calculated by means of the peak-energy frequency of the power spectral density obtained from the lift force. There is a fair agreement with the experimental trend from Norberg (2003).

Figure 6.21 shows an example of time traces of the force coefficients for  $Re = 100$ , in which high regularity is seen and a prominent peak energy is found. The Strouhal number calculated is  $St = 0.1998$  and twice that frequency is seen in the drag trace, reflecting the fact that the shedding cycle in the longitudinal direction is comprised of each shed vortice, whereas two vortices form each transverse cycle. In fact, as discussed in Rosetti, Vaz & Fajarra (2012), the differences between calculated and experimental Strouhal numbers and base pressure can be explained by the onset of the three-dimensional wake transition regime. In that issue, Williamson (1996) has identified that the mode A instability comprising vortex loops and streamwise vortex pairs affect the base suction and Strouhal frequency, driving smaller values than might be expected from extrapolation from

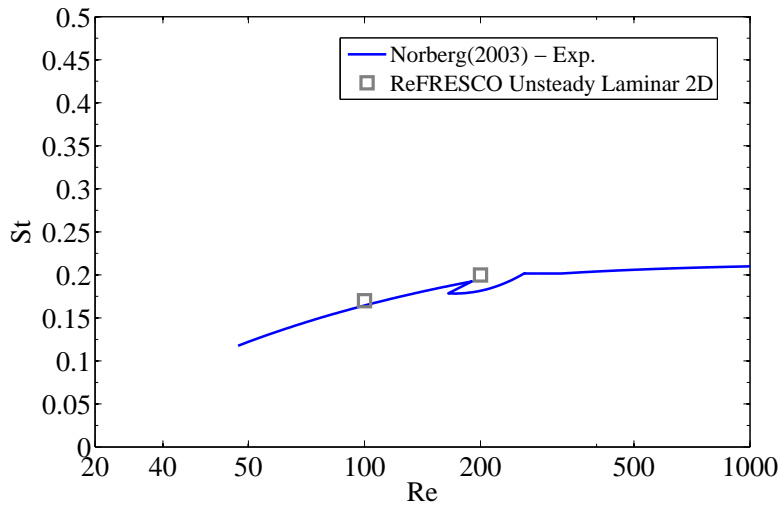


Figure 6.20: Strouhal number results from laminar calculations. Experimental formulas from Norberg (2003).

the steady laminar regime. The present modeling fails to capture such physical behavior. The increasing instabilities and three-dimensional nature of the flow tend to influence the flow in such a way to make the comparisons increasingly worse at higher Reynolds numbers and prior to the drag crisis.

In Figure 6.22, the same procedure is done with the time traces of separation angles, corroborating the peak-energy frequency (Strouhal number), but showing also some small energy in the second harmonic. Braza, Chassaing & Minh (1986) have found similar behavior in their simulations, which was related with weak instability of the shear layer next to the separation, associated with the formation of a “secondary eddy” adjacent to the separation point. This eddy appeared with the frequency of the second harmonic, at twice the frequency of shedding of main vortices (Strouhal frequency). As Reynolds number rises, the secondary vortices tend to become more pronounced. Eventually the secondary eddies merge with the main ones in the near wake, being convected downstream.

Evidently, the calculation of the global force filters higher harmonics, so they can hardly be noticed in the time traces of forces, masking the deficiency of the modeling. The relative deviations from the experimental trend are smaller than  $\approx 10\%$  ( $Re = 200$ ).

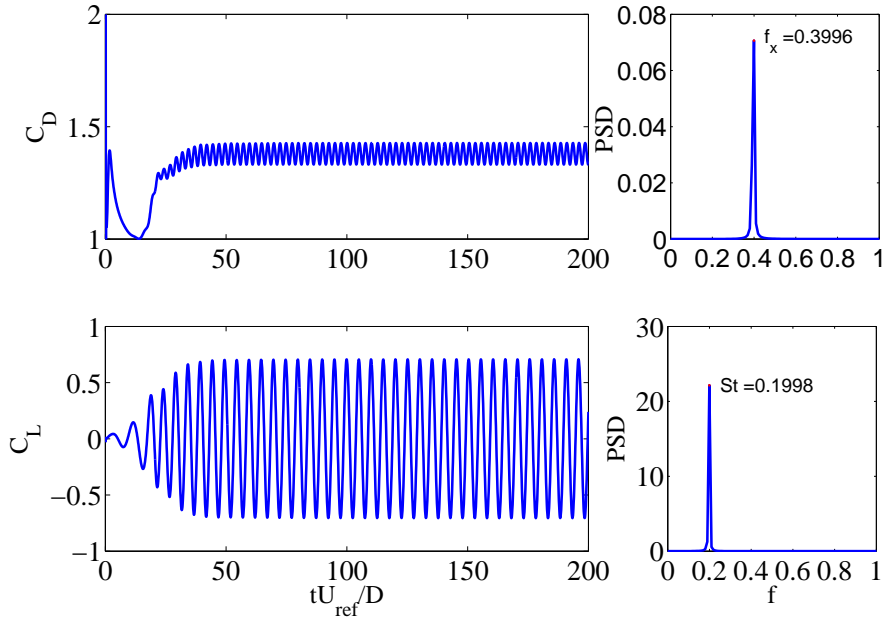


Figure 6.21: Drag and lift time traces and power spectrum densities from calculation with finest grid and time step for  $Re = 100$ . Only steady-state portion is used for the statistics.

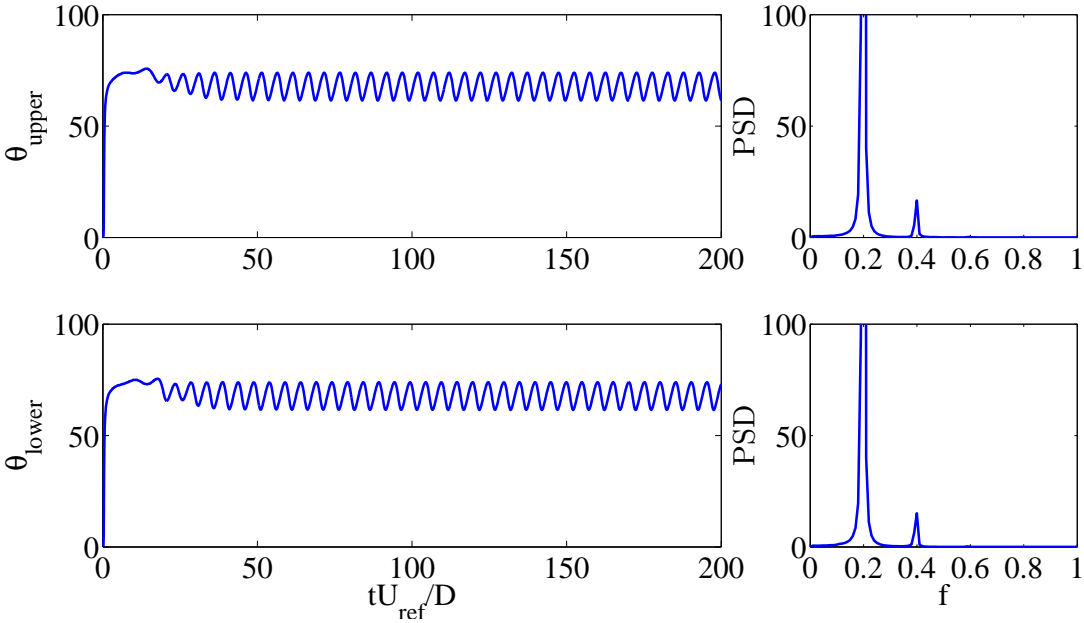


Figure 6.22: Time traces of separation angles and power spectrum densities from calculations with finest grid and time step for  $Re = 200$ . Both upper and lower separation angles are shown. Only steady-state portion is used for the statistics.

The field plot with normalized velocities presented in figure 6.23 shows variations consistent with the experimental observation, namely the vortex-shedding process and a more

subtle narrowing of the wake, associated with lower drag.

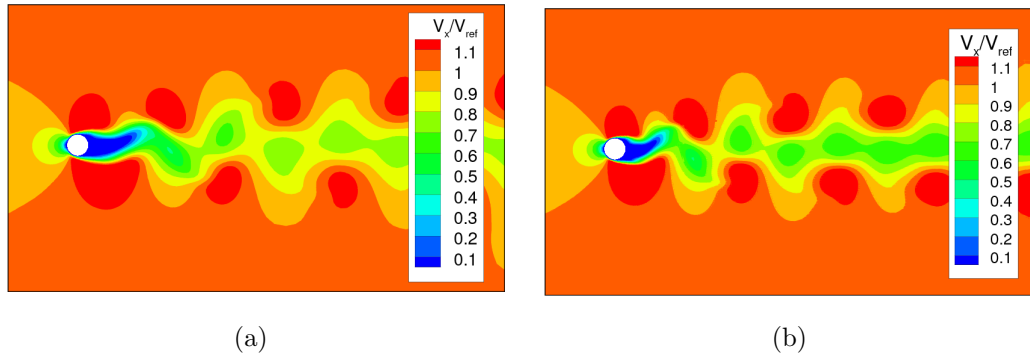


Figure 6.23: Field plots of normalized velocity at the point of largest lift coefficient. (a)  $Re = 100$ . (b)  $Re = 200$ .

### 6.5.3 Turbulent Regime

Figure 6.24 presents the drag coefficients for  $Re = 1,000; 10,000; 100,000; 500,000$ . The comparison with the experimental results is much less successful in this case than in the laminar calculations. Relative differences between experiments and calculations reach values as high as ca. 45% for  $Re = 1 \times 10^3$ . Moreover, the uncertainties are not as large as to justify the differences on account of the discretization errors, which means that the differences between experiments and calculations showed herein are due to modeling errors. Figure 6.25 shows the Strouhal numbers in the calculations, compared with experimental formulas derived from a large number of experiments. Better agreement is found, with differences up to ca. 36%, for  $Re = 1 \times 10^5$ .

It is worthwhile to observe the time traces of separation angles, figures 6.26 and 6.27, for  $Re = 1,000$  and  $Re = 10,000$ , respectively. One notes the presence of quite energetic higher harmonics, which are associated with the instabilities already seen for  $Re = 200$ . In fact, for  $Re > 1000$ , not only the secondary vortices are developed, but indeed a trail of small eddies that merge with the larger ones in the shear layers. Also in figures 6.26 and 6.27, one sees that the variation of the boundary-layer separation point is not symmetrical relatively to the mean value in steady-state. This interesting feature, enhanced in higher Reynolds numbers, is due to the two different dynamic positions (BRAZA; CHASSAING; MINH, 1986). During one cycle, when the separation angle is at its lowest value, there is an alternating vortex near the separation point, whereas in the highest value of the separation point, it encounters strongly convective flow.

Figure 6.28 shows the calculated RMS of lift coefficients compared to the experimental results from Norberg (2003). Very poor agreement is observed, especially for  $Re = 1,000$

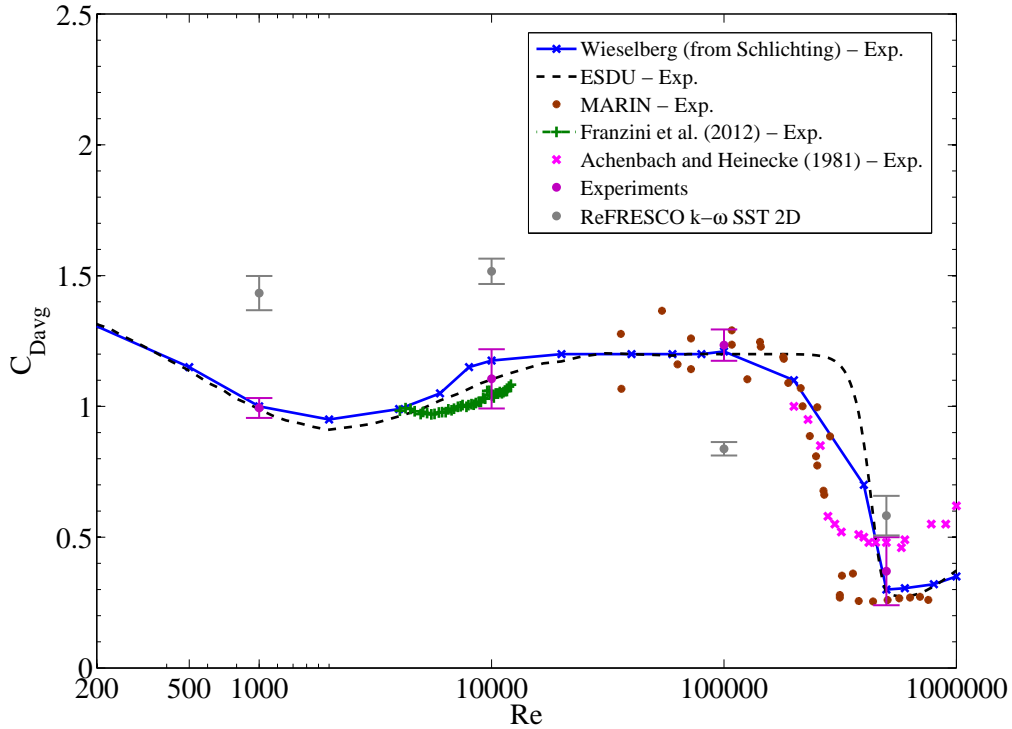


Figure 6.24: Drag coefficient results from turbulent calculations. Experiments from Schlichting H. (2000), ESDU (1985), Franzini et al. (2012), Achenbach & Heinecke (1981) and from MARIN. The label “Experiments” denotes the average experimental values and the error bars are calculated both for the experiments and for the calculations.

and  $Re = 10,000$ . In fact, the lift coefficient time traces were always very regular in the present calculations, therefore, the RMS is in practice linearly dependent on the lift coefficient amplitude. Moreover, it has been seen that the lift variation in the calculations is mainly due to the von Kármán-type vortex-shedding, i.e., shedding of very coherent and strong vortices, hence the regular traces and high amplitudes. It has also been discussed that the experimental results, especially for  $Re = 1,000 - 100,000$ , displays a strong three-dimensional character, from which one expects low regularity and lower amplitude of the lift traces and, hence, lower RMS value. The same spread behavior for the lift RMS is observed in different calculations and even experiments (NORBERG, 2003) indicating very high uncertainty in this quantity.

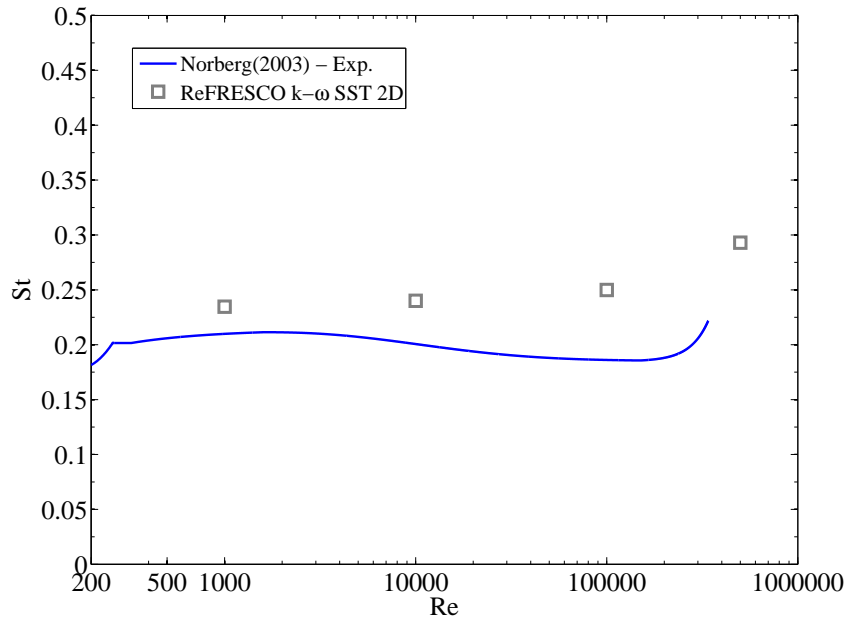


Figure 6.25: Strouhal number results from turbulent calculations. Experimental formulas from Norberg (2003).

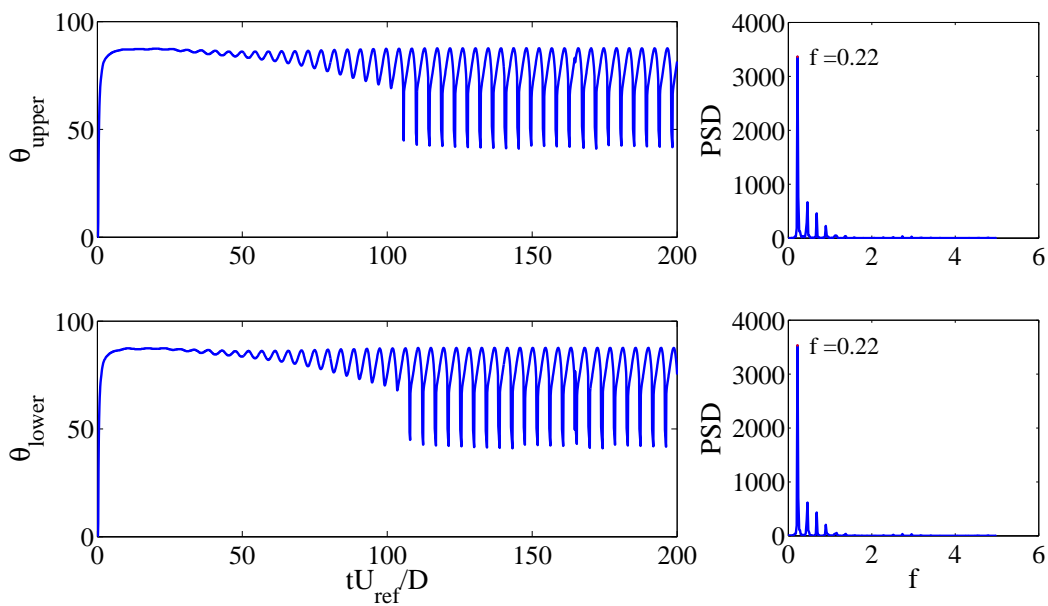


Figure 6.26: Time traces of separation angles for  $Re = 1,000$  with finest grid and time step. Only steady-state portion is used for the statistics.

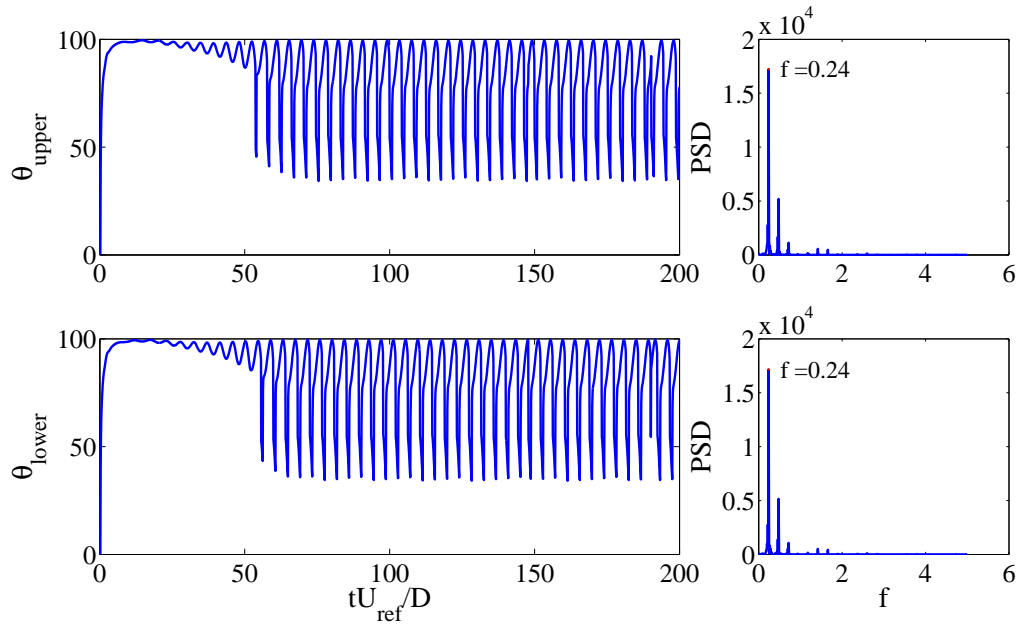


Figure 6.27: Time traces of separation angles for  $Re = 10,000$  with finest grid and time step. Only steady-state portion is used for the statistics.

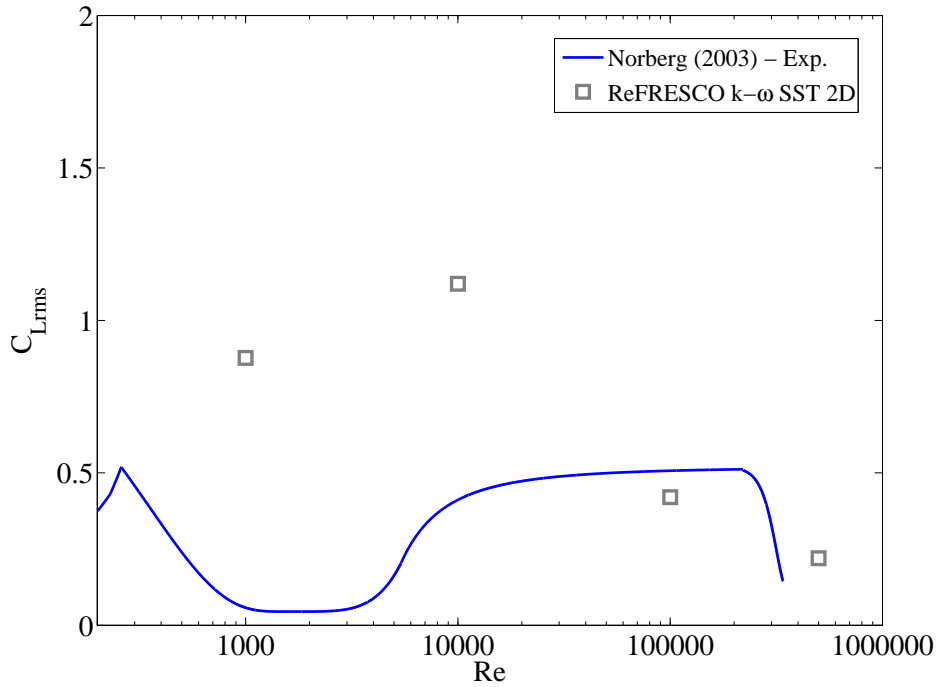


Figure 6.28: Strouhal number results from turbulent calculations. Experimental formulas from Norberg (2003).

Figure 6.29 shows the vorticity distributions for the turbulent calculations. Firstly, it is interesting to notice the secondary, smaller, vorticity cores adjacent to the cylinder wall in its upper part (in red) for  $Re = 1,000$  and  $Re = 10,000$ , figure 6.29 (a) and (b), as

commented before. Also, close examination of figure 6.29 (c) and (d) will show small eddies in the back of the cylinder, which will eventually merge with the larger ones. In all cases, the vortex cores show regions with constant colors. In these regions, the vorticity is nearly constant, showing that this fluid mass is rotating as a block as the vortices are convected in the wake. As Reynolds numbers increase, the size of these regions decrease, showing that the vortices become less coherent.

Figure 6.30 shows some streamlines of the flow in one particular instant. It is possible to see again the formation of the secondary structures, besides the strong main vortices. When the saddle structures are formed, the vortices detach from the shear layer and are convected in the wake.

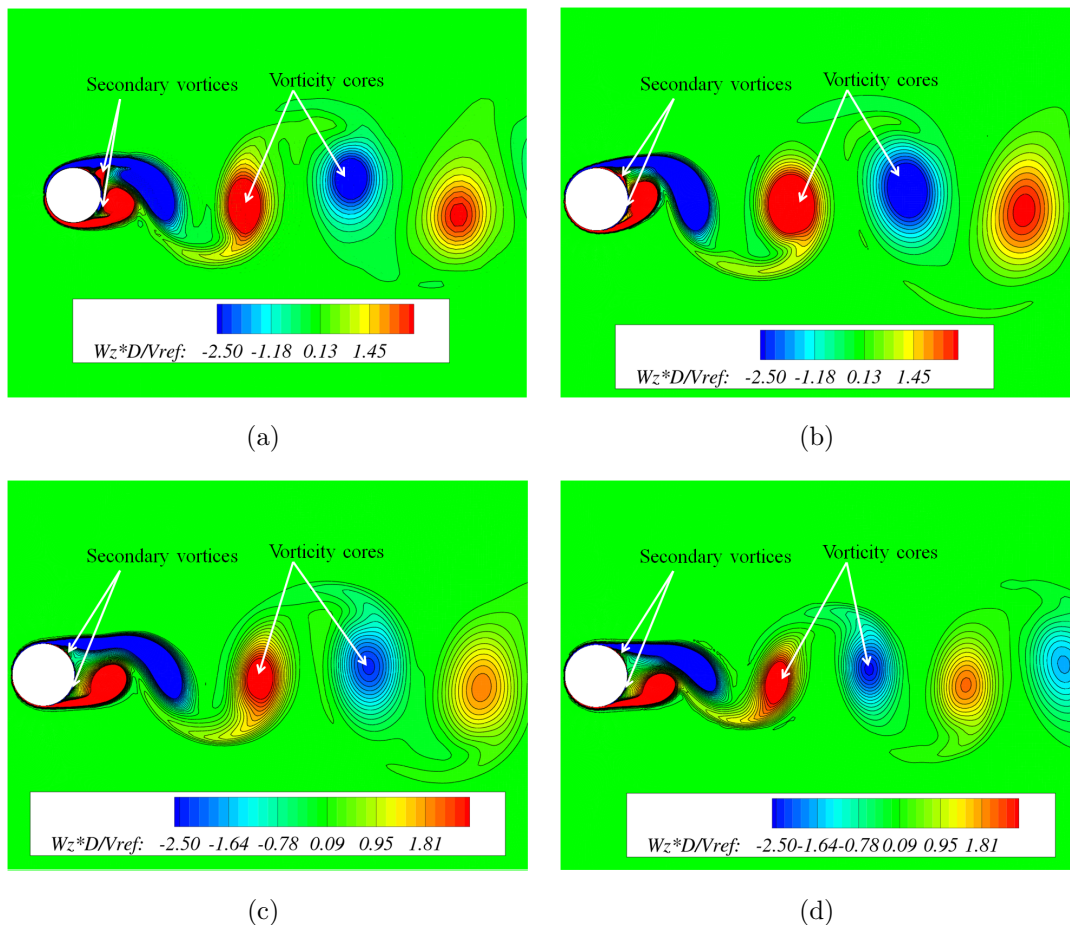


Figure 6.29: Field plots of normalized vorticity,  $\omega D / U_{ref}$  at the point of largest lift coefficient. (a)  $Re = 1,000$ . (b)  $Re = 10,000$ . (c)  $Re = 100,000$ . (d)  $Re = 500,000$ .

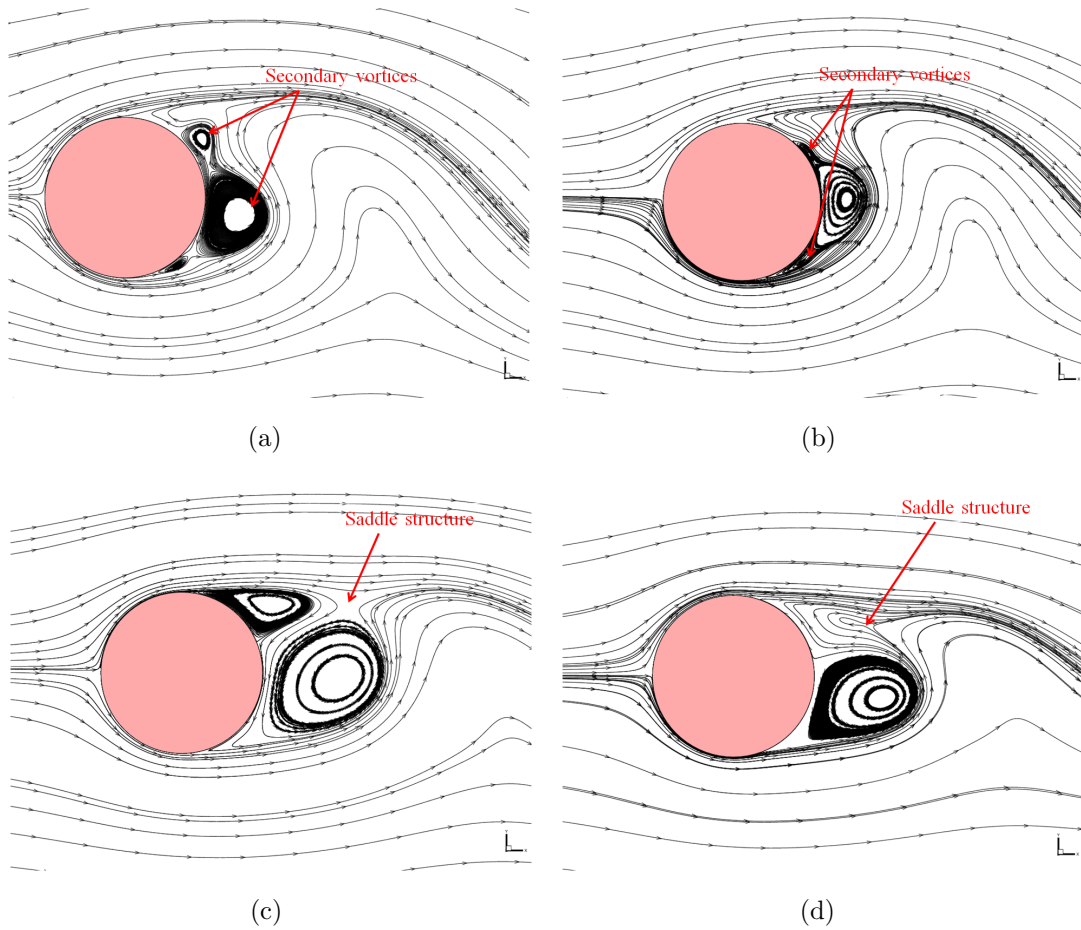


Figure 6.30: Field plots showing streamlines at the point of largest lift coefficient. (a)  $Re = 1,000$ . (b)  $Re = 10,000$ . (c)  $Re = 100,000$ . (d)  $Re = 500,000$ .

Further interesting features are observed in figure 6.31, which presents the normalized eddy viscosity. It is noticed that, as Reynolds numbers increase, the turbulence increases and plays larger and larger role in the overall nature of the flow. As a simplified manner of identifying the laminar-turbulent transition, one can compare the parts of the flow in which  $\nu_t < \nu$  and  $\nu_t > \nu$ . For the latter, it means that the flow is fully turbulent, whereas, for the former, it either means that the flow is laminar or transitional. It is not possible to clearly identify the transition length, however, it is possible to verify that the onset of turbulence is shifting upstream as  $Re$  is increased. It is interesting to observe that the onset of turbulence is downstream of the cylinder for  $Re = 1,000$  and  $Re = 10,000$ . Conversely, for  $Re = 100,000$  and  $Re = 500,000$ , the strong turbulent behavior is very close to the cylinder, showing that not only the wake but also the shear layers are mostly turbulent. It is most important to notice that no transition modeling other than the turbulence model itself is present.

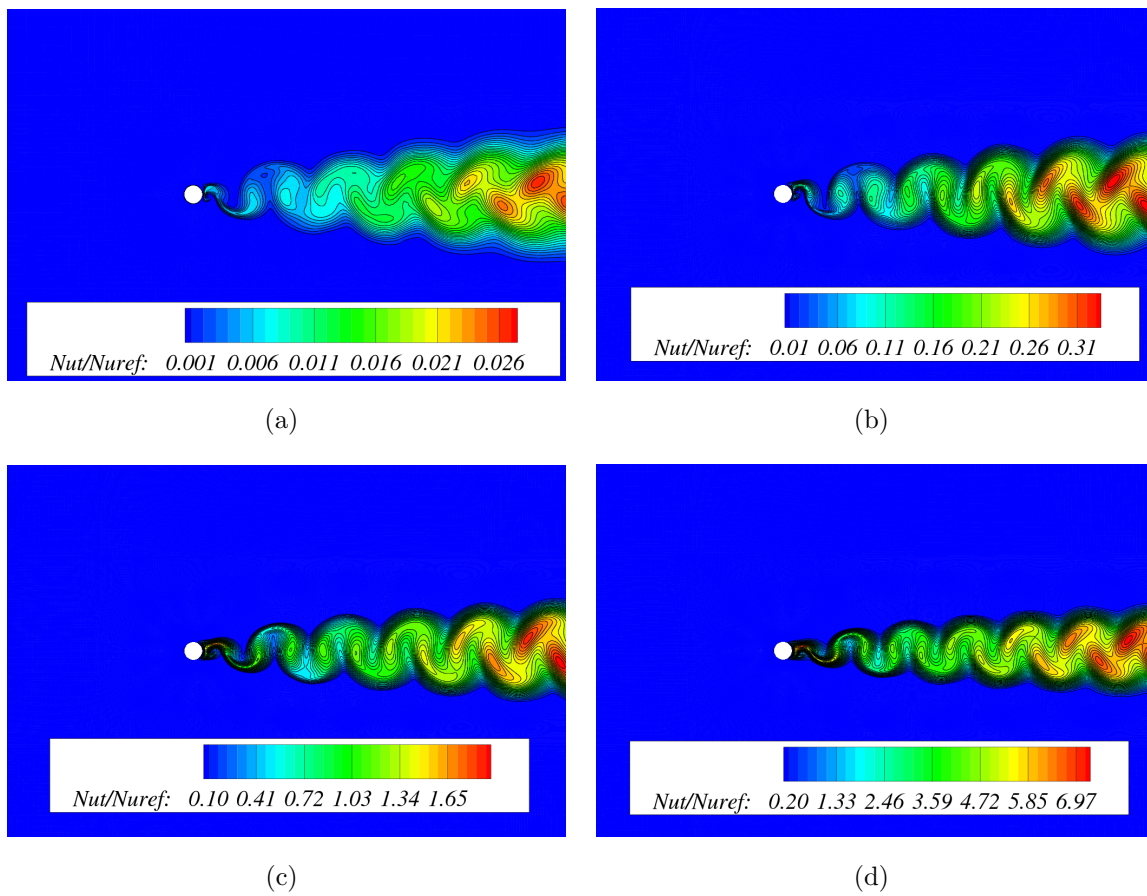


Figure 6.31: Field plots of normalized eddy viscosity,  $\nu_t/\nu$  at the point of largest lift coefficient. (a)  $Re = 1,000$ . (b)  $Re = 10,000$ . (c)  $Re = 100,000$ . (d)  $Re = 500,000$ .

## 6.6 Experimental Uncertainty

In order to proceed with a consistent validation procedure, the experimental uncertainties must also be determined. As it is quite rare to see experimental uncertainties in publications, the uncertainties estimation was conducted applying the procedure based on the Student-t distribution outlined in Chapter 5. Table 6.7 shows the experimental uncertainties for the drag coefficients in the steady laminar, unsteady laminar and turbulent ranges.

Table 6.7: Uncertainty estimation of the experimental drag coefficients by means of the standard deviations and variation coefficients, with a 90% level of confidence.

$Re$	$s$	$c(\%)$	$C_{Davg}$	$U_D$	$U_D/C_{Davg}(\%)$
5	0.77	17.00	4.54	3.44	75.87
10	0.10	3.38	2.93	0.44	15.08
20	0.005	0.24	2.10	0.02	1.05
30	0.02	0.94	1.88	0.079	4.20
40	0.02	1.22	1.74	0.09	5.45
50	0.01	0.43	1.63	0.03	1.93
100	0.01	0.97	1.41	0.06	4.34
200	0.004	0.27	1.31	0.02	1.20
1,000	0.01	0.85	0.99	0.04	3.81
10,000	0.07	6.08	1.11	0.11	10.24
100,000	0.04	3.30	1.23	0.05	3.89
500,000	0.11	30.04	0.37	0.13	35.34

## 6.7 Validation

Table 6.8 shows the results for the validation exercise concerning drag coefficients. In the laminar range, given that there were few experimental points for good experimental uncertainty estimation, one can consider that the results are validated, since either  $|E| < U_{val}$  or  $U_{val} > |E|$  by a small amount, mainly due to the larger experimental uncertainty. Also, the relative differences between the calculated and experimental values are so small that this is justified. However, for the turbulent calculations, the results are evidently not validated, since either  $|E| \gg U_{val}$  or experimental uncertainty overestimates the

validation uncertainty.

Table 6.8: Validation results for drag coefficients.

$Re$	$U_{val}$	$E$	Validated?
5	3.441	-0.09	Yes
10	0.44	0.12	Yes
20	0.02	0.04	Yes
30	0.08	-0.06	Yes
40	0.11	-0.13	Yes
50	0.03	-0.03	Yes
100	0.08	0.03	Yes
200	0.05	0.06	Yes
$1 \times 10^3$	0.08	0.44	No
$1 \times 10^4$	0.12	0.41	No
$1 \times 10^5$	0.06	0.39	No
$5 \times 10^5$	0.15	0.21	No

## 6.8 Final Remarks of the Chapter

A few comments can be made regarding the above results. Firstly, as stressed by Mittal & Balachandar (1995), Singh & Mittal (2005), beyond  $Re > 200$  the flow undergoes three-dimensional transitional instabilities, hence the two-dimensional computations tend to poorly represent the phenomena. The two-dimensional computations overestimate the drag and base suction due to a higher level of Reynolds stresses, which result in a shorter formation length behind the bluff body. More accurate modeling taking into account the important three-dimensional effects is addressed in the present work, as presented in the following Chapter.

Furthermore, in the cylinder-flow problem, very subtle aspects of laminar-turbulent transition play a crucial role and its improved modeling is required in the present context for a better agreement with the experiments. As a result of deficient transition-modeling, it is not possible to reproduce faithfully the instabilities of the shear layers and the correct separation point, in summary, the intricate interaction between free-shear layers, boundary layers and wake. That issue has been addressed in the present work and that shall be presented in the following Chapter.

In spite of several shortcomings of the  $k-\omega$  SST turbulence model in two-dimensional modeling, it is reassuring to find that many features of the flow indeed were captured by this approach. Firstly, the overall trends of all parameters were well captured, in-

cluding the qualitative behavior seen near the critical Reynolds numbers, which suggests that the drag crisis is mainly two-dimensional, as observed by Singh & Mittal (2005). Also, the qualitative aspects of the flow field and aspects such as the bifurcation of the Navier-Stokes equations leading to vortex-shedding, or also the secondary vortices associated with instabilities of the shear layer next to the separation. The evolution of the wake as  $Re$  is increased is also well represented, with its narrowing up to the drag crisis and shedding of less coherent vortices. Finally, in a qualitative manner, the evolution of the laminar-turbulent transition which is in fact reproduced by the  $k - \omega$  SST model somewhat earlier than in reality in terms of Reynolds number.

Table 6.9 presents a summary of the herein presented in tabular form. Figures 6.32, 6.33 and 6.34 show a summary of, respectively, the drag and RMS of lift coefficients and Strouhal numbers presented in this chapter in comparison with experimental results.

Table 6.9: Summary of numerical results for the cases presented herein.

$Re$	$C_{Davg}$	$C_{LRMS}$	$St$
5	4.44	-	-
10	3.05	-	-
20	2.18	-	-
30	1.82	-	-
40	1.61	-	-
50	1.48	-	-
100	1.38	0.23	0.17
200	1.38	0.50	0.20
1,000	1.41	0.87	0.23
10,000	1.52	1.12	0.24
100,000	0.84	0.43	0.25
500,000	0.58	0.22	0.28

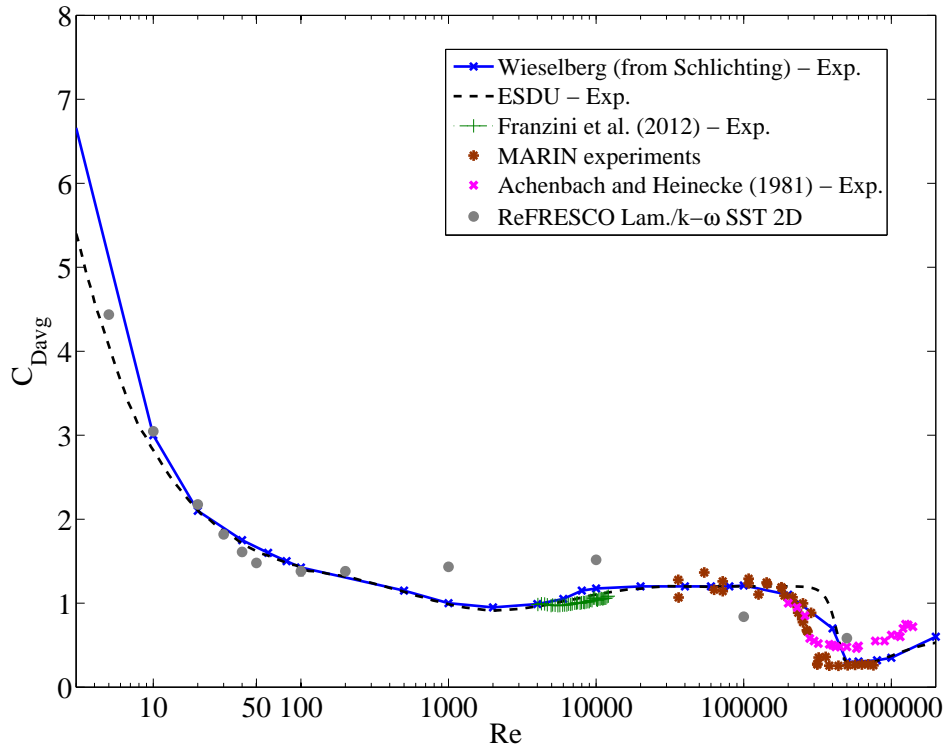


Figure 6.32: Drag coefficient results from the complete range of calculations. Experiments from Schlichting H. (2000), ESDU (1985), Franzini et al. (2012), Achenbach & Heinecke (1981) and from MARIN.

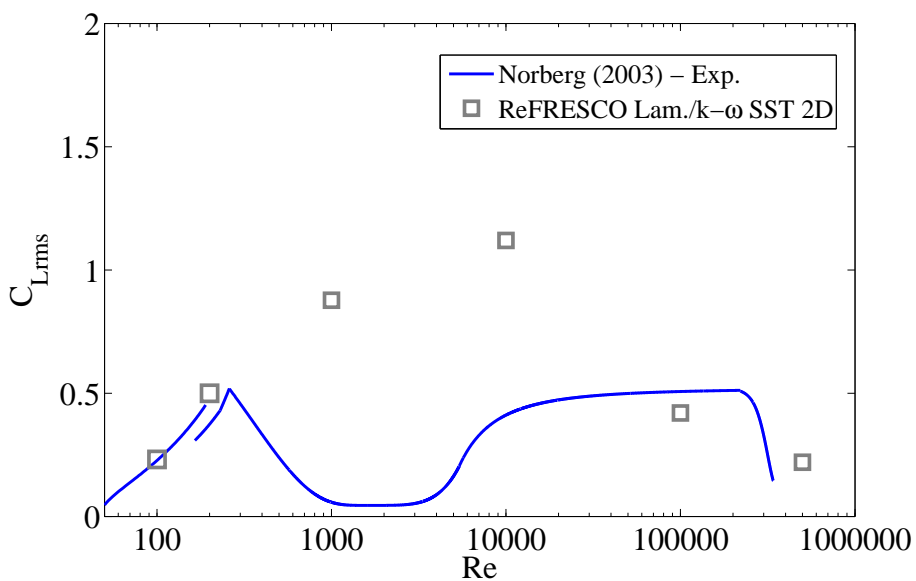


Figure 6.33: Drag coefficient results from the complete range of calculations. Experiments from Norberg (2003).

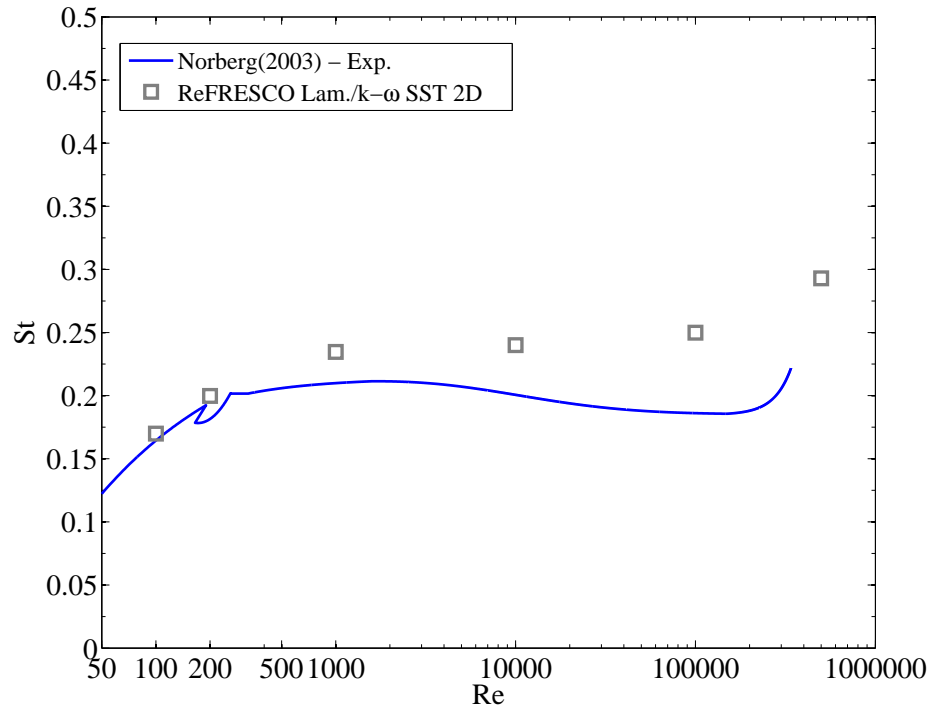


Figure 6.34: Drag coefficient results from the complete range of calculations. Experiments from Norberg (2003).



# Chapter 7

## The Rigid Fixed Cylinder Flow - Modern Modeling

*This chapter presents the improvements brought about by the new turbulence models implemented in ReFRESKO for the cylinder flow problem. Computations for Reynolds numbers ranging from 1,000 to  $7.57 \times 10^5$  will be presented. Three-dimensional and two-dimensional setups are respectively combined with Scale Adaptive Simulations and Local Correlation Transition Model. The numerical details and discretization studies are presented together with discussion regarding the improvements in flow prediction achieved by the new turbulence and transition models.*

*The objectives of this chapter are i) to delineate the capabilities of these state-of-the-art turbulence models for this problem; ii) systematically compare the results with the traditional modeling on a common basis; iii) consolidate the knowledge of these modern URANS models for the cylinder flow.*

### 7.1 Outline of the Calculations

The calculations with smooth fixed cylinder showed in this Chapter were carried out at Reynolds numbers from  $Re = 1,000$  to  $Re = 757,000$ , comprising the turbulent regime. Three main ranges are identified bearing in mind the capabilities of the turbulence models and the force quantification as their main quantitative aspect: range I comprises the laminar range, from  $Re = 1$  up to  $Re = 200$  (analyzed in the previous Chapter); range II ranges from  $Re = 1,000$  up to ca.  $Re = 100,000$ , in which the three-dimensional effects and instabilities play an important role in determining the loads; and finally the range

III, from ca.  $Re = 100,000$  up to  $Re = 757,000$ , in which boundary layer transition is the crucial aspect that determine the flow character and the forces.

In order to improve the computations and quantitative predictions obtained with the traditional modeling in range II, the newly implemented Scale Adaptive Simulation model is applied at  $Re = 1,000$ ;  $3,900$ ;  $20,000$ ;  $63,100$ ;  $100,000$ . In range III, the Local Correlation Transition Model is used at  $Re = 126,000$ ;  $252,000$ ;  $315,000$ ;  $506,000$ ;  $757,000$ .

## 7.2 Discretization Details

The domain outline and boundary conditions used in the calculations presented in this chapter are the same as used in chapter 6 being repeated here for convenience. Regarding the size of the domain, the inlet and lateral boundaries  $10D$  away from the cylinder axis and the outlet boundary can be located  $20D$  away from the cylinder. Figure 7.1 summarizes the calculation domain, the boundary conditions and the grid layout used in the two and three-dimensional calculations.

For the three-dimensional calculations done with the SST-SAS, the domain is four diameters long in the span-wise direction, whereas for the two-dimensional calculations there is only one cell in this direction. As for the results shown in chapter 6, the intermediate grids between the finest and the coarsest one are build by interpolation and for all the results with the finest grids,  $y^+ \leq 1$  in the nodes adjacent to the cylinder. The aspect ratio of these cells in the tangential direction has been kept low, up to ca. 5, so that  $x^+$  is also low. For the three-dimensional calculations done with SAS, grids from 6,048,950 to 18,558,208 cells are used, being generated by extrusion from fine two-dimensional ones, in which either 25 or 32 layers of cells were generated in the  $z$ -direction, thus dictating higher  $z^+$  values than for  $x^+$  and  $y^+$  due to clear limitation in grid sizes.

In the two-dimensional calculations with LCTM, four to six grids were used in each Reynolds numbers, with the number of cells ranging from approximately 469,376 (coarsest grid for  $Re = 63,100$ ) to 1,780,832 cells (finest grid for  $Re = 757,000$ ). The  $y^+$  and  $x^+$  values are kept the same as previously.

The finest grid and time step for each Reynolds number were evidently the ones of interest for analysis, but the results obtained with the coarser grids and time steps were useful to carry out the convergence analysis and derive the numerical uncertainties for the two-dimensional calculations.

It is worth pointing out that the two dimensional calculations showed in this chapter took

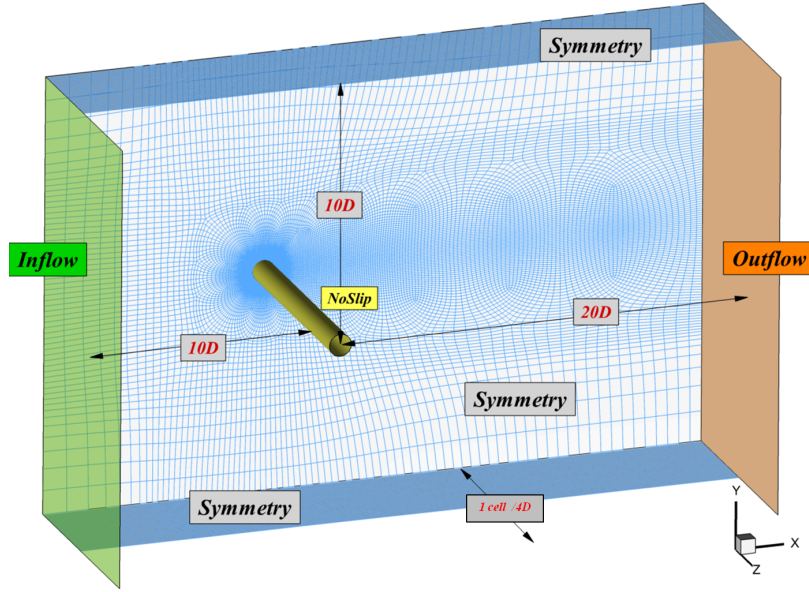


Figure 7.1: Grid and domain used in the calculations.

from a few weeks (with the coarse discretization) up to several weeks in the HPC cluster when the finest calculations were done due to the adopted strict convergence criteria. The three dimensional calculations took up to 5-6 months in the same cluster.

### 7.3 Scale Adaptive Simulations

Previous studies with ReFRESH (VAZ et al., 2007; PENGAN, 2010; KLAIJ, 2008) have shown small differences between two-dimensional and three-dimensional calculations with  $k-\omega$  SST for Reynolds numbers between  $Re = 10^4$  and  $Re = 10^5$ .

Conversely, Pereira, Vaz & Eça (2015) have shown that for a lower Reynolds number ( $Re = 3,900$ ), there are differences between two-dimensional and three-dimensional modeling with the same model. The same work also shows some variations due to changing boundary conditions from symmetry to cyclic at the top and bottom boundaries, but with a smaller extent. It has been argued that the observed behavior is associated in a lesser extent with turbulent fluctuations than with low frequency three-dimensional large-scale fluctuations. In that publication, the average drag coefficient with two-dimensional calculations is  $C_{Davg} = 1.642$ , whereas three-dimensional calculation produced  $C_{Davg} = 1.258$  with symmetry boundary conditions on the top and bottom boundaries and  $C_{Davg} = 1.206$  with cyclic boundary condition (the two latter with the same grid). A difference of ca. 25% from two-dimensional to three-dimensional modeling is thus observed, whereas the change in boundary condition produced a change of ca. 4%.

These observations combined with the analysis conducted in range II, which indicated that the physics is particularly sensitive to three-dimensional nature of the flow, motivated the implementation of the SST-SAS model. This model was applied as it is based on the SST and improves its modeling with little additional computational costs compared with 3D SST.

It is also worth noting that the traditional SST behavior is observed for the SST-SAS model with two-dimensional or steady state calculations and also for grids which are not very refined, which explains the convenient choice made herein. This section shows the results obtained with the three-dimensional calculations with the Scale Adaptive Simulation model implemented in ReFRESH for this thesis.

### 7.3.1 Solution Verification

#### 7.3.1.1 Iterative Convergence

Regarding iterative convergence criteria, normalized residuals of all quantities in the infinity norm below  $10^{-4}$ , i.e.  $L_\infty < 10^{-4}$ , as the example in figure 7.2 shows. Convergence to such levels is troublesome, mainly due to the very extended calculation times as the momentum equations in the z-direction are also solved.

#### 7.3.1.2 Convergence Analysis

A convergence analysis has been conducted for the SAS calculations based on different time steps and grids. As calculations lasted for several weeks, the convergence analyses were not done for all the Reynolds numbers, but instead in groups: for  $Re = 1,000$  and  $Re = 3,900$ , the analysis was done at  $Re = 3,900$ ; for  $Re = 20,000$ ,  $Re = 63,100$  and  $Re = 100,000$ , at  $Re = 100,000$ .

Figure 7.3 shows this sensitivity analysis. Apparently, for such finely discretized grids there is lower sensitivity than for the time steps. It has been noticed that the time-step refinement greatly increases the resolution of turbulent structures and thus the force results. Tables 7.1 and 7.2 show, respectively, the characteristics of the finest grids and time steps used for the SAS calculations. As commented above, these three-dimensional grids were constructed by extrusion from two-dimensional grids and the finest grids had 32 layers of cells in the z-direction.

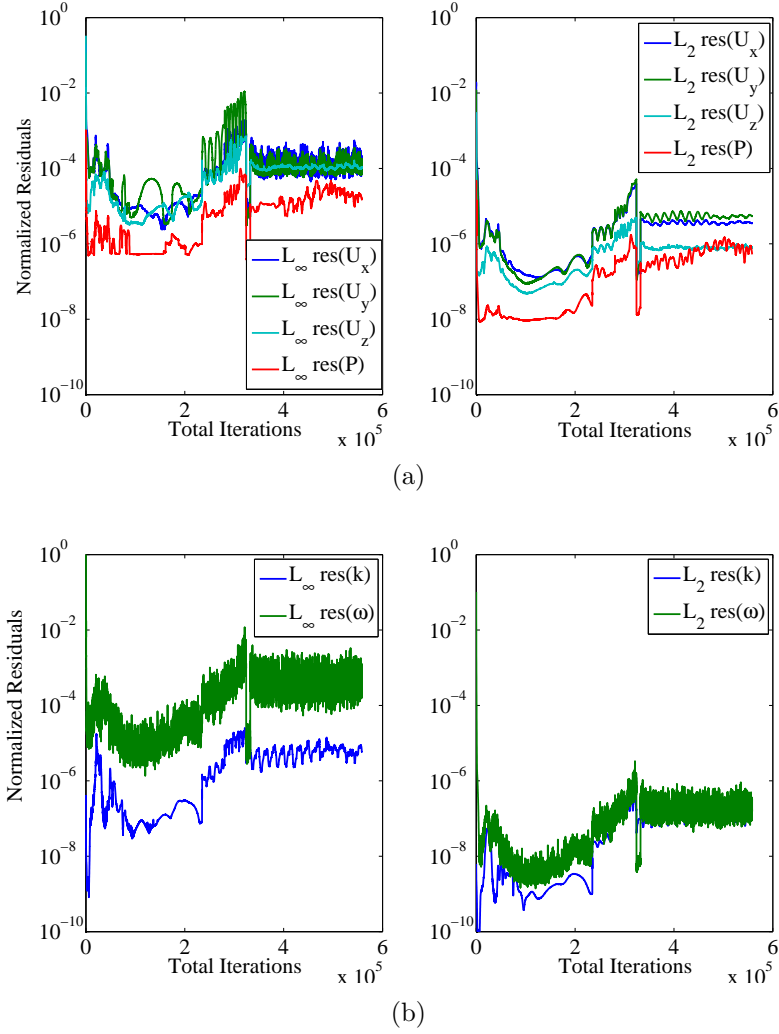


Figure 7.2: Infinity and RMS norms for evaluating the residuals of the flow quantities in the case  $Re = 6.31 \times 10^4$ . (a) Velocities and pressure. (b) Turbulent kinetic energy and turbulent frequency. Illustration of typical iterative convergence obtained for three-dimensional calculations.

Table 7.1: Details of the finest grids used for the turbulent calculations.

$Re$	Number of Cells	Circumferential Cells	$y_{max}^+$
1,000	12,439,296	2,219	0.38
3,900	12,439,296	2,219	1.01
20,000	18,558,208	2,900	0.1
63,100	18,558,208	2,900	1.09
100,000	18,558,208	2,900	1.21

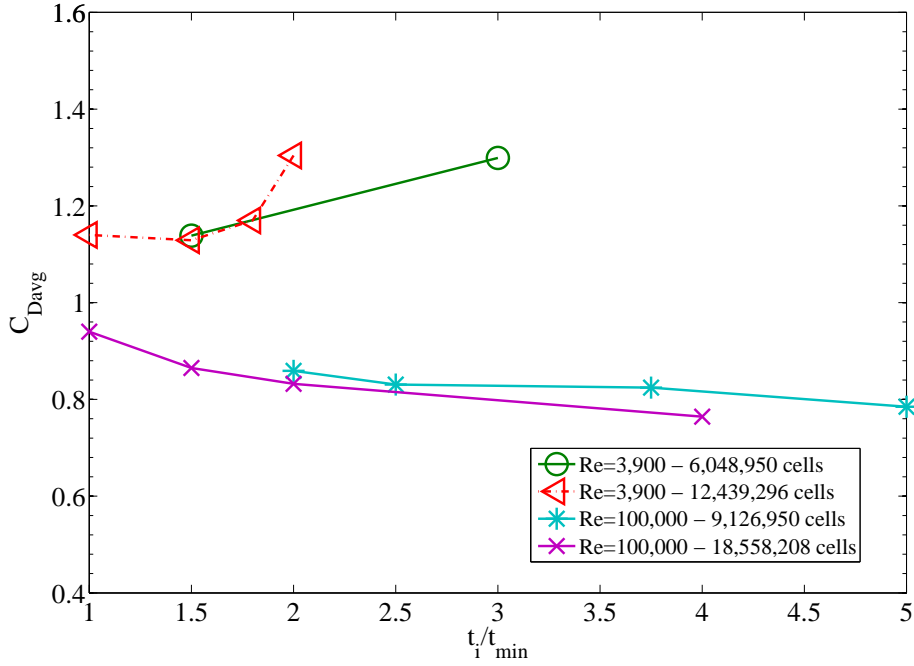


Figure 7.3: Convergence studies for the SAS calculations at  $Re = 3,900$  and  $Re = 100,000$ . The different lines represent calculations done with the same grids and the finest time steps are denoted by  $t_i/t_{min} = 1$ .

Table 7.2: Finest time discretization for the SAS calculations.

$Re$	Time Steps per Shedding Cycle
1,000	300
3,900	140
20,000	250
63,100	500
100,000	495

### 7.3.2 Improved Flow Prediction in Range II

Figures 7.4 and 7.5 show the time traces of drag and lift coefficients and their power spectra for, respectively,  $Re = 20,000$  and  $Re = 100,000$ . A decrease in the regularity is seen in the higher Reynolds number, reflecting the higher level of turbulent behavior. The strongest peaks in both cases correspond to the Strouhal frequencies and some energy is spread near those frequencies in both cases.

The improvement in drag coefficient prediction is seen in figure 7.6, which shows the coefficients for  $Re = 1,000$ ;  $Re = 3,900$ ;  $Re = 20,000$ ;  $Re = 63,100$ ;  $Re = 100,000$ . The results are improved when compared to the two-dimensional SST results, but the comparison is still not satisfactory for  $Re = 1,000$  and for  $Re = 100,000$ . For the latter, it is observed that boundary-layer transition plays a role as it is nearly at the critical transition region.

The SAS model shows nearly as poor performance in this Reynolds number as the two-dimensional SST and more advanced models, as the LES, DES, PANS etc. In fact, small improvements have been reached at the Reynolds numbers where boundary layer transition is decisive, as seen in Catalano et al. (2003), Sampaio & Coutinho (2000), Tremblay (2001).

It seems that the instabilities observed in the final portion of the shear-layer transition regime are not properly captured due to low grid resolution near the wall and, even due to the application of wall functions. Figure 7.6 also shows a less “smoothed” trend compared to SST.

The RMS values of the lift coefficients are presented in figure 7.7, in which similar behavior is observed: less correlated vortices cause weaker vortices and thus lift forces, decreasing the RMS to smaller values than in the two-dimensional calculations.

In that sense, there is an important difference between results with two-dimensional SST and three-dimensional SST-SAS, nearly 50% decrease in the Reynolds numbers between  $Re = 3,900$  and  $Re = 20,000$ , in much better comparison with the experiments in that range. This behavior has also been mentioned in Carmo et al. (2012) and Shur et al. (2005): the very low observed experimental lift amplitudes, down to  $C_L \approx 0.25$ , are quite difficult to match with applying different turbulence approaches. This situation is critical when laminar separation takes place and when large portion of the shear layer is laminar; as Reynolds numbers increase, the agreement with experimental lift coefficients is much better and even two-dimensional simulations become increasingly better compared to the experimental values.

The Strouhal numbers are presented in figure 7.8, in which a small improvement is seen compared to the two-dimensional calculations, which already showed a fair agreement with the experimental trends.

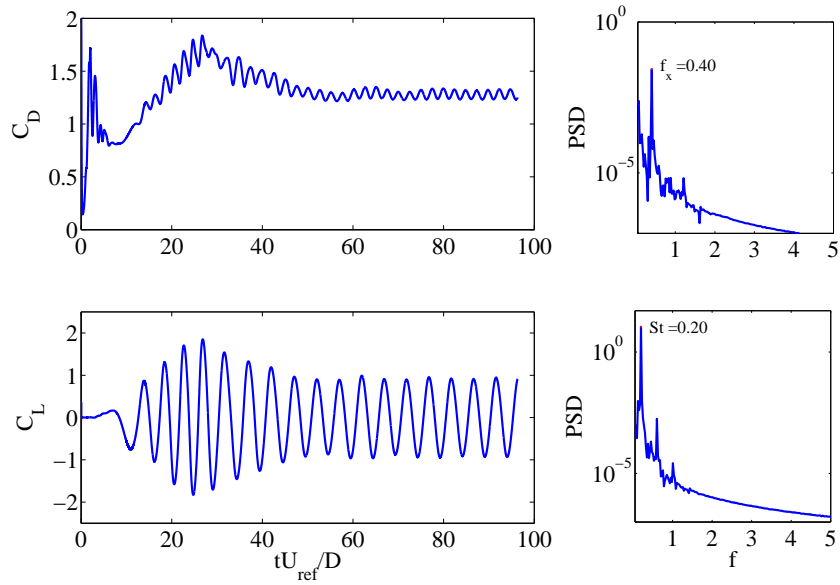


Figure 7.4: Drag and lift time traces and power spectrum densities from calculation with finest grid and time step for  $Re = 20,000$  with three-dimensional SST-SAS. The steady-state portion is used for the statistics.

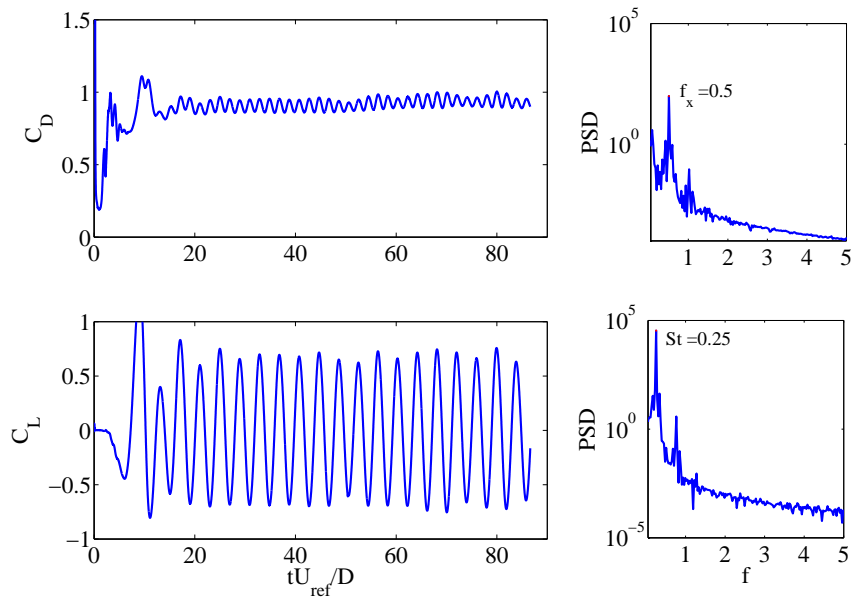


Figure 7.5: Drag and lift time traces and power spectrum densities from calculation with finest grid and time step for  $Re = 100,000$  with three-dimensional SST-SAS. The steady-state portion is used for the statistics.

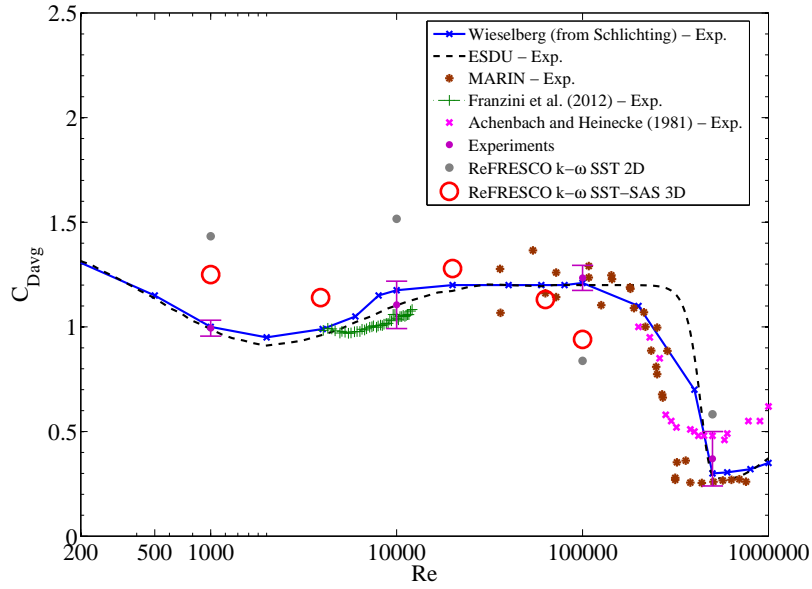


Figure 7.6: Drag coefficients from calculations with three-dimensional SST-SAS compared to two-dimensional SST results and experiments from Schlichting H. (2000), ESDU (1985), Franzini et al. (2012), Achenbach & Heinecke (1981) and from MARIN.

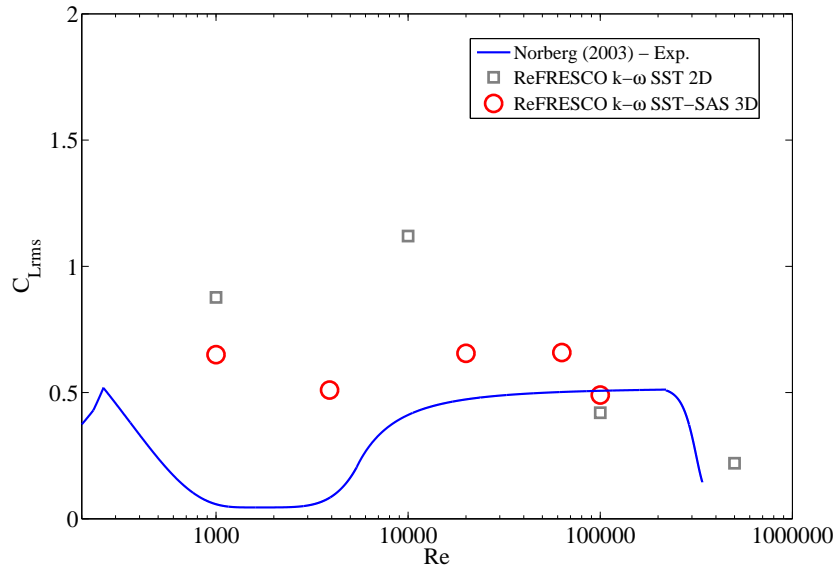


Figure 7.7: Strouhal number results from three-dimensional SST-SAS and two-dimensional SST models. Experimental values from Norberg (2003).

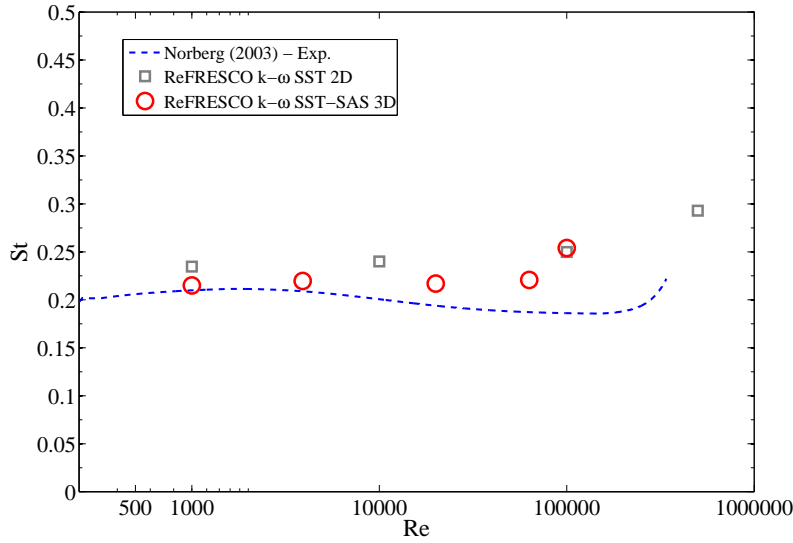


Figure 7.8: Strouhal numbers from calculations with three-dimensional SST-SAS compared to two-dimensional SST results and experiments from Norberg (2003).

Figure 7.9 shows a comparison of flow fields obtained with ReFRESCO using two-dimensional SST (PEREIRA; VAZ; EÇA, 2015), three-dimensional SST (PEREIRA; VAZ; EÇA, 2015) and three dimensional SST-SAS for  $Re = 3,900$ <sup>1</sup>. In these plots, Q-criterion isosurfaces ( $Q = \frac{1}{2}(W^2 - S^2)/\|[S]\|^2 = 0.2, 0.5, 1.0$ ) colored with nondimensional stream-wise velocity is shown. Obviously, the two-dimensional calculation in the first plot present prismatic flow structures in the span-wise direction, thus very different from the three-dimensional results.

The second plot shows that even the three-dimensional calculation done with the SST already enables the solver to capture quite a few three-dimensional structures, whereas the SST-SAS calculation shown in the third plot presents somewhat finer three-dimensional structures and larger variation of the flow velocity in the depicted isosurfaces.

The practical aspect of these results is that there should be an improvement of the calculated flow quantities due to the enhancement of the flow calculation.

In fact, for the two-dimensional calculation, Pereira, Vaz & Eça (2015) reported for their finest grid  $C_{Davg} = 1.642$ ; for the three-dimensional calculation, Pereira, Vaz & Eça (2015) reported the value  $C_{Davg} = 1.309$  with the finest grid; for the results presented herein with SST-SAS, a value of  $C_{Davg} = 1.14$  was obtained showing an improved comparison with the experimental value of figure 7.6,  $C_{Davg} = 0.99$ .

<sup>1</sup>As commented above, Pereira, Vaz & Eça (2015) have also reported on the differences between different boundary conditions for the top and bottom boundaries, however for the sake of this analysis, only the results obtained with symmetry conditions are presented.

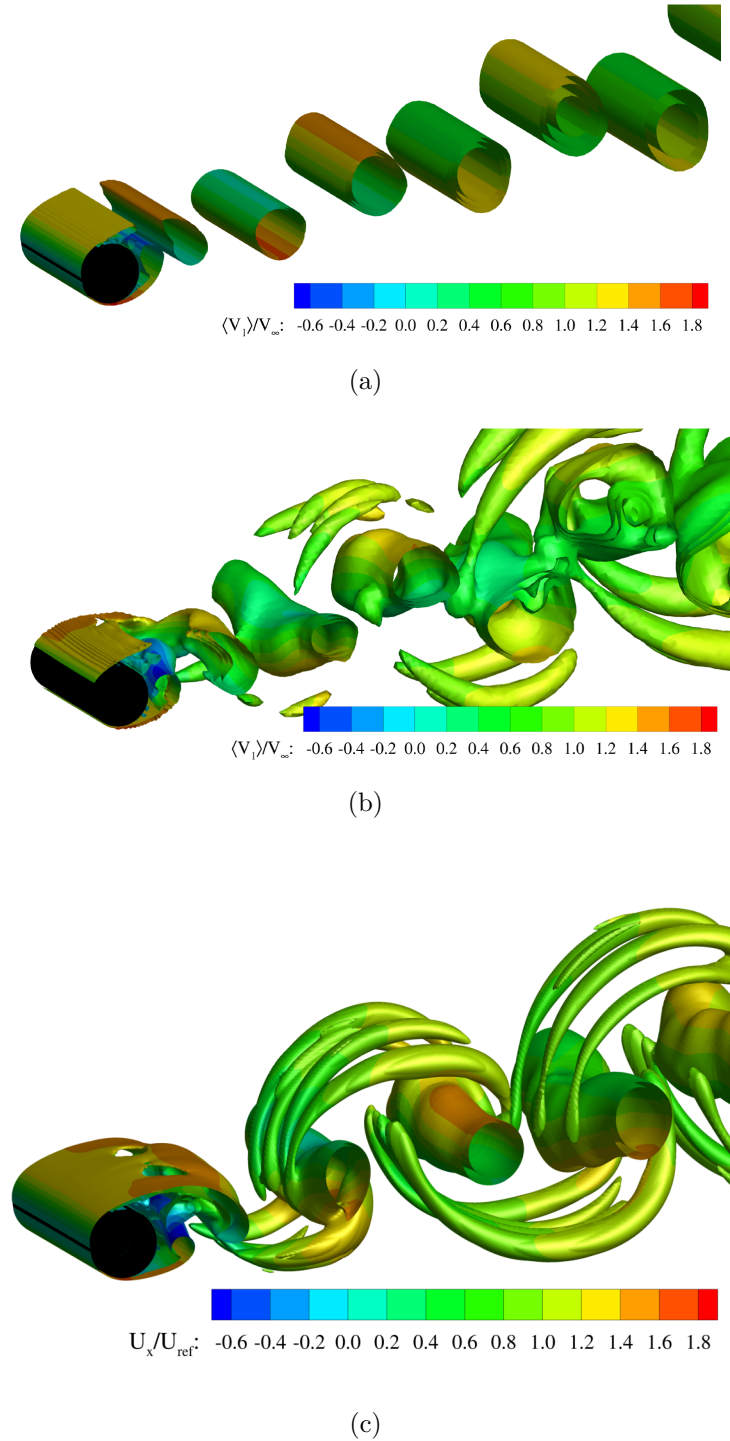


Figure 7.9: Q criterion isosurfaces ( $Q = \frac{1}{2}(W^2 - S^2)/\|S\|^2 = 0.2, 0.5, 1.0$ ) colored with nondimensional longitudinal velocity for calculations at  $Re = 3,900$  with ReFRESCO. (a) Two-dimensional calculations with SST model extracted from Pereira, Vaz & Eça (2015). (b) Three-dimensional calculations with SST model extracted from Pereira, Vaz & Eça (2015). (c) Present SST-SAS calculations.

Figures 7.10 and 7.11 show  $Q$ -criterion isosurfaces colored by nondimensional eddy viscosity and turbulence intensity, respectively for  $Re = 3,900$  and  $Re = 20,000$ . In the former, one notices low turbulence intensity and eddy viscosity values whereas, in the latter, the turbulence intensity and eddy viscosity near the body is much larger, indicating that transition moved upstream from wake, as commented above. Moreover, finer and more three-dimensional flow structures are observed in the larger Reynolds number. It is further interesting to notice in both figures that one can relate eddy viscosity and turbulence intensity according to the colors: the practical rule of relating normalized eddy viscosities above 10 to high turbulence seems a fair approximation in these cases.

Figure 7.12 shows the activation of the nondimensional SST-SAS term in equation 3.20,  $Q_{SAS}$  for  $Re = 20,000$  and  $Re = 20,000$ . Finer structures are seen in the latter due to the more developed turbulence and smaller turbulent scales. Also, much larger eddy viscosity is observed, again due to the larger Reynolds number. As commented by Carmo et al. (2012), SAS term acts lowering the eddy viscosity in those regions, thus decreasing dissipation and allowing the smaller scales to develop.

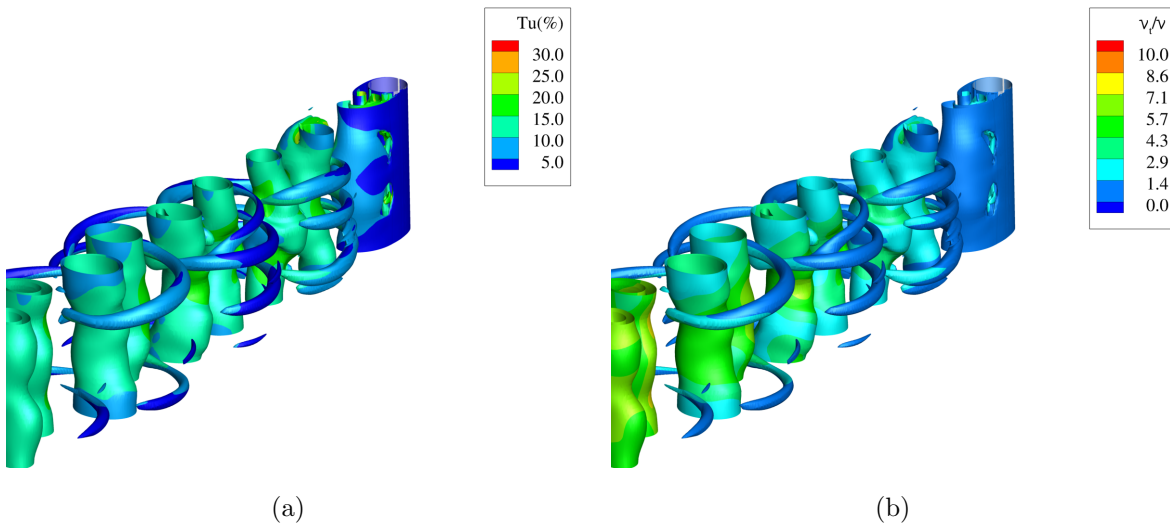


Figure 7.10:  $Q$ -criterion iso-surfaces ( $Q = \frac{1}{2}(W^2 - S^2)/\|[S]\|^2 = 0.2, 0.5, 1.0$ ) for  $Re = 3,900$ : (a) colored by turbulence intensity and (b) colored by nondimensional eddy viscosity.

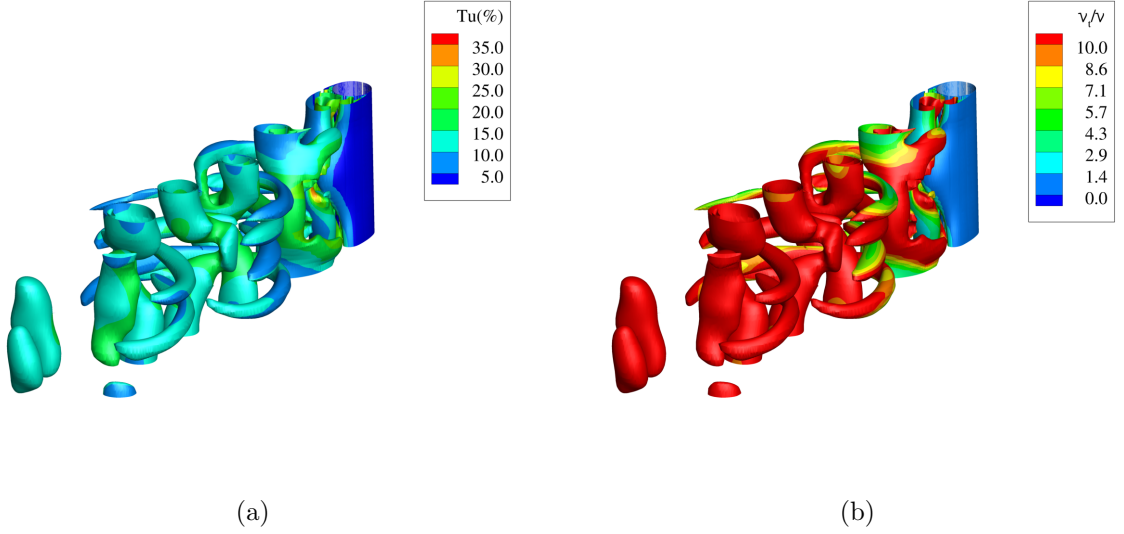


Figure 7.11: Q-criterion iso-surfaces ( $Q = \frac{1}{2}(W^2 - S^2)/\|S\|^2 = 0.2, 0.5, 1.0$ ) for  $Re = 20,000$ : (a) colored by turbulence intensity and (b) colored by nondimensional eddy viscosity.

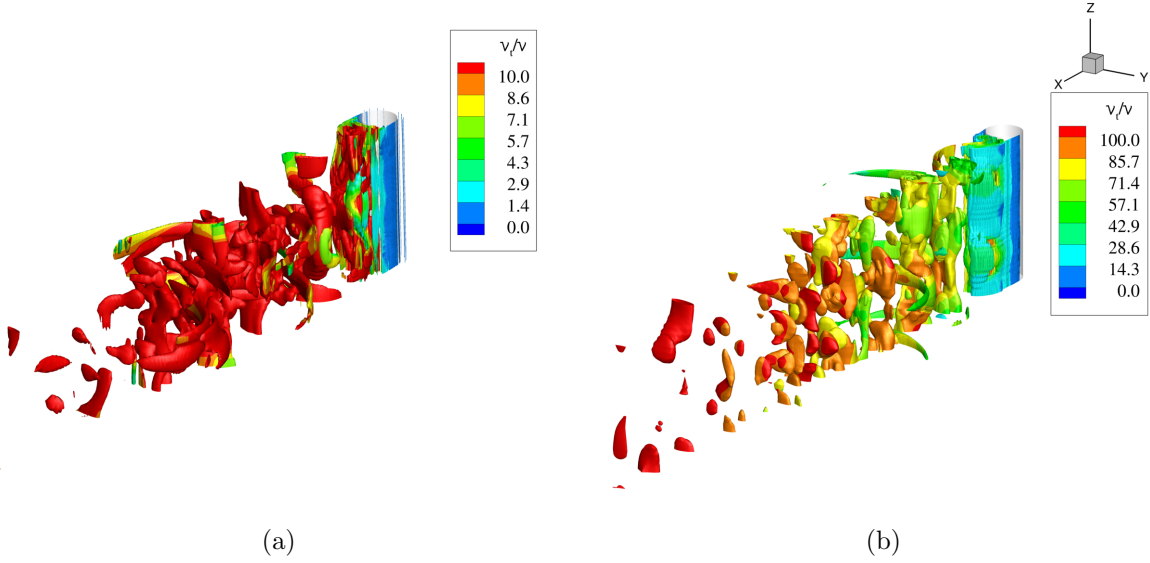


Figure 7.12: Activation of the SST-SAS term in equation 3.20,  $Q_{SAS}$ . Iso-surfaces with ( $Q_{SAS} D^2 / U_{ref}^2 = 0.2, 0.5, 1.0$ ) colored by nondimensional eddy viscosity for: (a)  $Re = 20,000$  and (b)  $Re = 100,000$ .

## 7.4 Local Correlation Transition Model

This section presents the improvements on the prediction of the flow achieved by using the LCTM, in comparison with the benchmark results obtained with SST in range III. As pointed out above, in this range boundary layer transition is a crucial aspect of the flow, strongly influencing the drag loads and upbringing a larger two-dimensional character to the flow. The modeling is thus two-dimensional, in a similar fashion as done with the SST.

### 7.4.1 Background Work for the LCTM

An extensive investigation of the implementation and performance of the LCTM for the flat-plate flow over a wide range of Reynolds numbers has been done prior to the cylinder application and that is described in Appendix A. As it is for a different application, the contents of that study are not included herein in detail, but the main findings and conclusions are important for the present work.

It has been concluded in that study that uncertainties are somewhat higher than using only the SST model without the LCTM. This issue has showed true for the present application as well, driving grids and time steps to be much finer than in the calculations in Chapter 6, especially for the uncertainty estimation. Also, it has been noticed in Appendix A that fine tangential discretization is needed for the correct estimation of transition onset and length.

In the present work, a very fine discretization of the near wall region has been achieved by means of the nested refinement technique. One could also improve the refinement with stretching towards known separation or transition regions in the cylinder, but that would require a grids specific for each case with changing stretching factors and would result in a different research direction, therefore, was not pursued in this work.

### 7.4.2 Outline of the Calculations

Calculations with the LCTM were done for the following Reynolds numbers in range III:  $Re = 126,000; 252,000; 315,000; 506,000; 757,000$ .

Three grids combined with three time steps were used for the calculations in each Reynolds numbers, with the number of cells ranging from approximately 1,195,800 to 1,780,000 cells (the grids are constructed from the ones used before). The finest grids and time

steps were used to obtain the results showed in the sequel. The results obtained with the coarser grids and time steps were useful to perform the uncertainty analysis and derive the numerical uncertainties showed later.

The details of the finest grids and time steps used in the calculations are showed in table 7.3.

As done in the previous sections, initialization of turbulence is done by setting the eddy viscosity as 1% of the laminar viscosity at the inflow boundary (very low values) and field.

Table 7.3: Details of the finest grids and the number of time steps in each shedding cycle used for the calculations.

$Re$	Number of Cells	$y^+$	Steps/Shedding Cycle
128,000	1,195,746	0.18	393
252,000	1,542,800	0.26	329
315,000	1,542,800	0.30	791
506,000	1,780,832	0.46	984
757,000	1,780,832	0.81	984

### 7.4.3 Verification

#### 7.4.3.1 Iterative Convergence

Round-off and iterative errors ought to be kept to a minimum when applying the approach to estimate uncertainty, in order to isolate discretization errors from the former ones. Round-off errors are minimized by using double precision. Regarding iterative errors, the transition model normally causes iterative convergence to be quite difficult. Bearing upon this fact, the following criteria was set: for momentum, pressure and turbulence equations,  $L_{inf} < 10^{-5}$  and, for transition equations,  $L_{inf} < 10^{-3}$  as showed in the example of figure 7.13.

#### 7.4.3.2 Numerical Uncertainty

The grid convergence and uncertainty properties of the calculations done with the LCTM are analyzed focusing on the drag coefficient  $C_D$ .

Table 7.4 shows, for each Reynolds number, the average drag coefficients ( $C_{Davg}$ ) in the

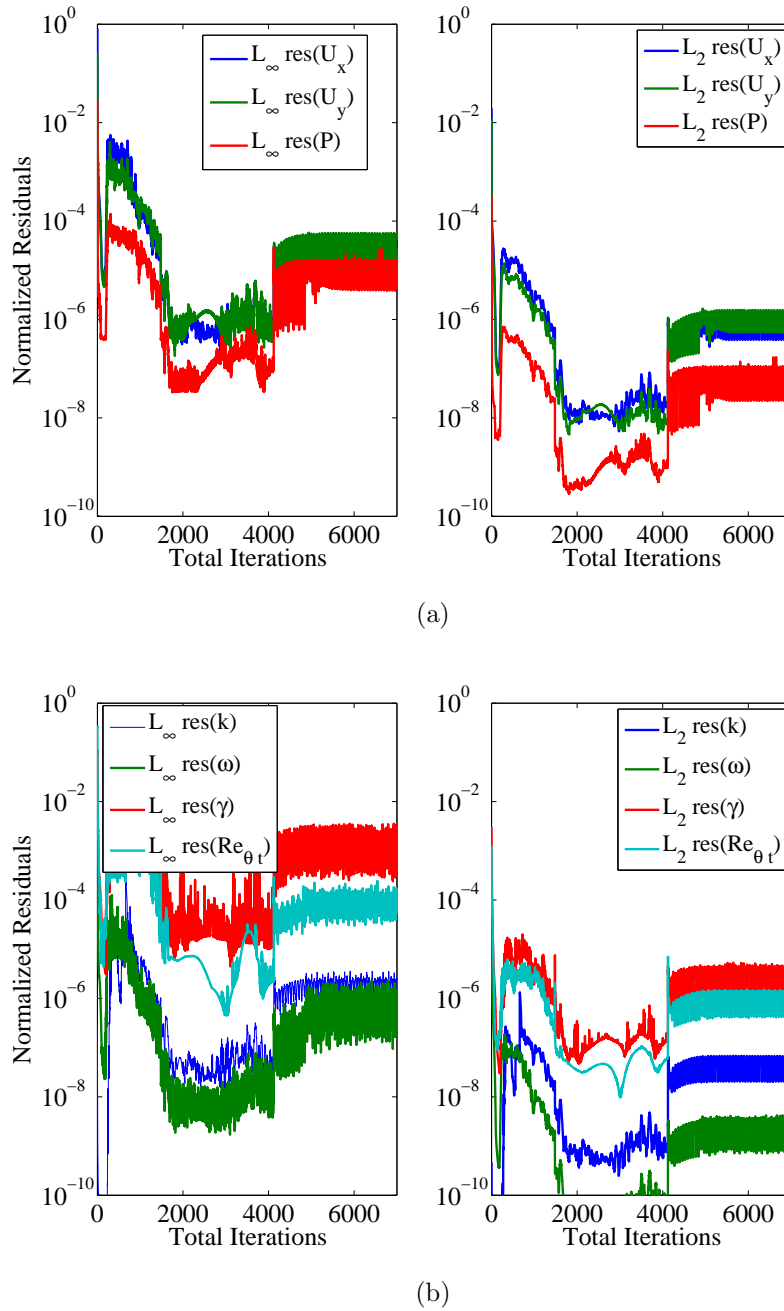


Figure 7.13: Infinity and RMS norms for evaluating the residuals of the flow quantities in the case  $Re = 757,000$  with the finest grid. (a) Velocities and pressure. (b) Turbulent kinetic energy ( $k$ ), turbulent frequency ( $\omega$ ), intermittency factor  $\gamma$  and the correlation  $Re_{\theta_t}$ . Typical iterative convergence obtained for the calculations of the present work.

finest calculations (at least ten cycles are used to define it, in which highly regular traces were found for the forces).

The uncertainties are under 10% upbringing that the values showed herein are at most up to near 10% from the “exact” solution that the mathematical model is able to obtain, with a 95% probability (which is the confidence level of the uncertainty estimation procedure).

Figure 7.14 shows the grid and time-step convergence characteristics of the drag coefficient for  $Re = 757,000$ . Second order convergence in time is observed, whereas first order in space is noticed.

Table 7.4: Uncertainty estimation and order of convergence for the calculations.

$Re$	$C_{Davg}$	$U(C_{Davg})(\%)$	$p_x$	$p_t$
128,000	1.12	3.5	1	2
252,000	0.89	6.1	2	1
315,000	0.75	9.6	2	1
506,000	0.52	2.1	2	2
757,000	0.40	6.7	1.1	0.8

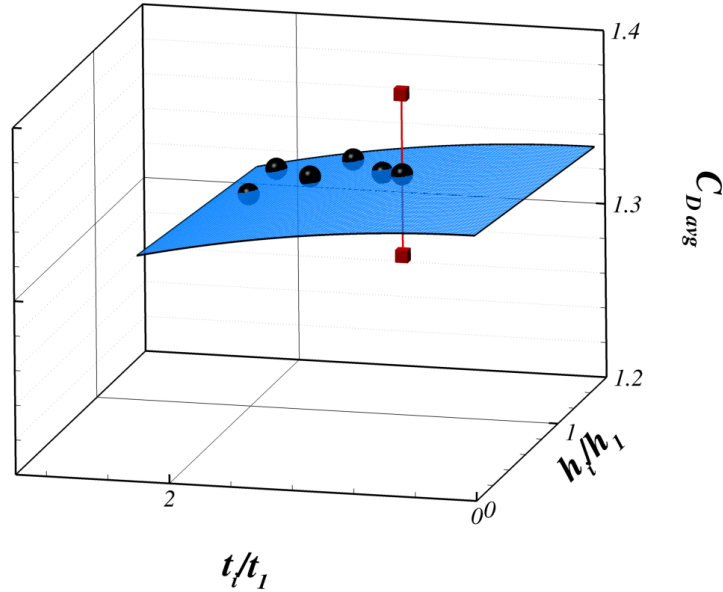


Figure 7.14: Example of grid and time step convergence of drag coefficients for  $Re = 128,000$  calculated with LCTM. The space convergence order is  $p_x = 1.0$ , whereas convergence order in time is  $p_t = 2.0$ .

#### 7.4.4 Improved Flow Prediction in Range III

In this section, the improvements on the prediction of the flow achieved by using the LCTM coupled with SST are presented for range III.

Figure 7.15 shows an example of the drag and lift coefficients traces and power spectra, in which a noteworthy similarity is noticed in the regularity of the solution when compared to the previous two-dimensional SST results. In fact, as shall be seen below, the LCTM

mainly changes transition location, without strongly altering the character of the solution compared to SST.

Figure 7.16 shows the drag coefficients calculated with the LCTM, in comparison with results obtained with SST, and experimental results. Note that experimental and numerical uncertainties with SST are calculated at Reynolds numbers similar to the ones showed herein, for which a V&V exercise has been presented above.

In particular, figure 7.16 shows that there is much better agreement between LCTM and experiments than between SST and the same experimental value, owing to the better prediction of transitional characteristics of the flow in the drag crisis region. It seems that SST tends to smooth out the drag coefficient curve and its values drop at around  $Re = 10,000$ , whereas the LCTM results remain at high values up to nearly  $Re = 100,000$ , presenting a much sharper dip of the drag coefficients curve than with the SST.

The improvement of drag prediction in the drag crisis region occurs due to an improvement in predicting the transition onset and length. More accurate prediction of the transition improves the prediction of boundary layer separation, a crucial aspect in cylinder flow dynamics, as most of the drag load is due to pressure forces.

It has been shown above that, using the SST (and most of the traditional turbulence models) the cylinder wake, shear layers and boundary layer turn turbulent at least one order of magnitude earlier in terms of Reynolds number than what is seen in the experiments. That is natural, since the SST was developed to deal with fully turbulent and not transitional flows.

Figure 7.17 shows the RMS of the lift coefficients calculated with the LCTM in comparison with the SST results and experimental values from Norberg (2003). There is not a clear improvement of the results compared to experiments at the lowest Reynolds number,  $Re = 126,000$ , with the LCTM over SST, whereas for the higher Reynolds numbers the agreement is better.

It seems that the lift coefficient is better predicted by the three-dimensional methods than two-dimensional and transition influences the drag loads more heavily than the lift. Figure 7.18 presents the Strouhal numbers obtained from the lift time traces calculated with the LCTM in comparison with the SST results showed before.

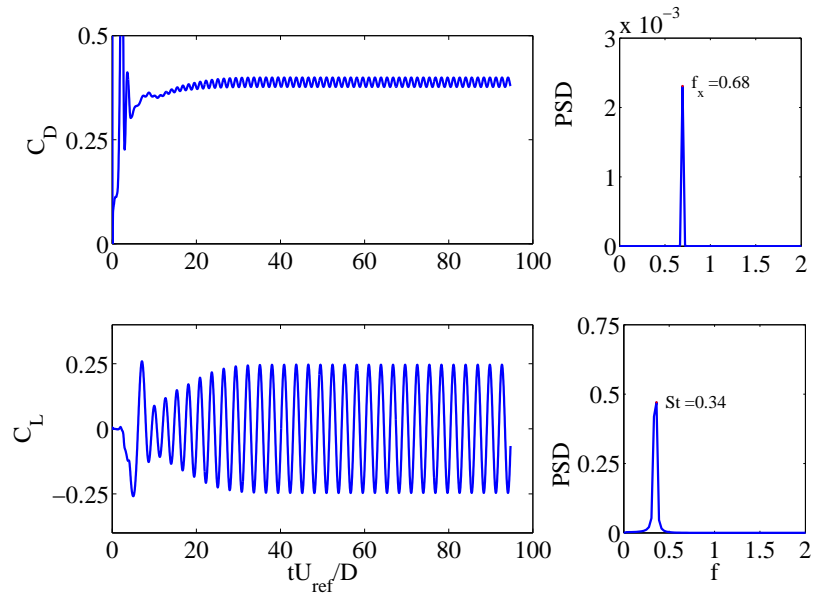


Figure 7.15: Drag and lift time traces and power spectrum densities from calculation with finest grid and time step for  $Re = 757,000$  with two-dimensional LCTM. The steady-state portion is used for the statistics.

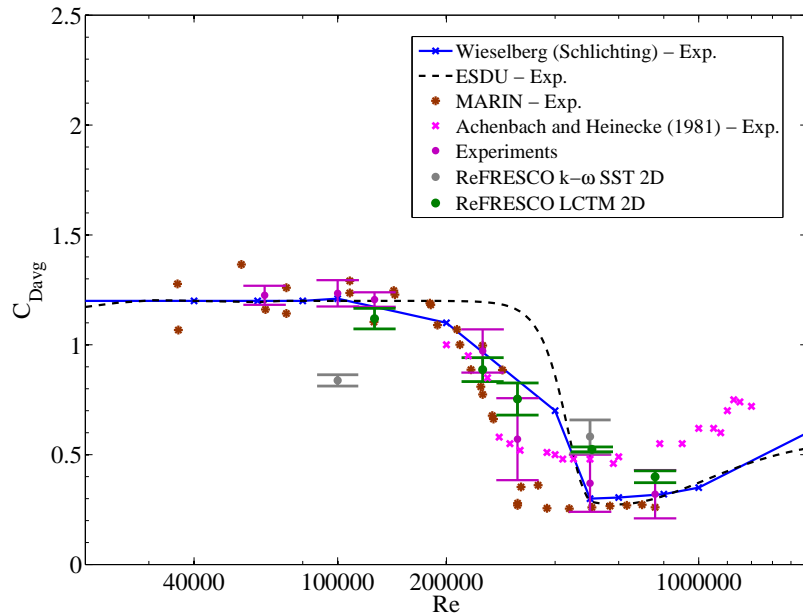


Figure 7.16: Drag coefficients for the present calculations with the LCTM in comparison with experiments from Schlichting H. (2000), ESDU (1985), Achenbach & Heinecke (1981), kindly contributed by MARIN and with previous numerical results shown in this thesis.

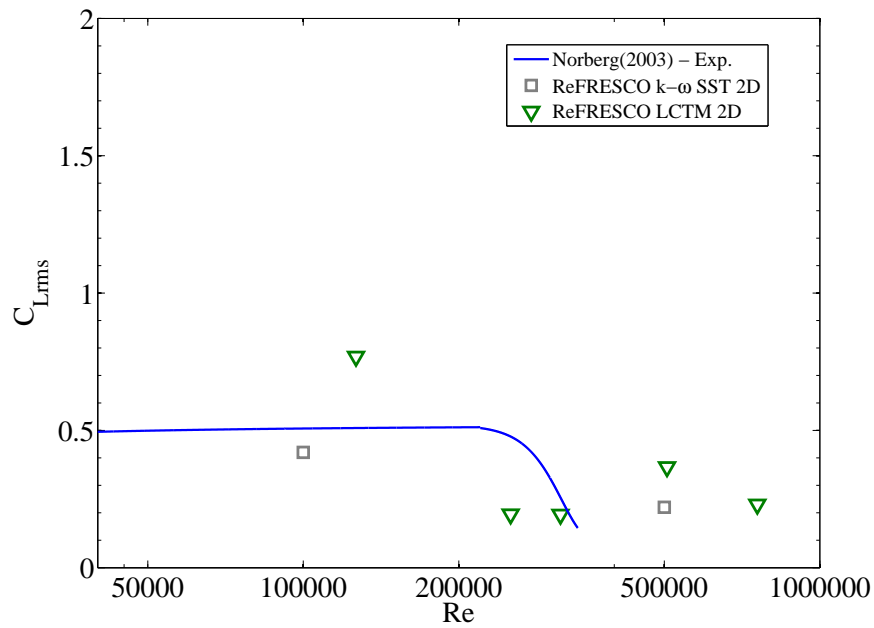


Figure 7.17: RMS of lift coefficients for the present calculations with the LCTM compared with experiments from Norberg (2003) and with previous numerical results shown in this thesis.

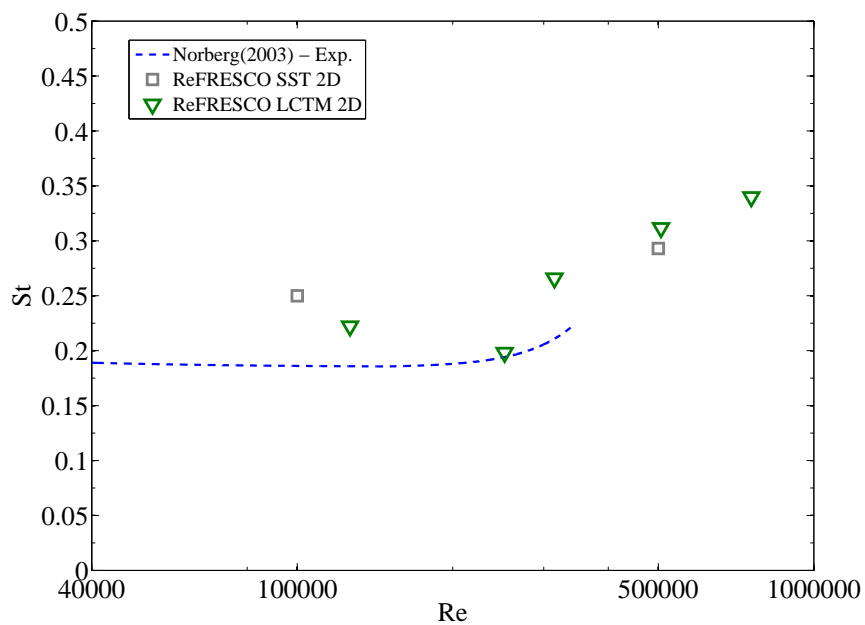


Figure 7.18: Strouhal numbers for the present calculations with the LCTM compared with experiments from Norberg (2003) and with previous numerical results shown in this thesis.

### 7.4.5 Flow Analysis

Figure 7.19 shows field plots for the finest calculation with  $Re = 128,000$ : the non-dimensional eddy viscosity is presented on the left-hand side and the intermittency on the right. The lower figures show a closer look of the transition regions of the top ones. The average separation angle measured counterclockwise from the back has been determined as  $\theta_{sep} = 92.00$ , whereas roughly at 90 degrees, the intermittency reaches 1.0 within the boundary layer turning it turbulent downstream.

In fact, boundary layer separation triggers separation-induced transition in this case. It is not a fortuitous event: separation-induced transition is present in the modeling by construction.

On the other hand, figure 7.20 shows the same plots for  $Re = 757,000$ . According to Williamson (1996) that is where the drag coefficients increase again, thus being a post-critical Reynolds number. In this case, transition takes place upstream of separation and that occurs downstream of the separation points for lower, pre-critical Reynolds numbers. For that reason, the wake is narrower and the drag coefficients are lower.

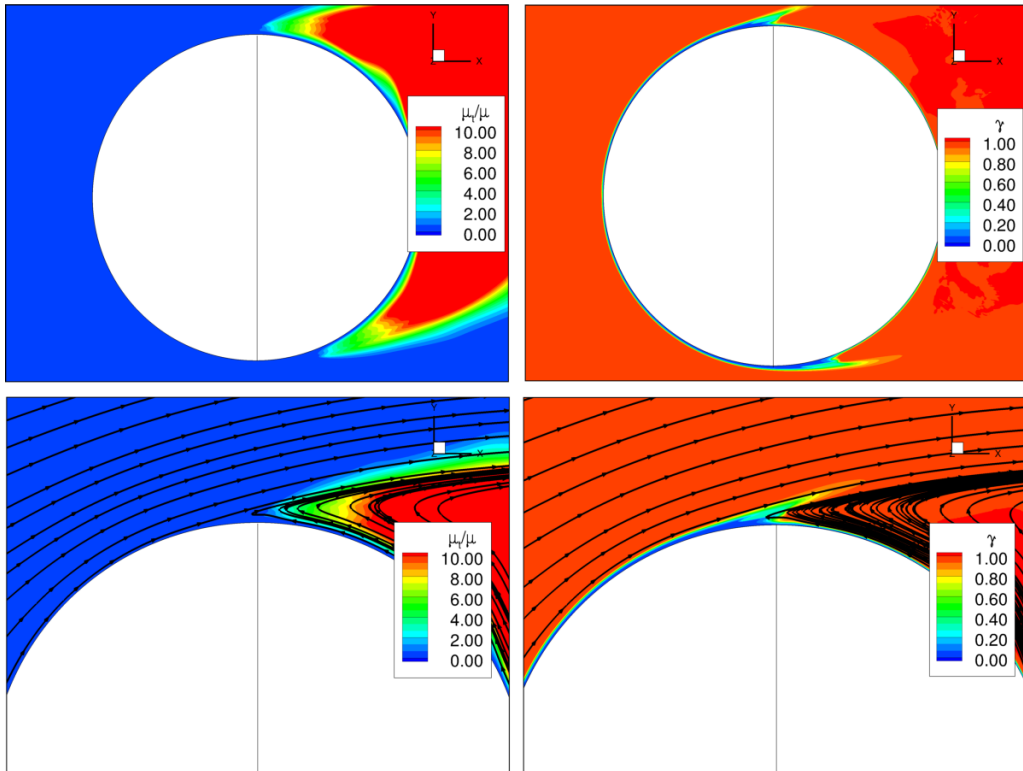


Figure 7.19: Field plots of normalized eddy viscosity and intermittency for  $Re = 128,000$ .

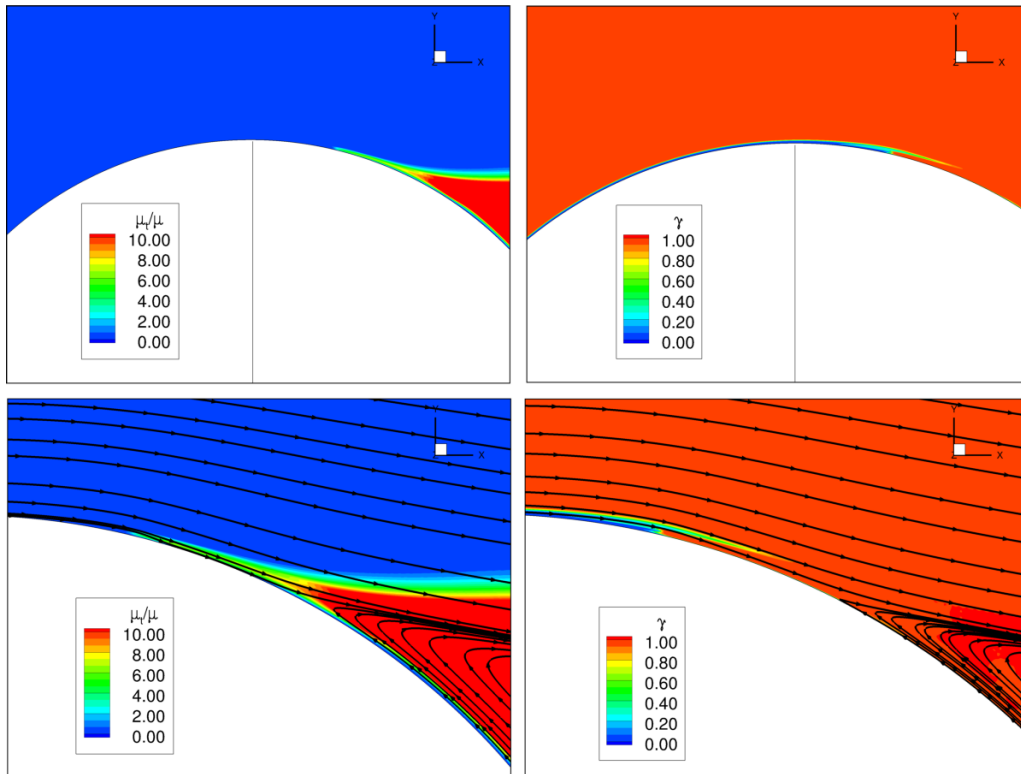


Figure 7.20: Field plots of normalized eddy viscosity and intermittency for  $Re = 757,000$ .

### 7.4.6 Experimental Uncertainty

The experimental uncertainties for the calculated Reynolds numbers are presented in table 7.5. They are derived from the cloud of experimental points in figure 7.16. These estimations are done as discussed in Chapter 5.

Table 7.5: Uncertainty estimation for the experiments

$Re$	$s$	$c(\%)$	$C_{Davg}$	$U_D$	$U_D/C_{Davg}(\%)$
128,000	0.06	4.81	1.18	0.07	5.66
252,000	0.17	17.22	0.97	0.20	20.26
315,000	0.39	68.62	0.57	0.37	65.43
506,000	0.11	30.04	0.37	0.13	35.34
757,000	0.14	43.51	0.32	0.11	35.80

### 7.4.7 Validation

A solution validation exercise was also done for the calculations with the LCTM according to the theory developed in chapter 5. Table 7.6 presents the results of this exercise.

According to the validation criteria the results are validated with the experiments (with some amount of flexibility for  $Re = 506,000$ ). Evidently, in this drag crisis region, the experimental points are highly spread and that is most likely due to different experimental conditions concerning inflow turbulence values, slightly different cylinder surface roughness and others. These differences, as small as they might be, can strongly influence the drag loads in this highly sensitive region. That reflects on the large experimental uncertainties seen, and therefore, in the validation results. Despite of that remark, considering the validation exercise done accordingly, one can consider that the approach is valid for the calculation of drag loads in this range of Reynolds numbers for practical applications.

Table 7.6: Validation exercise done for the calculations

$Re$	$U_{val}$	E	Validated?
128,000	0.08	0.06	Yes
252,000	0.21	0.08	Yes
315,000	0.39	0.18	Yes
506,000	0.13	0.15	Yes
757,000	0.12	0.08	Yes

## 7.5 Final Remarks of the Chapter

The turbulent range has been divided into two ranges according to the main flow features and bearing in mind modeling aspects. Range II is from  $Re = 1,000$  to ca.  $Re = 100,000$ , in which three-dimensional effects and instabilities play an important role in determining the loads; in range III, from  $Re = 100,000$  up to  $Re = 757,000$ , the boundary layer transition is the crucial aspects that determine the flow character and the forces.

This chapter reported on the use of the three-dimensional  $k-\omega$  SST-SAS in range II, in which an improvement on the force calculation is seen compared to the previous two-dimensional calculations done with SST. The calculated flow field in that range displays structures that are not fine enough thus causing too large forces due to overly coherent vortices and eddies. In fact, this is an issue related to the flow structures being resolved (which are too large) and those being simulated (which, for  $k-\omega$  SST are related to the boundary layer thickness and thus too large in comparison to reality). The SST-SAS naturally improves the turbulent flow scales modeling by using a local scale (the von Kármán scale) in a way that the local scales are smaller. It is only natural that energy is more broad-banded and the loads decrease.

Regarding flow modeling in range III, where transition plays an essential role, it has been noticed in the present study that the inclusion of the two additional transport equations (for  $\gamma$  and  $Re_{\theta_t}$ ) impacts negatively on the iterative converge of the calculations, specially comparing to the calculations done with the SST model. Large calculation times are to be expected for that reason. The LCTM is quite sensitive to space and time discretization, thus requiring highly refined grids near the wall, with both fine normal and tangential discretization. Regarding the former,  $y^+ < 1$  should be enforced. By means of requiring low iterative and round-off errors, the discretization errors were estimated and uncertainties of up to near 10% are achieved. The calculation results with fine grids and time steps showed that there is much more reasonable comparison with the experimental results and overall trends, in terms of drag loads, than seen before with URANS for these Reynolds numbers. It has been shown that SST seems to smooth out the drag coefficient curve and its values drop at around  $Re = 10,000$ , whereas the LCTM results remain at high values up to  $Re = 128,000$ , presenting a much sharper dip of the drag coefficients curve than with the SST. That is an important qualitative improvement due to and improvement in predicting the transition onset and length. More accurate prediction of the transition improves the prediction of boundary layer separation, a crucial aspect in cylinder flow dynamics, since most of the drag load is due to pressure. The drag coefficient values are also much better predicted when compared to the experimental trends. In order to consolidate the comparison, a validation exercise has been done, in which experimental and numerical uncertainties are considered, with the result that the results are validated with the experiments.

In order to summarize the results presented in this chapter, tables 7.7 and 7.8 show respectively the results obtained with the SST-SAS and with LCTM. Conversely, figure 7.21, figure 7.22 and figure 7.23 show respectively the drag coefficients, RMS of lift coefficients and Strouhal numbers calculated with the more advanced turbulence models in comparison with previous results and experimental ones.

Table 7.7: Summary of numerical results obtained with the finest grids and three-dimensional SST-SAS.

$Re$	$C_{Davg}$	$C_{LRMS}$	$St$
1,000	1.25	0.65	0.22
3,900	1.14	0.52	0.21
20,000	1.28	0.66	0.22
63,100	1.13	0.66	0.22
100,000	0.93	0.50	0.25

Table 7.8: Summary of numerical results obtained with the finest grids and two-dimensional LCTM.

$Re$	$C_{Davg}$	$C_{LRMS}$	$St$
128,000	1.34	1.07	0.27
252,000	0.89	0.44	0.20
315,000	0.76	0.23	0.27
506,000	0.52	0.37	0.31
757,000	0.39	0.23	0.34

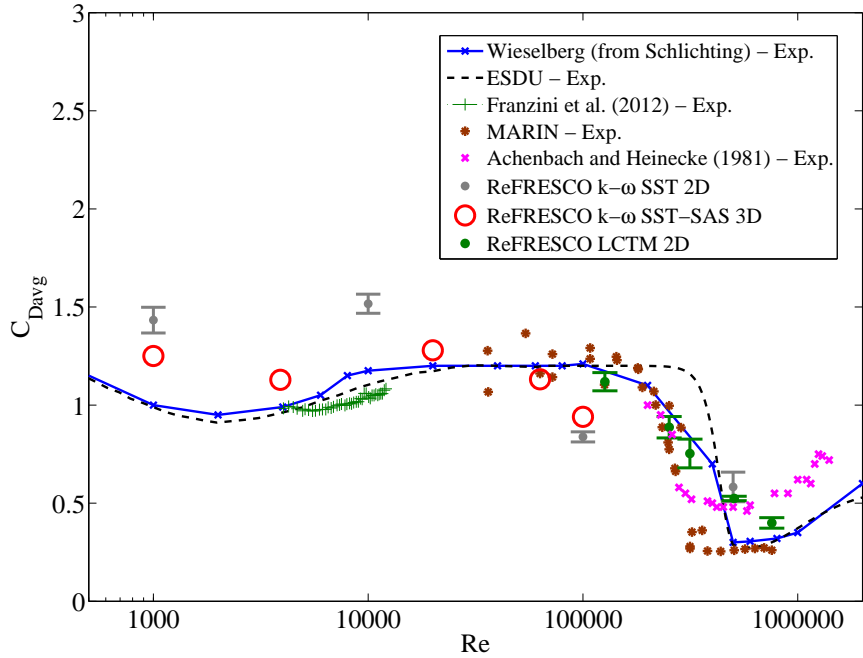


Figure 7.21: Drag coefficient results from the complete range of calculations. Experiments from Schlichting H. (2000), ESDU (1985), Franzini et al. (2012), Achenbach & Heinecke (1981) and from MARIN.

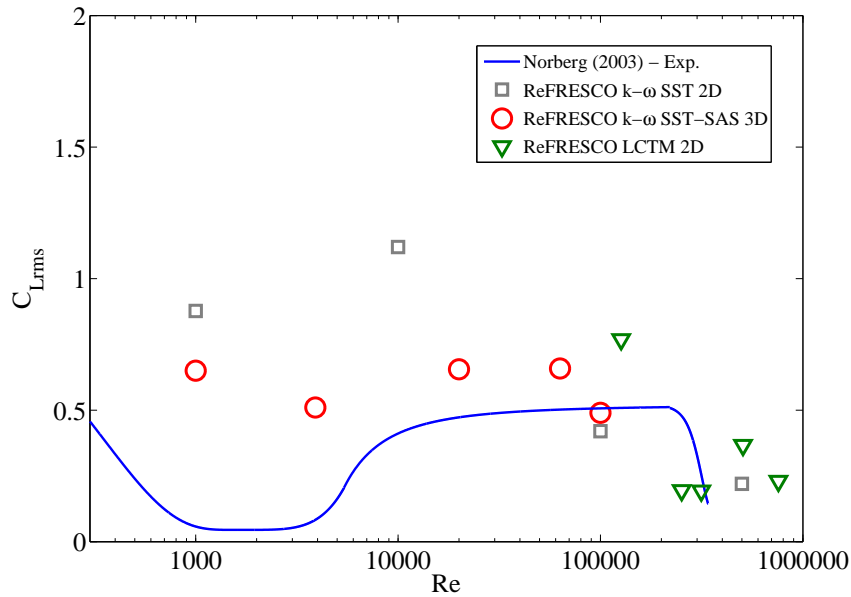


Figure 7.22: RMS of lift coefficient results from the complete range of calculations. Experiments from Norberg (2003).

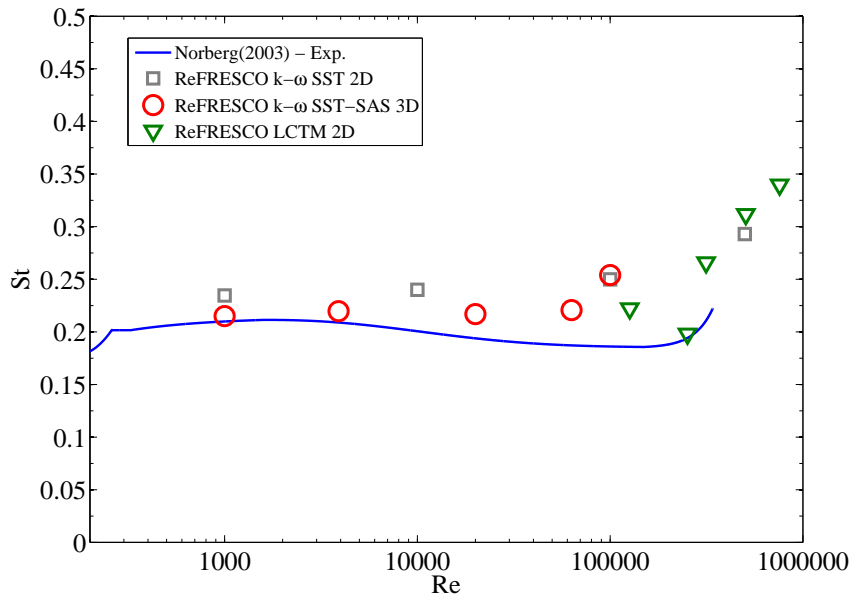


Figure 7.23: Strouhal number results from the complete range of calculations. Experiments from Norberg (2003).

# Chapter 8

## Rigid Cylinder in 1

## Degree-of-Freedom Imposed Motions

*This chapter will show the numerical study of one degree-of-freedom imposed motions to the rigid cylinder. The experimental results are comprised of benchmark data from Gopalkrishnan (1993), Sarpkaya (2004) and original experiments carried out at the Maritime Research Institute Netherlands - MARIN. The main objectives are: i) to assess the capabilities of the traditional and the more advanced turbulence and transition models used together with the moving body capabilities developed in this thesis; ii) to investigate the appropriate modeling strategies for this problem.*

### 8.1 Background

Forced sinusoidal oscillations have been studied by several researchers with the objective of predicting free vortex-induced vibrations. It is well accepted (SARPKAYA, 2004) that free and forced vibrations are different in their character. In free oscillations, “the motion is driven internally by the wake at an average frequency”, dictated by the past and present state of the flow and motion. In the forced vibrations, the frequency and amplitude are precisely driven, in such a way that the nature of the VIVs is regularized and the wake states are largely influenced by the regular motions, despite some irregularity is still seen.

The amplitude and frequency of oscillation dictate whether the wake response is locked-in, in which the motions control the wake and a state of resonance is observed. Conversely, in the unlocked state, the wake response is more irregular and the frequency content is widespread.

The motions described by the cylinder at the imposed frequency  $\tilde{\omega}_i$  (the tilde indicates dimensional frequencies) are defined as:

$$y(t) = A \sin(\tilde{\omega}_i t). \quad (8.1)$$

The lift force in the state of lock-in may be written as (PLACZEK; SIGRIST; HAMDOUNI, 2009):

$$F_L = F_{Li} \sin(\tilde{\omega}_i t + \phi_i) + F_{Ls} \sin(\tilde{\omega}_s t + \phi_s), \quad (8.2)$$

in which  $\tilde{\omega}_s$  is the Strouhal frequency,  $F_{Ls}$  is the lift force amplitude due to vortex shedding and  $F_{Li}$ , due to the imposed motion. The quantity  $\phi_i$  is the phase shift between lift force due to imposed motions and imposed motions, whereas  $\phi_s$  is the phase shift between vortex-shedding forces and motions. The lift coefficient is written as:

$$C_L = \frac{F_L}{\frac{1}{2}\rho L D U^2} = C_{Li} \sin(\tilde{\omega}_i t + \phi_i) + C_{Ls} \sin(\tilde{\omega}_s t + \phi_s). \quad (8.3)$$

Other frequency components may be present in the force response, but as stated by Gopalkrishnan (1993), the interest lies in the locked-in response of the wake, in which no power transfer between body and fluid takes place at frequencies other than the imposed motion frequency. Regarding the lock-in or “wake capture” issue, Gopalkrishnan (1993) has advanced on the work of other researchers and clearly identified it. As he stated it, “when the externally imposed cylinder oscillation frequency (or structural natural frequency, in the case of free oscillations) comes within a certain range of the Strouhal shedding frequency, there is an apparent breakdown of the Strouhal relation”. In that situation, the shedding frequency collapses onto the imposed (or natural structural frequency, in free motions) and “this is commonly accompanied by increased vortex strength, increased correlation length, and a reduction of random irregularities in the vortex-induced forces”. Gopalkrishnan also noted that the transition between lock-in and nonlock-in state takes place continuously, but very rapidly and even chaotic response can occur at the lock-in boundaries. The lock-in region is characterized in terms of the reduced velocity:

$$U_R = U T_i / D, \quad (8.4)$$

in which  $U$  is the inflow velocity,  $T_i$  is the imposed motion period and  $D$  is the cylinder diameter.

Considering the lift coefficient due to the imposed motion only (that is, the part of the lift force with frequency  $\tilde{\omega}_i$ ), the lift coefficient in phase with velocity and acceleration

are, respectively:

$$C_{Lv} = C_{Li} \sin \phi_i, \quad (8.5)$$

and

$$C_{La} = -C_{Li} \cos \phi_i. \quad (8.6)$$

The lift coefficient in phase with velocity determines the damping or exciting effect: when positive there is excitation, that is, a positive energy transfer from the fluid to the body; when negative, there is damping, with energy transfer in the opposite direction. Conversely, the lift coefficient in phase with acceleration determines the inertial added mass force. In this case, negative  $C_{La}$  denotes positive added mass and *vice versa*. As in Gopalkrishnan (1993), the coefficients presented in this chapter,  $C_{Lv}$  and  $C_{La}$  are the negative of the ones presented in Sarpkaya (2004),  $C_{dh}$  and  $C_{mh}$ , derived from Morison's equation.

In order to derive  $C_{Lv}$  and  $C_{La}$  from the calculations, two analyses procedures were implemented. The first method is based on the Hilbert Transform of the transverse displacement  $y(t)$  and the lift force  $F_L(t)$ , respectively expressed as:

$$\mathcal{H}(y(t)) = a_y(t)e^{j\phi_y(t)}, \quad (8.7)$$

and

$$\mathcal{H}(F(t)) = a_F(t)e^{j\phi_F(t)}, \quad (8.8)$$

in which  $a_y(t)$  and  $a_F(t)$  are respectively the time-dependent displacement and force amplitudes and  $\phi_y(t)$  and  $\phi_F(t)$  are the time-dependent displacement and force phase angles. The phase between the force and displacement is expressed as  $\phi_F(t) - \phi_y(t) = \phi$ . By filtering the lift force bracketing the imposed frequency, a regular trace is obtained, from which the lift amplitude is obtained. Equations 8.5 and 8.6 are then used to obtain  $C_{Lv}$  and  $C_{La}$ .

The results from this method are compared to another method in which the lift coefficients in phase with velocity and acceleration are directly calculated from the expressions:

$$C_{Lv} = \sqrt{\frac{2}{T_i} \frac{\langle C_L(t), \dot{y}(t) \rangle}{\sqrt{\langle \dot{y}(t), \dot{y}(t) \rangle}}}, \quad (8.9)$$

and

$$C_{La} = \sqrt{\frac{2}{T_i} \frac{\langle C_L(t), \dot{y}(t) \rangle}{\sqrt{\langle \ddot{y}(t), \ddot{y}(t) \rangle}}}, \quad (8.10)$$

in which  $\langle \cdot \rangle$  denotes the inner product operator,  $T_i$  is the period of the imposed motion. This time domain approach has the advantage that no filtering of the forces is necessary due to the calculation of the inner products. In all cases presented here, both methods were used ensuring consistent results.

## 8.2 Description of the Cases

Three sets of calculations with two-dimensional  $k-\omega$  SST, two-dimensional SST-LCTM and three-dimensional SST-SAS were conducted and will be presented in this chapter. In all cases, experimental data was used in order to support the analyses and conclusions.

The first calculation set was done to reproduce part of the experiments conducted by Gopalkrishnan (1993). In that work, the tests were conducted to measure loads on the cylinder under imposed motions transverse to the incoming flow with  $Re = 10,000$ , several motion amplitudes and a wide range of reduced velocities (or, conversely, frequencies) in and out of the lock-in region. In particular, the calculations showed for this thesis, the imposed motion non-dimensional amplitude is  $A/D = 0.3$  in the range  $3 < U_R < 10$ .

For the second calculation set, interest lies upon a higher Reynolds number,  $Re = 40,000-45,000$ , with two different sets of data: firstly, data contributed by MARIN, in which transverse imposed motions are done with  $A/D = 0.5$ ,  $Re = 40,500$  and  $3 < U_R < 8$ ; finally, the experimental set presented by Sarpkaya (2004) was explored, with  $Re = 45,000$ ,  $A/D = 0.5$  and  $3 < U_R < 10$ .

## 8.3 Setup and Grids

Figure 8.1 shows the grid layout and boundary conditions used in the calculations presented herein. In the present calculations, the circular domain was chosen after some preliminary tests done with the rectangular domain (used in the fixed cylinder calculations) showed artificial pressure oscillations at the edges, which influenced the calculations. The circular domain and grid showed in figure 8.1 ensures that this does not occur with the imposed motion calculations. Due to different domain outline, the boundary condi-

tions are also different for the present calculations.

The dimensions are also different from the fixed cylinder calculations: a domain radius of  $20D$  ( $D$  is the cylinder diameter) was found appropriate as smaller domain sized could influence the results. Furthermore,  $13D$  is the length in the span-wise direction.

Regarding the boundary conditions, at the top and bottom boundaries, symmetry condition is enforced. On the other hand, the inflow represents 38% of the circumference, whereas a pressure boundary condition is enforced at the remaining part of the domain.

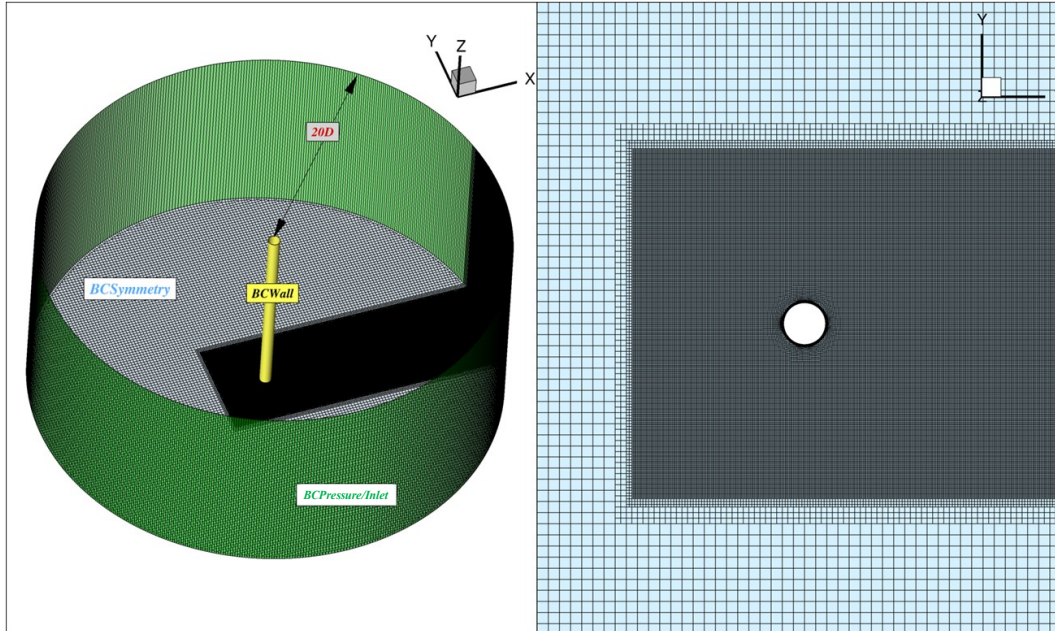


Figure 8.1: Setup and grid layout used in the calculations with imposed motion.

The grids used for the imposed motions calculations are geometrically similar, generated from each other using different base size elements with the same topology.

A sensitivity analysis applying the SST has been done with the grids to reach results independent from discretization for the lowest reduced velocities (yielding the largest relative flow velocity). For the two-dimensional calculations, grids analyzed ranged from 202,732 to 777,446 cells, where only the finest grid and time step were used for the calculation of all reduced velocities, table 8.1. Similarly, for the three-dimensional calculations, grids with 2,490,120 and 4,061,961 cells were analyzed with the different time steps for the lowest reduced velocity with the third set (SARPKAYA, 2004) ( $Re = 45,000$ ) and that grid was used for the other reduced velocities, see table 8.2. Figure 8.2 summarizes the

convergence study for both two-dimensional and three-dimensional studies.

As mentioned in the previous Chapter, the two-dimensional calculations took from a few weeks to up to two months with the same hardware as before, which is somewhat faster than seen for the fixed cylinder. This has been normal since, with imposed motions, the numerical transient behavior dissipates much earlier in this case. For the three-dimensional calculations, computational times have been up to near three months with the largest grids and finest time steps.

Table 8.1: Details of the finest grids used for the two-dimensional imposed motions calculations ( $y^+$  values showed are for SST).

$Re$	Num. of Cells	Circ. Cells	Steps/Cycle	$y_{max}^+$	Calculation Set
10,000	632,678	550	200	1.11	1 (GOPALKRISHNAN, 1993)
40,500	777,446	608	134	1.52	2 (MARIN)
45,000	777,446	608	260	1.21	3 (SARPKAYA, 2004)

Table 8.2: Details of the finest grids used for the three-dimensional imposed motions calculations with SST-SAS.

$Re$	Num. of Cells	Circ. Cells	Steps/Cycle	$y_{max}^+$	Calculation Set
10,000	4,061,961	432	200	0.11	1 (GOPALKRISHNAN, 1993)
40,500	4,061,961	432	300	1.12	2 (MARIN)
45,000	4,061,961	432	260	0.97	3 (SARPKAYA, 2004)

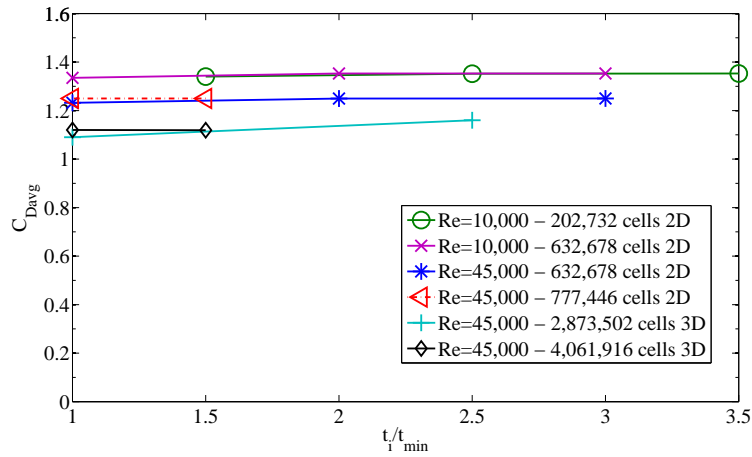


Figure 8.2: Grid and time step convergence analysis for the imposed motion calculations.

## 8.4 Iterative Convergence

Figures 8.3 and 8.4 show typical iterative convergence histories found in the present calculations, however more noisy iterative convergence has been noticed in some instances, requiring a large number of outer loops. The criteria for all quantities was  $L_\infty < 10^{-4}$ , both for two-dimensional and three-dimensional calculations.

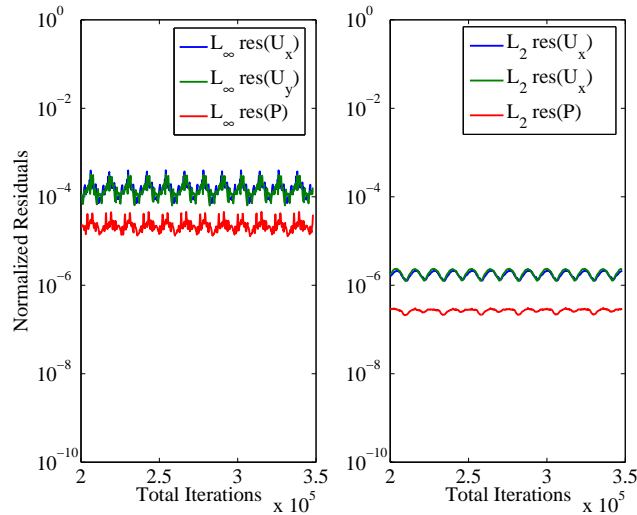


Figure 8.3: Typical velocity and pressure residuals for the calculations with imposed motions using two-dimensional  $k$ - $\omega$  SST. Results for  $U_R = 4.0$  in the first set of experiments (GOPALKRISHNAN, 1993).

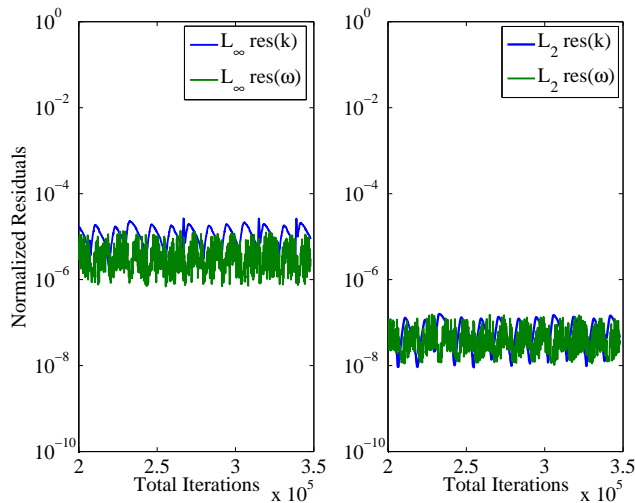


Figure 8.4: Typical turbulent quantities residuals for the calculations with imposed motions using two-dimensional  $k$ - $\omega$  SST. Results for  $U_R = 4.0$  in the first set of experiments (GOPALKRISHNAN, 1993).

## 8.5 Results with $Re = 10,000$ and $A/D = 0.3$

In this set of calculations, the numerical results from the calculations were compared with the experimental results from Gopalkrishnan (1993). In his work, he noted that the wake capture region (for a fixed Reynolds number) varies with  $A/D$  and, for  $A/D = 0.3$ , this region is comprehended between  $U_R = 4.5$  and  $U_R = 5.9$ .

In order to characterize the responses in and out of the lock-in region, close analysis is done for the results for  $U_R = 3.0$  (prior to the lock-in region),  $U_R = 10.0$  (after the lock-in region) and  $U_R = 5.0$  (in the lock-in region) calculated with two-dimensional  $k-\omega$  SST, two-dimensional Local Correlation Transition Model and three-dimensional Scale Adaptive Simulations.

Figure 8.5 shows the motion and lift traces for  $U_R = 3.0$  (thus prior to the wake capture region) and figure 8.6 shows the lift and drag time traces for the same reduced velocity, both calculated with SST. Some irregularity in the forces is noticeable, which also reflects on the frequency content of the time traces. However, the peak energy frequency of the lift corresponds to the imposed motion frequency (this term shall be omitted henceforth being replaced by “imposed motion frequency” or “imposed frequency” for conciseness),  $f = \tilde{f}_i D/U = 0.33$ , in spite of high energy associated with the vortex-shedding frequency,  $f_s = \tilde{f}_s D/U = 0.16$ .

The drag loads present even richer frequency content and appreciable higher harmonics of the shedding frequency,  $f_s$ , are noticed. It is instructive to recall that the conventional vortex street is comprised of two vortices shed per oscillation cycle, causing the drag to oscillate at twice the vortex-shedding frequency,  $2f_s$ . Interestingly enough, one notices higher energy associated with  $f_s$  than with  $2f_s$ . Appreciable energy is also perceived at the harmonics at  $3f_s$ ,  $4f_s$  and  $5f_s$ . Gopalkrishnan (1993) reported energetic drag response (for  $A/D = 0.75$  and  $A/D = 1.20$ , thus higher than the present) at  $2f_i$ , while  $f_i$  had little energy. In the present calculation for  $U_R = 3.0$ ,  $f_i = 2f_s$  and thus  $2f_i = 4f_s$  and the same pattern is observed.

Furthermore, analyzing the study done by Williamson & Roshko (1988), in which the vortex patterns are determined in the plot of  $A/D$  over  $f_s/f_i$  (in fact, they derive  $f_s$  assuming  $St = 0.2$ , resulting  $f_s = 0.2$ ), for the present case ( $A/D = 0.3$  and  $St/f_i = 0.61$ ), the expected vortex pattern is the C-mode, meaning that “near the cylinder we have the 2S or P+S modes, but the smaller vortices coalesce (...) immediately behind the body”. This is consistent with strong  $f_s$  energy and the observed higher harmonics.

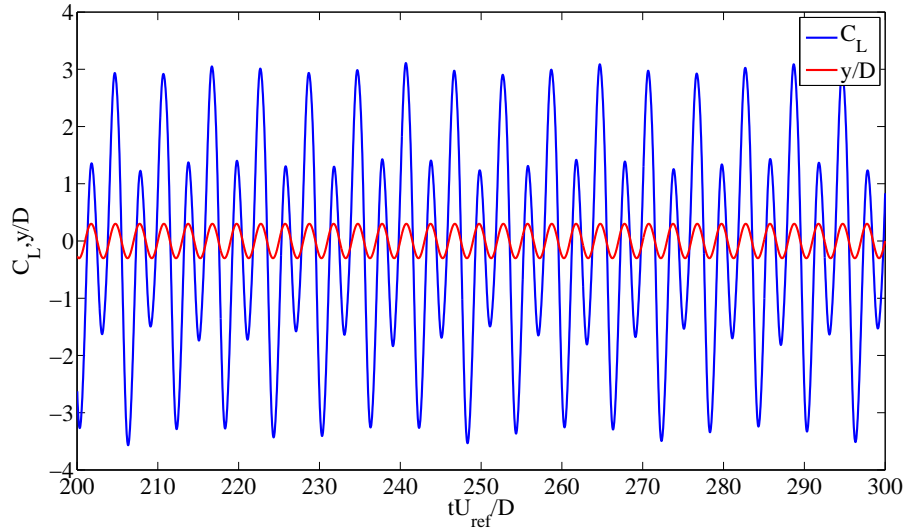


Figure 8.5: Imposed motion and lift coefficient traces with  $U_R = 3.0$  and two-dimensional SST for the first set of experiments (GOPALKRISHNAN, 1993).

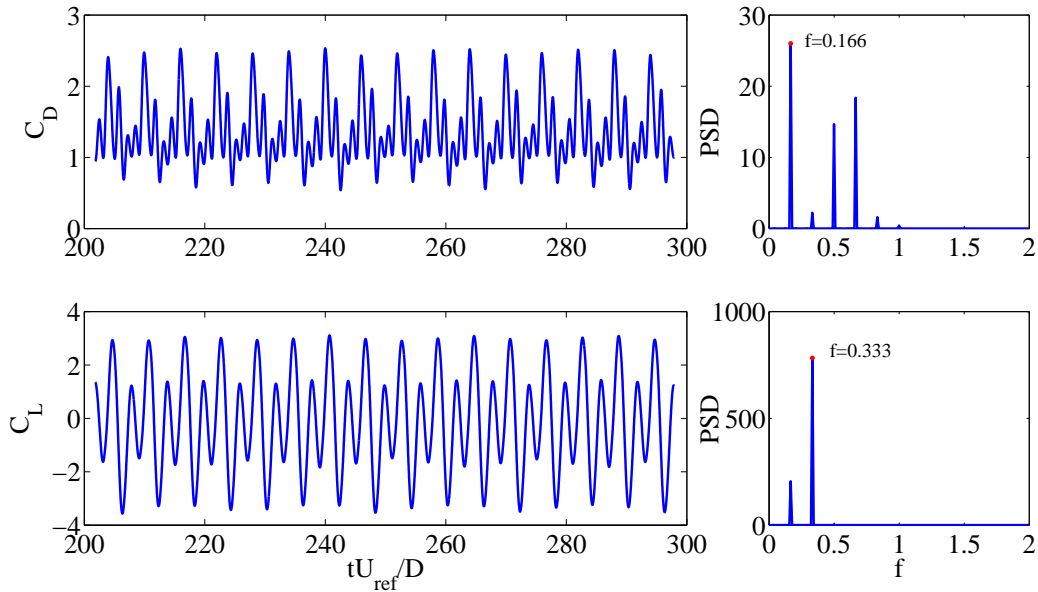


Figure 8.6: Drag and lift time traces on the cylinder with  $U_R = 3.0$  and two-dimensional SST for the first set of experiments (GOPALKRISHNAN, 1993).

Figure 8.7 shows the velocity field aligned with the flow direction at the minimum point of the lift force, in which the small structures mentioned by Williamson & Roshko (1988) are observed. Figure 8.8 shows the imposed motion traces and lift coefficients for the case with  $U_R = 10.0$ , thus also out of the lock-in range. Conversely, figure 8.9 shows the drag and lift coefficients and their spectra. The imposed nondimensional frequency for this calculation is  $f_i = 0.1$ , however the observed shedding frequency is  $f_s = 0.218$ , as seen from the lift spectrum. The drag spectrum, on the other hand, shows low energy in a wide frequency range, indicating that no definite pattern is markedly present, as also

noted by Gopalkrishnan (1993) for high imposed motion periods.

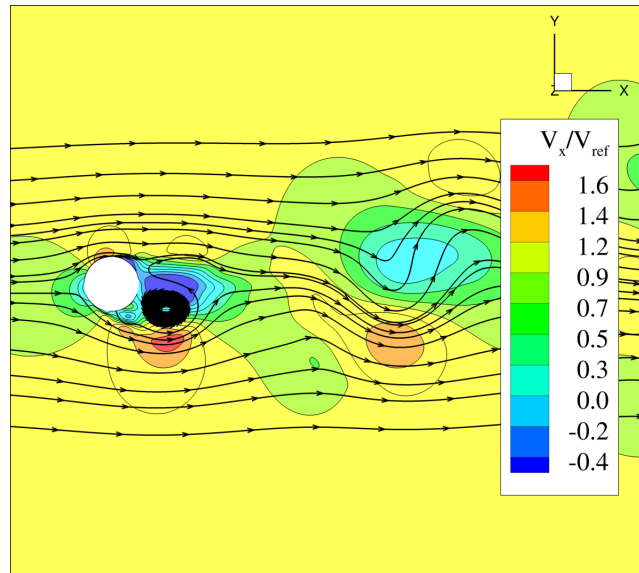


Figure 8.7: Nondimensional instantaneous velocity in the near wake of oscillating cylinder at  $U_R = 3.0$  and two-dimensional SST for the first set of experiments (GOPALKRISHNAN, 1993). Taken from the point of minimum lift coefficient.

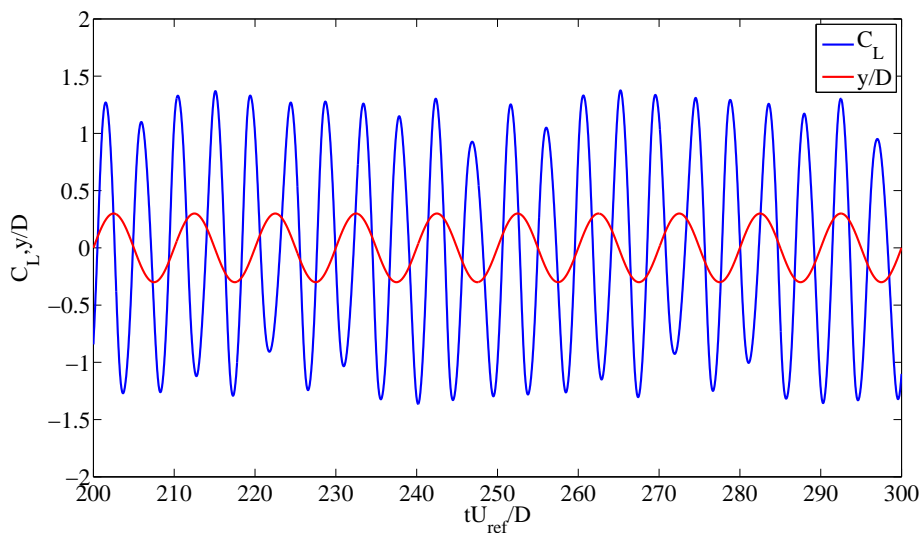


Figure 8.8: Imposed motion and lift coefficient traces with  $U_R = 10.0$  and two-dimensional SST for the first set of experiments (GOPALKRISHNAN, 1993).

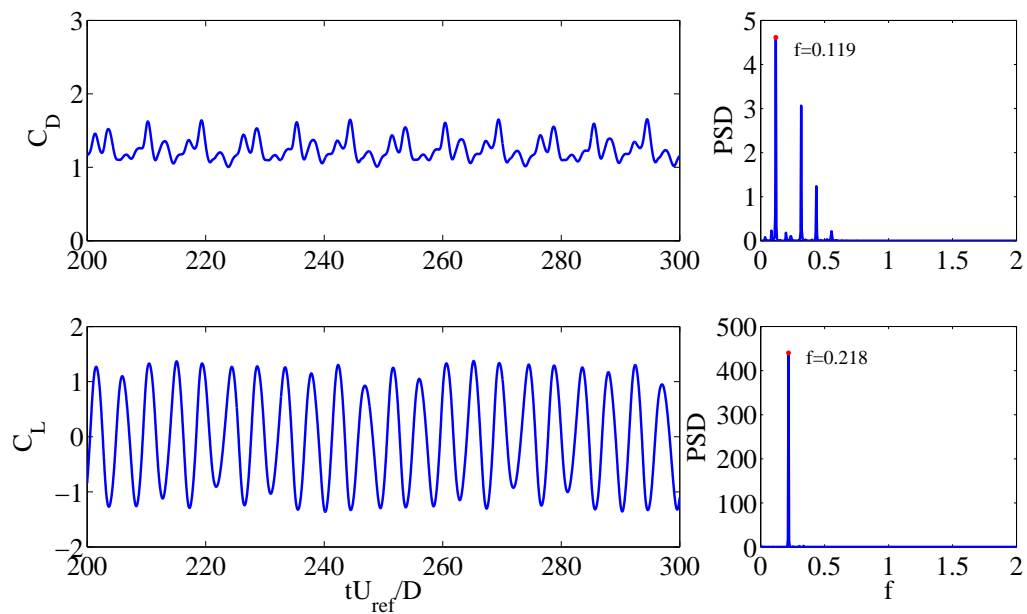


Figure 8.9: Drag and lift time traces on the cylinder with  $U_R = 10.0$  and two-dimensional SST for the first set of experiments (GOPALKRISHNAN, 1993).

Figure 8.10, in which the x-velocity is presented, also shows that it is difficult to define the vortex-shedding pattern, as identified by Williamson & Roshko (1988). In this case,  $St/f_i = 2.0$ , which falls into the region where Williamson could not define a vortical pattern.

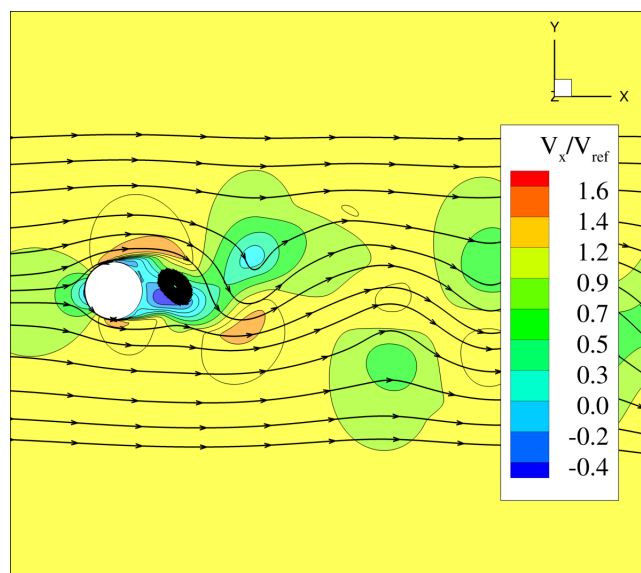


Figure 8.10: Nondimensional instantaneous velocity in the near wake of oscillating cylinder at  $U_R = 10.0$  and two-dimensional SST for the first set of experiments (GOPALKRISHNAN, 1993). Taken from the point of minimum lift coefficient.

Moving to the lock-in region, figure 8.11 shows the nondimensional motion and lift coefficient traces for  $U_R = 5.0$ , in which the imposed motion frequency is  $f_i \approx f_s = 0.2$ . The lift trace is markedly regular as a response to the imposed motions as the wake is in resonance.

Figure 8.12 shows the lift and drag coefficients for  $U_R = 5.0$  and their spectra, corroborating that both lift and drag are very regular and the peak frequencies correspond to the shedding frequency and double its value in the aligned direction.

Figure 8.13 shows the velocity in the x-direction. The 2S pattern is clearly seen, as predicted by Gopalkrishnan (1993).

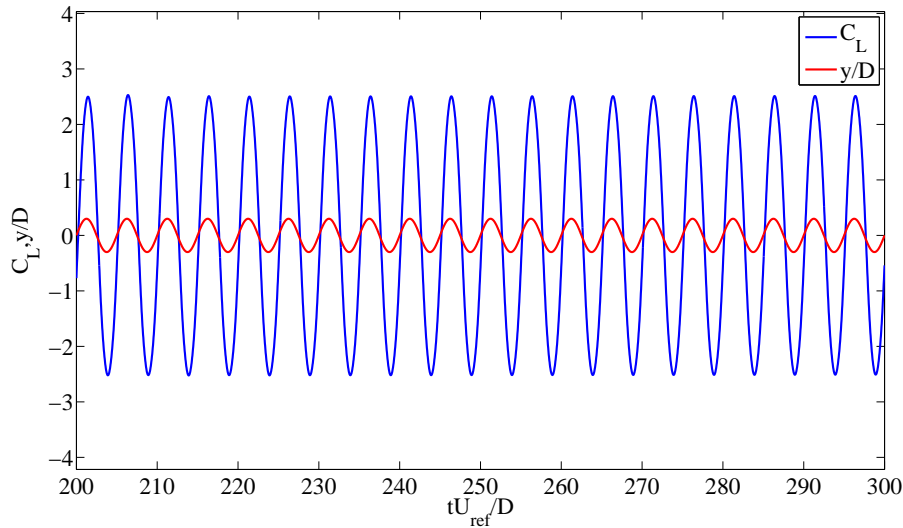


Figure 8.11: Imposed motion and lift coefficient traces with  $U_R = 5.0$  and two-dimensional SST for the first set of experiments (GOPALKRISHNAN, 1993).

It is instructive to compare the present results with the ones presented in Placzek, Sigrist & Hamdouni (2009), in which similar calculations are done, although the latter was done for lower Reynolds number,  $Re = 100$ . In particular, the present unlocked cases  $U_R = 3.0$  and  $U_R = 10.0$  are similar to the cases  $F = f_i/f_s = 1.50$  and  $F = 0.50$ , respectively.

On the other hand, the locked configuration  $U_R = 5.0$  corresponds to  $F = 0.90$  and  $F = 1.10$  in Placzek, Sigrist & Hamdouni (2009). Interestingly, in both results and the ones in Placzek, Sigrist & Hamdouni (2009) the same behavior is observed: for  $U_R = 3.0$  (similar to  $F = 1.50$ ), the lift peaks at  $f_i$  (peak frequency response equal to the imposed motion frequency); for  $U_R = 10.0$  (similar to  $F = 0.50$ ), the lift peaks at  $2f_i$  (peak response frequency equal to double the imposed motion frequency, which is equal to the shedding frequency); for  $U_R = 5.0$ , similar to  $F = 0.90$  and  $F = 1.10$ , the response frequency equals both imposed and shedding frequency as resonance is reached.

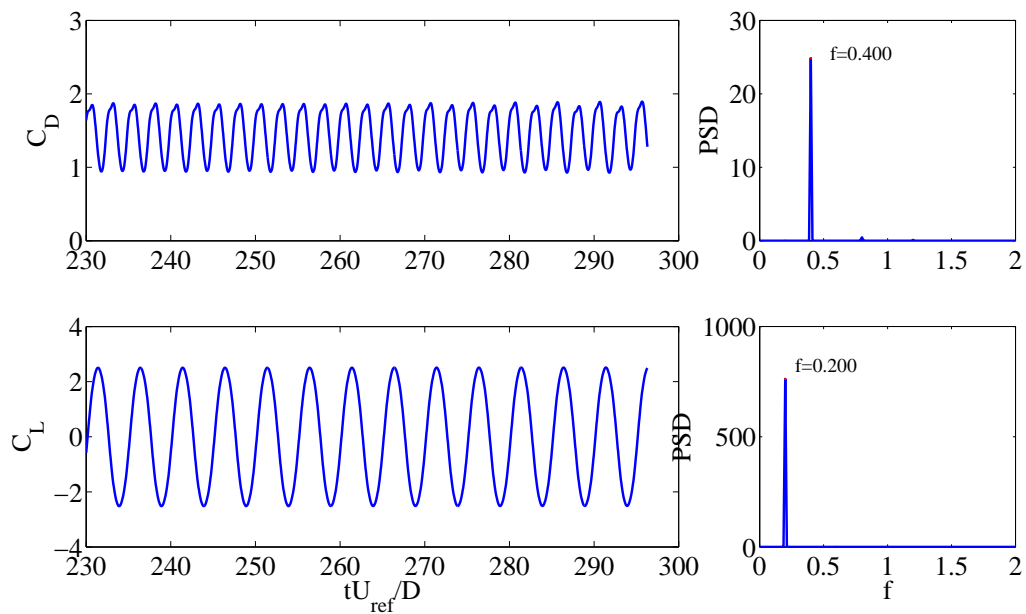


Figure 8.12: Drag and lift time traces on the cylinder with  $U_R = 5.0$  and two-dimensional SST for the first set of experiments (GOPALKRISHNAN, 1993).

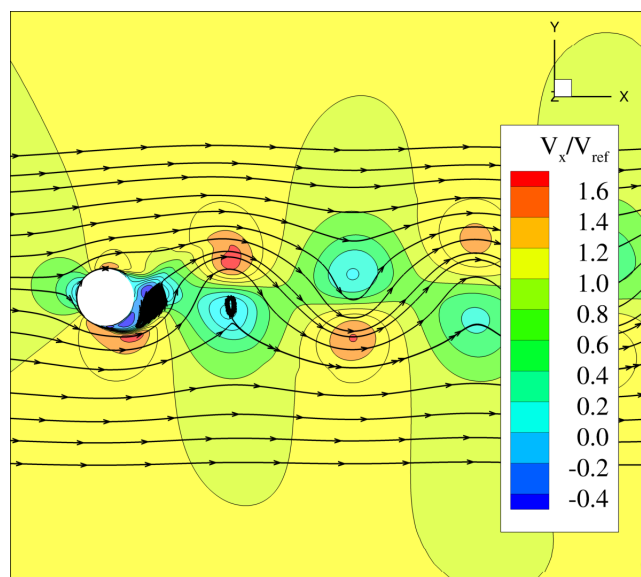


Figure 8.13: Nondimensional instantaneous velocity in the near wake of oscillating cylinder at  $U_R = 5.0$  and two-dimensional SST for the first set of experiments (GOPALKRISHNAN, 1993). Taken from the point of minimum lift coefficient.

Figure 8.14 shows the drag coefficients from the experiments in comparison with the calculated for the models  $k-\omega$  SST (two-dimensional), the LCTM (two-dimensional) and the SST-SAS (three-dimensional).

There is much better comparison between the numerical and experimental results than for the fixed cylinder at the same Reynolds number. It is likely that inertial effects due to cylinder motion are better captured in the simulations, than the turbulence-related

issues described above. Furthermore, small differences in the drag results are seen among different turbulence models for this case.

Likewise, there is good agreement between numerical and experimental results of the lift coefficients in phase with velocity and acceleration, respectively presented in figures 8.15 and 8.16, particularly in the resonance region, mainly due to more coherent and strong vortices, which cause stronger vortex-induced loads.

In the  $C_{Lv}$  results, figure 8.15, the positive values denote positive transfer of energy from the fluid to the cylinder, thus amplifying its free motions. The results thus indicate that between  $U_R \approx 5.0$  and  $U_R \approx 8.0$ , excitation would indeed take place and high vibration amplitude would be observed.

One also notices that the peak energy of the numerical results occurs at  $U_R = 5.50$ , instead of  $U_R = 6.00$ , as seen in the experiments. Small shifts of the resonance peaks from the natural Strouhal frequency of  $f = 0.20$  (or  $U_R = 5.0$ ) both in the experiments and in calculations are mainly due to lift coefficient magnitudes and phase shifts, which are highly sensitive to the flow conditions.

The  $C_{La}$  results, figure 8.15, show an abrupt variation of the lift coefficient in phase with acceleration in the resonance region. It is also relevant to mention that these results did not show a large difference when comparing the behavior of the three turbulence models, as the results are similar overall. Indeed, even analyzing the  $C_{Lv}$  and  $C_{La}$  coefficients, which are known to be extremely sensitive to flow conditions, the same trends are observed as well as similar quantitative behavior.

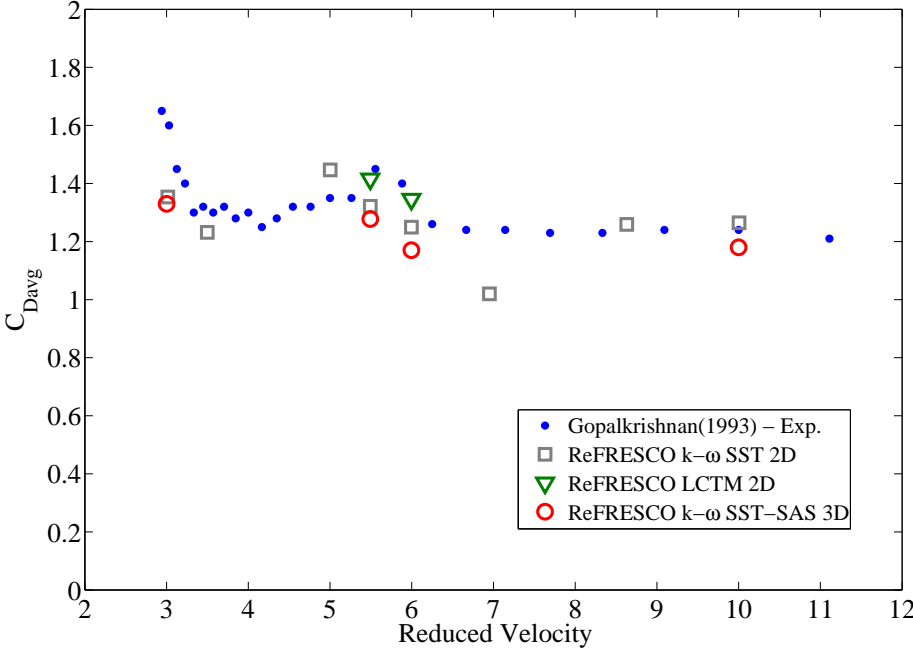


Figure 8.14: Drag coefficients for the calculations compared to Gopalkrishnan (1993).

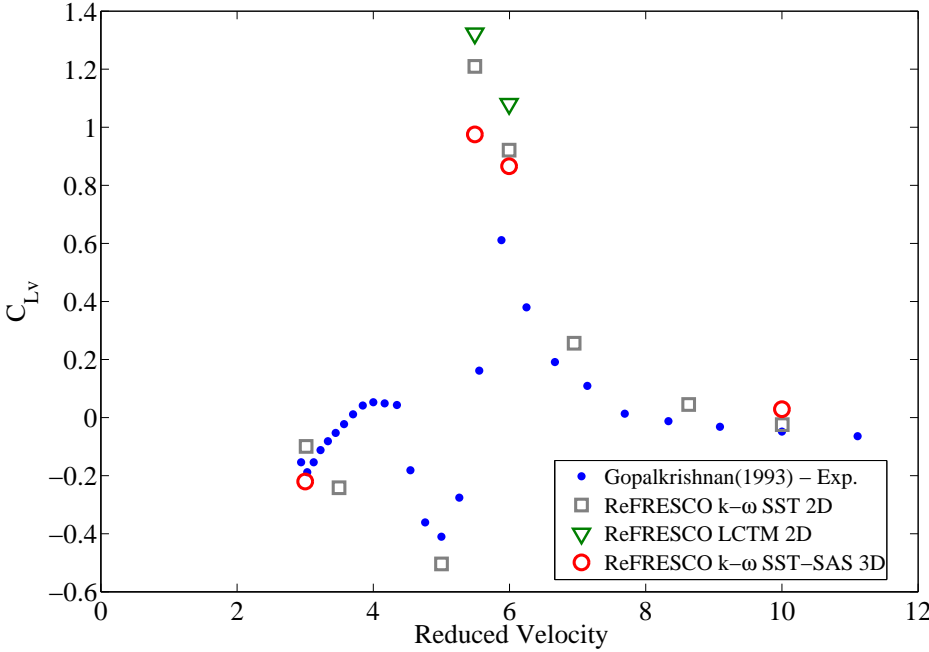


Figure 8.15: Lift coefficients in phase with velocity for the calculations compared to Gopalkrishnan (1993).

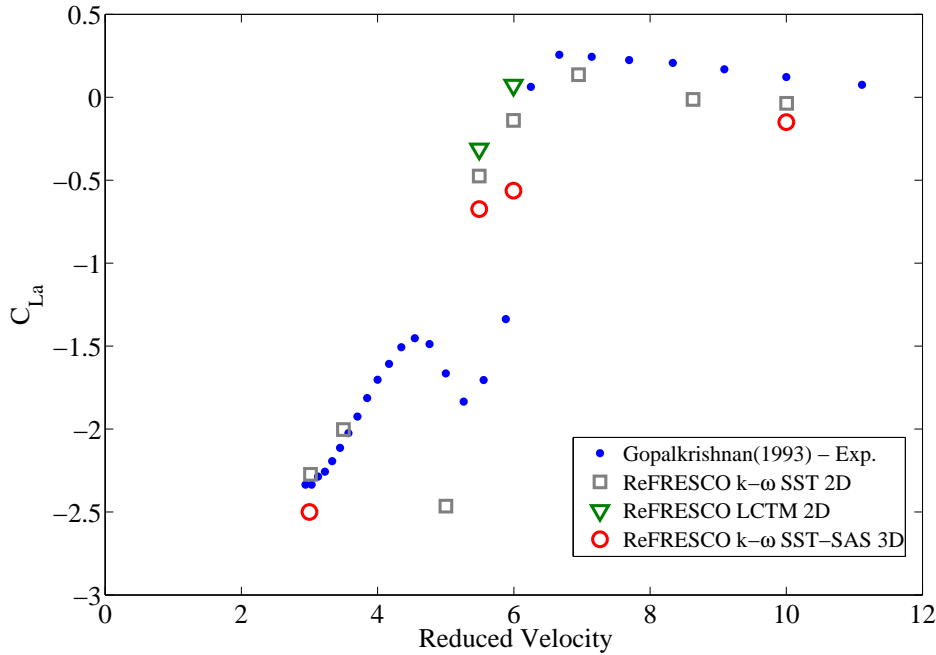


Figure 8.16: Lift coefficients in phase with acceleration for the calculations compared to Gopalkrishnan (1993).

## 8.6 Results with $Re = 40,000 - 45,000$ and $A/D = 0.5$

In this second set of calculations, higher Reynolds numbers are explored, ca.  $Re = 40,000$ , and higher imposed motion amplitude,  $A/D = 0.5$ . These are the conditions of the experimental results contributed by MARIN (in this case,  $Re = 40,500$ ) and the ones presented in Sarpkaya (2004), with  $Re = 45,000$ .

In order to compare the behavior of the two-dimensional SST and three-dimensional SST-SAS, figures 8.17, 8.18 and 8.19 show lift coefficients and imposed motion traces for  $U_R = 4.50$ ,  $U_R = 10.0$  and  $U_R = 5.50$ , again with the former two conditions in the unlocked and the latter in the locked regions.

For  $U_R = 4.50$ , there is a fair comparison between the traces from SST and SAS, with slightly lower amplitudes by the SAS. Close inspection will also show small difference in phase between the forces and motion, which reflect on different phase shifts resulting in different coefficients, as showed below.

A different behavior is observed for  $U_R = 10.0$ , for which the SAS displays lower amplitudes and more irregular behavior than for SST (in spite of not displaying single-frequency behavior, the SST solution is quite regular). A more regular behavior is observed for  $U_R = 5.50$ , which is in the resonance region.

Figure 8.20 shows the drag coefficients from calculations and MARIN experiments conducted in different years at the same conditions (Reynolds numbers, amplitude and frequencies). The calculations are done with the two-dimensional  $k-\omega$  SST, two-dimensional LCTM and the three-dimensional SAS. There is poor comparison between the experiments and the  $k-\omega$  SST and LCTM calculations, unlike the results obtained in the Gopalkrishnan (1993) set. The SST-SAS results show better agreement with the experimental values. The amplification of the drag in the resonance region is captured with the SST, although not the amplitudes. For  $U_R > 6.0$ , the drag coefficient decreases in the experiments and that is not seen in the SST or LCTM calculations, only with the SAS results.

As observed by Gopalkrishnan (1993), the correlation of shed vortices decreases outside of the lock-in region with an increased importance of instabilities in the unlocked configuration and that is more prominent for larger imposed motion amplitudes. By making use of that argument, it is evident that the two-dimensional calculations with the  $k-\omega$  SST and LCTM are not able to capture those features.

The Scale Adaptive Simulations, on the other hand, improve the drag predictions due to improved physical modeling that includes three-dimensional effects.

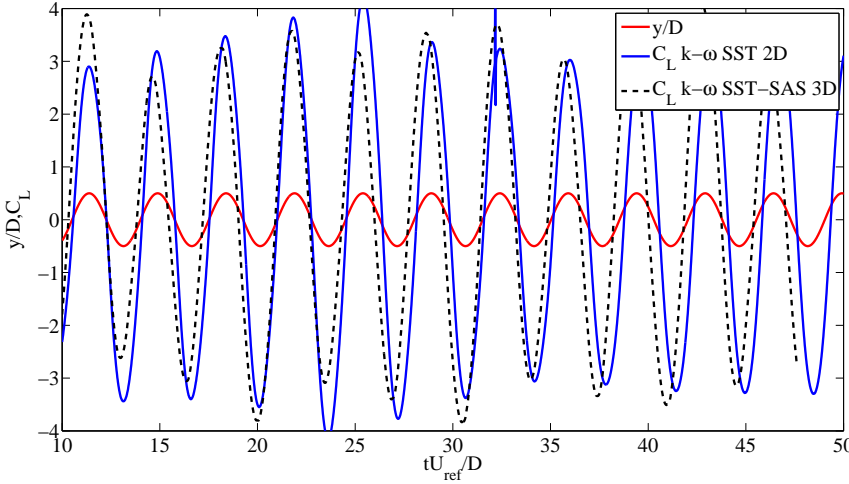


Figure 8.17: Lift time traces from calculations with two-dimensional SST and three-dimensional SST-SAS for  $U_R = 4.50$  and the conditions of Sarpkaya (2004).

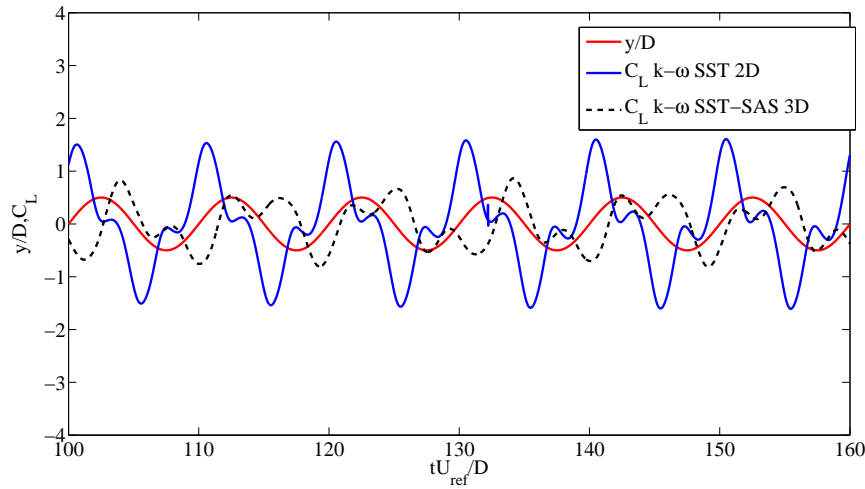


Figure 8.18: Lift time traces from calculations with two-dimensional SST and three-dimensional SST-SAS for  $U_R = 10.0$  and the conditions of Sarpkaya (2004).

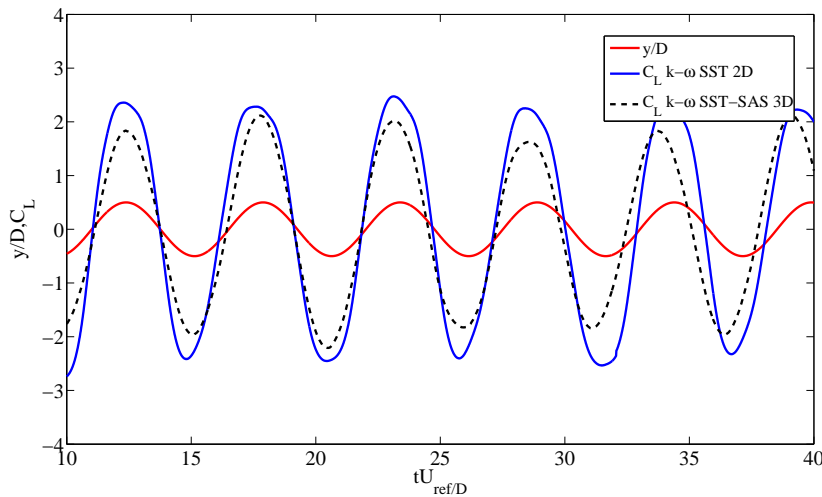


Figure 8.19: Lift time traces from calculations with two-dimensional SST and three-dimensional SST-SAS for  $U_R = 5.50$  and the conditions of Sarpkaya (2004).

Figures 8.21 and 8.22 show the comparison of numerical and experimental results for lift coefficients in phase with velocity from MARIN and Sarpkaya (2004), respectively. Interestingly, both plots show that the two-dimensional  $k-\omega$  SST results display a fair comparison with the experimental data within the resonance region whereas there is much worse comparison out of the lock-in range, especially for Sarpkaya (2004). The same observation done above on the improvements achieved with SAS results for both MARIN and Sarpkaya's experimental values. Figures 8.23 and 8.24 show the comparison of numerical and experimental of lift coefficients in phase with acceleration from MARIN and from Sarpkaya (2004), respectively. Interestingly, the differences between experiments and results

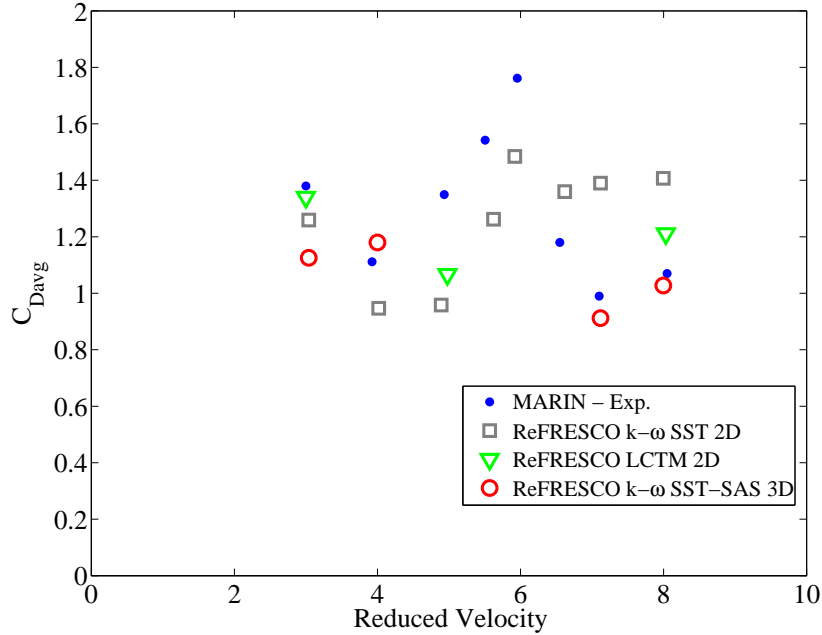


Figure 8.20: Drag coefficients for the calculations compared to the results from MARIN.

with two-dimensional  $k-\omega$  SST are much smaller than seen for the lift coefficients in phase with velocity.

As mentioned before, the lift coefficient in phase with acceleration is related to added mass, so there is a portion which corresponds to inertial fluid effects and a portion corresponding to viscous and turbulent contributions (evidently in a non-linear relation (SARPKAYA, 2004)).

It seems clear from the previous results that the URANS approach displays no difficulty in capturing inertial effects very precisely, whereas viscous effects remains the largest challenge.

As for the lift in phase with acceleration, in both figure 8.23 and 8.24, there is good comparison of the results, especially in the lock-in range. There are very small difference between SST and LCTM results, whereas SAS generally agrees better with the experiments. In order to further illustrate the differences in response in and out of the lock-in regions, figures 8.25 and 8.26 show the imposed motion and lift coefficient traces from MARIN experiments for  $U_R = 5.43$  and  $U_R = 7.80$ , respectively. The lift coefficient traces are filtered retaining  $f < 8$  Hz in order to remove high frequency noise, such as the carriage vibration.

The lift traces for  $U_R = 5.43$ , thus within the lock-in range, are more regular and narrow-banded than for  $U_R = 7.80$ .

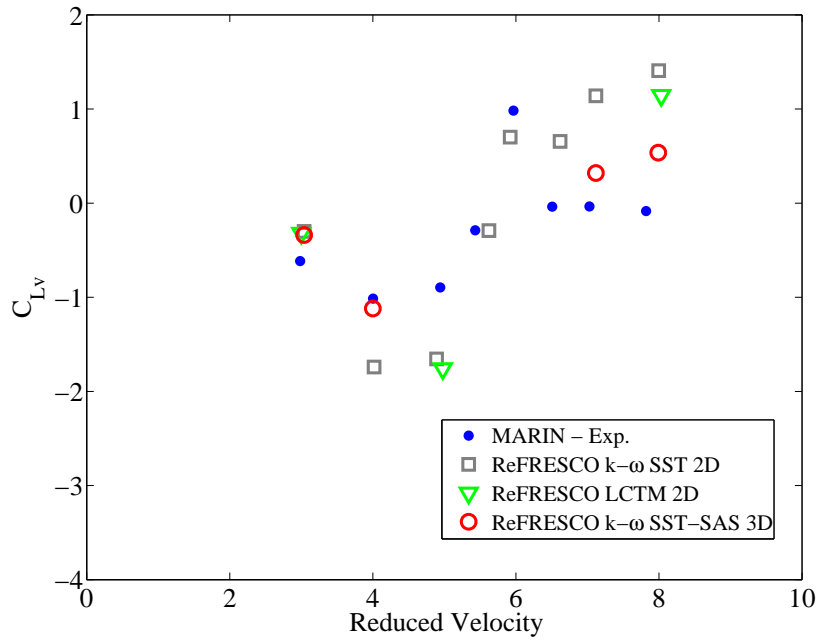


Figure 8.21: Lift coefficients in phase with velocity for the calculations compared to MARIN data.

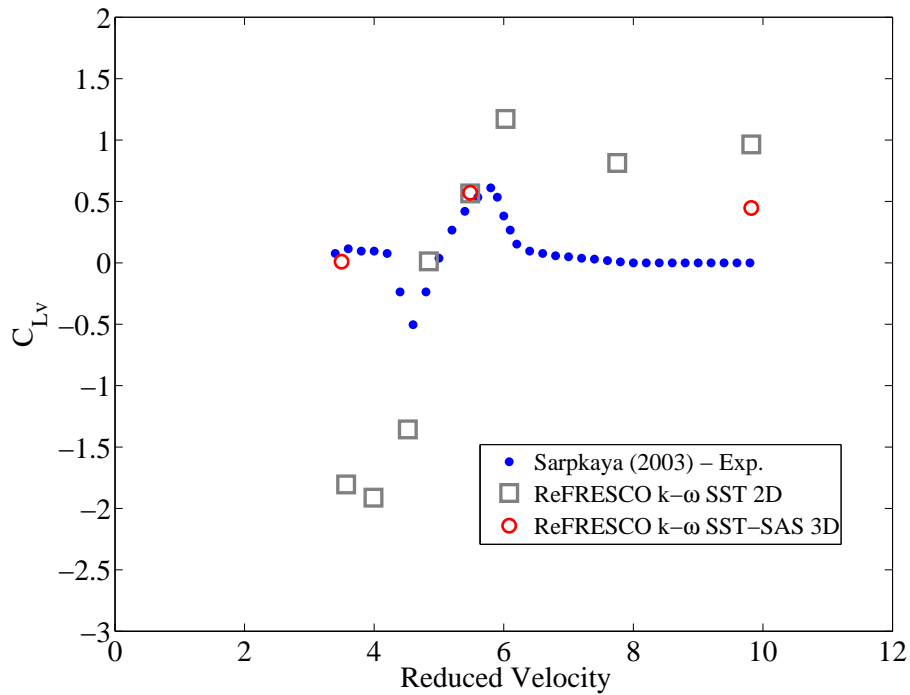


Figure 8.22: Lift coefficients in phase with velocity for the calculations compared to Sarpkaya (2004) data.

It is also interesting to notice that the magnitude of the lift coefficients is larger for  $U_R = 5.43$  than for  $U_R = 7.80$ , reflecting larger coherence and stronger vortices in the

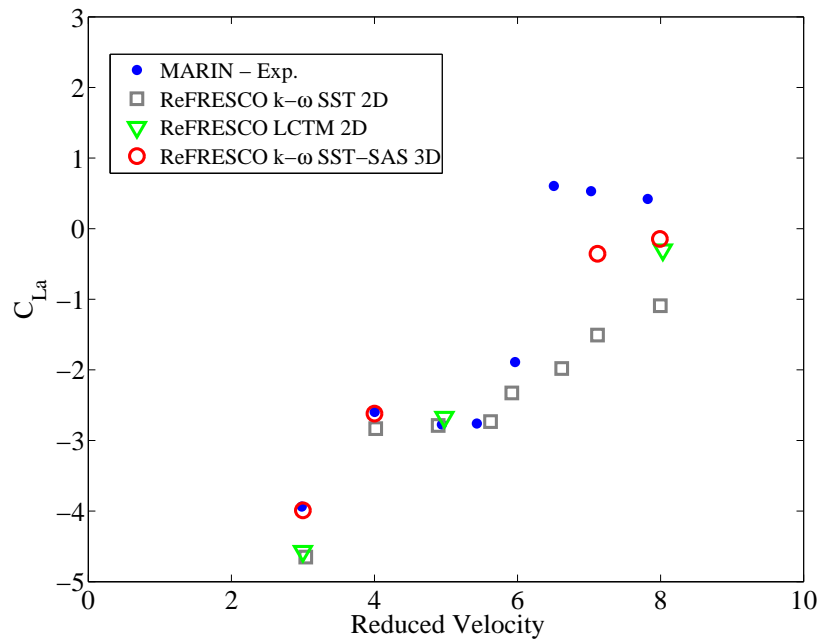


Figure 8.23: Lift coefficients in phase with acceleration for the calculations compared to MARIN data.

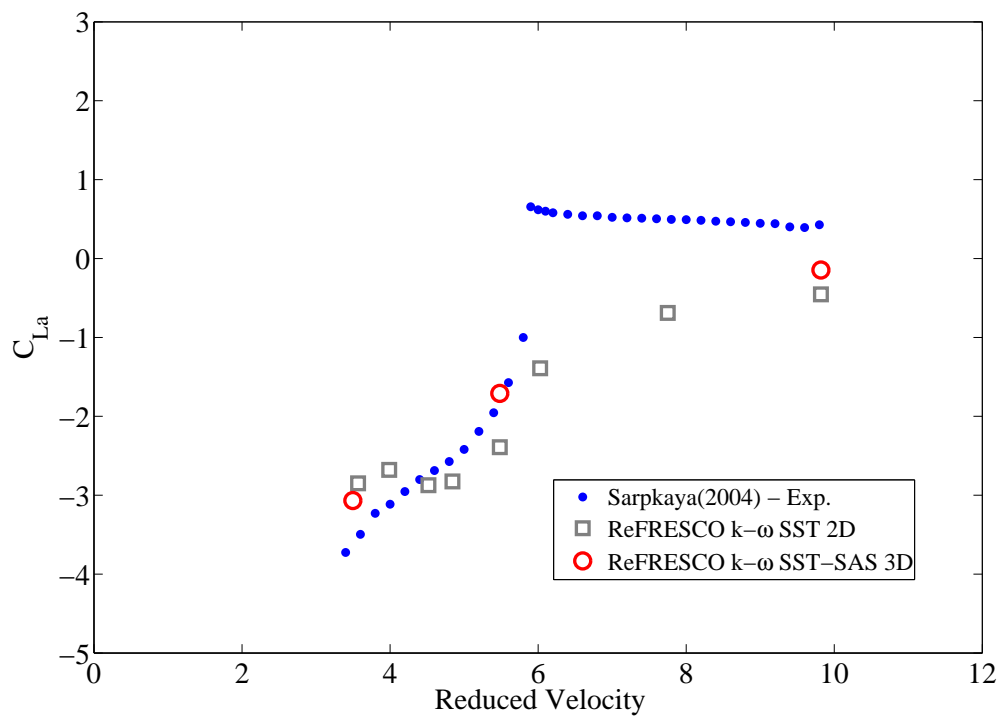


Figure 8.24: Lift coefficients in phase with acceleration for the calculations compared to Sarpkaya (2004) data.

former case. Moreover, it is pointed out that the small amplitude lift loads incur in larger measurement errors, thus the experimental values in unlocked configurations tend to carry

larger errors.

In order to illustrate some of the differences observed between two-dimensional SST and three-dimensional SAS results, figures 8.27 and 8.28 show slices of non-dimensional vorticity in the span-wise direction respectively for  $U_R = 3.50$  and for  $U_R = 5.50$  comparing the two-dimensional SST with the three-dimensional SAS calculations. In the results at  $U_R = 3.50$ , the SST result shows the shedding of more correlated vortices.

Furthermore, it is possible to note in the SAS result that the streamlines are three-dimensional behind the cylinder (as they leave the horizontal plane) and the wake oscillation is stronger in the SST.

Conversely, in the results for  $U_R = 5.50$ , the differences are less marked. However, one still notices stronger vortices in the two-dimensional solution, leading to larger amplitudes as seen in the traces of figure 8.19.

It is furthermore interesting to observe that some three-dimensionality in the shedding of vortices is observed in figure 8.29, in which two superimposed slices of vorticity contours (mid-span and at a distance of 5% of the cylinder span from the top) display some differences in the timing of the shed vortices, which in turn cause differences in the overall phase. For the resonant case, such differences were hardly noticed.

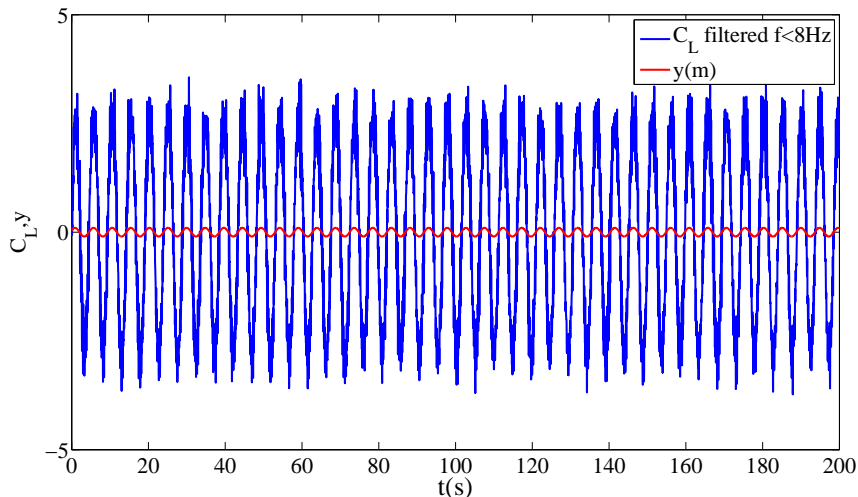


Figure 8.25: MARIN experimental time traces of imposed motions (in red) and measured lift coefficient (in blue) filtered retaining  $f < 8 Hz$  for  $U_R = 5.43$ . The imposed motion frequency in this case is  $f = 0.20 Hz$  and the force trace is filtered to remove the carriage vibration and other high frequency noise.

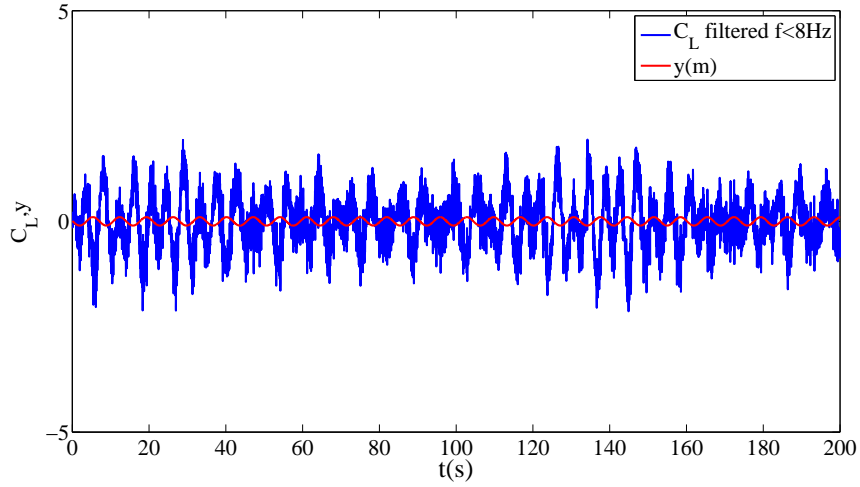


Figure 8.26: MARIN experimental time traces of imposed motions (in red) and measured lift coefficient(in blue) filtered retaining  $f < 8Hz$  for  $U_R = 7.80$ . The imposed motion frequency in this case is  $f = 0.14$  Hz and the force trace is filtered to remove the carriage vibration and other high frequency noise.

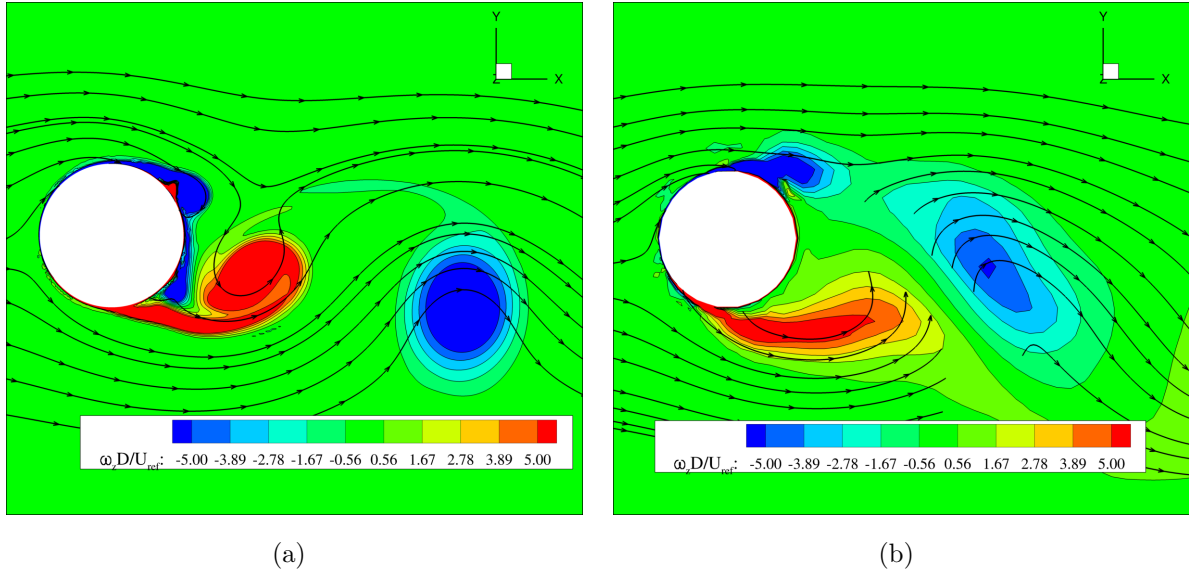


Figure 8.27: Non-dimensional vorticity and streamlines in the  $z$ -direction at the point of maximum lift coefficient with  $U_R = 3.50$  for the Sarpkaya (2004) set of calculations. (a) Calculations with two-dimensional SST. (b) Calculations with three-dimensional SST-SAS (slice taken from mid-span).

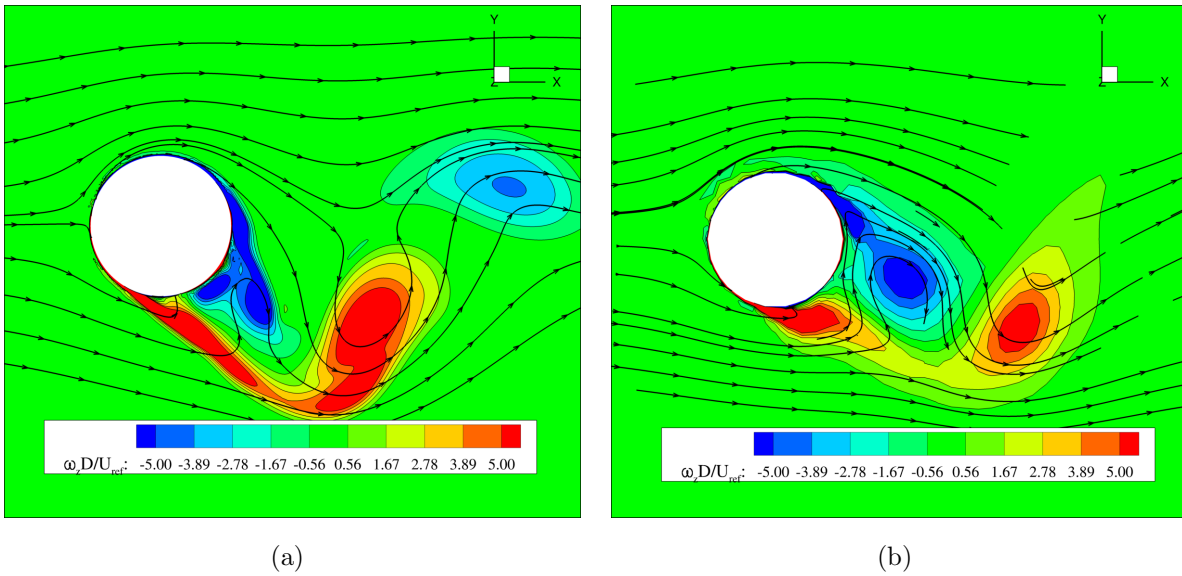


Figure 8.28: Non-dimensional vorticity and streamlines in the z-direction at the point of maximum lift coefficient with  $U_R = 5.50$  for the Sarpkaya (2004) set of calculations. (a) Calculations with two-dimensional SST. (b) Calculations with three-dimensional SST-SAS (slice taken from mid-span).

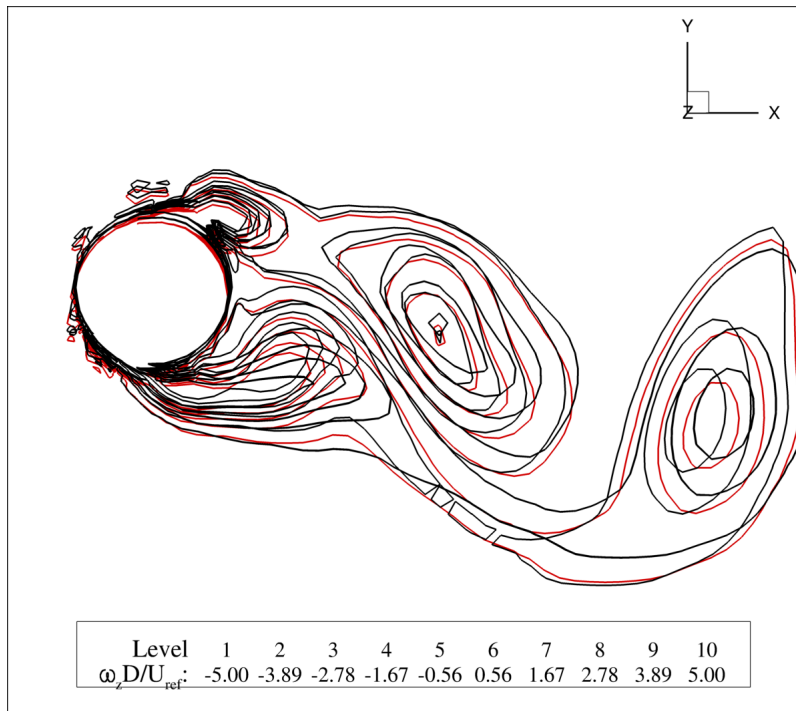


Figure 8.29: Line contours of vorticity in the z-direction at the point of maximum lift coefficient with  $U_R = 3.50$  for the Sarpkaya (2004) set of calculations. Two superimposed slices (mid-span, in black, and at a distance of 5% of the cylinder length from the top boundary, in red) are shown from calculation done with three-dimensional SST-SAS.

## 8.7 Final Remarks of the Chapter

This chapter has shown the application of sinusoidally imposed motions in the transverse direction of the flow with the use of two-dimensional  $k-\omega$  SST, two-dimensional LCTM coupled with  $k-\omega$  SST and three-dimensional  $k-\omega$  SST-SAS in comparison with experimental benchmark data from Gopalkrishnan (1993), Sarpkaya (2004) and experimental data from MARIN.

The range of Reynolds numbers considered in these calculations spans  $Re = 10,000$  to  $Re = 45,000$ , thus in the pre-critical range. It is then natural that transition is not relevant as the Reynolds numbers are low. Consequently, the results obtained with LCTM and SST are quite similar, evidencing that the LCTM did not substantially change the flow character predicted by SST.

Conversely, the comparison between two-dimensional  $k-\omega$  SST and three-dimensional  $k-\omega$  SST-SAS must take into account another interesting issue. The behavior within the locked region is somewhat distinct from the unlocked range. In the locked region, a resonant behavior takes place, in which flow structures are more correlated and coherent, thus stronger vortices are formed. On the other hand, in the unlocked region, there is more irregular force. For this reason, both two-dimensional SST and three-dimensional SST-SAS perform similarly in the locked region, where more coherent flow is observed. In the unlocked region, the increasing irregular behavior associated with more three-dimensional flow is naturally better predicted by SST-SAS than SST, thus force prediction agrees better with experimental results for SST-SAS than for SST.

The following Chapter will present results for the free motions of the rigid cylinder in two degrees of freedom, in which the trend identified in the present Chapter is more marked, namely that the different models perform similarly, particularly in the resonant region.



# Chapter 9

## Rigid Cylinder in 2 Degrees-of-Freedom Free Motions

*This chapter shows the studies and results concerning the implementation of free rigid-body motion capability developed in ReFRESKO for this thesis. In particular, the two degrees-of-freedom vibrations of a rigid cylinder with low mass ratio are studied over a range of reduced velocities. The main objectives are: i) to study the numerical approach and physics involved; ii) to study the behavior of different turbulence models with free body-motions.*

*The numerical results are compared with experimental results from Jauvits & Williamson (2004) and from Franzini (2013).*

*The coupling of state-of-the-art turbulence models and a free-moving body is an original contributions of this thesis.*

### 9.1 Background

Following the structure adopted in this thesis, the implementation of the free rigid cylinder motions in two degrees-of-freedom within the framework of ReFRESKO will be benchmarked against experimental results.

In particular, the low mass ratio experiments from Jauvits & Williamson (2004) and from Franzini (2013) are used herein. In these experiments, single cylinders free to oscillate in two degrees-of-freedom is tested over a wide range of reduced velocities, spanning  $U_R \approx 3.0$  up to  $U_R \approx 14.0$ .

Jauvits & Williamson (2004) have shown that the two degrees-of-freedom (motion in the

transverse and in-line directions) behavior is quite similar compared to the one degree-of-freedom case (motion only in the transverse direction) for  $m^* > 6.0$ : in-line response is negligible for most reduced velocities and the transverse direction response is similar to that of one degree-of-freedom cylinder (KHALAK; WILLIAMSON, 1996; KHALAK; WILLIAMSON, 1997). The one degree-of-freedom behavior is featured by the initial, upper and lower branches of vibration response showed in figure 9.1 reproduced from Jauvits & Williamson (2004). Khalak & Williamson (1996), Khalak & Williamson (1997) have showed that the initial branch is associated to the 2S shedding mode (two single vortices shed each cycle), whereas the upper and lower branches, to the 2P mode (two pairs of vortices shed each cycle). The two peaks within the in-line resonance range correspond to the SS and AS shedding modes, in which one notes the shedding of a symmetric and an asymmetric pair of vortices, respectively.

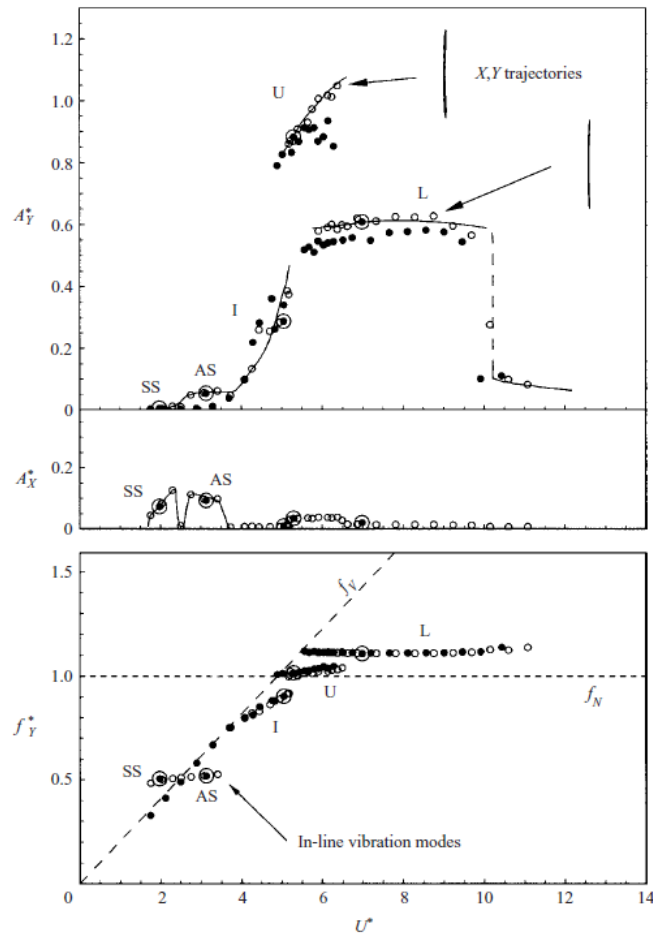


Figure 9.1: Nondimensional transverse ( $A_Y^*$ ) and in-line ( $A_X^*$ ) responses and transverse response frequency ( $f_Y^*$ ) over reduced velocity ( $U^*$ ) for  $m^* = 7.0$ ,  $Re = 2000 - 11000$  and  $(m^* + C_a)\zeta = 0.0117$ . The black symbols correspond to Y-only case and the white, to XY motions (JAUVITS; WILLIAMSON, 2004).

Conversely, Jauvits & Williamson (2004), Pesce & Fujarra (2005), Fujarra et al. (2001), Williamson & Jauvits (2004) among others have more recently reported that the behavior observed for  $m^* < 6.0$  is markedly different compared to  $m^* > 6.0$ : initial, super-upper and lower branches are now observed. Similarly to high mass ratio case, the initial branch is featured by the 2S mode (two single vortices shed each cycle) and the SS and AS modes are present. Much larger transverse vibrations are observed in the super-upper branch (instead of an upper branch) associated with the shedding pattern 2T, featured by two triplets of vortices in each vibration cycle. The lower branch is associated with the 2P mode (shedding of two pairs of vortices each cycle).

Figure 9.2 show the transverse and in-line amplitudes and vibration frequencies for the case with  $m^* = 2.6$  from Jauvits & Williamson (2004). The very distinct response in the super-upper branch is associated with the resonance of the transverse degree-of-freedom, marked by  $f_Y/f_n \approx 1.0$ .

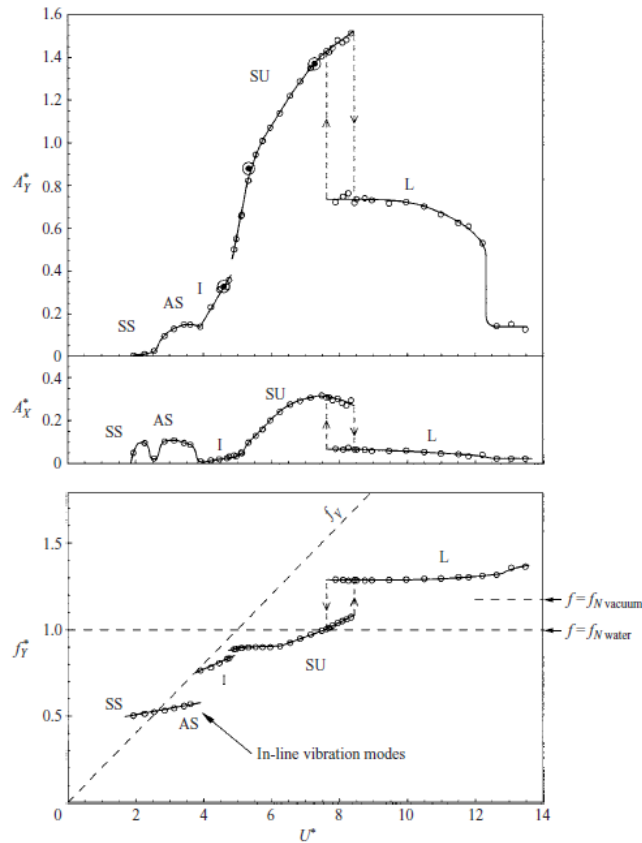


Figure 9.2: Nondimensional transverse ( $A_Y^*$ ) and in-line ( $A_X^*$ ) responses and transverse response frequency ( $f_Y^*$ ) over reduced velocity ( $U^*$ ) for  $m^* = 2.60$ ,  $Re = 1000 - 15000$  and  $(m^* + C_a)\zeta = 0.013$  (JAUVITS; WILLIAMSON, 2004).

## 9.2 Description of the Cases

Two sets of calculations were conducted, namely using the two-dimensional  $k-\omega$  SST and three-dimensional  $k-\omega$  SST-SAS. In both sets of calculations, the dynamic setup is based on the experiments reported in Jauvits & Williamson (2004) and Franzini (2013). Table 9.1 shows the dynamic setup in the experiments and present calculations.

Indeed, the mass ratio  $m^*$  and  $(m^* + C_a^{pot})\zeta$  are both very low in these cases and it is known that this situation might cause numerical problems as the system might be “too light” and large motions take place.

Leroyer (2004) and Bettle (2012) have noted that a Lipschitz condition must be met for stability of the iterative solution process. In their work, the authors comment that the large values of added-mass are the primary cause of such instabilities. They also point out a remedy related to using a relaxation factors blending accelerations values from different iterations. A pseudo added-mass approach can similarly be devised, in such a way that these values vanish upon convergence. In this work, however, the strongly coupled implicit approach has been adopted so that no stability problems were encountered and this has not been necessary.

Moreover, the predictor-corrector scheme nested within the outer loops has been updated at each 10 outer loops or less, and the dynamic equation convergence criteria is set to  $10^{-6}$ , which is typically achieved with two or three predictor iterations.

It is important to note that the computational burden added to the calculations is mostly due to updating the flow field within the outer loops, however, it is still less costly than the procedure implemented in Bettle (2012), in which the outer loops are nested within the predictor corrector scheme and not the contrary as done herein.

Table 9.1: Details of the dynamic setup in the experiments reported in Jauvits & Williamson (2004), Franzini (2013) and the dynamic properties of the system considered herein.

Source	L/D	$Re$	$m^*$	$(m^* + C_a^{pot})\zeta$
(JAUVITS; WILLIAMSON, 2004)	10-7.5	1,000-15,000	2.6	0.013
(FRANZINI, 2013)	13	3,000-15,000	2.6	0.031
Present work	13	4,000-19,000	2.6	0.032

In the results showed herein, the reduced velocity is calculated as:

$$U_R = \frac{U_{ref}}{f_{ny}D}, \quad (9.1)$$

in which  $f_{ny}$  is the natural transverse frequency and  $D$  is the cylinder diameter.

The maximum displacement amplitudes are defined as:

$$(A/D)_{max} = \frac{A_{max} - A_{min}}{2D}. \quad (9.2)$$

### 9.3 Setup and Discretization

Figure 9.3 shows the grid layout and boundary conditions used in the calculations presented herein. In a similar way, for the imposed motions cases, the top and bottom boundaries correspond to symmetry condition, the farfield boundary is composed of an inflow condition (38% of the circumference) and a pressure outflow boundary condition for the remainder of the far-field boundary.

Moreover, the far-field boundary is located at a distance of  $20D$  from the cylinder axis, ensuring that there is negligible influence in the flow near the cylinder. The length in the span-wise is  $13D$ , hence an aspect ratio of 13 is chosen for the calculations.

The grids are the same used for the imposed motions calculations at  $Re = 45,000$  presented in Chapter 8, as the Reynolds numbers showed in the present exercise are similar but smaller than those for the imposed cylinder case (in the present case, the maximum Reynolds number tested is  $Re = 14,000$  and in that case is  $Re = 45,000$ ). It is worth noting that two-dimensional and three-dimensional calculations are done herein, respectively using the  $k-\omega$  SST and  $k-\omega$  SST-SAS.

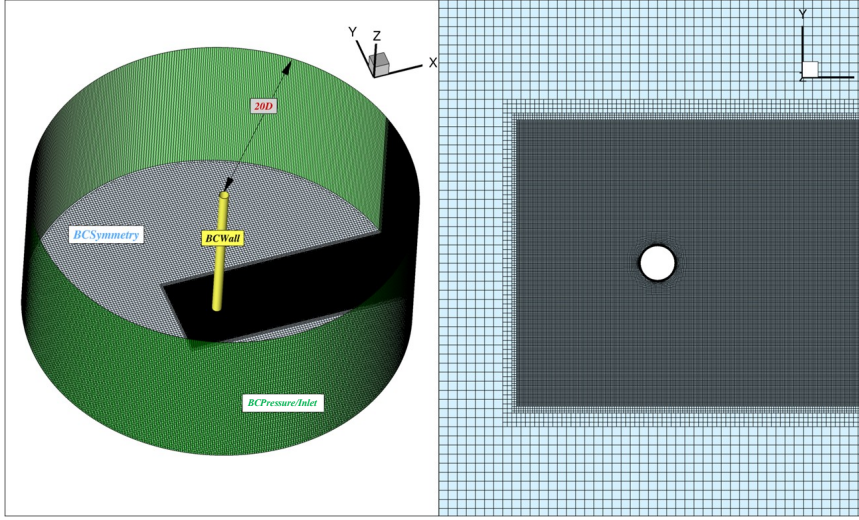


Figure 9.3: Setup and grid layout used in the calculations with two degree-of-freedom motions.

Table 9.2 and 9.3 present the details of the grid and time steps used in a sensitivity analysis respectively for the two dimensional  $k-\omega$  SST and three-dimensional  $k-\omega$  SST-SAS calculations. The convergence of transverse and in-line amplitudes as a function of time step refinement is oscillatory in both cases but relative variations smaller than 5% is noticed for the transverse amplitudes. It was concluded that using  $T_{hydro}/\Delta t = 540$  ( $T_{hydro} = D/U$ ) is appropriate for both two-dimensional and three-dimensional calculations. Very similar computational times have been required to the imposed motion calculations: for the two-dimensional calculations, up to two months in the HPC cluster. For the three-dimensional calculations, computational times have been up to near three months with the finest discretization.

Table 9.2: Details of the grid and sensitivity analysis for the two-dimensional  $k-\omega$  SST calculations.

Num. of cells	Circ. cells	Time steps/Nat. freq.	$T_{hydro}/\Delta t$	$y_{max}^+$	$y_{max}/D$	$x_{max}/D$
777,446	608	540	1288	0.04	1.38	0.34
	608	270	644	0.07	1.41	0.45
	608	180	429	0.07	1.22	0.28

Table 9.3: Details of the grid and sensitivity analysis for the three-dimensional  $k\text{-}\omega$  SST-SAS calculations.

Num. of cells	Circ. cells	Time steps/Nat. freq.	$T_{hydro}/\Delta t$	$y_{max}^+$	$y_{max}/D$	$x_{max}/D$
	432	600	1400	0.90	1.26	0.34
4,061,916	432	540	1288	0.92	1.05	0.31
	432	270	644	0.84	0.85	0.30

## 9.4 Iterative Convergence

Figure 9.4 and 9.5 show typical iterative convergence of the calculations. The criteria is set at  $L_\infty < 10^{-4}$ . As done for the imposed motion calculations, the criteria for all quantities is defined as  $L_\infty < 10^{-4}$ , both for two-dimensional and three-dimensional calculations respectively done with  $k\text{-}\omega$  SST and  $k\text{-}\omega$  SST-SAS. As commented above, the criteria for the predictor-corrector scheme is  $10^{-6}$ , which adds little burden to the computational process.

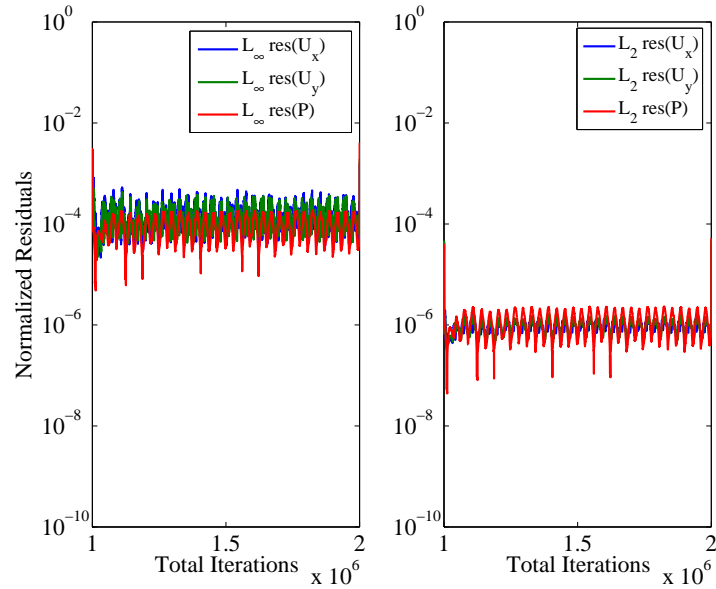


Figure 9.4: Typical iterative convergence for the velocity and pressure.

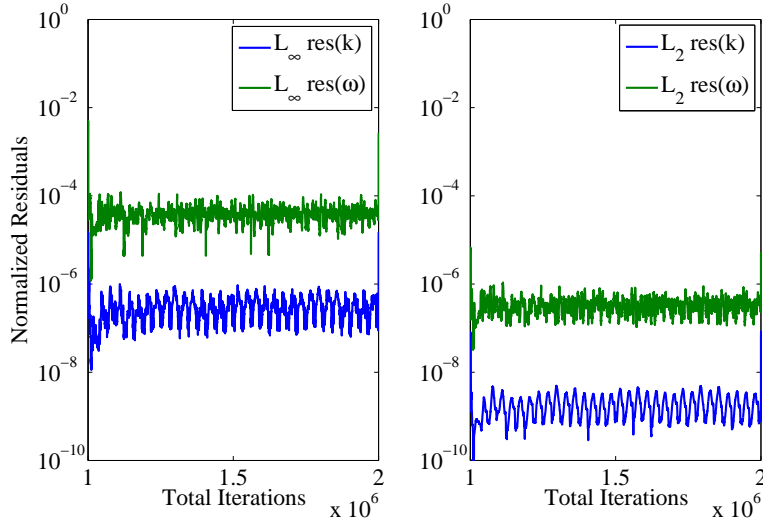


Figure 9.5: Typical iterative convergence for the turbulent quantities.

## 9.5 Decay Analysis

Decay analyses are carried out with the two-dimensional  $k$ - $\omega$  SST and the three-dimensional  $k$ - $\omega$  SST-SAS calculations to ensure that the dynamic properties of the system are appropriately modeled and to obtain natural period and damping values. The decay is modelled by the following equation:

$$m\ddot{y} + c\dot{y} + ky = 0, \quad (9.3)$$

in which the damping coefficient is defined as:

$$\zeta = \frac{c}{2M_{total}\omega_n}, \quad (9.4)$$

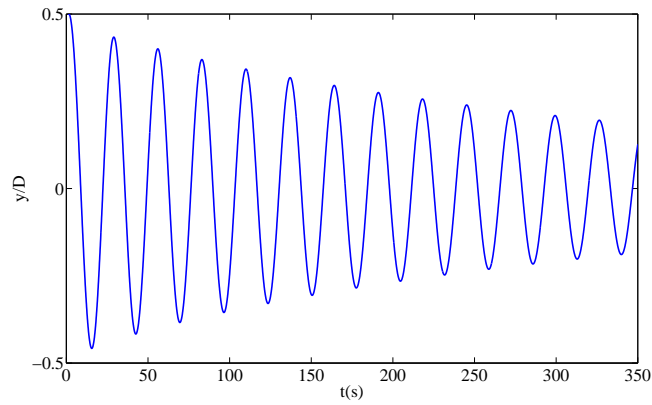
in which  $M_{total}$  includes structural and added mass and  $\omega_n$  is the natural frequency of vibration in the transverse direction.

In these calculations, initial uniform velocity field with  $U = 0.0001m/s$  is applied and an initial displacement of  $0.5D$  is given and the system is left to decay. The natural period and damping are calculated by means of standard decay analysis method (CHAKRABARTI, 1994).

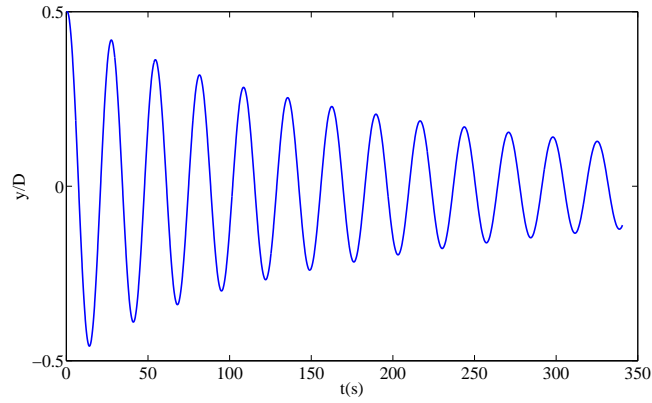
Table 9.4 shows the natural frequencies and damping values obtained in the decay analysis for the two-dimensional and three-dimensional calculations, whereas figure 9.6 shows the time traces. Negligible difference is observed.

Table 9.4: Natural periods and damping values for the two-dimensional and three-dimensional calculations.

Case	Natural frequency (Hz)	$\zeta_{linear}$
k- $\omega$ SST 2D	0.037	0.8%
k- $\omega$ SST-SAS 3D	0.037	0.9%



(a)



(b)

Figure 9.6: Time traces of the transverse motions in the decay calculations. (a) two-dimensional calculations with k- $\omega$  SST. (b) three-dimensional calculations with k- $\omega$  SST-SAS.

## 9.6 Vortex-Induced Vibrations

Figure 9.7 shows the transverse and in-line non-dimensional amplitudes of vibration from the calculations done with two-dimensional  $k-\omega$  SST and three-dimensional  $k-\omega$  SST-SAS compared to the results from Jauvits & Williamson (2004), Franzini (2013).

Regarding the in-line motions, similar behavior is observed for the calculations and for the experiments. The in-line resonance near  $U_R \approx 3.0$  is observed as well as the high amplitude response reaching  $x/D \approx 0.4$ , due to coupling with the transverse motions. There is no discernible difference in the behavior between the results from the two models.

Regarding the amplitudes in the transverse motions, the calculations with both SST and SST-SAS capture the experimental trends: amplitudes in the initial, super upper branches agree well with the experimental results, although the SST-SAS response shows earlier transition from the super-upper to lower branch than SST and slightly lower peak amplitude. The amplitudes in the lower branch are somewhat higher than observed in the experiments for both sets of calculations.

It is quite interesting to observe that not only the trends, but also the very high level of amplitudes over  $y/D = 1.0$  are captured in both cases, indicating that the performance of both models is similar over the complete range of reduced velocities. Note also that the Reynolds numbers in these calculations are ranging  $Re \approx 1,000 - 10,000$ , in which it has been shown that it is quite troublesome to capture the experimental force measurements in the fixed cylinder (Chapters 6 and 7).

Conversely, for  $Re = 10,000$ , the imposed motion calculations showed in Chapter 8 that the agreement between the results with different turbulence models and experiments from Gopalkrishnan (1993) was better than seen for the fixed cylinder case, due to the imposed motion effects. The results showed in this Chapter display further improvements in the agreement between numerical results, mainly in terms of amplitudes.

In the real environment, the structure response filters the wide turbulent spectrum, in such a way that the high energy frequencies influence the motions and flow details such as instabilities and small scale turbulence are relatively less important compared to the fixed cylinder case. It is also important to note in this regard that cylinder forces are much more sensitive to those aspects than cylinder motions, which is more relevant in the resonance range.

Figure 9.8 shows the ratio between transverse vibration frequencies and transverse natural frequency over the reduced velocities. The range  $U_R = 2.0 - 4.0$  corresponds to the

initial branch. One notes one point for  $U_R = 2.5$ , in which  $f_y/F_{ny} \approx 1.0$ , characteristic of indefinite excitation amplitude, due to a weak vortex shedding. A few other points at higher reduced velocities display  $f_y/f_{ny} \approx 0.5$ , which corresponds to the initial branch behavior, with high in-line response at twice the natural vibration frequency.

For higher reduced velocities, a stronger synchronization behavior is noticed with  $f_y/f_{ny}$  slightly lower than 1.0 in the calculations with both turbulence models and in the experiments. That interesting behavior of vibration frequency was pointed out by Khalak & Williamson (1997): the vibration frequency follows neither the Strouhal frequency nor the natural frequency  $f_{ny}$  remaining slightly below it, in a clear difference between the experimental results with low and high mass ratio as, in the latter, the frequency locks onto the natural frequency. It is only near  $U_R = 7.5$  that  $f_y/f_{ny} \approx 1.0$  for the two-dimensional SST, which corresponds to the peak amplitude response, see figure 9.7. For the same reduced velocity, the result of the three-dimensional calculation with SST-SAS has shifted to the lower branch with  $f_y/f_{ny} > 1.0$  and lower response amplitude. The response in the lower branch is marked by  $f_y/f_{ny} > 1.0$ , with increasing values that tend more closely to a linear relation between frequency and reduced velocity.

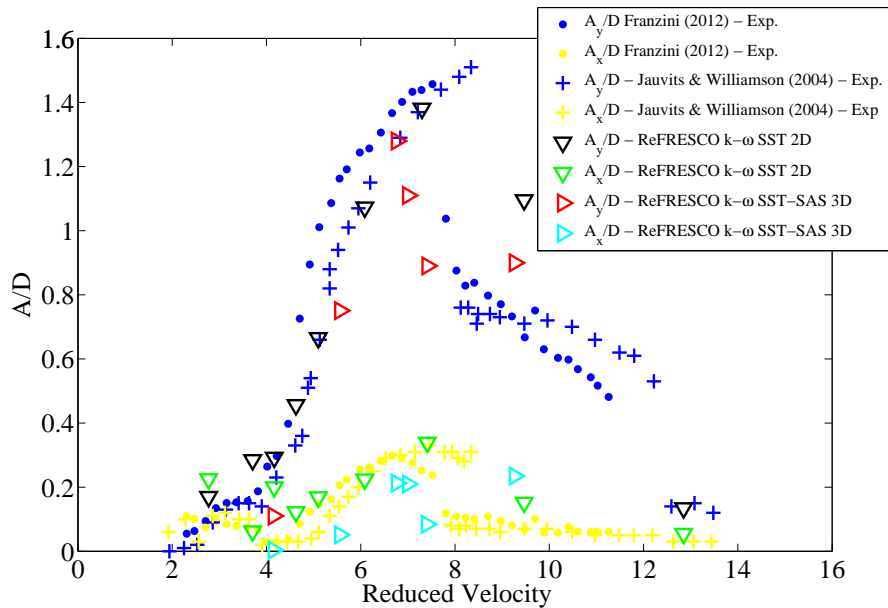


Figure 9.7: Non-dimensional amplitudes over reduced velocity of two degrees-of-freedom free oscillating cylinder compared to Franzini (2013) and Jauvits & Williamson (2004).

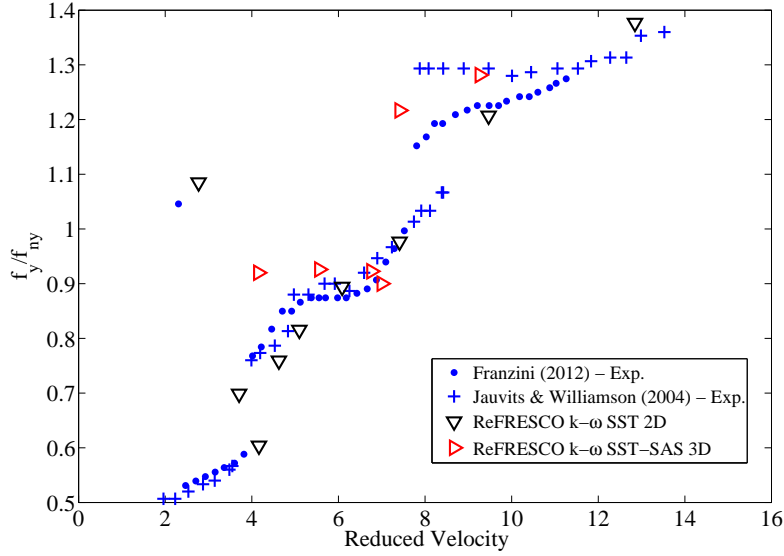


Figure 9.8: Ratio between transverse vibration frequency and transverse natural frequency over reduced velocity for two degrees-of-freedom free oscillating cylinder compared to Franzini (2013) and Jauvits & Williamson (2004).

The average drag coefficients over reduced velocities are presented in figure 9.9. A fair comparison between the two-dimensional SST and experiments is seen, somewhat closer than that of the three-dimensional SST-SAS results. For both cases, however, the results are slightly over-predicted in the lower branch.

From a phenomenological perspective, as discussed by Khalak & Williamson (1997), there is a massive increase of the average drag coefficient magnitude compared to the fixed cylinder case, both in experiments and in the present calculations.

From the experimental standpoint, the average drag coefficient showed in Chapter 6 is  $C_{Davg} = 1.1$  for  $Re = 10,000$ , whereas in the experiments in Franzini (2013),  $C_{Davg} = 3.5$  for  $U_R = 7.5$  and  $Re \approx 10,000$ , thus three-times the stationary value. Conversely, the two-dimensional SST value for the fixed cylinder is  $C_{Davg} = 1.5$  and for the moving cylinder,  $C_{Davg} = 3.0$ , in a two-fold increase. This is mainly due to the resonant behavior in the transverse direction. Similarly, figure 9.10 and 9.11 respectively show the RMS of the drag and lift over reduced velocities from the calculations and experiments.

A large amplification of the fluctuations in the drag forces is noticed both in the experimental and numerical results with a peak at  $U_R \approx 6.5$ , thus somewhat below the peak amplitude response at  $U_R = 7.5$ .

Results with both turbulence models follow the experimental trends and fairly agree in

quantitative terms for the drag RMS. The RMS of lift coefficients peaks at  $U_R \approx 5.0$ , near the transition from the initial to the supper upper branch, in which large lift fluctuations are seen.

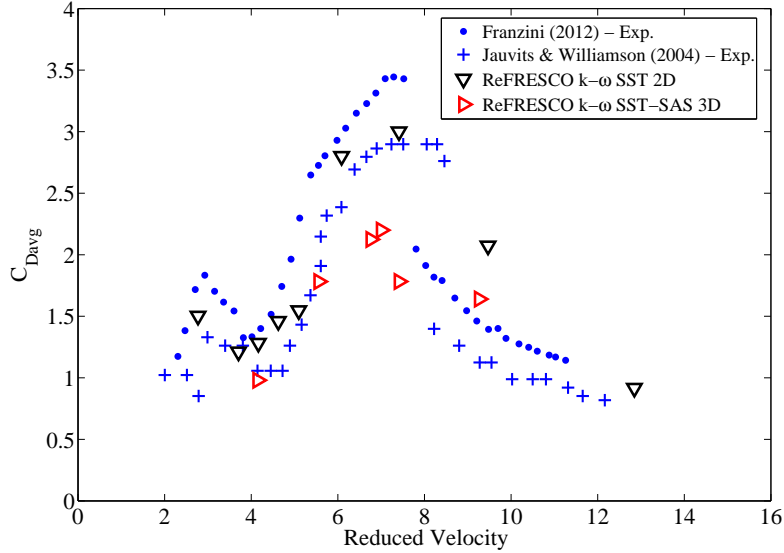


Figure 9.9: Average drag coefficients over reduced velocity for the two degrees-of-freedom free oscillating cylinder compared to the experimental results in Franzini (2013) and Jauvits & Williamson (2004).

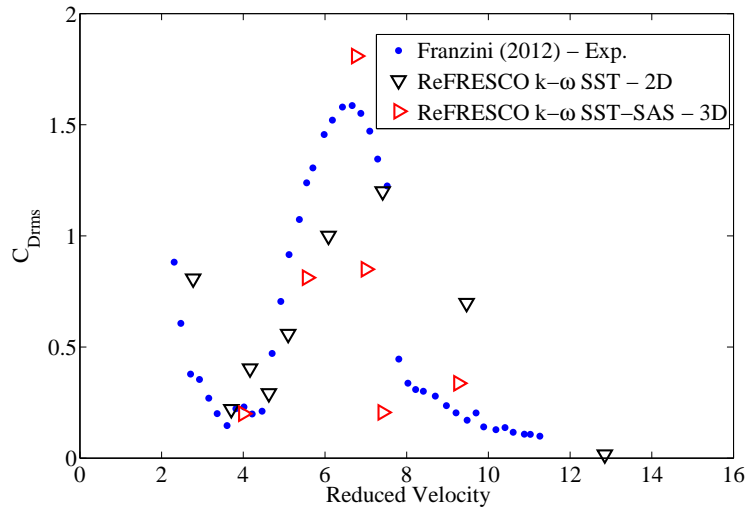


Figure 9.10: RMS of drag coefficients over reduced velocity for the two degrees-of-freedom free oscillating cylinder compared to the experimental results in Franzini (2013).

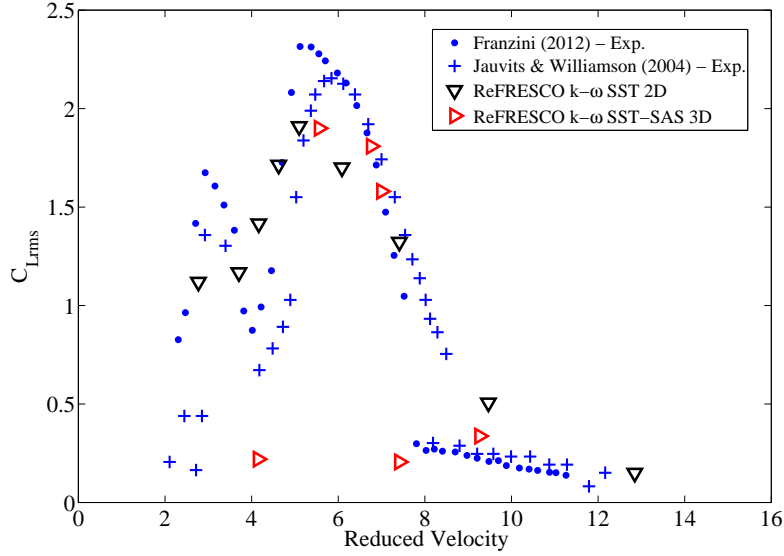


Figure 9.11: RMS of lift coefficients for the two degrees-of-freedom free oscillating cylinder over reduced velocity compared to the experimental results in Franzini (2013) and Jauvits & Williamson (2004).

The added mass coefficient results that will be discussed and presented herein pertain the total hydrodynamic force in phase with acceleration as commonly done in offshore engineering. This issue has been much discussed in the literature, for instance by Sarpkaya (2001), Williamson & Govardhan (2004). The former has shown that the viscous and inertia forces do not operate independently and it is not possible to divide the time-dependent force into an inviscid inertial force and a viscous force, both for longitudinal and transverse forces, meaning that the added mass coefficients showed herein are composed of both inertial and viscous parts in a non-linear relation. Sarpkaya stated that “the creation, convection, and diffusion of vorticity affect both components of the force, because the unsteady flow is neither a juxtaposition of steady-flow states nor a juxtaposition of impulsively started unsteady-flow states”. That means that it is generally not correct to assert that the added mass reflects only the inertial or potential flow content of the flow. In order to calculate the added mass, the procedure applied herein is adapted from Fujarra & Pesce (2002):

$$\frac{F[F_L]}{F[y]} = m_a \omega^2 - i c_v \omega, \quad (9.5)$$

in which  $F[\cdot]$  is the Fourier transform of the time signature. In this frequency domain approach, the added mass is determined for each frequency band and the added mass results showed herein correspond to the peak-energy frequency of the transverse displacement.

Figure 9.12 shows the added mass coefficients calculated by means of equation 9.5 in comparison with the experimental results from Franzini (2013). For low reduced velocities, the added mass tends to large values, which can be seen in a didactic manner as a large virtual mass that the accelerating system has to pull.

The calculations are somewhat spread in that region reflecting a weakly synchronized force due to vortex shedding, in turn meaning that the transverse motions are not predominantly determined by vortex shedding.

As reduced velocity is increased, the added mass decreases and an abrupt change is seen from the initial to the super-upper branch at  $U_R \approx 4.0$ . In the super-upper branch,  $4.0 < U_R < 7.5$ , the added mass coefficients vary between  $C_a = 4.0$  and  $C_a = 0$  and the experimental trend and values are closely followed by calculations with both two-dimensional SST and three-dimensional SST-SAS. The zero-crossing added mass is nearly at  $U_R = 7.5$ , indicating the resonant peak response. For  $U_R > 7.5$ , there is an asymptotic behavior of the added mass coefficients towards  $C_a = -1$ , which is characteristic of linear dynamic systems excited with frequencies much larger than their natural frequencies (CUNHA, 2005).

An interesting conclusion can be drawn from the results showed previously: there are very small differences in all the results showed with the two-dimensional and three-dimensional calculations done with  $k-\omega$  SST and  $k-\omega$  SST-SAS, respectively, as observed in the example of figure 9.13, which shows comparisons between forces and motions with these two models. This is consistent with the argument that the small scale flow details such as small scale turbulent eddies and non-isotropic effects are less relevant for the free-moving cylinder than for the fixed cylinder.

In the following sections, the dynamic and flow behavior will be more closely analyzed in each of the response branches.

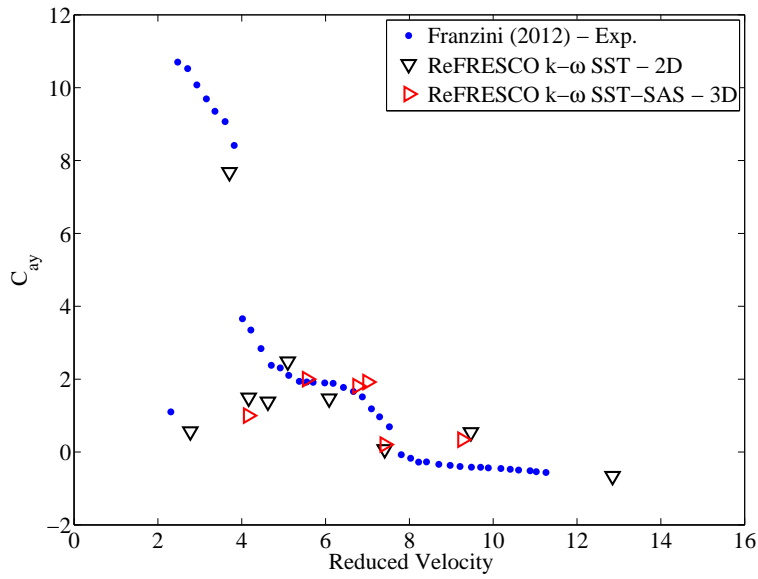


Figure 9.12: Added mass coefficients over reduced velocity for the two degrees-of-freedom free oscillating cylinder compared to the experimental results in Franzini (2013).

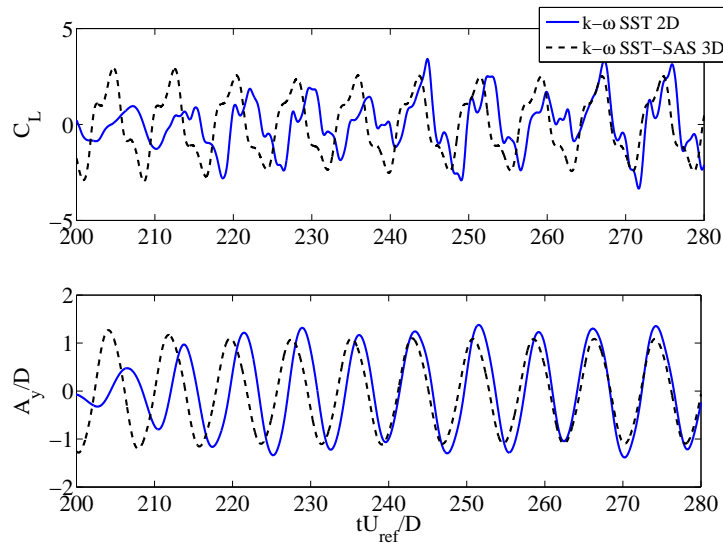


Figure 9.13: Time traces of transverse vibrations and forces comparing two-dimensional SST and three-dimensional SST-SAS for the peak-response reduced velocities (respectively  $U_R = 7.1$  and  $U_R = 7.5$ ).

## 9.7 Initial Branch

Figure 9.14 shows the time traces of in-line and transverse response and their power spectra, whereas figure 9.15 shows the drag and lift coefficients with their spectra. A quite irregular behavior of the in-line response and drag coefficients is noticed reflecting on spread power spectra. Nevertheless, the magnitude of the fluctuations is quite small in both motions and drag forces, as also noticed in the experiments.

The transverse results, conversely, are more regular, however remaining at low amplitudes. The peak energy non-dimensional frequency of the lift coefficients and transverse vibrations is  $f = f_{dim}D/V$ , so it can be directly compared to Strouhal number,  $St$ . In this case, the peak energy frequency is  $f = 0.19$ , which is very near the experimental value for the stationary cylinder  $St = 0.2$ , for  $Re = 5,400$ . That means that the Strouhal relation is followed in this case, a result already shown in figure 9.8 and in the experimental results from Jauvits & Williamson (2004) and Franzini (2013). Moreover, the in-inline peak frequency corresponds to twice the transverse peak energy frequency, which takes place due to the fact that one in-line cycle is comprised of the shedding of one vortex and two, for transverse direction.

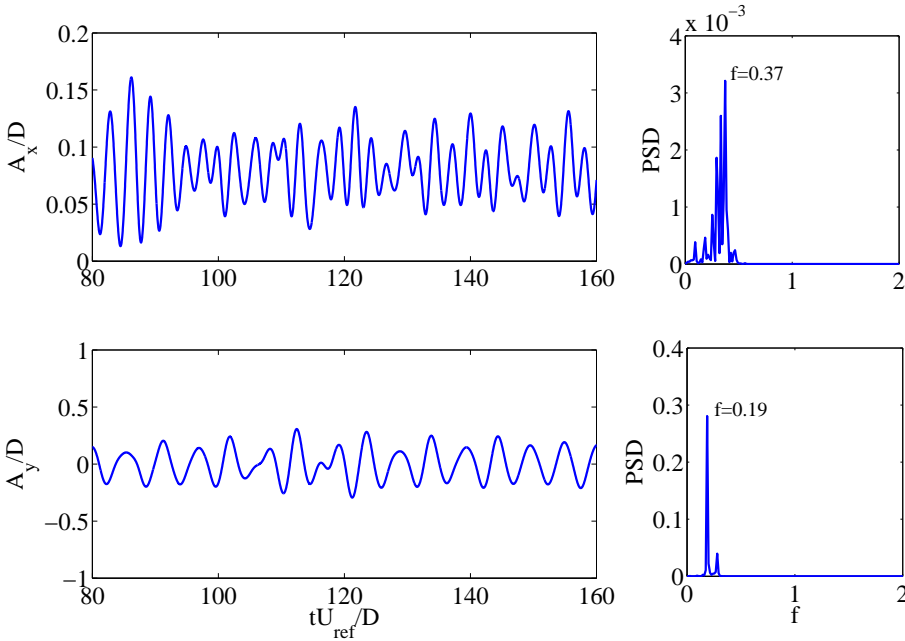


Figure 9.14: Time signatures of non-dimensional in-line and transverse motions and power spectra for  $U_R = 4.0$  with the two-dimensional  $k-\omega$  SST. The frequencies are made non-dimensional by multiplication with  $D/V$ .

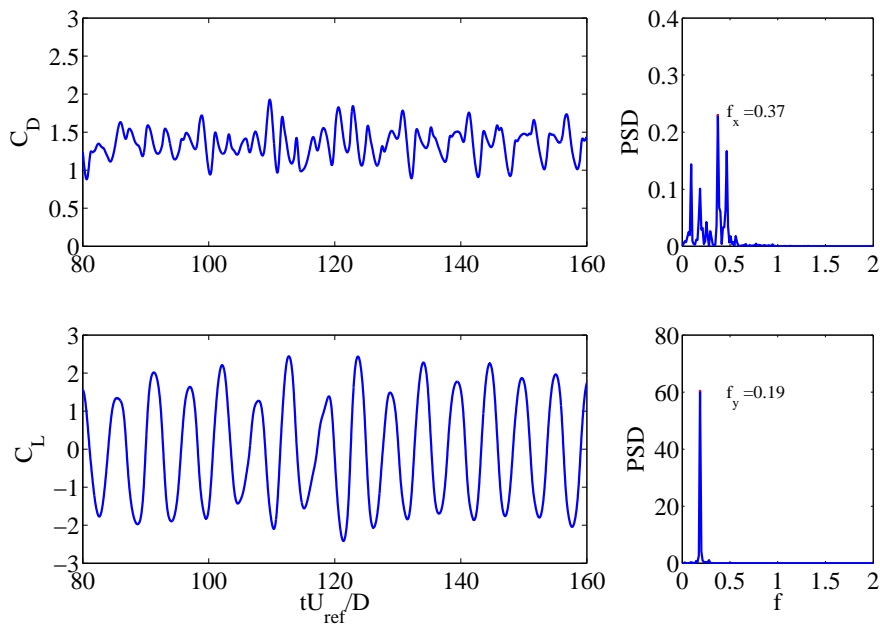


Figure 9.15: Time signatures of drag and lift coefficients and power spectra for  $U_R = 4.0$  with the two-dimensional  $k-\omega$  SST. The frequencies are made non-dimensional by multiplication with  $D/V$ .

The non-dimensional  $z$ -vorticity is presented in figure 9.16, in which the 2S mode is evident as one pair of vortices is shed each cycle, similarly to the von Kármán vortex street.

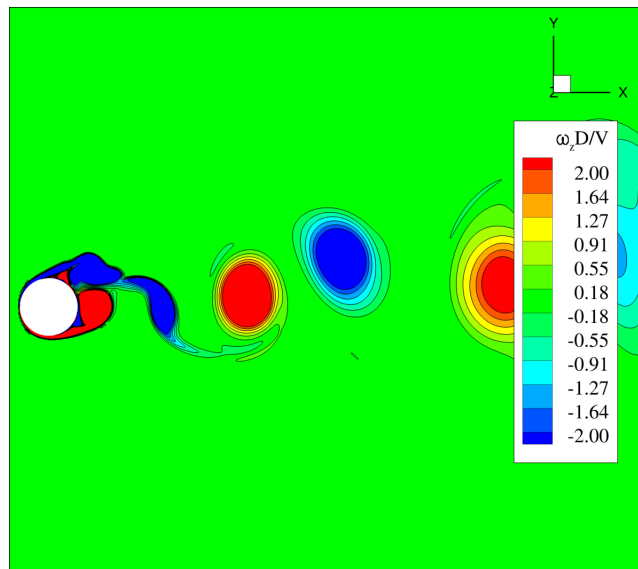


Figure 9.16: Non-dimensional  $z$ -vorticity at the instant of minimum transverse displacement for  $U_R = 4.0$  calculated with the two-dimensional  $k-\omega$  SST.

## 9.8 Super Upper Branch

Within the super-upper branch, the both in-line and transverse amplitudes are larger than in the initial branch, as seen in figure 9.17, as well as the drag and lift forces showed in figure 9.18.

The in-line motion results and drag coefficients show large fluctuations and somewhat irregular behavior. The transverse motions are quite regular and with a very well defined frequency  $f = 0.13$ , thus below the Strouhal number  $St = 0.2$ .

The lift time trace displays large energy at the same frequency  $f = 0.13$ , but also discernible energy at three-times the shedding frequency, which Jauvits & Williamson (2004) found to be related to the 2T mode (two triplets of vortices are shed in each cycle). Figure 9.19 shows the non-dimensional vorticity at the minimum displacement instant, in which it is possible to identify the 2T shedding mode, with three vortices shed each half cycle.

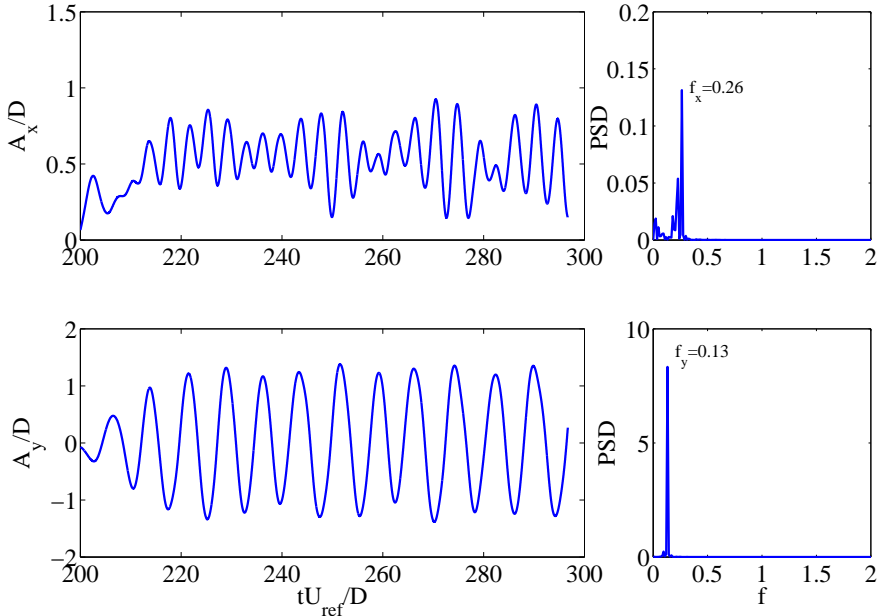


Figure 9.17: Time signatures of non-dimensional in-line and transverse motions and power spectra for  $U_R = 7.5$  with the two-dimensional  $k-\omega$  SST. The frequencies are made non-dimensional by multiplication with  $D/V$ .

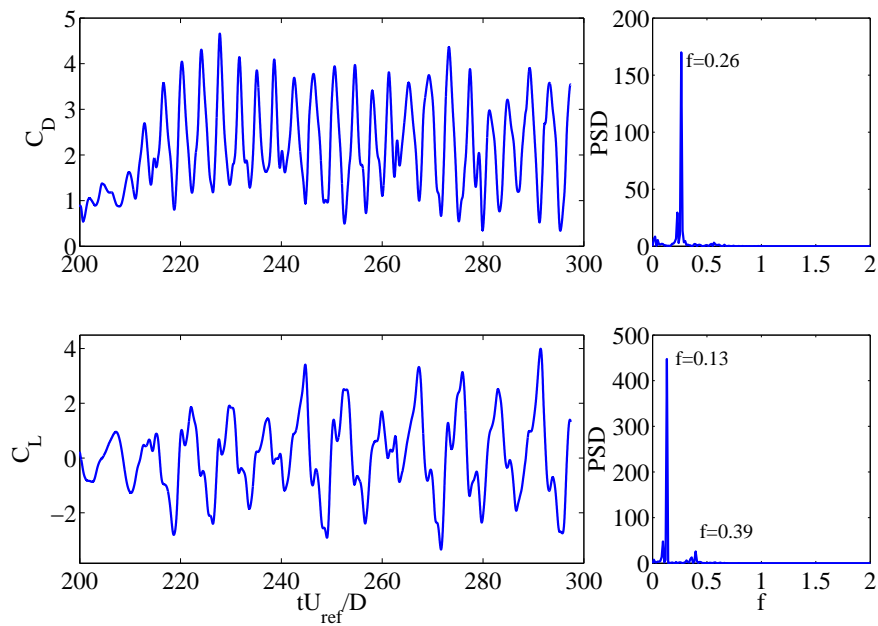


Figure 9.18: Time signatures of drag and lift coefficients and power spectra for  $U_R = 7.5$  with the two-dimensional  $k-\omega$  SST. The frequencies are made non-dimensional by multiplication with  $D/V$ .

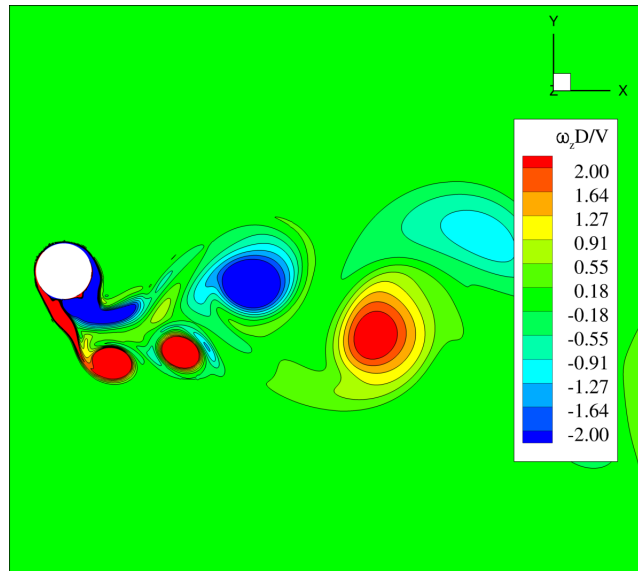


Figure 9.19: Non-dimensional  $z$ -vorticity at the instant of minimum transverse displacement for  $U_R = 7.5$  calculated with the two-dimensional  $k-\omega$  SST.

## 9.9 Lower Branch

In the lower branch, small in-line and transverse motion amplitudes are seen in figure 9.20. Figure 9.21 shows the drag and lift coefficients and power spectra. The in-line vibration and drag loads show small fluctuations and amplitudes, whereas the transverse motion display irregular and low-amplitude motions, in spite of regular lift trace. The transverse motion frequency is at  $f = 0.14$ , thus lower than what the Strouhal relation would indicate.

Figure 9.22 shows the shedding pattern in the lower branch, namely the 2P mode, with two pairs of vortices shed each cycle.

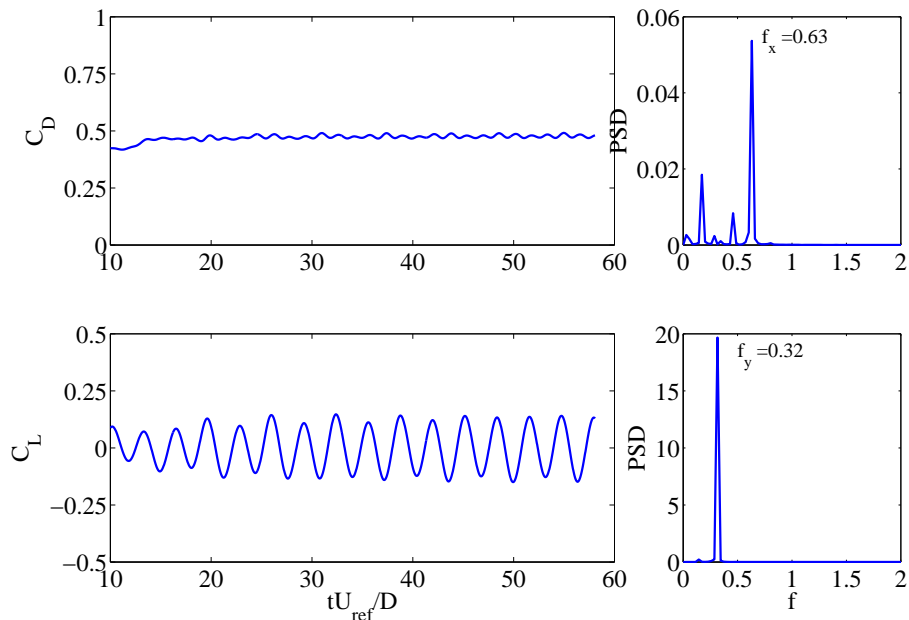


Figure 9.20: Time signatures of non-dimensional in-line and transverse motions and power spectra for  $U_R = 13.0$  with the two-dimensional  $k-\omega$  SST. The frequencies are made non-dimensional by multiplication with  $D/V$ .

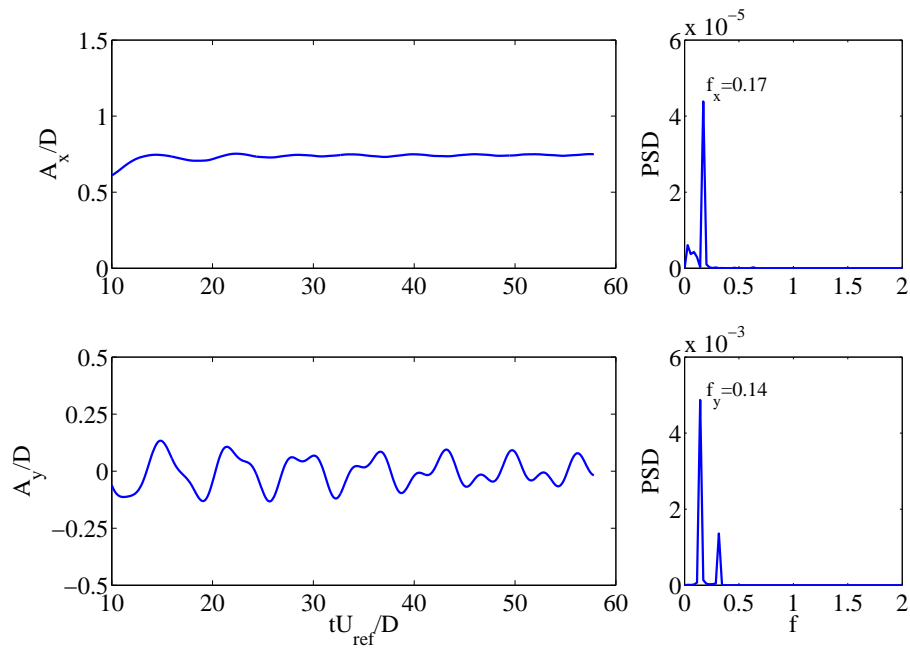


Figure 9.21: Time signatures of drag and lift coefficients and power spectra for  $U_R = 13.0$  with the two-dimensional  $k-\omega$  SST. The frequencies are made non-dimensional by multiplication with  $D/V$ .

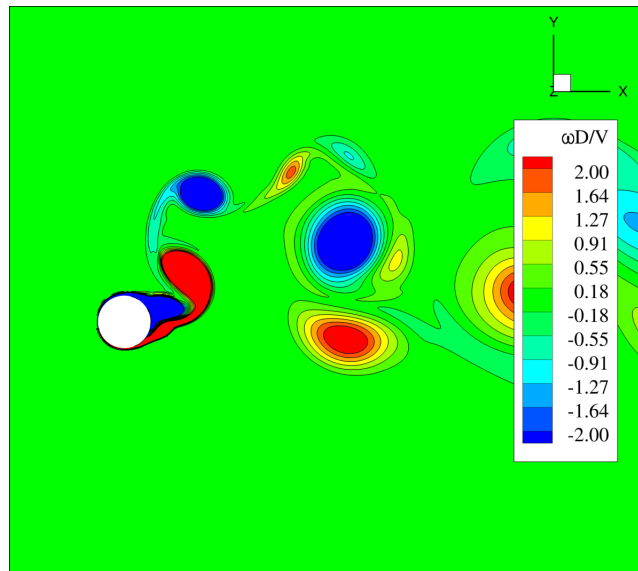


Figure 9.22: Non-dimensional  $z$ -vorticity at the instant of minimum transverse displacement for  $U_R = 13.0$  calculated with the two-dimensional  $k-\omega$  SST.

## 9.10 Final Remarks of this Chapter

The calculations presented herein concern the two degrees-of-freedom vortex-induced vibrations of a cylinder with  $m^* = 2.6$  and  $Re = 4,000 - 19,000$ .

Previous studies in the literature have usually showed high mass-ratio structures, one degree-of-freedom systems and very low Reynolds. Few publications have presented conditions such as the ones showed herein and none has been found which was compared to the benchmark results of Jauvits & Williamson (2004), Franzini (2013). These results are quite different compared to high mass ratio structures.

Differently from the cases analyzed in the previous chapters, here the main quantities that characterize response are the in-line and response amplitudes, instead of forces. The turbulence models used in these calculations are the two-dimensional  $k-\omega$  SST and three-dimensional  $k-\omega$  SST-SAS. LCTM has not been shown as, for these Reynolds numbers, no transitional behavior is observed as demonstrated in the previous chapter.

It is quite interesting to observe that there are small differences in terms of motions when comparing the results obtained with SST and SST-SAS. That has been attributed to the fact that, both in the experiments and calculations, a filtering of the forces takes place and the body mainly responds in frequencies which are, in fact, captured in the calculations.

That is the main reason why the comparison with experiments has gradually improved from a fixed to a free moving cylinder.



# Chapter 10

## Conclusions

*In this chapter, a summary of the achievements is made and main conclusions are discussed. Future work, improvements and new directions of research in the present context are also proposed.*

### 10.1 Main Conclusions

The flow about circular cylinder is one of the most important ones in fluid mechanics. It is not only considered as a toy problem, but also of high practical importance in itself as many structures present similar geometric details. Engineering applications including risers, piles, floating platforms such as spars, moncolumns, semi-submersibles and TLP's are examples that display cylindrical structures and are applications for which the subject studied in this thesis might be relevant. In that sense, it is also worth mentioning devices applied to harvest clean energy, such as VIVACE (BERNITSAS et al., 2009), for which the issues touched in the present work are important. On the other hand the cylinder flow condenses a wide range of interesting aspects also observed in flows around many other blunt bodies. The interaction of boundary layer, separating free shear layers and wake gives rise to the vortex shedding phenomenon, three-dimensional instabilities, laminar-turbulent transition, vortex-induced vibrations and more. A great deal of modeling aspects must be quite well developed in a CFD code, if one is to correctly capture the most important features of this flow at different Reynolds numbers.

The present doctoral work is mainly focused on the modeling of turbulence and fluid-structure interaction capabilities within the Reynolds Average Navier Stokes approach for application to the flow around cylinders in restrained condition, under imposed motions and free to move.

In particular, the modeling, implementation, and applications have been done within the framework of ReFRESKO. The contribution of the present doctoral work was on the modeling, implementation and application of the state-of-the-art turbulence models  $k-\omega$  SST-SAS, Local Correlation Transition Model and of coupling of rigid body equations of motion with the flow solver for free body motion calculations.

From a more general perspective, this doctoral work has been focused on understanding the capabilities and limitations of the traditional engineering modeling for this problem, identifying and improving modeling aspects by means of the use of new turbulence and transition models. This has been mainly pursued for the fixed cylinder case, which can be considered the most challenging case of this thesis. Furthermore, the relevance of turbulence modeling and other issues for the case of cylinder under imposed motions have been studied, as well as for the free moving cylinder, reaching observations and conclusions that apply to the modeling of other engineering flows.

A systematic approach has been taken to build credibility onto the CFD calculations by means of doing grid and time step sensitivity studies, strict iterative convergence control and verification and validation procedures, when possible.

The fixed cylinder flow has been herein divided into three ranges, according to the most important modeling features identified in each range. In range I, from  $Re = 1$  to  $Re = 200$  the flow is laminar and the modeling applied herein, namely two-dimensional steady and unsteady calculations, showed appropriate. In range II, from  $Re = 1,000$  to  $Re = 63,100$ , three-dimensional effects and instabilities play an important role in determining the loads. The two-dimensional modeling cause an over-prediction of drag and lift loads due to higher level of Reynolds stresses, more coherent and strong vortices and inaccurate boundary layer separation prediction. In range III, the subtle aspects of laminar-turbulent transition play a crucial role and its improved modeling is required. As a result of deficient transition-modeling, it is not possible to faithfully reproduce the instabilities of the shear layers and the correct separation point, in summary, the intricate interaction between free-shear layers, boundary layers and wake.

In spite of these shortcomings, the overall trends of all parameters were well captured, including the qualitative behavior seen near the critical Reynolds numbers, which suggested that the drag crisis is mainly two-dimensional, as recognized by Singh & Mittal (2005).

Also, the qualitative aspects of the flow field and aspects such as the bifurcation of the Navier-Stokes equations leading to vortex-shedding, or also the secondary vortices associated with instabilities of the shear layer next to the separation.

The evolution of the wake as Reynolds number is increased is also well represented, with

its narrowing up to the drag crisis and shedding of less coherent vortices. Also, in a qualitative manner, the evolution of the laminar-turbulent transition which is in fact reproduced by the SST model somewhat earlier than in reality in terms of Reynolds number.

The Scale Adaptive Simulations have improved the modeling in range II. This model naturally improves the turbulent flow scales modeling by using a local scale (the von Kármán scale) in a way that the local scales are smaller allowing break-up of larger structures to smaller ones. It is only natural that energy is more broad-banded and the loads decrease.

The Local Correlation Transition Model has been applied in range III. In that region, transition plays an essential role and thus such modeling seems appropriate. It is necessary to notice that the extensive application of this model for the cylinder flow is indeed increasing the range of applications of the model, as the correlations (which in fact contain the information on the physics of the flow) were devised from flat plate flow.

It is reassuring to notice that the calculation results revealed much more reasonable comparison with the experimental results and overall trends, in terms of drag loads, than seen before with URANS for these Reynolds numbers.

It has been shown that SST seems to smooth out the drag coefficient curve and its values drop at around  $Re = 10,000$ , whereas the LCTM results remain at high values up to nearly  $Re = 100,000$ , presenting a much sharper dip of the drag coefficients curve than with the SST. That is an important qualitative improvement due to a more accurate prediction of the transition onset and length. More accurate prediction of the transition improves the prediction of boundary layer separation, a crucial aspect in cylinder flow dynamics, since most of the drag load is due to pressure. The drag coefficient values are also much better predicted when compared to the experimental trends.

The evaluation of the fluid-structure interaction between fluid and cylinder with imposed sinusoidal motions has been studied with the application of two-dimensional  $k-\omega$  SST and LCTM and the three-dimensional  $k-\omega$  SST-SAS. Due to low Reynolds number flows, transition did not play an important role and thus the LCTM results showed very similar to those with the SST.

Conversely, the comparison between two-dimensional SST and three-dimensional SST-SAS revealed interesting issues. Within the locked region, a resonant behavior takes place, with flow structures more correlated and coherent, with stronger vortices and narrow banded force spectrum.

In the unlocked region, however, the energy is more spread, causing more irregular force (also in the experiments). Thus, both two-dimensional SST and three-dimensional SST-

SAS perform similarly in the locked region, with forces similarly predicted and in good agreement with experiments. In the unlocked region, the increasing irregular behavior associated with more three-dimensional flow is better predicted by SST-SAS than SST, thus force prediction agrees better with experimental results for SST-SAS.

The two-degrees of freedom vortex induced vibrations of a cylinder with low mass ratio feature as main quantities that characterize response the in-line and response amplitudes. The turbulence models used in these calculations are the two-dimensional  $k-\omega$  SST and three-dimensional  $k-\omega$  SST-SAS. LCTM has not been shown as, for these Reynolds numbers, no transitional behavior is observed as demonstrated in imposed motion results.

It is quite interesting to observe that there are small differences in terms of motions when comparing the results obtained with SST and SST-SAS. That has been attributed to the fact that, both in the experiments and calculation a filtering of the forces takes place and the body mainly responds in frequencies which are captured by the calculations. As mentioned, that is the main reason why the comparison with experiments has gradually improved from a fixed to a free-moving cylinder and this observation is of paramount importance considering that such simplifications in the flow modeling for engineering applications can be made without excessively harming the responses.

The overview of the results showed in this thesis also permit some more practical conclusions, drawn below.

The turbulence modeling showed decisive for the fixed cylinder flow. The three-dimensional structures, instabilities and turbulent eddies determine flow separation and strongly influence on the drag and lift loads. A more broad-banded spectrum is seen on the forces and not only the frequencies associated to vortex-shedding. The force calculation is naturally very sensitive to the effects of turbulence in the flow.

For the imposed motions, the small-scale flow details such as small-scale turbulent eddies and non-isotropic effects are less relevant than for the fixed cylinder due to a more correlated flow, which forms due to the motions, mainly within the resonance range.

For the free-moving cylinder, both in the experiments and calculation, a filtering of the forces takes place and the body mainly responds in frequencies which are captured by the calculations. That is the main reason why the comparison with experiments has gradually improved from a fixed to a free moving cylinder.

## 10.2 Perspectives

The scope of this work has been defined covering a reasonably wide range of issues, from the implementation and testing of turbulence models and body-moving capabilities to the study of the complex cylinder flow. Thus a number of further activities and side investigations identified during the course of this work were left aside (and a number of other issues was pursued due to curiosity or need of larger understanding) with the purpose of keeping focus on what was identified as the most important issues for this thesis.

Within the stationary cylinder investigation, the two-dimensional  $k-\omega$  SST application was exhaustively studied within the most common range of engineering applications in terms of Reynolds numbers. It is worth investigating the improvements of the three-dimensional calculations with the same model to better understand its limitations. Furthermore, the assessment of different boundary conditions would also be of added value. In this work, a choice was made for the three-dimensional SAS-SST as it encompasses the improvements of three-dimensional calculations as well as the improvements of its more advanced conceptual modeling.

Both SAS and LCTM models improved the flow prediction in their main range of applications: the SAS was better at predicting more three-dimensional character of the flow, with better resolution of fine turbulent scales, whereas the LCTM improved the prediction of laminar-turbulent transition. It would only be natural to combine these features into a new hybrid model which could do both things at the same time, in a new “SAS-LCTM-SST” turbulence model. To the author’s knowledge, research in that direction is being carried out, but it has not been made public.

Within the imposed and free motions, a range of different issues can be identified, such as the effects of adding more degrees of freedom to the dynamic system (which has deep consequences in the formulation due to the adopted reference frames), varying the mass ratio and damping values, among others.

With respect to engineering applications, it would be interesting to investigate these issues with different and more complex geometries, from square cylinders to ships and offshore platforms. It seems plausible that the conclusions drawn here also apply in these other cases. Another issue in the edge of knowledge is the development and application of tools for the simulation of flexible body together with a CFD solver, which would require a great deal of creativity to circumvent the computational power restrictions.

During the last few years the CFD community has seen great improvements in the modeling of complex flows and applications, from the modeling of cylinder flow to that of a

ship with propeller and rudder in full scale. Hardware development has also helped this movement with new-generation, faster and integrated processors with a new many-cores trend, wide-band networks and others combined with more efficient software. CFD has transited from being sometimes discredited to a very helpful tool, which can be more cost-effective than model testing for many applications. In spite of that, one should be aware that care should be taken when doing calculations for practical applications, in that good practices concerning the investigation of: i) iterative errors and ii) discretization errors should be taken into account. It is evidently not possible to carry out verification and validation practices thoroughly always, but some sensitivity investigation is advisable to determine proper setups. Conversely, a good overview of the engineering activity is also beneficial, in that excessive fastidiousness can impair applications in real situations when cost-effectiveness and time are normally restrictions, thus a good amount of common sense is required of the engineers.

# References

- AAIA-GUIDE. *Guide for Verification and Validation of Computational Fluid Dynamics Simulations*, 1998.
- ACHENBACH, E.; HEINECKE, E. On vortex shedding from smooth and rough cylinders in the range of reynolds numbers  $6 \times 10^3$  to  $5 \times 10^6$ . *Journal of Fluid Mechanics*, v. 109, p. 239–251, 1981.
- AL-JAMAL, H.; DALTON, C. Vortex Induced Vibration Using Large Eddy Simulation at a Moderate Reynolds Number. *Journal of Fluids and Structures*, v. 19, p. 73–92, 2004.
- ASME-GUIDE. *ASME Guide on Verification and Validation in Computational Fluid Dynamics and Heat Transfer*, 2008.
- BALAY, S.; ABHYANKAR, S.; ADAMS M. F. AND BROWN, J.; BRUNE, P.; BUSCHELMAN, K.; EIJKHOUT, V.; GROPP, W. D.; KAUSHIK, D.; KNEPLEY, M. G.; MCINNES, L. C.; RUPP, K.; SMITH, B. F.; ZHANG, H. *PETSc Users Manual*, 2013.
- BASU, R. Aerodynamic Forces on Structures of Circular Cross-Section. Part 1. Model-Scale Data Obtained Under Two-Dimensional Conditions in Low-Turbulence Streams. *Journal of Wind Engineering and Industrial Aerodynamics*, v. 21, p. 273–294, 1985.
- BERNITSAS, M.; BEN-SIMON, Y.; RAGHAVAN, K.; GARCIA, E. The VIVACE Converter: Model Tests at High Damping and Reynolds Number Around  $10^5$ . *Journal of Offshore Mechanics and Arctic Engineering*, v. 131(1), p. 1–12, 2009.
- BETTLE, M. *Unsteady Computational Fluid Dynamics Simulations of Six-Degrees-of-Freedom Submarine Manoeuvres*. Thesis (PhD) — University of New Brunswick, 2012.
- BLACKBURN, H.; GOVARDHAN, R.; WILLIAMSON, C. A Complementary Numerical and Physical Investigation of Vortex-Induced Vibration. *Journal of Fluids and Structures*, v. 15, p. 481–488, 2000.
- BLACKBURN, H.; HENDERSON, R. A Study of Two-Dimensional Flow Past an Oscillating Cylinder. *Journal of Fluid Mechanics*, v. 385, p. 255–286, 1999.
- BRAZA, M.; CHASSAING, P.; MINH, H. Numerical Study and Physical Analysis of the Pressure and Velocity Fields in the Near Wake of a Circular Cylinder. *Journal of Fluid Mechanics*, v. 165, p. 79–130, 1986.

- BRAZA, M.; CHASSAING, P.; MINH, H. H. Prediction of Large-Scale Transition Features in the Wake of a Circular Cylinder. *Phys. Fluids A*, v. 2, p. 1461–1471, 1990.
- BUTCHER, J. Numerical Methods for Ordinary Differential Equations in the 20th Century. *Journal of Computational and Applied Mathematics*, v. 125, p. 1–29, 2000.
- CARMO, B. *On Wake Interference in the Flow around Two Circular Cylinders: Direct Stability Analysis and Flow-Induced Vibrations*. Thesis (PhD) — Imperial College London, 2009.
- CARMO, B.; ASSI, G.; MENEGHINI, J.; ARANHA, J.; VOLPE, E. *Turbulência*: ABCM, EPUSP, 2012.
- CATALANO, P.; WANG, M.; IACCARINO, G.; MOIN, P. Numerical Simulation of the Flow Around a Circular Cylinder at High Reynolds Numbers. *Heat and Fluid Flow*, v. 463-469, p. 24, 2003.
- CHAKRABARTI, S. *Offshore Structure Modeling*: World Scientific, 1994.
- CUNHA, L. *Vibração Induzida por Vórtices: Análise Crítica de Modelos Fenomenológicos*. Thesis (MSc) — University of São Paulo. In Portuguese, 2005.
- DENNIS, S. The Numerical Solution of the Vorticity Transport Equation. In: *Lecture Notes in Physics*, 1973. v. 2, p. 120.
- DENNIS, S.; CHANG, G. Numerical Solutions for Steady Flow Past a Circular Cylinder at Reynolds Numbers up to 100. *Journal of Fluids Mechanics*, v. 42, p. 471–489, 1970.
- DONG, S.; KARNIADAKIS, G. DNS of Flow Past a Stationary and Oscillating Cylinder at  $Re = 10000$ . *Journal of Fluids and Structures*, v. 20, p. 519–531, 2005.
- EÇA, L. Evaluation of Numerical Error Estimation Based on Grid Refinement Studies with the Method of the Manufactured Solutions. *Computers & Fluids*, v. 38, p. 1580–1591, 2009.
- EÇA, L.; HOEKSTRA, M. The Numerical Friction Line. *J. Marine Science and Technology*, 4 v. 13, p. 328–345, 2008.
- EÇA, L.; SARAIVA, G.; VAZ, G.; ABREU, H. The pros and cons of wall functions. In: *Proceedings of the 34th International Conference on Ocean, Offshore and Arctic Engineering, OMAE2015-41518.*, 2015.
- EÇA, L.; VAZ, G.; HOEKSTRA, M. A Verification and Validation Exercise for the Flow Over a Backward Facing Step. In *Proceedings of ECCOMAS CFD 2010, Lisbon, Portugal*, June 2010.
- EÇA, L.; VAZ, G.; ROSETTI, G.; PEREIRA, F. On the Numerical Prediction of the Flow Around Smooth Circular Cylinders. In: *Proceedings of the 33rd International Conference on Offshore Mechanics and Arctic Engineering, OMAE2014-23230.*, June 2014.
- EGOROV, Y.; MENTER, F. Development and Application of SST-SAS Turbulence Model in DESIDER Project. *Adv. in Hybrid RANS-LES Modelling*, p. 261–270, 2008.

- ERCOFTAC. *Classic Collection Database*. 1990.  
<http://cfd.mace.manchester.ac.uk/ercoftac/>. Accessed: 2012-09-30.
- ESDU. *Circular Cylindrical Structures: Dynamic Response to Vortex Shedding, Part 1: Calculation Procedures and Derivation*. Regent Street, London W1R 7AD, UK, 1985. 251-259.
- FERZIGER, J.; PERIC, M. *Computational Methods for Fluid Dynamics*. 3<sup>rd</sup>. ed.: Springer Verlag, 2002.
- FORNBERG, B. A Numerical Study of Steady Viscous Flow Past a Circular Cylinder. *Journal of Fluid Mechanics*, v. 98, p. 819–855, 1980.
- FORNBERG, B. Steady Viscous Flow Past a Circular Cylinders up to Reynolds Number 600. *Computers & Fluids*, v. 61, p. 297–320, 1985.
- FRANZINI, G. *Investigação Experimental do Escoamento ao Redor de Cilindros Inclinados, Sujeitos a Condições de Contorno Assimétricas nas Extremidades*. Thesis (PhD) — University of São Paulo. In Portuguese, 2013.
- FRANZINI, G.; GONÇALVES, R.; FUJARRA, A.; MENEHINI, J. Experimental Forces Measurements on the Flow Around a Fixed and Yawed Cylinder in the Presence of Free-Surface. In *Proceedings of the ISOPE 2012 22nd International Ocean and Polar Engineering Conference*, 2012.
- FUJARRA, A.; PESCE, C. Experiments on VIV Added Mass with Elastically Mounted Cylinder in Water. In: *Proceedings of the 21st International Conference on Offshore Mechanics and Artic Engineering*, 2002.
- FUJARRA, A.; PESCE, C.; FLEMMING, F.; WILLIAMSON, C. Vortex-Induced Vibration of a Flexible Cantilever. *Journal of Fluids and Structures*, v. 15, p. 651–658, 2001.
- GABBAI, R.; BENAROYA, H. An overview of modeling and experiments of vortex-induced vibration of circular cylinders. *Journal of Sound and Vibration*, v. 282, p. 575–616, 2004.
- GIRIMAJI, S. Partially-Averaged Navier-Stokes Model for Turbulence. *Journal of Applied Mechanics*, v. 73, p. 413–421, 2006.
- GOPALKRISHNAN, R. *Vortex-Induced Forces on Oscillating Bluff Cylinders*. Thesis (PhD) — Massachusetts Institute of Technology, 1993.
- HE, X.; DOOLEN, G. Lattice Boltzmann Method on a Curvilinear Coordinate System: Vortex Shedding Behind a Circular Cylinder. *Physical Review E*, v. 56, p. 434–440, 1997.
- HENDERSON, R. Details of the Drag Curve Near the Onset of Vortex Shedding. *Physics of Fluids*, v. 7, p. 2102–2104, 1995.
- HIRT, C.; AMSDEN, A.; COOK, J. An Arbitrary Lagrangian-Eulerian Computing Method for All Flow Speeds. *Journal of Computational Physics*, v. 135, p. 203–216, 1997.

- JAUVITS, N.; WILLIAMSON, C. The Effect of Two Degrees of Freedom on Vortex-Induced Vibration at Low Mass and Damping. *Journal of Fluid Mechanics*, v. 509, p. 23–62, 2004.
- KHALAK, A.; WILLIAMSON, C. Dynamics of a Hydroelastic Cylinder with Very Low Mass and Damping. *Journal of Fluids and Structures*, v. 11, p. 455–472, 1996.
- KHALAK, A.; WILLIAMSON, C. Fluid Forces and Dynamics of a Hydroelastic Structure with Very Low Mass and Damping. *Journal of Fluids and Structures*, v. 11, p. 973–982, 1997.
- KLAIJ, C. *Simulation of the Flow Around Cylinders with CFX and Fresco*. MARIN Report, 2008.
- LANGTRY, R.; MENTER, F. Correlation-Based Transition Modeling for Unstructured Parallelized Computational Fluid Dynamics Codes. *AIAA Journal*, v. 47 (12), p. 2894–2906, 2009.
- LAUNDER, B.; SHARMA, B. Application of the Energy Dissipation Model of Turbulence to the Calculation of Flow near a Spinning Disc. *Letters in Heat and Mass Transfer* 1, v. 2, p. 131–138, 1974.
- LEONARD, B. A Stable and Accurate Convective Modelling Procedure Based on Quadratic Upstream Interpolation. *Computer Methods in Applied Mechanics and Engineering*, v. 19, p. 59–98, 1979.
- LEROYER, A. *Etude du Couplage Écoulement/Mouvement Pour les Corps Solides ou à Déformation Imposée par Résolution des Équations de Navier-Stokes. Contribution à la Modélisation Numérique de la Cavitation*. Thesis (PhD) — Ecole Centrale Nantes. In French, 2004.
- LIU, C.; ZHENG, X.; SUNG, C. Preconditioned Multigrid Methods for Unsteady Incompressible Flows. *Journal of Computational Physics*, v. 139, p. 35–57, 1998.
- MALAN, P.; SULUKSNA, K.; JUNTASARO, E. Calibrating the  $\gamma$ - $Re\theta$  Transition Model for Commercial CFD . *AIAA Aerospace Sciences Meeting*, jan. 2009.
- MARZOUK, O. One-Way and Two-Way Couplings of CFD and Structural Models and Application to the Wake-Body Interaction. *Applied Mathematical Modeling*, v. 35, p. 1036–1053, 2011.
- MENDES, P.; BRANCO, F. Analysis of Fluid-Structure Interaction by an Arbitrary Lagrangian-Eulerian Finite Element Formulation. *International Journal for Numerical Methods in Fluids*, v. 30, p. 897–919, 1999.
- MENEGHINI, J.; BEARMAN, P. Numerical Simulation of High Amplitude Oscillatory-Flow About a Circular Cylinder Using a Discrete Vortex Method. *In Proceedings of AIAA Shear Flow Conference, Orlando, AIAA Paper 93-3288*, p. 1–11, 1993.
- MENTER, F. Two-Equation Eddy-Viscosity Turbulence Models for Engineering Applications. *AIAA Journal*, v. 32, p. 1598–1605, 1994.

- MENTER, F.; EGOROV, Y. Re-Visiting the Turbulent Scale Equation. *In: Proc. IUTAM Symp. One Hundred Years of Boundary Layer Research. Springer. Gottingen, 2004.*
- MENTER, F.; EGOROV, Y. The Scale-Adaptative Simulation Method for Unsteady Turbulent Flow Predictions. Part 1: Theory and Model Description. *Flow Turbulence Combustion*, v. 85, p. 113–138, 2010.
- MENTER, F.; EGOROV, Y.; RUSCH, D. Steady and Unsteady Flow Modelling using  $k - \sqrt{k}L$  Model. *Heat and Mass Transfer*, v. 5, 2005.
- MENTER, F.; KUNTZ, M.; LANGTRY, R. Ten Years of Industrial Experience with the SST Turbulence Model. *Turbulence, Heat and Mass Transfer 4*, p. 625–632, 2003.
- MENTER, F.; LANGTRY, R.; VOLKER, S. Transition Modelling for General Purpose CFD Codes. *Flow Turbulence and Combustion*, v. 77, p. 277–303, 2006.
- MITTAL, R.; BALACHANDAR, S. Effect of Three-Dimensionality on the lift and drag of Nominally Two-Dimensional Cylinders. *Physics of Fluids*, v. 8, p. 1841–1865, 1995.
- MITTAL, S.; KUMAR, V. Flow-Induced Vibrations of a Light Circular Cylinder at Reynolds Numbers  $10^3$  to  $10^4$ . *Journal of Sound and Vibration*, v. 245, p. 923–946, 2001.
- MITTAL, S.; KUMAR, V.; RAGHUVANSHI, A. Unsteady Incompressible Flow Past Two Cylinders in Tandem and Staggered Arrangements. *Journal of Fluids and Structures*, v. 25, p. 1315:1344, 1997.
- NETO, P. L. de O. C. *Estatística*: Edgard Blucher, in Portuguese, 2005.
- NIEUWSTADT, F.; KELLER, H. B. Viscous Flow Past Circular Cylinders. *Computers & Fluids*, v. 1, p. 59–71, 1973.
- NOBARI, M.; NADERAN, H. A numerical Study of Flow Past a Cylinder with Cross Flow and Inline Oscillation. *Computers and Fluids*, v. 35, p. 393–415, 2006.
- NORBERG, C. Fluctuating Lift on a Circular Cylinder: Review and new Measurements. *Journal of Fluids and Structures*, v. 17, p. 57–96, 2003.
- ONG, M.; UTNES, T.; HOLMEDAL, L.; MYRHAUG, D.; PETTERSEN, B. Numerical Simulation of Flow Around a Smooth Circular Cylinder at High Reynolds Numbers. *International Conference on Computational Methods in Marine Engineering. MARINE 2007*, 2007.
- PATANKAR, S. *Numerical Heat Transfer and Fluid Flow*: Routledge, 1980.
- PENGAN, B. *Numerical Accuracy in RANS Simulations of the Flow Around a Cylinder*. Thesis (MSc) — ENSIETA, 2010.
- PEREIRA, F.; VAZ, G.; EÇA, L. On the Use Hybrid Turbulence Models. *In the Proceedings of NUTTS 2014, Gothenburg, Sweden, 2014.*
- PEREIRA, F.; VAZ, G.; EÇA, L. Flow Past a Circular Cylinder: a Comparison Between RANS and Hybrid Turbulence Models for a Low Reynolds Number. *In Proceedings of the ASME 34th International Conference on Ocean, Offshore and Arctic Engineering*, 2015.

- PESCE, C.; FUJARRA, A. The “Super-Upper Branch” VIV Response of Flexible Cylinders. In: *4th Bluff-Bodies Wakes and Vortex-Induced Vibrations Conference BBVIV4*, 2005.
- PLACZEK, A.; SIGRIST, J.; HAMDOUNI, A. Numerical Simulation of an Oscillating Cylinder in a Cross-Flow at Low Reynolds Number: Forced and Free Oscillations. *Computers & Fluids*, p. 80–100, 2009.
- REFRESCO. *ReFRESCO Website*. 2015. www.refresco.org. Accessed: 2015-05-17.
- ROSETTI, G. F.; VAZ, G.; FUJARRA, A. URANS Calculations for Smooth Circular Cylinder Flow in a Wide Range of Reynolds Numbers: Solution Verification and Validation. *ASME J. Fluids Eng.*, v. 134, p. 121103, 2012.
- RUMSEY, C. Apparent Transition Behavior of Widely-Used Turbulence Models. *Heat and Fluid Flow*, v. 28, p. 1460–1471, 2007.
- RUMSEY, C.; SPALART, P. Turbulence Model Behavior in Low Reynolds Number Regions of Aerodynamic Flow Fields. In: *Proceedings of AIAA 38th Fluid Dynamics Conference and Exhibit, Seattle, WA, USA, (AIAA Paper 2008-4403)*., 2008.
- SALTARA, F. *Simulação Numérica do Escoamento ao Redor de Cilindros*. Thesis (PhD) — University of São Paulo. In Portuguese, 1999.
- SAMPAIO, P.; COUTINHO, A. Simulating Vortex Shedding at High Reynolds Numbers. In: *Proceedings of the Tenth (2000) International Offshore and Polar Engineering Conference*, 2000.
- SARPKAYA, T. On the Force Decomposition of Lighthill and Morison. *Journal of Fluids and Structures*, v. 15, p. 227–233, 2001.
- SARPKAYA, T. A Critical Review of the Intrinsic Nature of Vortex-Induced Vibrations. *Journal of Fluids and Structures*, v. 19, p. 389–447, 2004.
- SCHLICHTING H., G. K. *Boundary Layer Theory*: Springer Verlag, 8th edition, 2000.
- SCHUBAUER, G.; KLEBANOFF, P. Contributions on the Mechanics of Boundary Layer Transition. 3489 *NACA TN*, 1955.
- SHIELS, D.; LEONARD, A.; ROSHKO, A. Flow-Induced Vibration of a Circular Cylinder at Limiting Structural Parameters. *Journal of Fluids and Structures*, v. 15, p. 3–21, 2001.
- SHUR, M.; SPALART, P.; SQUIRES, K.; STRELETS, M.; TRAVIN, A. Three Dimensionality in Reynolds-Averaged Navier-Stokes Solutions Around Two-Dimensional Geometries. *AIAA Journal*, v. 43, p. 1230–1242, 2005.
- SINGH, S.; MITTAL, S. Flow Past a Cylinder: Shear Layer Instability and Drag Crisis. *International Journal of Numerical Methods in Fluids*, v. 47, p. 75–98, 2005.
- SPALART, P.; ALLMARAS, S. A One-Equation Turbulence Model for Aerodynamic Flows. In *the Proceedings of AIAA 30th Aerospace Sciences Meeting, Reno, Nevada, USA, (AIAA Paper 92-0439)*, 1992.

- SPALART, P.; DECK, S.; SHUR, M.; SQUIRES, K.; STRELETS, M.; TRAVIN, A. A New Version of Detached-Eddy Simulation, Resistant to Ambiguous Grid Densities. *Theoretical Computational Fluids Dynamics*, v. 20, p. 181–195, 2006.
- SPALART, P.; RUMSEY, C. Effective Inflow Conditions for Turbulence Models in Aerodynamic Calculations. *AIAA Journal*, v. 45, No. 10, p. 2544–2553, 2007.
- TAKAMI, H.; KELLER, H. Steady Two-Dimensional Viscous Flow of an Incompressible Fluid Past a Circular Cylinder. *Physics of Fluids*, v. 12, p. (Suppl II–51), 1969.
- TRAVIN, A.; SHUR, M.; STRELETS, M.; SPALART, P. Detached-Eddy Simulations Past a Circular Cylinder. *Flow, Turbulence and Combustion*, v. 63, p. 293–313, 1999.
- TREMBLAY, F. *Direct and Large-Eddy Simulation of Flow Around a Circular Cylinder at Subcritical Reynolds Number*. Thesis (PhD) — Technical University of Munich, 2001.
- TUANN, S.; OLSON, M. Numerical Studies of the Flow Around a Circular Cylinder by a Finite Element Method. *Computers & Fluids*, v. 6, p. 219, 1978.
- VAZ, G.; MABILAT, C.; WAL, R. van der; GALLAGHER, P. Viscous Flow Computational on Smooth Cylinders a Detailed Numerical Study with Validation. In: *Proc. of Offshore Mechanics, Arctic and Ocean Engineering Conference, San Diego, OMAE Paper 2007-29275*, 2007.
- VON KÁRMÁN INSTITUTE. *VKI Turbulence Modelling Lecture Notes*, 2008.
- WILCOX, D. Reassessment of the Scale-Determining Equation for Advanced Turbulence Models. *AIAA Journal*, v. 11, p. 1299–1310, 1988.
- WILCOX, D. *Turbulence Modeling for CFD*: DCW Industries, 1993.
- WILLIAMSON, C. Vortex Dynamics in the Cylinder Wake. *Annual Review of Fluid Mechanics*, v. 28, p. 477–539, 1996.
- WILLIAMSON, C.; GOVARDHAN, R. Vortex-Induced Vibrations. *Annual Review of Fluid Mechanics*, v. 36, p. 413–455, 2004.
- WILLIAMSON, C.; JAUVITS, N. A High-Amplitude 2T mode of Vortex-Induced Vibration for a Light Body in XY Motion. *European Journal of Fluid Mechanics B/Fluids*, v. 23, p. 107–114, 2004.
- WILLIAMSON, C.; ROSHKO, A. Vortex Formation in the Wake of an Oscillating Cylinder. *Journal of Fluids and Structures*, v. 2, p. 355–388, 1988.
- WILSON, R.; CARRICA, P.; STERN, F. Unsteady RANS Method for Ship Motions with Application to Roll for a Surface Combatant. *Computers and Fluids*, v. 35, p. 501–524, 2006.
- WITH, G. d.; HOLDO, A.; HULD, T. The Use of Dynamic Grid Adaptation Algorithms for the Modeling of Flow Around a Circular Cylinder in Sub-Critical Flow Regime. *International Journal for Numerical Methods in Fluids*, v. 41, p. 789–808, 2003.



# APPENDIX



# Appendix A

## Investigation of the Properties of the LCTM in the Flat Plate Flow

*This appendix presents the studies carried out with the local correlation transition model coupled with the  $k$ - $\omega$  SST for the flat plate flow. It has been done with the purposes of verifying the implementation, improving the understanding of the model and studying the influence of different parameters in its behavior.*

### A.1 Calculation Setup

#### A.1.1 Description of Test-Cases

Two different sets of calculations will be presented. The first set was chosen to study the behavior of the LCTM in comparison with traditional turbulence models in low and high Reynolds numbers, from  $Re = 10^{3.0}$  to  $Re = 10^{9.5}$ , with intervals of  $10^{0.5}$  (fourteen Reynolds numbers). This range covers the laminar to fully turbulent regimes. In this “Numerical Friction Line Study”, the one-equation model of Spalart and Allmaras (SPALART; ALLMARAS, 1992), the two-equations models  $k$ - $\sqrt{kL}$  (MENTER; EGOROV; RUSCH, 2005) and  $k$ - $\omega$  SST (MENTER; KUNTZ; LANGTRY, 2003) will be compared with the Local Correlation Transition Model (LCTM) (LANGTRY; MENTER, 2009).

In the second set of calculations, the objective is to reproduce the experimental conditions from the ERCOFTAC Classic Database T3 series (ERCOFTAC, 1990) and from Schubauer and Klebanoff (S&K) (SCHUBAUER; KLEBANOFF, 1955) with calculations

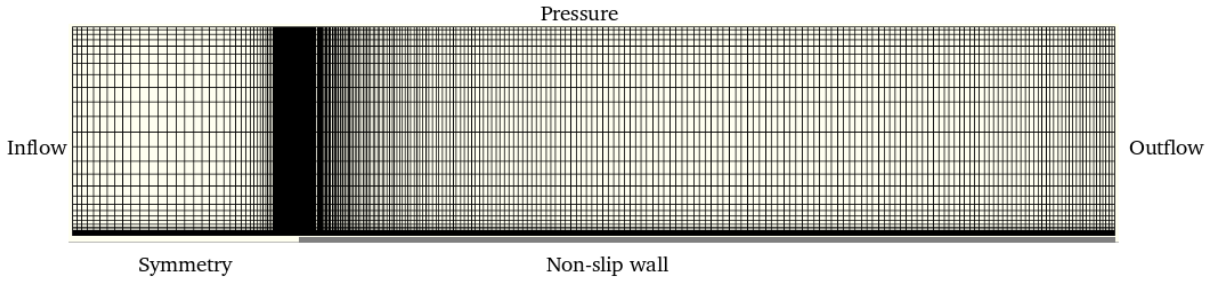


Figure A.1: Annotated view of the flat plate domain, showing an example grid.

done with  $k-\omega$  SST and LCTM. This set will be referred to as “ERCOFTAC”.

## A.1.2 Domain and Boundary Conditions

The domains for both studies are rectangular, as showed in figure A.1. For the Numerical Friction Line calculations, the length of the plate is  $L = 1m$ , the domain measures  $1.25L$  long by  $0.25L$  high. By calculating the analytic solutions for the boundary layer thickness of laminar and turbulent flows proposed by Blasius ( $4.91x/\sqrt{Re_x}$ ) and Schultz-Grunow ( $0.382xRe_x^{1/5}$ ) (SCHLICHTING H., 2000), the laminar boundary layer is thickest at  $Re = 10^3$ , with ca. 5mm and, for the turbulent solution, ca. 24mm at  $Re = 10^6$ . In both cases the upper boundary is more than 10 times the expected boundary layer thickness.

For the ERCOFTAC tests, the plate is no longer dimensionless and measures 1.70m long and 0.30m high, as in the experimental setup.

## A.1.3 Grids

Ten different cartesian, structured grids were used for each test case - with the finest grid containing more than four times the cells of the coarsest (doubled in 2-dimensions). Although only three grids are required to fit a trend-line for uncertainty analysis, using 10 will decrease the sensitivity of the uncertainty analysis to noise in the results. Table A.1 shows the number of nodes in the  $x$ - and  $y$ -directions.

Stretching in the  $x$ -direction was applied to reduce the distance between normal grid-lines at the leading edge - with the aim of improving resolution in the transition region. The factor used was 25, implying that the first cell from the leading edge be 25 times finer in  $x$  than if uniform distribution had been used. The number of cells ( $ny$ ) in the  $y$ -direction varies to ensure a consistent number of cells in the boundary layer as the Reynolds number

increases. The values for  $y$ -stretching were fixed for each Reynolds number such that the grids remained geometrically similar. The value for the  $y$ -stretching factor at any Reynolds number was  $0.19686 \times Re^{0.715}$ . By means of stretching, at least 45 nodes were within the boundary layer at the outlet for every Reynolds number. The  $y^+$  values were kept below 1.0, both for Numerical Friction Line and ERCOFTAC, with the finest grids always closer to 0.1, as  $\omega$ -based models require this condition for proper viscous sublayer calculation and consistent grid convergence.

Table A.1: Number of nodes in x- and y- direction for grids G1-G10.

$\log_{10}(Re)$		G1	G2	G3	G4	G5	G6	G7	G8	G9	G10
All	nx	898	842	786	730	674	618	562	506	450	394
3.00-4.00	ny	90	82	74	66	58	50	42	34	26	18
4.50-5.00	ny	103	95	87	79	71	63	55	47	39	31
5.50-6.00	ny	116	108	100	92	84	76	68	60	52	44
6.50	ny	129	121	113	105	97	89	81	73	65	57
7.00	ny	142	134	126	118	110	102	94	86	78	70
7.50-8.00	ny	153	145	137	129	121	113	105	97	89	81
8.50	ny	165	157	149	141	133	125	117	109	101	93
9.00-9.50	ny	177	169	161	153	145	137	129	121	113	105
ERCOFTAC	ny	177	169	161	153	145	137	129	121	113	105

#### A.1.4 Numerical Details

The momentum convection scheme was the (second-order) quadratic upwind interpolation for convective kinematics (QUICK) with flux limiters and the turbulence and transition convection scheme used first-order upwind discretization (UD1). The momentum, turbulence and transition equations were solved using the generalized minimal residual method (GMRES) and the pressure was solved using the conjugate gradient (CG) method. Matrix pre-conditioning was performed using the modified Jacobi technique and the extrapolation of all boundaries was zeroth order. More details on those methods can be found in a number of references, such as Ferziger & Peric (2002). All calculations were converged down to residual machine accuracy, except for the calculations with the transition model, in which convergence stalled before machine accuracy. Therefore, several non-linear iterations were needed. Nevertheless, the calculation times for all cases here shown varied from minutes for the coarser grids up to hours for the finest grids, in a normal modern workstation.

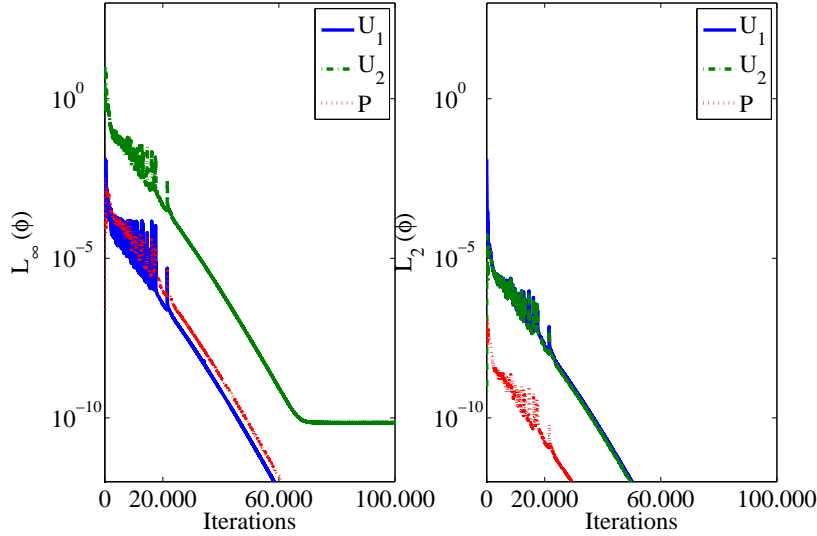


Figure A.2: Example of iterative convergence at  $Re = 10^{7.5}$  with G1. Residuals of velocities and pressure are presented.

## A.2 Numerical Friction Line Study

### A.2.1 Iterative Convergence

The following criteria was adopted concerning iterative convergence: all the equations had to be converged in the infinity norm to  $L_{inf} = 10^{-12}$ . This was somewhat difficult with the LCTM, especially for the transitional Reynolds numbers,  $Re = 10^6 - 10^7$ , and in the  $\tilde{R}e_{\theta t}$  equation, see the example in figures A.2 and A.3. As also recognized by Langtry in private communication, it can be quite difficult to converge the  $\tilde{R}e_{\theta t}$  equation as it is not a field variable, but a mathematical artifact to transform a global variable (the correlation) into a local one. Nevertheless, when convergence did stagnate, it was always at a low value of the residual, as showed in figure A.3.

### A.2.2 Order of Convergence and Uncertainty

Analysis of the grid convergence and uncertainty properties of the calculations have been done with the four models for the force coefficient  $C_D$ . The local skin friction coefficient is defined as:

$$C_f = \frac{\mu \left( \frac{\partial u}{\partial y} \right)_{(y=0)}}{\frac{1}{2} \rho U_\infty^2 L}, \quad (\text{A.1})$$

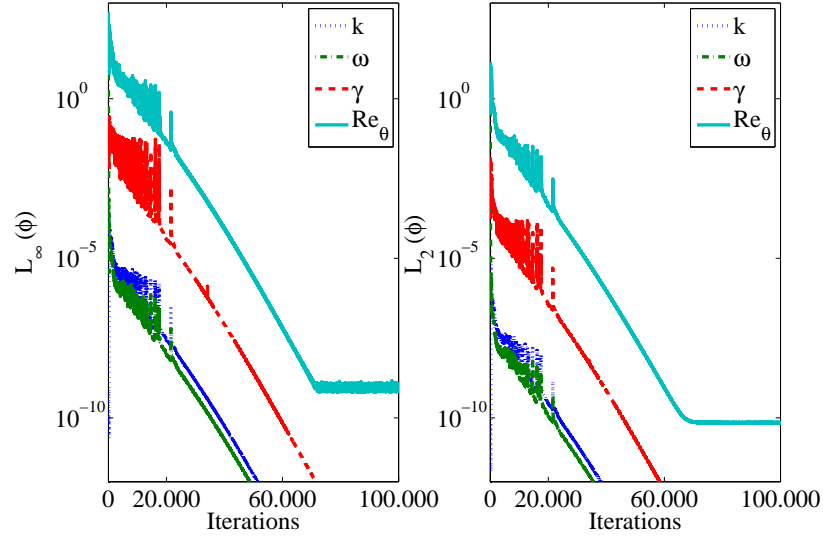


Figure A.3: Example of iterative convergence at  $Re = 10^{7.5}$  with G1. Residuals of turbulence variables are presented.

whereas the reference force per unit width is given by the integration of the above equation:

$$C_D = \frac{1}{L} \int_0^L C_f dx = \frac{1}{L} \int_0^L \frac{\mu \left( \frac{\partial u}{\partial y} \right)_{(y=0)}}{\frac{1}{2} \rho U_\infty^2 L} dx. \quad (\text{A.2})$$

Furthermore, the following reference Blasius solution will be used for the laminar flow on the flat plate (SCHLICHTING H., 2000):

$$C_f = \frac{0.664}{\sqrt{Re_x}}, \quad (\text{A.3})$$

in which the local Reynolds number is defined as  $Re_x = xU_\infty/\mu$ , where  $x$  is the distance from the leading edge. For the turbulent friction line, the Schultz-Grunow proposal is used (SCHLICHTING H., 2000):

$$C_f = 0.37[\log_{10}(Re_x)]^{-2.584}. \quad (\text{A.4})$$

Figures A.4-A.5 show, respectively, the uncertainty and order of convergence of the calculations done with the four turbulence models, Spalart and Allmaras,  $k-\sqrt{kL}$ ,  $k-\omega$  SST and LCTM; fourteen Reynolds numbers; and ten grids each, a total of 560 calculations. Overall, there are low uncertainties, most of them below 4%, except for LCTM in  $Re = 10^{7.0}$  and  $Re = 10^{7.5}$ , which showed noisy convergence and slightly higher uncertainty. On the other hand, the order of convergence showed to be between  $p = 1.0$  and  $p = 2.0$ , which is consistent, since the discretization schemes used for the momentum equations are second

order.

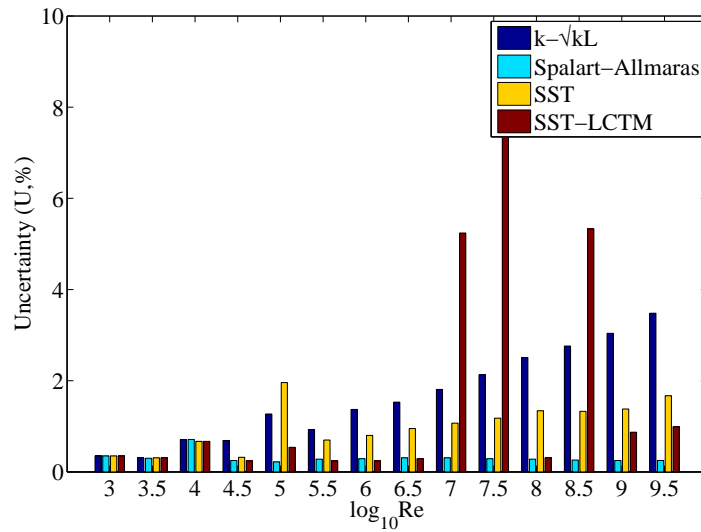


Figure A.4: Uncertainty quantification for all turbulence models in the entire range of Reynolds numbers. Overall, low uncertainties are observed.

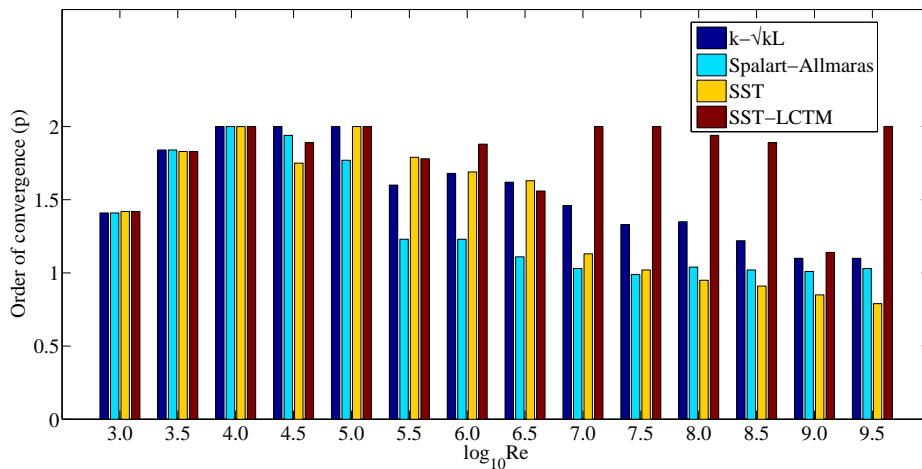


Figure A.5: Orders of grid convergence for all turbulence models. Consistent behavior is observed as orders are between  $p = 1.0$  and  $p = 2.0$ .

Figures A.6, A.7 and A.8 show, as an example, the grid convergence of the force coefficients for the LCTM of  $Re = 10^{3.5}$ ,  $10^{6.0}$ ,  $10^{9.0}$ . Somewhat noisy grid convergence is a result of a very small changes in the transition location, which then affects the overall drag coefficient. The uncertainties obtained are nevertheless low enough to permit a correct modeling error comparison between the LCTM and the other models.

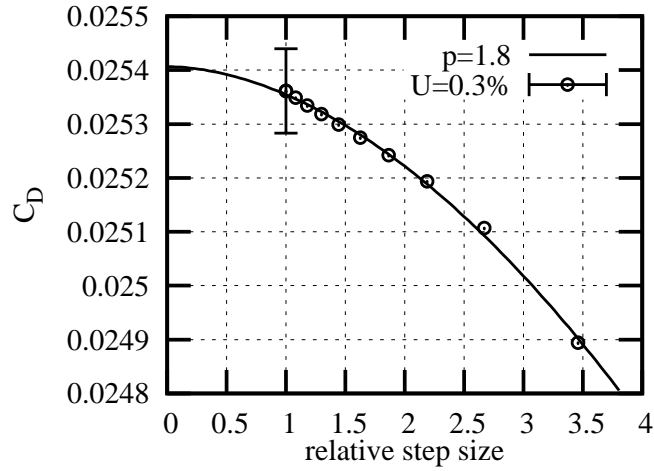


Figure A.6: Grid convergence of the drag coefficients for  $Re = 10^{3.5}$  with LCTM.

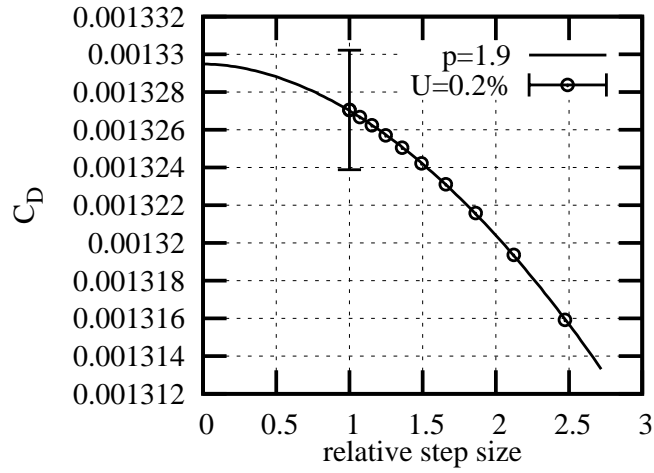


Figure A.7: Grid convergence of the drag coefficients for  $Re = 10^{6.0}$  with LCTM.

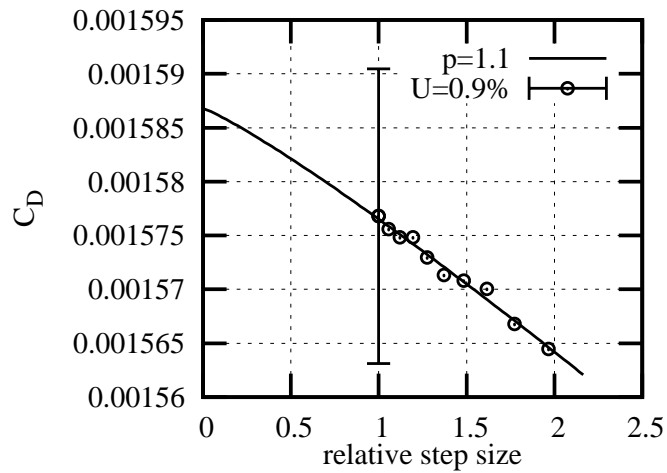


Figure A.8: Grid convergence of the drag coefficients for  $Re = 10^{9.0}$  with LCTM.

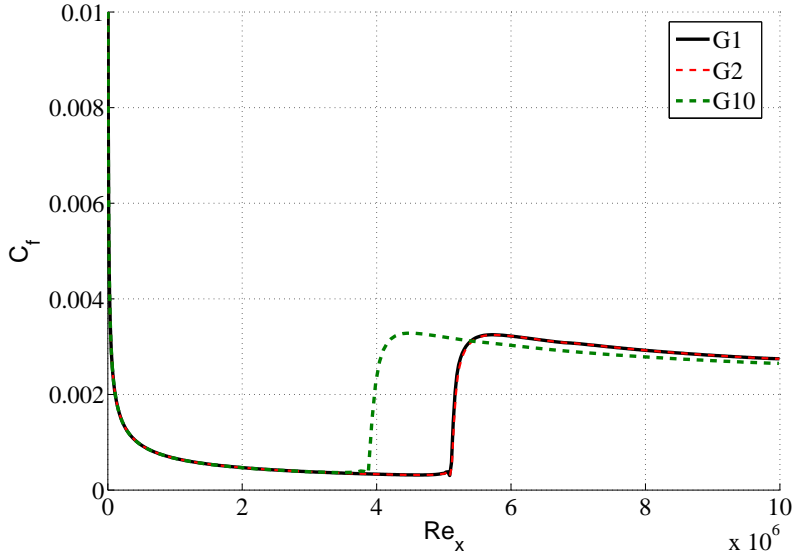


Figure A.9: Grid sensitivity of  $C_f$  line for  $Re = 10^{7.0}$ .

### A.2.3 Grid Sensitivity

This section presents a few examples of the grid sensitivity study done to obtain grid independent solutions. It is important to note, as pointed out by Langtry & Menter (2009), that LCTM requires highly refined grids especially in the normal direction to the wall ( $y$ -refinement). In his work, it is recommended to keep  $y^+$  between 0.01 and 1 since smaller  $y^+$  tends to push transition downstream whereas larger values cause earlier transition. Note that the tangential ( $x$ ) direction must be very well refined so that the model is able to closely reproduce the information contained in the empirical correlations.

Figures A.9 and A.10 show, respectively, calculations of friction lines for  $Re = 10^{7.0}$  and  $Re = 10^{7.5}$ , as examples of grid dependency results. In both plots,  $G1$  is the finest grid, with  $898 \times 153$ ;  $G2$  is nearly as fine,  $842 \times 145$ ; and  $G10$  is designed to be quite coarse with  $394 \times 81$ .  $G1$  and  $G2$  are fine enough to produce consistent results in terms of the friction and drag coefficients and the lines nearly coalesce.  $G10$ , on the other hand, is coarse, shows important grid dependency and transition onset is shifted to an earlier position. It is important to notice that all grids have very small  $y^+$ , thus this dependency is strictly related to the low grid ( $x$  and  $y$  directions) density.

### A.2.4 Nominal Results

Transition on a flat plate boundary layer occurs close to  $Re_x = 10^5 - 10^6$ , with a laminar portion of the plate around 56% for  $Re = 10^{6.25}$  and 0.03% for  $Re = 10^{9.5}$  (SCHLICHTING H., 2000). Transition is therefore most important, at least for engineering purposes, at

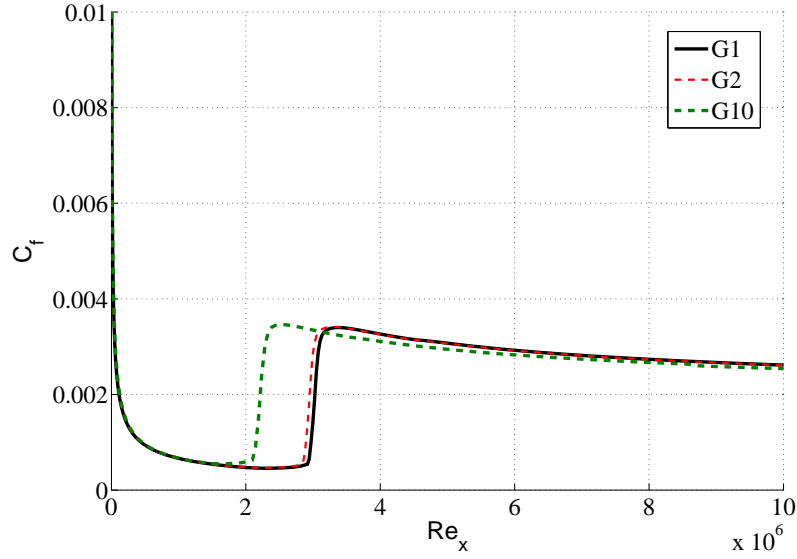


Figure A.10: Grid sensitivity of  $C_f$  line for  $Re = 10^{7.5}$ .

moderate Reynolds numbers. Nevertheless, one should not deem it non-relevant for full-scale structures, as most model tests of ships and offshore structures (and some full-scale offshore structures, such as risers) occur at those moderate Reynolds numbers and their results are used to the design of these structures. It is thus important to understand and interpret these small-scale tests results in order to correctly extrapolate them to higher Reynolds numbers.

As observed by Wilcox (1993) with  $k-\omega$  model, the following events take place for a calculation with the flat plate: the computation starts in a laminar region with  $k = 0$  in the boundary layer and a small free-stream value of  $k$ ; initially,  $P_k$  and  $P_\omega$  are small and dissipation of both  $k$  and  $\omega$  exceed production and energy is entrained from the free-stream and spreads through the boundary layer by molecular diffusion; at the critical Reynolds number,  $Re_{xc}$ , production overtakes dissipation in the  $k$  equation and turbulent kinetic energy is amplified in the boundary layer together with eddy viscosity - this is the onset of transition;  $k$  continues to grow and, further downstream, production overtakes dissipation in the  $\omega$  equation and  $\omega$  is amplified until balance is found in the  $k$  equation - with that, transition of the boundary layer is complete.

Bearing the above elements in mind, consider figure A.11. It shows friction coefficient from calculation with all four models compared to theoretical lines for laminar and turbulent solutions (equations A.3 and A.4, respectively) for the case  $Re_L = 10^{3.5}$ . In this case, all models exhibit consistent laminar character, as one should expect for such a low Reynolds number. Even with reasonable velocity gradient near the wall, this is not high enough to trigger large production of  $k$  and  $\nu_t/\nu > 1$ , which would indicate turbulent behavior.

Rumsey and Spalart (RUMSEY; SPALART, 2008) have observed that the transition location for the SST model occurs around  $Re_x = 40,000$  for low Mach numbers ( $Ma = 0.2$ ) and SA yields transition at  $Re_x = 20,000$  for the same situation. Wilcox (1993) has identified a lower transition onset for the  $k - \omega$  model at around  $Re_x \approx 12,000$ . The Tollmien-Schlichting waves do not begin forming until  $Re_x = 90,000$ , according to Schlichting H. (2000). It is quite clear that assessment of such turbulence models should not be merely done regarding their transition-prediction capability as their modeling focus and development is upon fully turbulent flows. However, the point made here is that transitional flows are dealt with in engineering applications, for instance in model tests and laboratory experiments. Therefore, the transition-prediction performance of these models cannot be disregarded for such applications and complementing them with e.g. the LCTM is viable alternative as it was devised exactly to cope with this type of flow. In this sense, Rumsey & Spalart (2008) have also advocated to use LCTM or other appropriate models meant to deal with transition.

Figure A.12, in which friction coefficients are presented for  $Re = 10^{6.5}$ , illustrates the same behavior observed by Rumsey and Spalart: an artificially early transition for both SST<sup>1</sup> and SA. Moreover,  $k - \sqrt{kL}$  also displays the same behavior. It is interesting to note, furthermore, that the SA and  $k - \sqrt{kL}$  lines display a mild transition, in which laminar behavior does not really occur. The SST, on the other hand, displays a sharp and short transition length, in which the eddy viscosity increases rapidly and so does the friction coefficient. This was also noted by Rumsey (2007).

Differently from the other models, The LCTM does not show any sign of transition to turbulent boundary layer, which in turn, results in laminar friction coefficients. In this case, although gradients are indeed high enough to trigger the turbulent production in SST, SA and  $k - \sqrt{kL}$ , the empirical correlations embedded in the LCTM prevent the production term from growing all over the boundary layer, thus preventing turbulent behavior. It is evident that this is a qualitative result, where no experimental counterpart is showed for these idealized conditions. It is therefore, not consistent to label behavior as “right” or “wrong”. Comparison with experimental results will be presented further ahead in the paper with the purpose of analyzing consistency with reality.

Figure A.13 shows friction coefficient distributions for  $Re_L = 10^{9.5}$ , a high Reynolds number, for the four models together with laminar and turbulent boundary layer analytical solutions. At this high Reynolds number, all three turbulence models perform their best

---

<sup>1</sup>Rumsey showed that SST displays an inconsistent grid-dependent transitional behavior due to the turbulence decay in the field, for which a remedy is to impose certain free-stream and floor values for the turbulent quantities. This indeed can solve the grid-inconsistency behavior but, of course, not transition location.

as the boundary layer is, in fact, mostly turbulent. Transition is seen with LCTM at  $Re_x \approx 4 \times 10^6$ , which corresponds to roughly 0.15% of the plate length. Transition to turbulent behavior occurs very early in the boundary layer and, for such a high Reynolds number, it is almost irrelevant for the force results: the drag forces calculated with SST and LCTM varies only about 2%, which is comparable with the uncertainty levels.

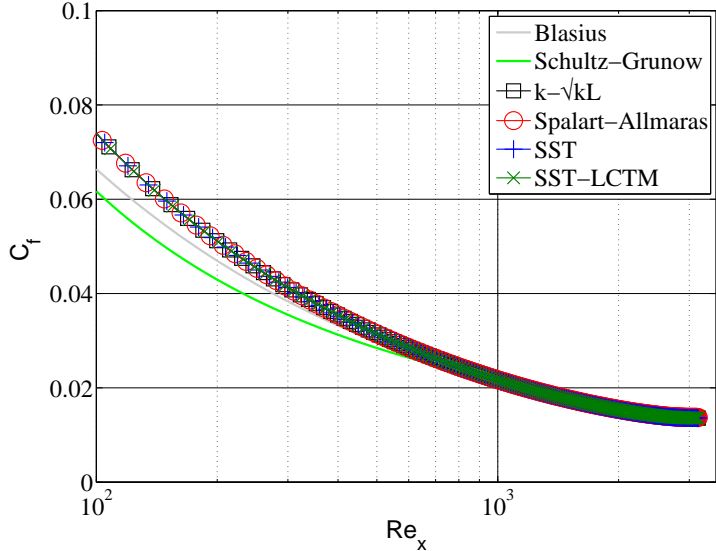


Figure A.11: Friction lines for  $Re = 10^{3.5}$ . For this Reynolds number, behavior is expected to be fully laminar and all turbulence models here exhibit consistent solutions.

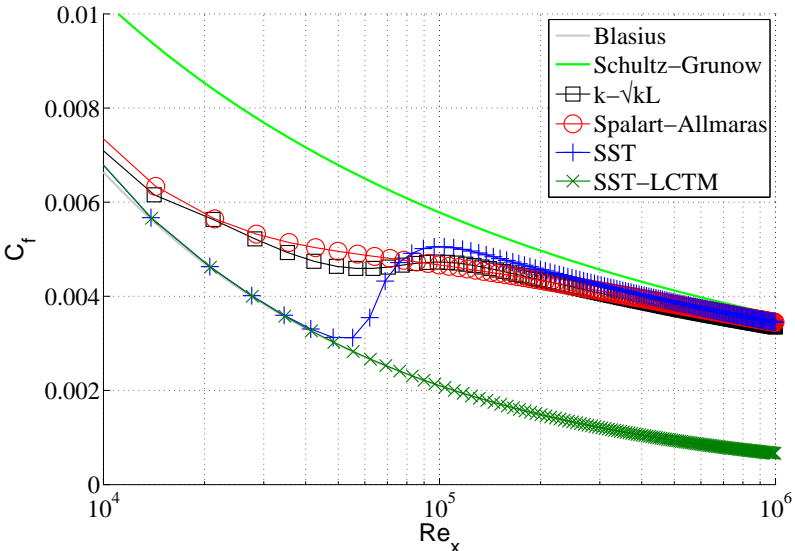


Figure A.12: Friction lines for  $Re = 10^{6.0}$ . This Reynolds number fall into the range of transitional numbers and only LCTM does not predict turbulent behavior.

Attention is now focused on what happens very close to the wall with SST and LCTM. Figures A.14 and A.15 show the  $u^+ - y^+$  relations for, respectively,  $Re = 10^{6.5}$  and

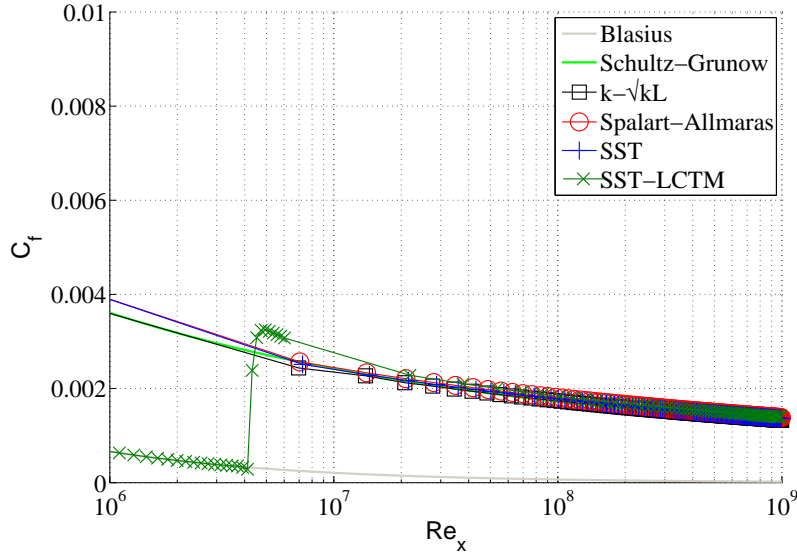


Figure A.13: Friction lines for  $Re = 10^{9.5}$ , a fully turbulent Reynolds number.

$Re = 10^{9.5}$  at  $x/L = 0.50$ . In the first plot,  $x/L = 0.50$  corresponds to  $Re_x = 1.58 \times 10^6$ : figure A.12 indicates that SST has transitioned to turbulence at this position, whereas LCTM is still laminar. Note that LCTM friction line follows the laminar trend  $u^+ = y^+$  (viscous sublayer solution), whereas SST follows the log layer. As intermittency factor remains  $\gamma = 0$ , turbulence production is prevented and thus friction remains laminar. On the other hand  $x/L = 0.50$  for  $Re = 10^{9.5}$  corresponds to  $Re_x = 1.58 \times 10^9$  at which position, both lines are turbulent, comprising viscous sublayer, buffer and log layers in a very similar way. It is reassuring to notice that LCTM behaves very similarly to SST when the transition model predicts fully turbulent flow.

Figures A.16 and A.17 show, respectively,  $k^+$  and  $\nu_t/\nu$  vs.  $y^+$  for  $Re = 9.50$  at  $x/L = 0.50$ . SST and LCTM display similar trends in both plots with an increase of turbulent kinetic energy and eddy viscosity as distance from the wall is increased.

### A.2.5 Influence of Inflow Turbulence

Transition is largely influenced by upstream turbulence levels, even more than the usual turbulence models. The larger the inflow turbulence, the earlier transition takes place. Moreover, bypass transition can be promoted if inflow turbulence is large enough. Conversely, laminar inflow tends to produce natural transition, as with all the results showed above. In this section, one can observe how the inflow turbulence values can influence transition.

In order to initialize and set the inflow values for turbulent kinetic energy and turbulence

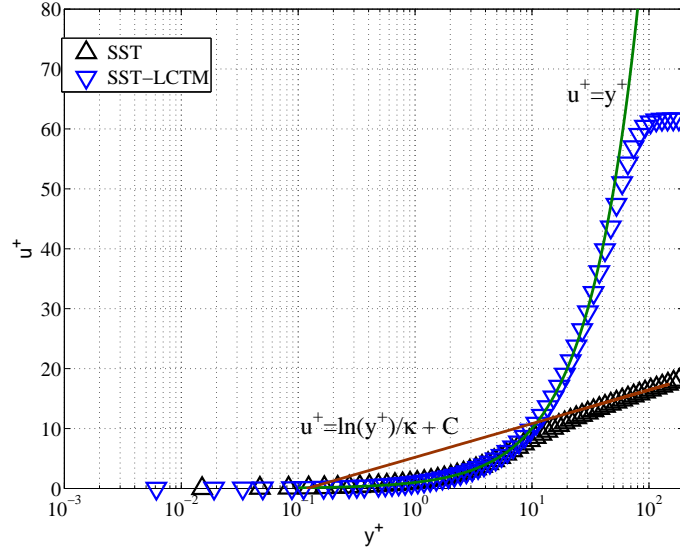


Figure A.14: Near wall behavior for  $Re = 10^{6.5}$  at  $x/L = 0.50$  ( $Re_x = 1.58 \times 10^6$ ) with SST and LCTM.  $u^+ - y^+$  relations differ in the two models.

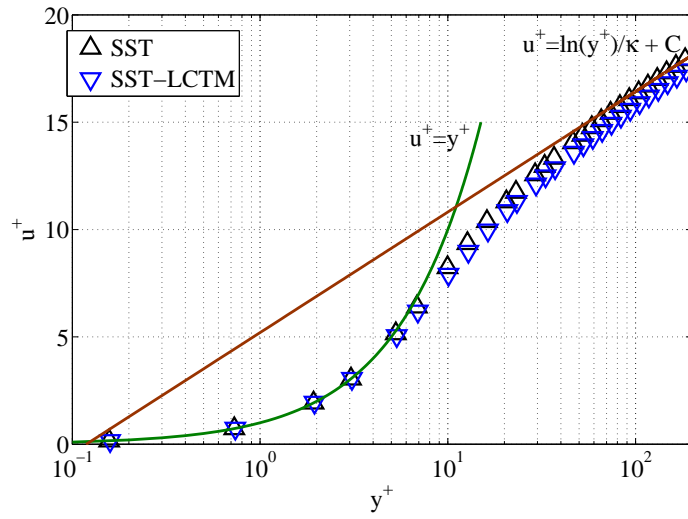


Figure A.15: Near wall behavior for  $Re = 10^{9.5}$  at  $x/L = 0.50$  ( $Re_x = 1.58 \times 10^9$ ) with SST and LCTM. Both boundary layers are turbulent and  $u^+ - y^+$  relations show nearly no difference.

intensity, most codes (as indeed with ReFRESCO) set values for eddy viscosity by means of a relation with laminar viscosity,

$$f = \mu_t / \mu, \tag{A.5}$$

because it is easier to relate to that than to kinetic energy itself. Taking into account this ratio one may consider two common ways of setting the turbulence quantities  $k, \omega$ :

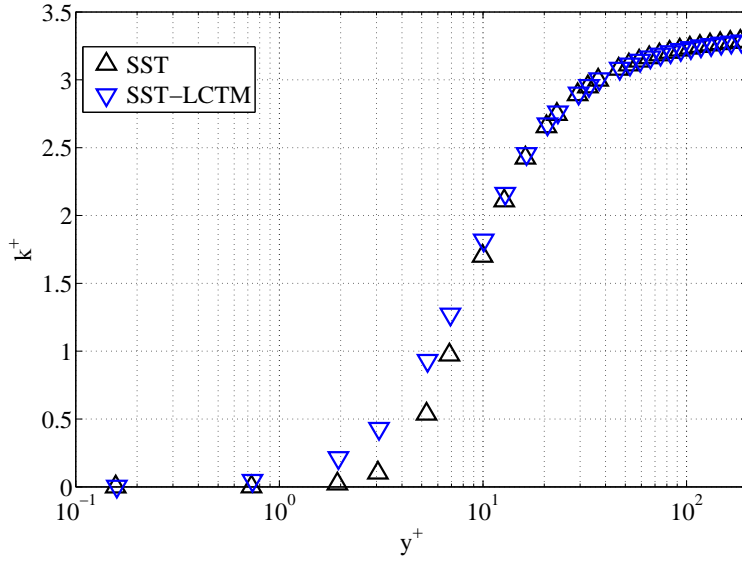


Figure A.16:  $k^+ - y^+$  relation for  $Re = 9.50$  at  $x/L = 0.50$  with SST and LCTM. Differences in  $k^+$  are very small, but one notices a milder transition of boundary layer with LCTM.

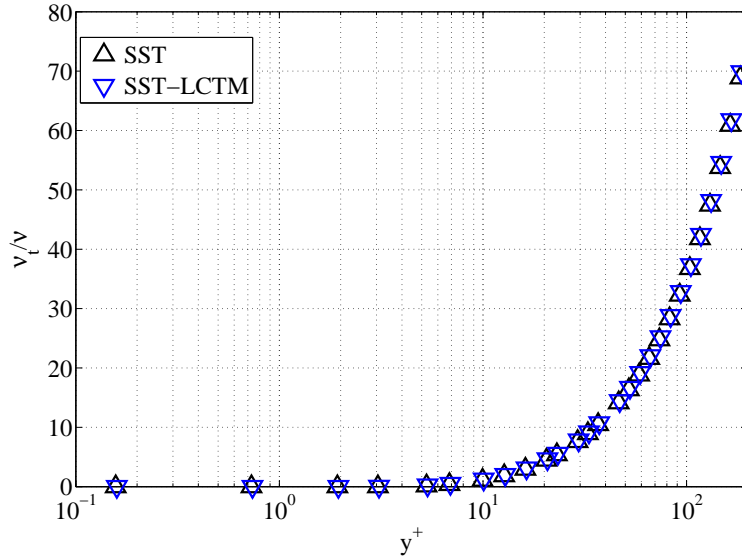


Figure A.17:  $\nu_t/\nu - y^+$  relation for  $Re = 9.50$  at  $x/L = 0.50$  with SST and LCTM. Almost no differences are observed.

- By setting  $f$  or  $\mu_t/\mu$  and computing  $k$  and  $\omega$  using dimensional considerations,

$$k = f\nu \times 10 \frac{U_{ref}}{L_{ref}}, \quad (\text{A.6})$$

and,

$$\omega = 10U_{ref}/L_{ref}. \quad (\text{A.7})$$

- By setting  $\mu_t/\mu$  and the turbulence intensity  $Tu$ , and computing  $k$  and  $\omega$  using

$$k = \frac{3}{2}Tu^2U_iU_i, \quad (\text{A.8})$$

and,

$$\omega = \frac{k}{f\nu}. \quad (\text{A.9})$$

One might consider at a glance that the options are equivalent, but as also noted by Spalart & Rumsey (2007) there is an important difference related to the turbulence decay that each option determines. Investigation is done on these two options of setting inflow turbulence and their respective influence on the LCTM.

Consider figures A.18 and A.19, in which the inflow turbulence is varied for  $Re = 6.50$  and  $Re = 9.50$ , respectively. The two inflow options are investigated in four different results:  $\nu_t/\nu = 0.01$ ;  $\nu_t/\nu = 100$ ;  $\nu_t/\nu = 100 - Tu = 1\%$ ;  $\nu_t/\nu = 100 - Tu = 10\%$ . Results are in fact consistent in the sense that increasing turbulence (in either option) shifts the transition region to an earlier position. Moreover, as the equations above show,  $\nu_t/\nu = 0.01$  corresponds to very low  $k$  and thus  $Tu$  levels. This is then appropriate when an ideal laminar inflow is desired. Let us now observe the lines for  $\nu_t/\nu = 100$ : evidently, transition is earlier for  $Tu = 10\%$  than for  $Tu = 1\%$ , but the condition  $\nu_t/\nu = 100$  alone determines yet another turbulence level at the inflow. As a matter of fact, the turbulence intensity distribution in the field, within and near the boundary layer is more relevant than the level in the inflow, but the second is heavily influenced by the first. Indeed, as observed by Spalart & Rumsey (2007) lower inflow eddy viscosity implies larger turbulence decay rates and conversely larger inflow turbulence values imply larger decay rates (these are numerical rather than physical observations). This clearly influences transition onset since the correlations are basically functions of turbulence levels.

## A.3 ERCOFTAC calculations

### A.3.1 Setup and Settings

The purpose of this section is to compare the numerical results against ERCOFTAC (T3A, T3B and T3A-) and Schubauer & Klebanoff (1955) (S&K) experimental data, see table A.2. The ERCOFTAC data covers bypass transition cases whereas the S&K experiments exhibit natural transition. Although the domain and grid will not be the same

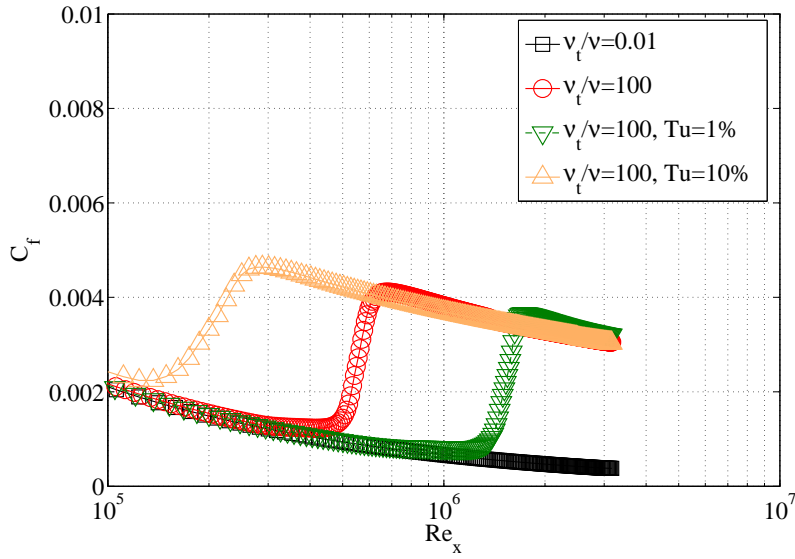


Figure A.18: Sensitivity of the friction coefficients to variations in the inflow turbulence for  $Re = 10^{6.5}$ .

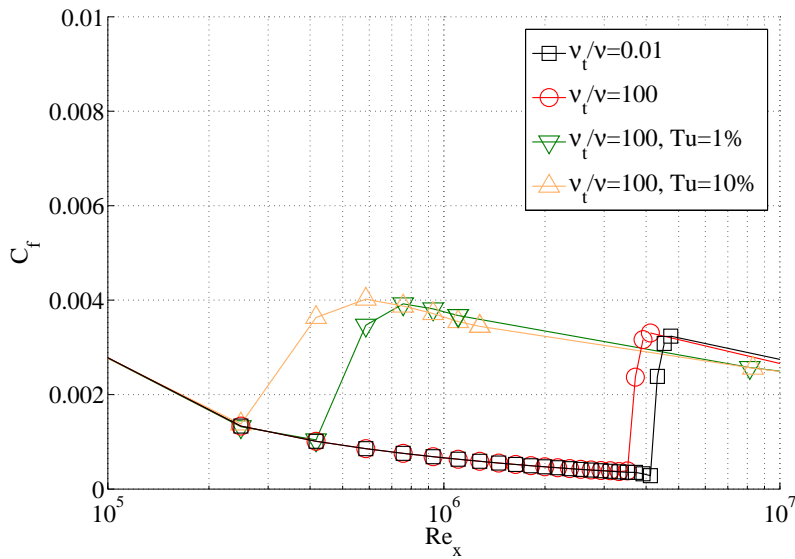


Figure A.19: Sensitivity of the friction coefficients to variations in the inflow turbulence for  $Re = 10^{9.5}$ .

as in the previous investigation, the resolution and stretching of the grid is maintained as well as the numerical setup.

The inflow conditions are velocity ( $U_\infty$ ) and eddy viscosity ratio  $\mu_t/\mu$ , and usual water properties ( $\rho = 998 \text{ kg/m}^3$  &  $\mu = 1.002 \times 10^{-3} \text{ kg/ms}$ ), such that the velocity from the experiments is scaled appropriately. The four test-cases are detailed in table A.2, in which one notices two sets of results. In the first (EV), the inflow value of eddy viscosity is fixed, as in the first option described above. In the second set (EV+TU), both eddy

viscosity values and turbulence intensity on the inflow were fixed. The eddy viscosity and turbulence intensity at the inlet were controlled such that the measured value of free stream turbulence intensity at the first data point of the calculation matched the experimental results.

In the original testing of the LCT models, Langtry & Menter (2009) reduced the inflow region to help achieve the correct turbulence intensity in a similar way, and the turbulence intensity was specified at the inflow. In another article, which aims to validate a different implementation of the LCT models (MALAN; SULUKSNA; JUNTASARO, 2009), the inflow region was reduced again and the values for  $k$  and  $\omega$  were specified at the inflow providing a closer match to experimental results.

Qualitative tests were also done to determine if there was any impact on the results due to the top boundary condition. The results were similar to the previous domain - the height and type of the boundary was insignificant.

Table A.2: Test cases and inlet conditions for the transition test cases.

Case	Velocity, m/s	(EV) $\nu_t/\nu$	(EV+TU) $\nu_t/\nu-Tu(\%)$
T3A	0.361	90	90-3.3
T3B	0.629	600	600-6.5
T3A-	1.325	28	28-0.874
S&K	3.353	7.8	7.8-0.3

### A.3.2 Nominal Results

In this section, analysis is done on the results obtained applying the setup and settings above for the EV and EV+TU options. Let us firstly present the uncertainty values and order of convergence results of the ERCOFTAC  $C_D$  calculations in figure A.20. As noticed in the “Numerical Friction Line” results, uncertainties are kept below 8% and the order of convergence is between  $p = 1.0$  and  $p = 2.0$ .

Firstly notice the turbulence decay computed 0.1m above the plate compared to the measured in the experiments in figures A.21, A.23 and A.22 for, respectively, T3A, T3B and T3A- with both EV and EV+TU. The S&K (SCHUBAUER; KLEBANOFF, 1955) results are not shown because no experimental data for turbulence decay was reported. These plots show that the EV option invariably promotes larger turbulence decay rate than the EV+TU, which is not physically consistent with experiments. On the other hand, the EV+TU option did provide the correct turbulent decay and turbulence values compared to the experiments. The improved capacity of capturing the turbulence decay and turbulence values in the field is essential for the transition model as correlations rely

on turbulent intensity in the field to determine transition onset and length. Therefore, in order to apply the LCTM correctly, it is vital to compute turbulence intensity rightly in the entire field independently from LCTM itself.

Cases T3A and T3B (figures A.21 and A.23, respectively) show larger inflow turbulence intensities than T3A- (figure A.22), which also determines a faster decay in the first two cases than in the second one. This is entirely determined by the turbulence model itself and not the transition model.

The following results in figures A.24, A.25, A.26 and A.27 show, respectively, the S&K, T3A-, T3A and T3B friction lines calculated using both EV and EV+TU options. Note that the EV+TU results show an overall slightly better comparison with the experiments than the EV option. This is due to a more accurate prediction of the turbulence decay, which in turn allows the correlations to provide more accurate transition onset and length and thus more accurate friction lines. Again, note that the cases T3A and T3B are emulating more abrupt transition process due to high inflow turbulence. The amplitude of the deep is missed in  $C_f$  for that case of very large turbulence level. On the other hand, T3A- and S&K emulate natural transition process, occurring at very low inflow turbulence levels. In those cases, LCTM performs its best.

### A.3.3 Analysis of the Flow Field

In this section, some features of the flow field are investigated by inspecting the boundary layer very close to the plate. Attention is focused on the T3A- case representing natural transition and on T3B for the bypass case. Figures A.28, A.29 and A.30 show, respectively, eddy viscosity, turbulence intensity and intermittency factor fields for  $T3A-$  on the left and  $T3B$  on the right. We readily notice in figure A.28 that  $T3B$  displays a much thinner laminar region due to the larger inflow turbulence and figure A.29 shows that

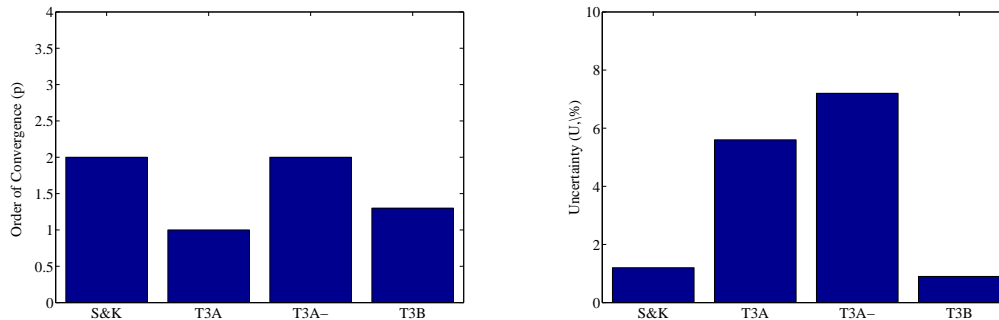


Figure A.20: Order of convergence ( $p$ ) of the ERCOFTAC calculations on the left and uncertainty results ( $U, \%$ ) on the right.

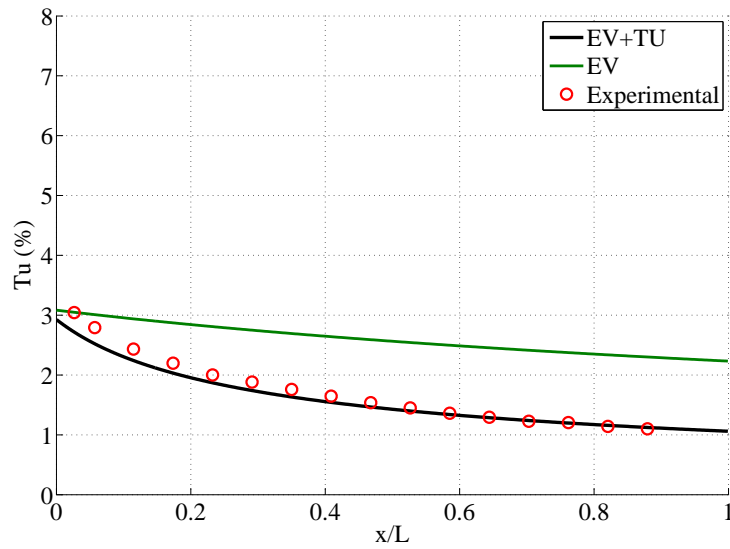


Figure A.21: Turbulence intensity measured at an horizontal line placed 0.1m above the plate for the case T3A.

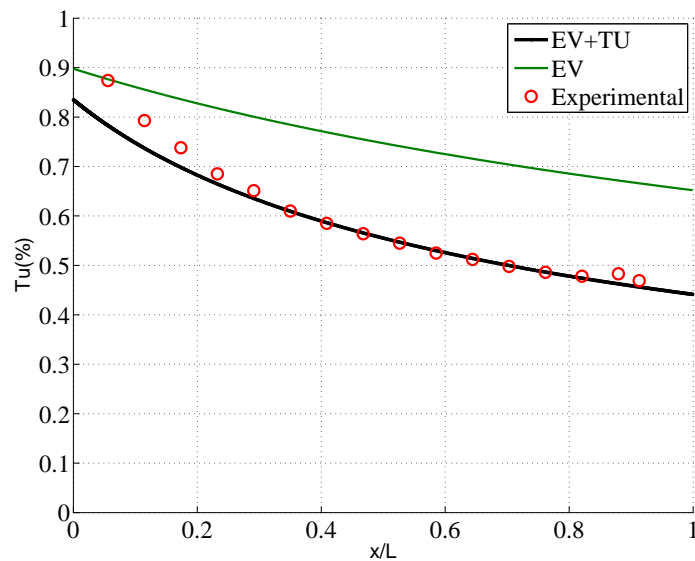


Figure A.22: fig:Turbulence intensity measured at an horizontal line placed 0.1m above the plate for the case T3A-.

the zones of high eddy viscosity correspond to the zones of high turbulent intensity. It is also interesting to notice in figure A.30 that where intermittency is near zero, turbulence intensity is kept at low values and thus transition is delayed which corresponds to reality. Let us now relate the field observations with the previous results in figures A.25 and A.27 for  $T3A-$  and  $T3B$ , respectively. In  $T3A-$ , the friction line is turbulent as of  $x/L \approx 0.8$ , which is also seen in the field plots of figures A.28, A.29 and A.30. On the other hand, for  $T3B$ , turbulent behavior is present upstream, at  $x/L \approx 0.09$ , for which reason almost no laminar behavior is seen in the field plots of the same figures.

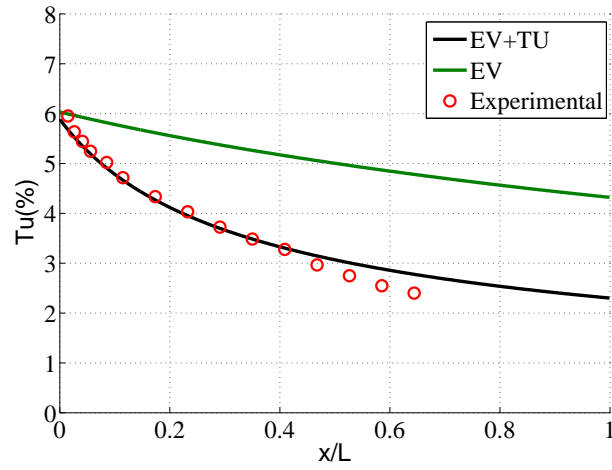


Figure A.23: Turbulence intensity measured at an horizontal line placed 0.1m above the plate for the case T3B.

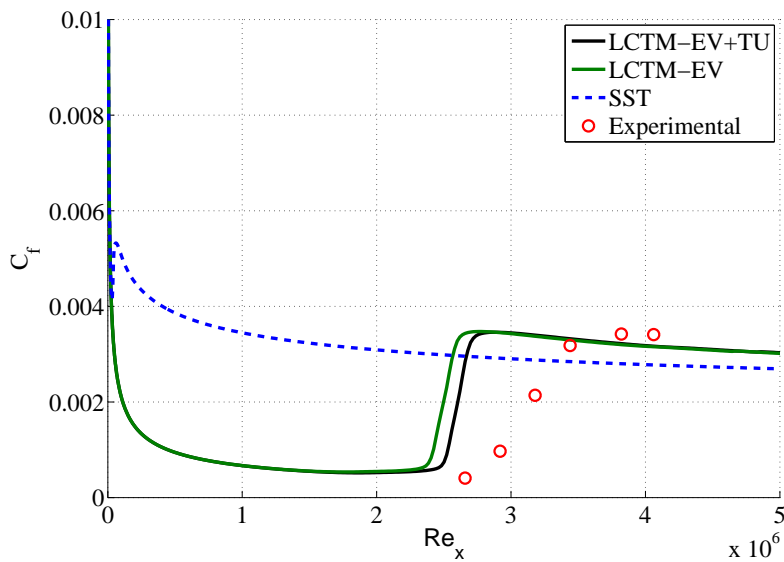


Figure A.24: Friction lines obtained with SST and LCTM models in comparison with experimental results (SCHUBAUER; KLEBANOFF, 1955) for case S&K with EV and EV+TU. EV+TU shows better comparison with the experiments because of a better turbulence decay prediction.

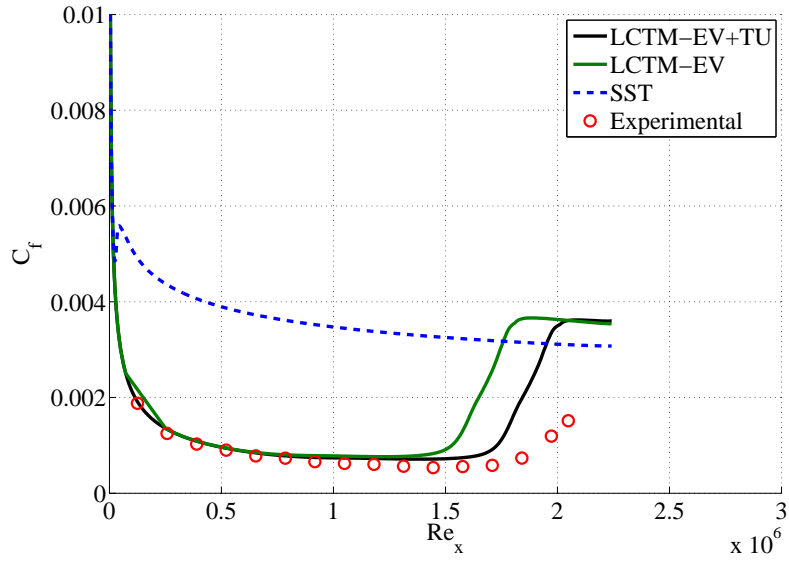


Figure A.25: Friction lines obtained with SST and LCTM models in comparison with experimental results (ERCOFTAC, 1990) for case T3A- with EV and EV+TU. EV+TU shows better comparison with the experiments because of a better turbulence decay prediction.

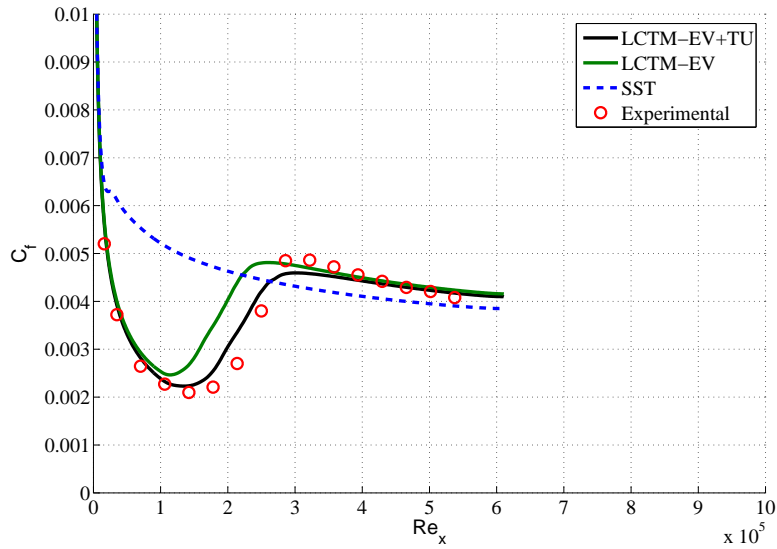


Figure A.26: Friction lines obtained with SST and LCTM models in comparison with experimental results (ERCOFTAC, 1990) for case T3A with EV and EV+TU. EV+TU shows better comparison with the experiments because of a better turbulence decay prediction.

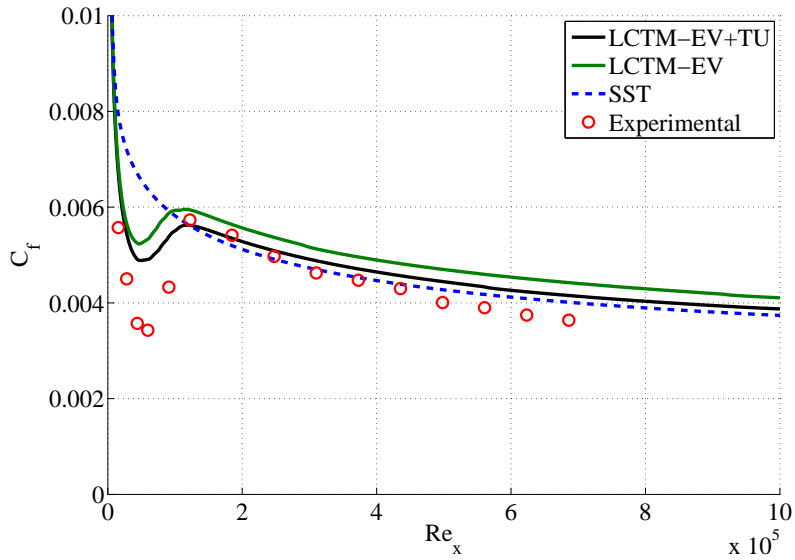


Figure A.27: Friction lines obtained with SST and LCTM models in comparison with experimental results (ERCOFTAC, 1990) for case T3B with EV and EV+TU. EV+TU shows better comparison with the experiments because of a better turbulence decay prediction.

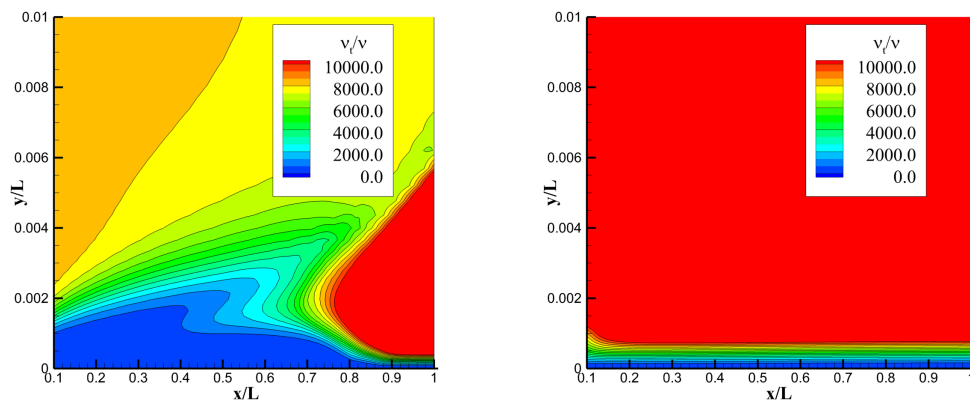


Figure A.28: Non-dimensional eddy viscosity field for case *T3A-* on the left plane and *T3B* on the right. Both are done with EV+TU option.

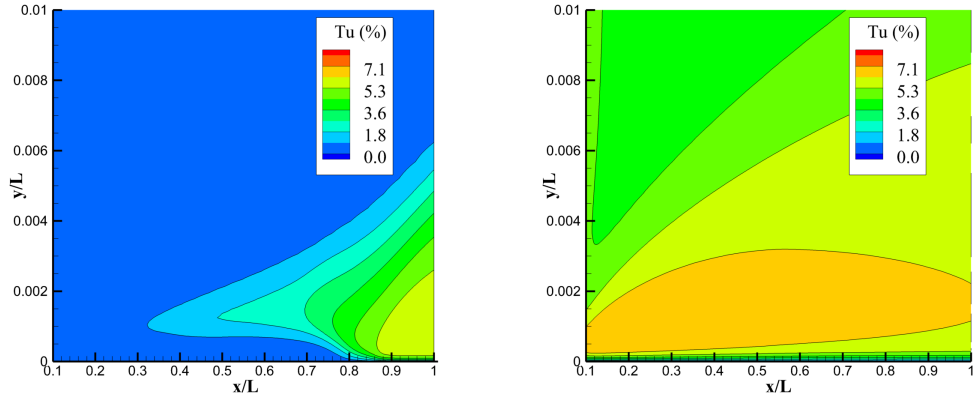


Figure A.29: Turbulence intensity field for case  $T3A-$  on the left plane and  $T3B$  on the right. Both are done with EV+TU option.

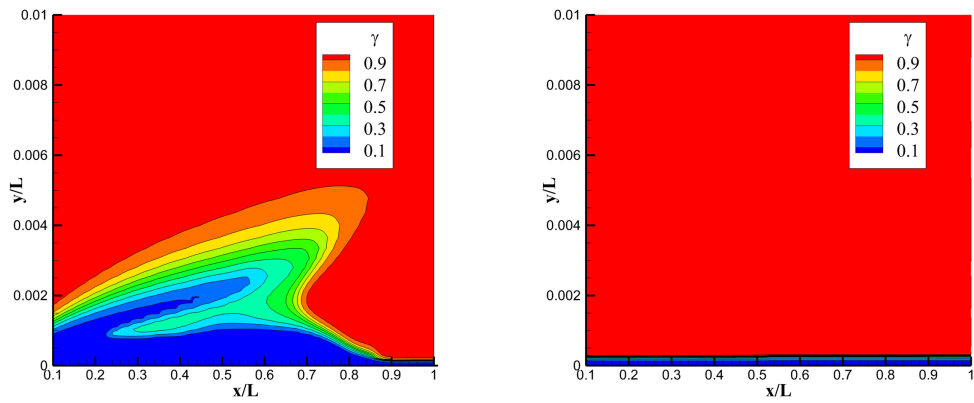


Figure A.30: Intermittency factor field for case  $T3A-$  on the left plane and  $T3B$  on the right. Both are done with EV+TU option.